

Alma Mater Studiorum – Università di Bologna

DOTTORATO DI RICERCA IN
SCIENZE CHIMICHE

Ciclo XXVII

Settore Concorsuale di afferenza: 03/B1

Settore Scientifico disciplinare: CHIM/03

PHOTOPHYSICAL INVESTIGATION OF LIGHT-HARVESTING SYSTEMS
FOR SOLAR-TO-FUEL CONVERSION

Presentata da: MARIA PIA GULLO

Coordinatore Dottorato
Prof. Aldo Roda

Relatore
Prof. LUCA PRODI

Correlatore
Dott. ANDREA BARBIERI

Esame finale anno 2015

TABLE OF CONTENTS

Abstract.....	1
 Chapter 1	
1. Introduction.....	3
1.1. Sun as the most convenient energy source.....	3
1.1.1. Some hints about natural photosynthesis.....	5
1.2. Artificial photosynthesis: new frontier for solar energy conversion...	6
1.2.1 Artificial Antenna Systems.....	7
1.2.1.1. Porphyrins and dendrimers as antenna systems.....	7
1.2.1.2. Transition metal complexes as antenna systems.....	11
1.3. Energy Transfer Theory.....	13
1.3.1. The Förster (Coulomb) mechanism.....	14
1.3.2. Dexter (exchange) mechanism.....	15
1.3.3. Energy Transfer in Photosynthetic Process.....	16
1.4. Dye sensitized solar cells for solar energy conversion.....	17
1.4.1. Solar Conversion Efficiency and Dye Sensitization.....	19
1.5. Excited States of Transition Metal Complexes: general remarks.....	20
1.6. References.....	24
 Chapter 2	
2. Pt(II), Ru(II), Ir(III) and Rh(III) coordination assemblies with π-bonded bidentate quinonoid and thioquinonoid organometallic ligands: examples of design of chromophores with improved photophysical properties.....	27
2.1. Introduction.....	27
2.2. Results and Discussion.....	29
2.2.1. Ir(III), Rh(III) and Ru(II) coordination assemblies with π -bonded Catecholate ligand.....	29
2.2.1.1. Cyclometallated Ir(III) and Rh(III) coordination assemblies with π -bonded Catecholate ligand.....	30
2.2.1.2. Polypyridyl Ru(II) heteroleptic complexes with quinonoid organometallic linker.....	40
2.2.2. Square-planar Pt(II) chelated by novel (Catecholate /Benzenedithiolate)M complexes.....	43
2.2.2.1. Bipyridyl Platinum(II) with π -bonded Catecholate ligand.....	44
2.2.2.2. Neutral Cyclometalated Platinum(II) Complexes with π -bonded Benzenedithiolate.....	49
2.3. Conclusions.....	52
2.4. References.....	53

Chapter 3

3. Photophysical investigation of multichromophoric arrays arranged around different types of rigid organic scaffolds.....	57
3.1. Introduction.....	57
3.1.1. Antenna systems.....	57
3.1.1.1. Triptycene.....	58
3.1.1.2. Spirobifluorene.....	59
3.1.2. Systems for lighting.....	59
3.1.2.1. White emission and Julolidine.....	60
3.1.2.2. Iridium(III) complexes.....	61
3.2. Results and Discussion.....	61
3.2.1. Antenna systems.....	61
3.2.1.1. Triptycene series.....	61
3.2.1.2. Spirobifluorene series.....	75
3.2.2. Systems for lighting.....	82
3.2.2.1. Julolydine series.....	82
3.2.2.2. Benzoxazolyl-phenolate Iridium(III) complexes.....	99
3.3. Conclusions.....	106
3.4. References.....	107

Chapter 4

4. Self-organizing corroles as novel structural platform for the artificial photosynthesis.....	112
4.1. Introduction.....	112
4.1.1. Corroles.....	112
4.1.2. Self-assembly.....	114
4.2. Results and Discussion.....	115
4.2.1. Absorption.....	115
4.2.2. Emission at RT temperature.....	117
4.2.3. Emission at low temperature and solvent effect.....	119
4.2.3.1. Lifetime Analyses.....	122
4.3. Aggregation.....	124
4.4. Conclusions.....	128
4.5. References.....	128

Chapter 5

5. Photophysical investigation of PSI immobilized on hematite surface for solar to fuel conversion.....	130
5.1. Introduction.....	131
5.2. Results and discussion.....	133
5.2.1. Nanostructuring of the PSI-LHCI-sensitized semiconductor	

substrates for the fabrication of a device sustaining both photocurrent production and H ₂ evolution.....	133
5.2.1.1. Construction of the PSI-based photoanode.....	133
5.2.1.2. I-V characterization and Investigation of photochemical activity.....	137
5.2.1.3. Sustained photo-electrochemical H ₂ production using PSI-LHCI-functionalised hematite/FTO photoanode.....	138
5.2.2. Photophysical investigation.....	140
5.2.2.1. Absorption.....	140
5.2.2.2. Emission.....	142
5.2.2.3. Energy transfer and Time resolved fluorescence analysis..	144
5.3. Conclusions.....	153
5.4. References.....	154

Chapter 6

6. Experimental Section.....	157
6.1. Absorption spectra.....	157
6.2. Emission spectra.....	157
6.3. Luminescence lifetime measurements.....	158
6.4. Transient absorption.....	158
6.5. Energy transfer.....	159
6.6. References.....	160

Chapter 7

7. Final Remarks.....	161
7.1. References.....	166

Abstract

In recent years, an increasing attention has been given to the design and preparation of new supramolecular systems with the goal to optimize their performances as antennas for light collection. This is a challenging task that finds great interest not only for studies of solar energy conversion but also in the fields of photonic and optoelectronic. The aim of this thesis, performed in the framework of the ESF-EUROCORES “SolarFuelTandem” project, was just the study of supramolecular systems capable of performing one of the basic action of the natural photosynthetic apparatus, such as the light energy collection.

A synthetic antenna should consist of a multichromophoric architecture with large UV-Vis absorption cross-section, panchromatic absorption, well-defined and fixed spatial orientation of the chromophoric components and suitable energy gradients between them, in order to funnel absorbed energy toward a specific site, through fast energy-transfer processes.

Among the systems investigated in this thesis, three suitable classes of compounds can be identified: 1) transition metal-based multichromophoric arrays, as useful models for antenna construction, 2) free-base *trans*-A₂B-phenylcorroles, as self-assembling systems to make effective mimics of the photosynthetic system, and 3) a natural harvester, the Photosystem I, immobilized on the photoanodic unit of a solar-to-fuel conversion device.

The discussion starts with the description of the results obtained with quinonoid organometallic systems, able to fulfil some of the above mentioned absorption requirements. The photophysical investigation of such compounds, in particular in the case of some Ru(II) polypyridin derivatives, display their ability as panchromatic absorbers, resulting from the introduction of the widely versatile metalated catecholate ligand.

The photophysical study has been extended to supramolecular architectures suitably organized in energy and space, through the introduction of different central molecular scaffolds, such as spiro-bifluorene and trypticene. The new trypticene-based Ir-Os supramolecular assemblies and the Pt-Ir-Os arrays bearing a spiro-bifluorene bridge exhibit fast and efficient energy transfer processes. And in both systems, collected photons are completely funnelled to the unique final collector Os-based, with efficiencies that approach unit, denoting for the arrays the suitability as models for the construction of efficient antenna systems.

The investigation has gone on moving towards another type of chromophoric systems, based on free-base *trans*-A₂B-phenylcorroles with different substituents on the *meso*-phenyl ring. Besides the expected good performances in terms of absorption and emission, these molecules, as result of a planned design, display the tendency to self-organize into dimers through intermolecular hydrogen bond. This behavior makes them good candidates as novel structural platform for solar energy conversion, by mimicking natural self-aggregates antenna systems.

To conclude the work, the photophysical analysis moved towards a natural light-harvester, immobilized on the hematite surface of the photoanodic unit of a bio-hybrid

dye-sensitized solar cell, also capable to sustain hydrogen evolution. The natural super-complex PSI-LHCI extracted from the extremophilic red microalga *C. merolae* displays just a slight distortion of its protein structure upon immobilization on the semiconductor surface and almost complete retention of the overall functionality in term of energy transfer efficiency.

The importance of the entire work is related to the need for a deep understanding of the energy transfer mechanisms occurring in supramolecular architectures, useful to gain insights and improve the strategies for governing the directionality of the energy flow in the construction of well-performing antenna systems.

Chapter 1

1. Introduction

1.1. Sun as the most convenient energy source

The energy crisis and the concomitant environmental emergency are nowadays some of the major global problems. Thus, the reduction of dependence on fossil fuels, such as coal and oil, and the development of technology to produce clean energy are tasks of primary importance.

The scientific community is still trying to find solutions for such emergency and solar energy conversion seems to be a suitable replay. Every hour actually, earth surface receives an amount of energy from the sun approximately equal to that produced from fossil fuels for global consume in one year. Moreover, the sun emits light with a wide range of wavelengths, going from the ultraviolet to the infrared and peaking in the visible (see **Figure 1.1**), enabling its collection by many kinds of artificial devices.

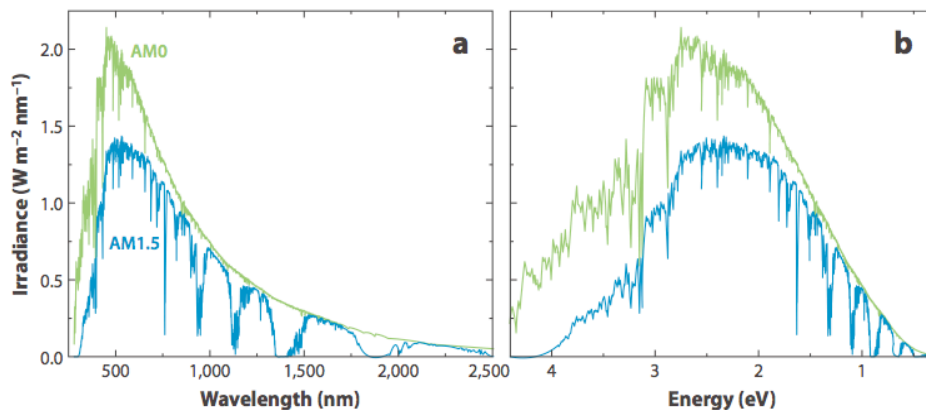


Figure 1.1. (a) Solar irradiance spectra outside the Earth's atmosphere [denoted by AM0 (green line)] and at sea level [denoted by AM1.5 (blue line)] displayed as a function of wavelength and (b) the same spectra plotted as a function of energy. (G. F. Moore and G. W. Brudwig, *Annu. Rev. Condens. Matter Phys.* 2011, **2**, 303-327)

Devices that, upon efficient harvesting of solar energy, are also able to perform its conversion into chemical energy, as in natural photosynthetic organisms, represent cleaner, renewable and theoretically more efficient method of energy production, compared to the utilization of fossil fuels.

The enormous potentiality of such approach is suggested by the big power expressed by natural photosynthesis in the solar energy conversion, since it is able to convert into dry biomass an amount of solar light ten times higher than the total amount of energy globally used by humans.¹

Photosynthetic organisms such as plants, algae and bacteria have developed efficient systems to harvest and to use solar source in driving their metabolic reactions: sunlight supplies the energy for the reduction of carbon dioxide to carbohydrates and for transformation of water into oxygen, useful to burn those fuels. Oxidation of the fuels

generates the energy needed to sustain life. To perform such processes, natural photosynthesis requires the combined and cooperative action of many components, as pictorially represented in **Figure 1.2**. First of all, an antenna system has to create a connection between the energy source and the active structure, absorbing efficiently the sunlight and transferring the collected energy to a reaction centre complex, able to convert solar into electrochemical energy (redox equivalents). Then, a water oxidation complex (D) has to use this redox potential to catalyse the conversion of water to hydrogen ions, electrons, stored as reducing equivalents, and oxygen. A second catalytic system (A) uses the reducing equivalents to produce fuels such as carbohydrates, lipids or hydrogen gas.

Inspired by such natural processes, in the last century, the main goal of the scientists has been to design well performing systems able to exploit the promising and powerful energy source that is the sun, through low-cost and efficient nanoscale photovoltaic or photoelectrochemical devices. To this purpose, many practical and cost effective technologies have been employed, achieving capture and direct conversion of solar energy in fuels capable of being stored and transported, as in natural photosynthesis. However, the problems of stability, efficiency and cost-effectiveness of such fully integrated devices still are the main bottleneck of the overall approach, particularly in systems achieving artificial photosynthesis, whose obtained performances are still below the efficiencies necessary for practical application.

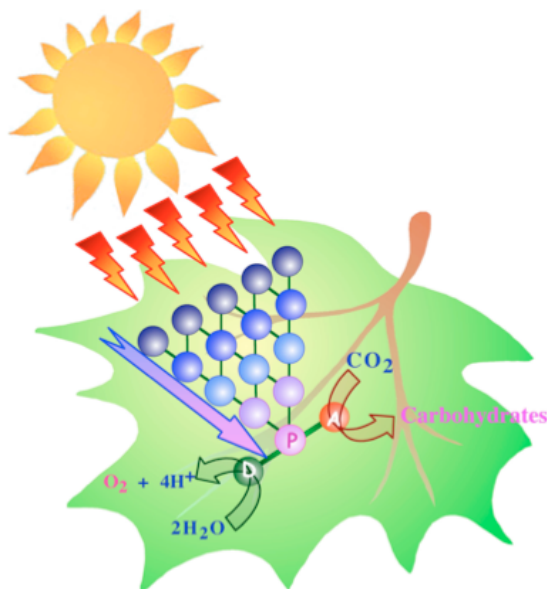


Figure 1.2. Simple scheme of natural photosynthetic process.

Thus, further research will be needed to identify the most promising artificial photosynthetic systems and to exploit their potential in larger scale than that of the laboratory production.

The first step for application and development of the photosynthetic bio-inspired technology is the complete understanding of the basic mechanisms driving the natural processes, in order to gain inspiration for construction of artificial structures and production of new suitable technology. Good practice examples of systems that using

solar light are able to transform it in storable energy, as in nature, are offered by artificial photosynthesis-based devices and dye sensitized solar cells.

1.1.1. Some hints about natural photosynthesis

Photosynthesis is the process used by some living organisms to absorb and then transform solar light into chemical energy for storage purposes, as mentioned above. In plants, algae and some bacteria families, this process is responsible for the release of molecular oxygen, as result of water oxidation, and of the removal of carbon dioxide from the atmosphere, used to produce carbohydrates (oxygenic photosynthesis). Some types of bacteria instead produce organic compounds but not oxygen, through the photosynthesis (anoxygenic photosynthesis), extracting electrons from molecules different from water.

The photosynthetic process in plants and algae occurs in small organelles known as chloroplasts that are located inside the cells, while the most primitive oxygenic cyanobacteria and anoxygenic photosynthetic bacteria, are not provided with such organelles.

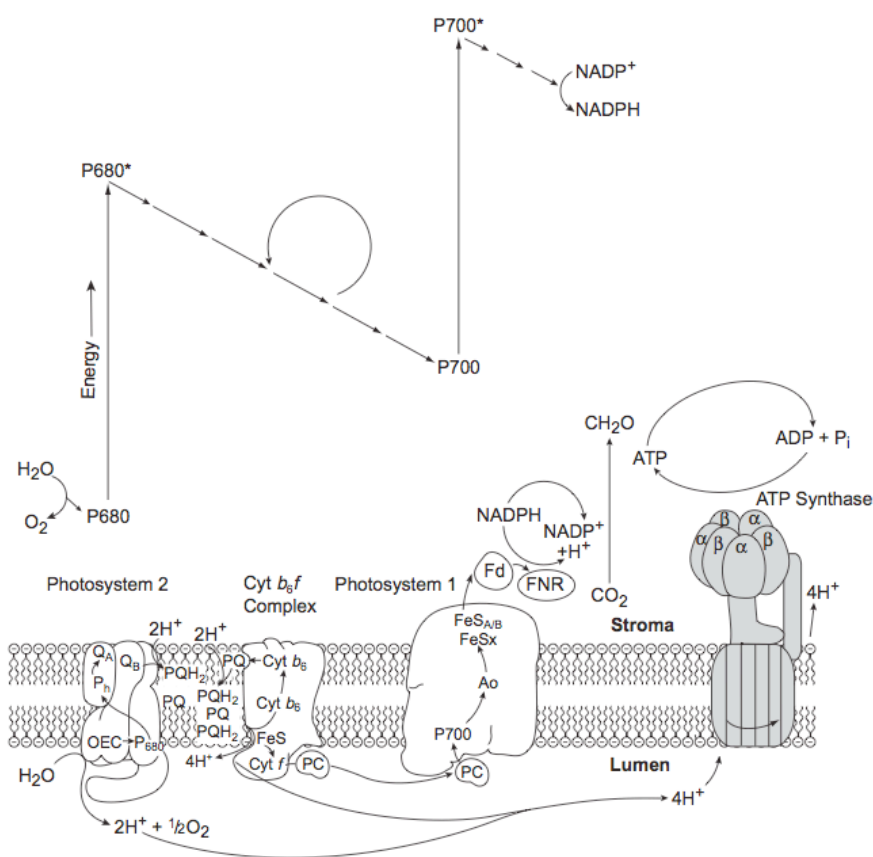


Figure 1.3. Schematic diagram of the non-cyclic electron transfer pathway found in oxygenic photosynthetic organisms. The upper diagram is an energetic picture of the electron transport pathway, incorporating the major reactions of photosynthesis. The lower diagram is a spatial picture, showing the major protein complexes and how they are arranged in the photosynthetic membrane. Neither view alone gives a complete picture, but together they summarize much information about photosynthetic energy storage. (R. E. Blankenship, *Molecular Mechanisms of Photosynthesis*, Blackwell Science Ltd, 2002)

Even if the single steps of the whole process can differ from one photosynthetic organism to the other, the basic principles involved are similar. Photosynthesis can be divided in two macro-phases, the one employing light, based on electron and proton transfer reactions, and the other one occurring in the dark, comprising the biosynthesis of carbohydrates from CO₂. To be more precise, in most cases, five distinct steps can be identified:

- absorption of solar energy
- transfer of excitation energy to a reaction centre by antenna pigments
- charge separation at a reaction centre and solar-energy-conversion into chemical redox energy
- migration of holes and electrons to spatially separate electron donors and acceptors
- partial storage of the absorbed excitation energy.

The main steps of the natural process are performed in oxygenic photosynthetic living organisms by two large multimeric pigment-protein complexes, denoted as Photosystem I (PSI) and Photosystem II (PSII), working in series and responsible for light harvesting, charge separation and charge transfer.

They are arranged around the common blueprint, containing a reaction centre (RC), with the P700 and P680 chlorophyll special pairs, coupled to light-harvesting complexes, LHCI and LHCII, respectively. Other important components are several protein subunits and hundreds of cofactors as chlorophylls, carotenoids, quinones Q_A and Q_B, iron-sulfur [4Fe-4S] clusters (in PSI), pheophytins, tyrosines (Tyr), [Mn₄Ca] clusters (in PSII), cytochromes and histidines² (see **Figure 1.2**). All these structures are located into the cellular organelles in which the photosynthetic process takes place.

1.2. Artificial photosynthesis: new frontier for solar energy conversion

The term “artificial photosynthesis” usually refers to a molecular based system properly designed in order to be able to convert solar light into chemical energy, by mimicking natural processes and structures. Artificial photosynthetic systems should most likely include four basic features: i) antennas for light harvesting; ii) a reaction centre for charge separation; iii) an oxidation and a reduction catalyst and iii) a membrane to provide physical separation of the products.

Every of these components have been extensively investigated and the knowledge so gained so far will greatly facilitate the development of efficient devices, leading to the production of affordable and energy-rich fuels from natural sunlight.

The literature about this topic is enormously extended but since the main subject of the present work is the study of new types of models for antenna systems, some indications about the development of such component will be discussed.

1.2.1 Artificial Antenna Systems

An antenna for light harvesting is a multicomponent system in which several chromophoric species convey the absorbed solar incident light to a common collector unit. Artificial light-harvesters are inspired to the natural corresponding complex, whose structural elegance and chemical efficacy have suggested the way to collect light by building artificial analogues, mostly involving porphyrin-based chromophores³.

To act as good antenna system a multichromophoric architecture should display large UV-Vis absorption cross-section, stability towards photodecomposition, a fully organized structure and well-defined spatial orientation of the chromophores, with fixed relative positions and orientations of the active molecular components.

Differently from natural systems, that transfer the excitation energy between weakly coupled chromophores via Förster-type mechanism⁴ and thus by through-space interactions, artificial arrays use more strongly coupled chromophoric units,⁵ communicating also through electron exchange interactions.

The energy transfer-based process imposes energetic requirements for the energy levels of the components: in particular the energy of the acceptor excited state has to be lower or equal to the energy of the excited state of the donor, and able to populate in the overall mechanism the final acceptor component with high efficiency. Thus, suitable energy gradients between the energy levels of the comprising units is another fundamental requirement in the design of novel supramolecular architectures acting as antennas.

Starting from this basic knowledge, in recent years big efforts have been devoted to the planning of proper assembling of artificial components,⁶ introducing new strategies to perform a good spatial and energetic control of the distinct units.

To ensure a suitable spatial orientation of the single building blocks, the choice of the connections between them is fundamental. Good linkages can ensure the necessary electronic coupling (through space or through bond) and thus fast energy transfer. In nature, the suitable arrangement between chromophores is achieved through the support of the thylakoid membrane in which they are embedded. Chemists instead, trying to mimic such organization, gained good results by means of covalent or coordination bonds, as linking-way for the molecular species instead of weak and not efficient intermolecular interactions, blocking in the desired positions the single units.

In the attempt to find compounds that could match all described requirements, many reported investigations have been carried out on porphyrins⁷ and transition metal complexes of the second and third rows with polypyridine-type ligands,⁸ also employed in multinuclear complexes.⁹

1.2.1.1. Porphyrins and dendrimers as antenna systems

The class of porphyrinoid macrocycles has always been largely investigated since they are the main molecules responsible for collection of solar light in natural antenna systems and reaction centres are just chlorophylls (Chls), belonging to such family with their metallated porphyrin-based structure.

Many efforts have been devoted to the investigation of their absorption and emission behaviour and also to the study of their remarkable aggregation properties, since in nature such chromophores are very suitably organized in aggregated structures.

One of the first examples of synthetic systems that try to approach such organization is that of covalently linked porphyrin dimers, displaying highly efficient excitation energy transfer over short distances.¹⁰ More recent results have been achieved by synthesizing cyclic porphyrin arrays, thus bigger than simple dimer (oligomers), with units linked by covalent, non-covalent or metal coordination bonds.¹¹ The arrays obtained through covalently bonded monomers have been the ones of most difficult synthesis but they have displayed the highest structural robustness. Instead non-covalently assembled arrays are usually affected by the environment and can be synthesized with relatively easy methods.

When such macrocycles contain the appropriate components, they tend spontaneously to self-aggregate and form large arrays, particularly when they are involved in organometallic systems, coordinating a metal centre (most reported examples of used metals are Zn, Re, Ru, Pd, and Pt)¹¹ through the pyridine nitrogen atoms. In such cases, the presence of the metal enables further types of aggregation interactions, increasing the self-aggregation tendency.

Further developments of covalent and non-covalent molecular design of light harvesting multiporphyrin arrays report systems with various molecular geometries, such as ring-, star-, windmill-shaped and dendritic architectures.

The arrangement of the components is fundamental because the three-dimensional displacement obviously affects the communication between chromophores and consequently the efficiencies of energy transfer processes.¹²

In particular, since crystal structure of the light-harvesting antenna complex LHCII of the purple bacterium *Rhodospseudomonas acidophila* has been demonstrated to comprise chromophoric units arranged in circular mode,¹³ many efforts have been devoted to the synthesis of cyclic arrays, to study excitation energy transfer along them. In particular, among the light-harvesting chromophores employed, there are not only porphyrins but also phthalocyanines, both closely related to chlorophyll derivatives.

Other examples are related to extremely long, porphyrin-based ribbons, wheels and rings.¹⁴ One case is that of *meso-meso* linked porphyrin rings composed of four, six, and eight 5,15-diaryl-substituted zinc porphyrins, characterized by a fully organized wheel-shaped arrangement. They display good properties as light-harvesting models, acting as platform for very efficient excitation energy hopping processes along the ring circuit with similar rates with respect to the natural photosynthetic antenna.¹⁵

Another example is represented by a series of *meso*-pyridine-substituted zinc(II) porphyrins, assembling into squares (**Sn**), and the corresponding *meso-meso*-linked dimers (see **Figure 1.3**), giving rise to three-dimensional boxes (**Bn**). In all the cases, well-defined spatial arrangement makes them suitable as model for light-harvesting antennas.¹⁶

Further studies have been focused on the synthesis of several types of clusters, dye-loaded zeolites¹⁷ and polymers, with good results.

All these systems, even if they perform efficient and fast energy transfer processes, display one important limit in term of channeling the absorbed light to the specific point of the structure, that in a real antenna should link the charge separation system. To overcome such limit, an energy gradient is required and thus in the arrays, more careful design and choice of chromophores have to be performed.

A good example of working antenna systems, without the above mentioned problem, is offered by a molecular heptad containing metal (**Figure 1.5**), composed of four real light-absorbing components such as two bis(phenylethynyl)anthracene and two borondipyromethene antennas linked to a hexaphenylbenzene core that also links two zinc porphyrins. The anthracene derivative absorbs strongly in the blue region of the spectrum between 450 and 500 nm, differently from porphyrin that in such region is almost transparent to the light. The two borondipyromethene (BODIPY) units absorb in the 450-550 and 330-430 nm ranges. The two kinds of antennas through singlet-singlet energy transfer, funnel excitation energy to the porphyrins, which in the end donates an electron to the self-assembled fullerene, generating a charge-separated state. Such system works efficiently both as antenna and reaction centre.¹⁸

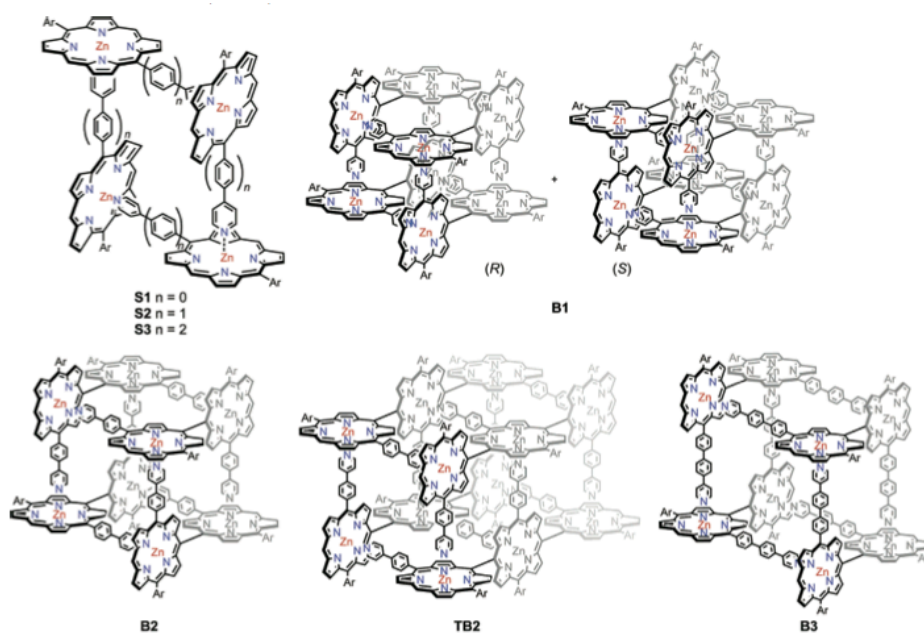


Figure 1.4 Structures of S1-S3, B1-B3, and TB2. (I. W. Hwang; T. Kamada; T. K. Ahn; D. M. Ko; T. Nakamura; A. Tsuda; A. Osuka; D. Kim, *J. Am. Chem. Soc.* 2004, **126**, 16187-16198)

Further investigation has been conducted taking into account the requirements in terms of arrangement of the single components for antennas production, driving the synthesis of systems with very particular structural organization, denoted as dendrimers. They have been designed inspired by the array of chlorophyll molecules of natural antennae of the green plants.

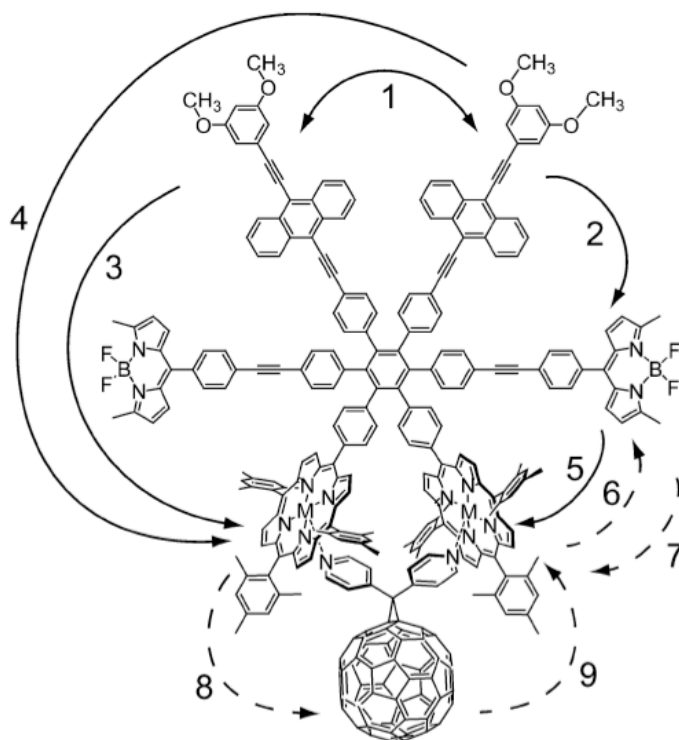


Figure 1.5. Singlet excitation energy and electron transfer pathways observed in heptad and model compounds. (Y. Terazono; G. Kodis; P. A. Liddell; V. Garg; T. A. Moore; A. L. Moore; D. Gust, *J. Phys. Chem. B* 2009, 113, 7147-7155)

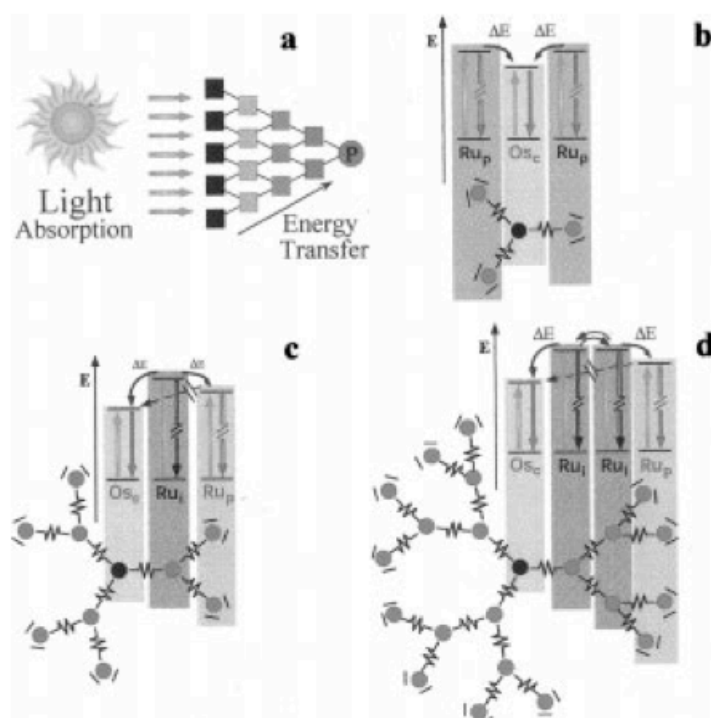


Figure 1.6. (a) Schematic representation of a light-harvesting system. Light is absorbed by an array of chromophores, and the electronic energy is then channelled to a reaction centre (P). (b) Energy migration patterns for tetranuclear compounds. Energy migration pattern for a decanuclear (c) and a docosanuclear (d) complex. (V. Balzani; S. Campagna; G. Denti; A. Juris; S. Serroni and M. Venturi, *Acc. Chem. Res.*, 1998, **31**, 26-34)

Such class of molecules is characterized by a hyper-branched three-dimensional structure with regular treelike units, allowing for the insertion of several chromophoric moieties. Besides the fully organic arrays, an interesting example of dendrimer is offered by a redox-active series, based on polypyridyl transition metal complexes.¹⁹ Architectures of Ru (II) or Os(II) polypyridine complexes have been largely employed as building blocks for such systems and the step-by-step synthetic strategies used allowed for a good control of electrochemical behaviour, absorption properties and direction of energy transfer process (**Figure 1.6**).

1.2.1.2. Transition metal complexes as antenna systems

In the past 30 years, extensive investigations have been devoted to metal complexes of the second and third transition rows with polypyridine-type ligands²⁰ because such systems seemed to satisfy most of the requirements postulated for a well performing antenna system.

The use of transition metal complexes as building blocks is very appealing for several reasons. In particular, they are very versatile and simple modifications of their structure allow to suitably tailoring the energetics (excited-state energies and redox potentials) by judicious choice of metals and ligands. Furthermore they possess defined geometries and the possibility to tune the strength of the ligand coordination from very strong to very labile.

Actually, metal coordination compounds, exhibiting absorption bands of metal-to-ligand charge transfer (MLCT) nature at relatively low energy, have been largely employed as photosensitizers.²¹ Literature offers a wide range of examples of molecular model systems based on transition metal complexes, designed taking into account their light absorption and excited-state electron transfer properties. Many examples involve as prototype complex $[\text{Ru}(\text{bpy})_3]^{2+}$ (bpy = 2,2'-bipyridine)²² that displayed such useful properties to make it a good model for the design of many other compounds and architectures.

The excited state of $[\text{Ru}(\text{bpy})_3]^{2+}$ responsible for the emission is a triplet metal-to-ligand charge-transfer (³MLCT) state, having an energy of about 2.12 eV with a long lifetime, close to 0.5 μs , and a luminescence quantum yield of 0.028.²³ Its relatively slow radiative deactivation process makes ³MLCT state available for many applications.

Anyway, it is clear that a single chromophore is not capable of efficiently powering artificial photosynthesis because first of all, it is very difficult for one molecule to absorb the complete range of the solar spectrum. Thus, the design of new multicomponent systems started, properly choosing units in order to reach systems with different chromophoric properties. First of all, the synthesis of dinuclear systems has been performed, followed by the preparation of nine tetranuclear²⁴ and six decanuclear²⁵ mixed-metal and/or mixed-ligand species.

As expected, the properties of each metallic building block tend to undergo perturbations upon incorporation into multicomponent systems, thus the behaviour of the new array is not always a mere sum of the features of the single components. The photochemical and photophysical behavior reported for mononuclear complexes might become very different from that of the corresponding dinuclear or polynuclear

derivatives due to appearance of intercomponent processes, such as electron and energy transfer, and due to the orbital mixing.

The new approaches in the preparation of multimetallic species are based on the decoration of starting metallic frameworks with additional organic moieties and ligands. Different combinations of metal ions, peripheral ligands and modular bridging units have been used trying to find the most suitable structure. The design has been thought in order to optimize electronic interaction and distance between the chromophores, and to allow the transport of energy or charge, the charge separation, or multiredox processes. The variety of highly branched polynuclear metal complexes obtained so far presents big heterogeneity of components and thus different properties, such as the presence of cavities of various sizes, surfaces with specific functions, sites for multi-electron transfer catalysis, better absorption ability and gradients for photoinduced directional energy and electron transfer.

Covalently linked dyads are the simplest class of supramolecular architecture for the study of photoinduced energy and electron transfer processes. They have been pre-programmed introducing new rigid structural components to perform a control of the overall geometry and to keep in fixed orientation and at the desired distances the metal units. A widely employed method to achieve such result is based on the use of bridging spacers, such as alkanes, alkynes, saturated molecules, polyphenyls to link together the peripheral chromophoric sites.

The choice of the bridge is a key task in the construction of multichromophoric architectures, and in the attempt to obtain suitable modules that can act also as photoactive partners inside the arrays, exploration of new building materials and linkers have been performed.

Many examples of bridging ligands have been reported, such as systems constituted by spacers, saturated or conjugated molecules connected to the chelating sites, or multichelating organic ligands (pyridine, pyrazine or pyrimidine). The use of phenyl or diphenyl derivatives as spacers has been described by several authors and extremely rapid and efficient photoinduced processes have been reported for systems containing them. Instead, when a saturated spacer, like bicyclo[2.2.2]octane, is introduced as a component of the bridging ligand, even in presence of phenyl spacer, the electronic coupling between the chromophores drastically decreases and the photoinduced processes become much slower. It is clear therefore that one can modulate the rates of energy and electron transfer processes with an appropriate choice of the spacer.

An evolution in the design of supramolecular structures is represented by the introduction of photoactive bridging scaffolds. Such strategy has been thought in order to reproduce the ability of the natural systems in harvesting light of the entire UV-Vis range or, even better than the natural system, of the NIR spectral portion, through the use of red-absorbers. Thus in the attempt to enhance the overall efficiency of the harvesting process, the construction of highly efficient absorbers has been achieved.

One example is that of the truxene scaffold, a planar system composed of a heptacyclic polyarene structure, with good ability in light absorption. It can be easily trifunctionalized giving rise to the formation of star-shaped multichromophoric arrays, in which it acts as good energy donor and photoactive partner.²⁶ In such system, the good choice of the pattern of substitution based on many chromophoric units, besides the

good photophysical properties, produced also the required energy cascade leading to the sensitization of the final energy collector.

Such example, together with many others similar, confirms the suitability of supramolecular chemistry in achieving elaborated tasks, since if a single molecular component can be involved in simple acts, supramolecular species can perform functions.

1.3. Energy Transfer Theory

The main action of an antenna system, upon the solar light collection, is based on the funnel of such energy to the final collector responsible for its transformation. Such action in nature is performed by means of fast and efficient energy transfer steps, enabled by the suitably organized structure. Since the construction of artificial antennas tries to reproduce such process inside the new structures, it is important to clarify what exactly it is.

Energy transfer or resonance energy transfer (RET) is an electrodynamic phenomenon, occurring between the excited state of one molecule, acting as donor, and the ground state of another, with properties of acceptor. After the donor transfers its excitation energy to the nearby acceptor moiety, it is deactivated to a lower state (generally the ground state) while the acceptor is excited to a higher state. The phenomenon does not involve emission and reabsorption of photons but it originates from the energy exchange between donor and acceptor, whose oscillating dipoles are of similar resonance frequency.²⁷ It is substantially different from the radiative energy transfer, comprising instead emission and reabsorption of photons, as result of inner filter effects and thus depending on non-molecular optical properties of the specimen (such as the size of the cell containing the sample, the path length, the optical densities of the sample at the excitation and emission wavelengths and the geometric arrangement of the excitation and emission light paths).

Differently, the factors that affect RET processes are the superimposition between donor emission and acceptor absorption spectra, donor quantum yield, relative orientation of the transition dipoles of donor and acceptor and separation between the two species. The solvent does not produce particular effects on the efficiency of the process.

By means of resonance energy transfer, more information about compounds properties can be achieved than what gathered by the other fluorescence phenomena, furthermore because it can take place even when donor and acceptor are at long distances.

The energy transfer processes in supramolecular systems can be viewed as radiationless transition between two excited states localized in different regions of the structure. Therefore, the rate constant can be obtained by an appropriate expression of the Fermi's Golden Rule:

$$k_{en} = \frac{4\pi^2}{h} (H^{en})^2 FC^{en}$$

where H^{en} is the electronic coupling between the HOMO and LUMO levels of the energy-donor and -acceptor components, involved in the energy transfer process and FC^{en} is the Franck-Condon factor.

Depending on the system under investigation and on the experimental conditions, the two terms display a different weight, due to the different dependence of the process rate on the parameters of the system, such as spin of ground and excited states and donor-acceptor distance. As function of them, two different mechanisms can occur (see **Figure 1.7**).

1.3.1. The Förster (Coulomb) mechanism

The coulombic mechanism, also called Förster-type or through-space mechanism, is a long-range process and it does not require direct contact between donor and acceptor. For such process, the main term is the dipole-dipole interaction²⁸ that makes the process to be ruled by the same selection rules as the corresponding electric dipole transitions of the two partners. Coulombic energy transfer is therefore expected to be efficient in systems in which the radiative transitions connecting the ground and the excited state of each partner have high oscillator strength. The rate constant for the dipole-dipole coulombic energy transfer can be expressed as a function of the spectroscopic and photophysical properties of the two molecular components and of their distance.

The rate constant for the dipole-dipole energy transfer can be written as:

$$k_{en}^F = \frac{8.8 \times 10^{-25} K^2 \Phi_{em} J^F}{n^4 \tau r_{DA}^6}$$

where ϕ_{em} is the quantum yield for donor emission, τ is its emission lifetime, n is the refraction index of the solvent, K^2 is the orientation factor, regarding the relative orientation of donor and acceptor transition dipole moments ($K^2 = 2/3$ for random orientation), J_F is the Förster overlap integral and r_{DA} is the distance between the two reaction partners.

J_F measures the extent of superimposition between luminescence of donor and absorption of acceptor, thus the degree of resonance between donor and acceptor transition. It can be calculated from the overlap between the emission spectrum of the donor, $A(\bar{\nu})$ and the absorption spectrum of the acceptor expressed in molar absorptivity units, $D(\bar{\nu})$.

$$J_F = \frac{\int A(\bar{\nu})D(\bar{\nu})\bar{\nu}^{-4} d\bar{\nu}}{\int A(\bar{\nu})d\bar{\nu}}$$

Moreover, the dependence from distance is defined by the term $1/r^6$ thus the rate constant is proportional to the inverse sixth power of interchromophoric distance and energy transfer occurs efficiently also at larger distances than the molecular diameters because it does not need the formation of encounter complex.

An example of efficient coulombic mechanism is that of singlet-singlet energy transfer between large aromatic molecules, as in natural antenna systems of photosynthetic apparatus, as mentioned above.²⁹

1.3.2. Dexter (exchange) mechanism

The Dexter mechanism is based on an exchange interaction between donor and acceptor, resumable in a double electron transfer process in which one electron from the LUMO of the excited donor jumps to the empty LUMO of the acceptor, and the other from the HOMO of the acceptor goes towards the HOMO of the donor (see **Figure 1.6**). In this case, the process is governed by spin selection rules enabling the spin conservation in the reacting pair as a whole. Actually, the exchange mechanism can occur also when the excited states involved are spin forbidden in the usual spectroscopic sense.

The typical example of an efficient exchange mechanism is that of triplet-triplet energy transfer and thus, exchange energy transfer from the lowest spin forbidden excited state is expected to be the usual for metal complexes.³⁰

The expression obtained by Dexter⁵ for energy transfer processes between molecules coupled by an exchange interaction is the following:

$$k_D = \frac{4\pi^2(H^{en})^2}{h} J_D$$

where H^{en} is the electronic term, obtained from the electronic coupling between donor and acceptor and exponentially dependent on distance, while J_D is the nuclear factor, defined as Dexter overlap integral, calculated with both the donor emission and acceptor absorption spectra normalized to the unity, as follows:

$$J_D = \frac{\int A(\bar{\nu})D(\bar{\nu})d\bar{\nu}}{\int A(\bar{\nu})d\bar{\nu} \int D(\bar{\nu})d\bar{\nu}}$$

the electronic term H^{en} is obtained from the electronic coupling between donor and acceptor, exponentially dependent on distance:

$$H^{en} = H^{en}(0) \exp\left[-\frac{\beta^{en}}{2}(r_{DA} - r_0)\right]$$

where β^{en} is the attenuation factor for the exchange energy transfer, r_{DA} is the distance between the two reaction partners, donor and acceptor (in Å) while r_0 is the effective average orbital radius of the donor and the acceptor.

The independence from the oscillator strengths and the exponential decrease of the energy transfer rate as function of donor-acceptor distance, imply that no Dexter-type energy transfer process can occur at major distances than the contact one.

This is true according to the original and narrow formulation but the exchange mechanism can be extended also to systems in which donor and acceptor are coupled through a connecting bridge.

The connecting unit between donor and acceptor components in supramolecular structures has a role in mediation of both electron and energy transfer processes. In these cases, if the bridge levels are much higher in energy than donor and acceptor, consequently the electron tunnels in a single step from donor to acceptor, without really moving along the wire. While when the energy levels of the bridge are low enough to become intermediate between the initial and final states, it is directly involved in the electron or energy transfer, and the rate constant of the process displays a very small distance dependence.

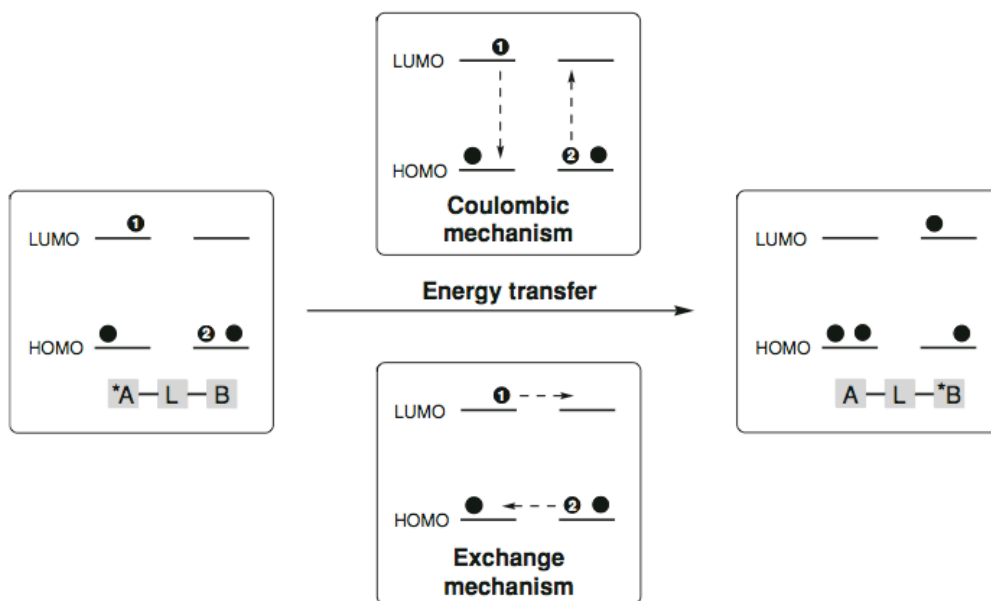


Figure 1.7. Pictorial representation of the coulombic and exchange energy transfer mechanism. (P. Ceroni and V. Balzani, *The Exploration of Supramolecular Systems and Nanostructures*, by Photochemical Techniques, Lecture Notes in Chemistry, Springer Science+Business Media B.V 2012)

Finally, when there is complete mixing among the donor/bridge/acceptor orbitals (large coupling limit) the bridge essentially acts as an incoherent molecular wire, as happens for conjugated conducting polymers, and the behaviour of the system is expected to go according to an ohmic regime, with distance dependence of the rate inversely proportional to the bridge length.

1.3.3. Energy Transfer in Photosynthetic Process

Most of the natural photosynthetic pigments, harvesting and funneling the relatively diffuse source of photons from the sun to the reaction centre, are incorporated into protein-based structures that ensure them a spatial and energetic fixed organization. The fixed arrangement allows excitation energy to migrate from lower wavelength-absorbing pigments, located at the more distal sections of the antenna complex, to longer wavelength-absorbing chromophores that are proximal to the reaction centre. During this transfer process from excited-state of donor pigments to ground-state of acceptor pigments, a loss of photonic energy as heat provides a degree of irreversibility to the overall process.

This singlet-singlet energy transfer between chlorophyll pigments is well described by the Förster model that, for weakly coupled donor and acceptor pigments, uses the Golden Rule expression in the context of a dipole-dipole approximation.⁴ Its efficiency is in general increased by several factors, such as a good spectral overlap between donor emission and acceptor absorption, a high fluorescence quantum yield of the isolated donor pigment and a large extinction coefficient for the acceptor. A suitable tuning of these parameters can be found in natural systems, evolutionary optimized in order to improve their performances in spite of the competitive electron-transfer processes, which require higher spatial overlap between involved states.

Moreover, to limit the negative effect of singlet oxygen, rapid quenching of chlorophyll triplet states occurs by energy transfer to carotenoid pigments. This is an example of the elaborate regulation, protection and repair mechanisms developed by nature in order to reduce the risk of photodamage for the organism.³¹ Unlike singlet-singlet energy transfer, this triplet-triplet transfer cannot take place via a dipole-dipole mechanism, because it results forbidden, and likely occurs by an electron exchange process requiring close orbital contact (within ~ 10 Å),⁵ but the rate of Dexter type energy transfer mechanism decreases exponentially with increasing donor-acceptor distance. Thus, definitely, although the difference in Förster and Dexter mechanisms, it is not always simple to discriminate which one can properly define a certain energy-transfer process, due to the ambiguous borders between them in natural highly organized photosynthetic antenna systems.

1.4. Dye sensitized solar cells for solar energy conversion

The use of organized molecular structures to achieve special tasks, as made by nature in photosynthesis, is a good way to build devices for light energy conversion not only in biomimetic photosynthetic apparatus but also in dye-sensitized solar cells, molecularly engineered in order to be able of directly converting sunlight into electrical power.

Although the prominent technology in this field has been based on the solid-state p-n junction devices, the new generation of dye-sensitized solar cells (DSSCs) emerged as particularly interesting kind of an integrated photoelectrochemical system.

DSSCs were first developed by Grätzel and coworkers and represent a promising alternative to the more expensive solid-state photovoltaic devices,³² being relatively inexpensive and efficient. This class of devices displays a fully organized sandwich-type structure, consisting of a dye-sensitized photoanode, a redox mediator and a counter electrode, as reported in **Figure 1.8**.

The photocatodic unit contains a thin catalytic layer (usually, platinum or graphene) instead the composite photoanodic unit comprises a transparent conducting substrates, such as fluorine doped tin oxide (FTO) on the glass, a semiconductive layer, usually composed of nanoporous TiO₂, and a dye adsorbed onto the surface of the semiconductor. Between the photoelectrodes, there is an electrolyte solution (usually containing the I₃⁻/I⁻ pair) to close the circuit.

The working mechanism of a DSSC comprises more steps, involving every unit of the multilayers structure. The process starts from the absorption of incident solar energy,

operated by the photoanode, exciting one electron of the dye from the (highest occupied molecular orbital) HOMO to the (lowest unoccupied molecular orbital) LUMO level. Electrons from the excited state of the dye are injected to the conduction band of the semiconductive TiO_2 , oxidizing the chromophore. The TiO_2 film has been engineered as porous and nanostructured with very high surface roughness and small particle sizes (almost 20 nm) in order to enable more efficient light harvesting, through enhancement of the contact surface available for adsorption of the dye.

The process of electron injection into the semiconductor has to be faster than the recombination, that deactivates the excited state of the dye to its ground state. Once injected in the conduction band of the semiconductor, the electrons migrate through the nanoporous network of TiO_2 and after, through the external circuit, towards the photocathode.

The electrolyte solution, which is in contact with the dye, closes the circuit by donating electrons to the dye and so restoring its initial form.

Electrolyte then diffuses towards the catalytic electrode where the reduction reaction takes place and it is ready for another cycle by accepting electrons from the external circuit.

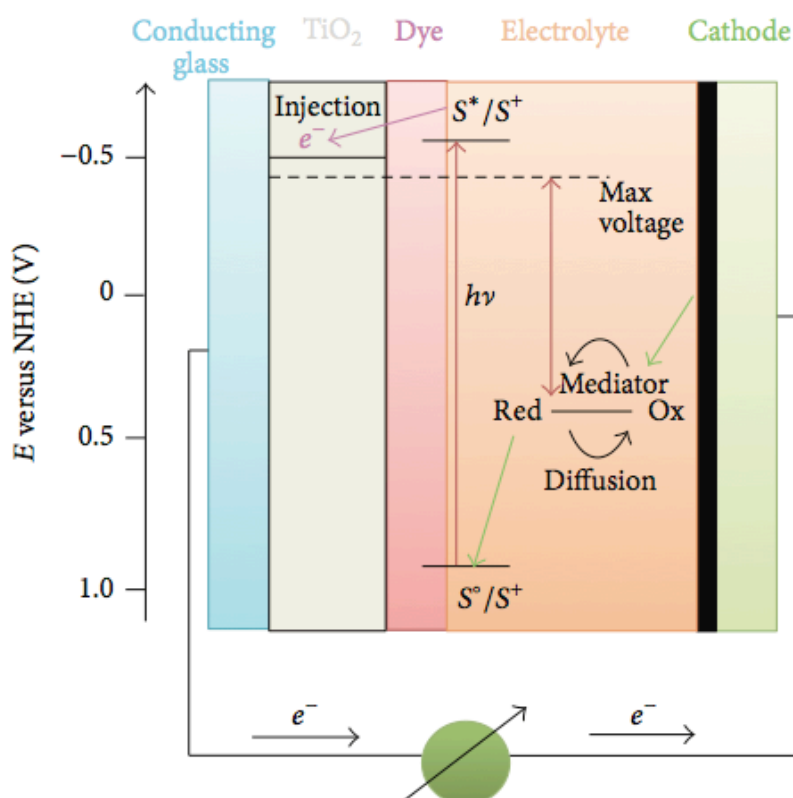


Figure 1.8. Structure and working principle of DSSC, with $S^0/S^+/S^*$ representing sensitizer in the ground state, oxidized state, and excited state, respectively. Red/Ox = redox mediator. (U. Mehmood; S. Rahman; K. Harrabi; I. A. Hussein and B. V. S. Reddy, *Advances in Materials Science and Engineering* 2014, **2014**, 1-12)

The basic requirements for the structure are of energetic nature: the LUMO of the photosensitizer should be more negative than the conduction band of the semiconductor,

while the HOMO more positive than the redox potential of the electrolyte. This energetic levels arrangement is at the basis of a working DSSC.

Among the dyes in use, many natural organic compounds can be counted, but the best results have been obtained so far with transition metal complexes, particularly Ru-based. The major drawback of the organic dyes, as compared to the Ru(II) dyes, is the lower lifetimes of their excited states that might enhance recombination processes.

1.4.1. Solar Conversion Efficiency and Dye Sensitization

The overall solar conversion efficiency (η) is the result of the balance of many variables and it is expressed as follows

$$\eta = (J_{sc} \times V_{oc} \times FF) / P_{in}$$

P_{in} is the total solar incident power, FF is the cell fill factor, function of the diode quality factor, V_{oc} is the open-circuit voltage (difference between the Nernstian potential of the solution and the semiconductor quasi-Fermi level) and J_{sc} the short-circuit photocurrent density.

Upon several trials made during the time, some guidelines have been produced in order to increase the device efficiencies. In particular, to enhance the J_{sc} value, the simplest strategy is based on an increase of the solar light collection efficiency. Thus, for instance, the design of dyes that are able to absorb in both UV-Vis and near-IR region can be a good goal, avoiding loss of solar radiation since its spectrum covers from the near-UV region to the near-IR region. The optical gap of the dye should be indeed reduced to improve absorption at longer wavelengths. This aim can be achieved either by lowering the LUMO energy level (low-energy 1MLCT and 3MLCT states for metal complexes) or by raising the HOMO level. Unfortunately, in agreement to the energy gap-law, this type of intervention can enhance the probability of non-radiative deactivation pathways, competitive with the electron injection.

The increasing of the V_{oc} value instead can be obtained by employing redox couples potential to more positive values always ensuring enough overpotential between it and the dye, to allow for the regeneration of the dye at an acceptable rate.

The best photovoltaic performance both in terms of conversion yield and long-term stability has been achieved with polypyridyl complexes of ruthenium and osmium. Sensitizers having the general structure $ML_2(X)_2$, where L stands for 2,2'-bipyridyl-4,4'-dicarboxylic acid, M is Ru or Os and X represents a halide, cyanide, thiocyanate, acetyl acetonate, thiocarbamate or water substituent, are particularly promising. The better value of solar conversion efficiency for this type of device, falling around the 11.18%, has been registered in presence of N3 or Red dye as sensitizer, $[RuL_2(NCS)_2]^{2+}$ (L = 2,2'-bipyridyl-4,4'-dicarboxylic acid), with carboxylic group useful for anchoring on the semiconductor surface.

After many years of investigation, another well-performing complex, defined black dye, has been obtained but no improvement in efficiency has been gained. It is a Ru(II) complex, tri(cyanato)-2,2',2''-terpyridyl-4,4',4''-tricarboxylate Ru(II) that allowed for a solar to power conversion efficiency of 10.4% in full sunlight, slightly lower than for N3. Thus, new approaches have been experimented.

One widely explored strategy to increase the light harvesting efficiency introduced later, was based on the use of supramolecular assemblies as sensitizer, composed of a certain number of metal complex units linked by suitable bridging ligands, instead of mononuclear unit. The increase in the overall cross-section for light absorption compared to the case of a simple molecular sensitizer is the reason for the increasing in light absorption. Moreover, the multicomponent structure allows for the occurring of efficient intramolecular energy transfer that can increase the electron injection ability of the dye into the semiconductive layer.

The efficacy of such an approach has been confirmed by the preparation of the Ru(II) trinuclear complex $[(\text{NC})\text{Ru}(\text{bpy})_2(\text{CN})\text{Ru}(\text{dcbH}_2)_2(\text{NC})\text{Ru}(\text{bpy})_2(\text{CN})]^{2+}$,³³ in which energy transfer takes place from the peripheral chromophores to the central unit – Ru(dcbH₂)₂– with high efficiency.

Beside such example, many other different multinuclear polypyridinic complexes of d⁶ metal ions have been used in this field of application³⁴ taking advantage from their overall suitable properties with respect to the organic molecules. Many reported examples are the result of planned modification of the basic polypyridyl metal frameworks, whose MLCT states energy displays wide possibilities to be tuned by modifying anchoring and/or ancillary ligands or by changing their substitution pattern.

Organic dyes such as porphyrins and phthalocyanines have attracted considerable attention also in such field due to the similarity with respect to the natural photosensitizers. However, porphyrins cannot compete with the N3 or black dye due to their lack of red light and near-IR absorption. Phthalocyanines show intense absorption bands in this spectral region but they display serious problems related to aggregation and to the unsuitable energetic position of the LUMO level, which is too low for electron transfer to the TiO₂.

Thus, despite the abundant research the transition metal complexes produce the best effects on DSSC performances.

1.5. Excited States of Transition Metal Complexes: general remarks

Since this work is mostly based on supramolecular structures composed of transition metal complexes, some information about theoretical aspects related to them has to be provided.

The photochemistry of transition metal complexes has undergone an impressive growth in the last few decades. The king of such class of compounds is represented by prototype complex $[\text{Ru}(\text{bpy})_3]^{2+}$, whose investigation has been for sure one of the most extensive. A unique combination of chemical stability, redox properties, excited-state reactivity, luminescence emission and excited-state lifetime, during the last 40 years, have stimulated its application in an enormous variety of fields, such as photochemistry, photophysics, photocatalysis, electrochemistry, photoelectrochemistry, chemi- and electrochemi-luminescence, and electron and energy transfer. And moreover many derivative compounds have been synthesised in the attempt to improve or refine its properties. In the same period, Ir(III), Os(II), Re(I), Rh(III) and Pt(II) polypyridine

complexes have been largely explored, trying to understand how they are influenced by the identity of the ligands present on their coordination sphere.

The study of such systems has to comprise necessarily the evaluation of their basic electronic excited-state properties. The main five types of electronic transitions, which can be found in these coordination compounds are the following:

- Metal-centred (**MC**) transitions (e.g. d-d electronic transitions) are not permitted by Laporte rules but partially allowed due to vibronic and spin-orbit couplings and consequently they usually exhibit lower extinction coefficients with respect to charge-transfer (CT) transitions. According to the Laporte selection rule, electronic transitions that conserve either symmetry or asymmetry with respect to an inversion centre are forbidden.
- Ligand-to-metal charge transfer (**LMCT**) transitions involve promotion of electrons from occupied ligand orbitals to the partially empty metal centred d orbitals. They are low-lying states when at least one of the ligands is easy to oxidize and the metal is easy to reduce.
- Metal-to-ligand charge transfer (**MLCT**) transitions originate from excitations from metal d-based orbitals to low-lying empty orbitals located on the ligand, typically of π^* character. They are expected at the low-energy when the metal is easy to oxidize and the ligand is easy to reduce, as in Ru(II) polypyridyl complexes.
- Intra-ligand (**IL**) transitions arise from electron migration between ligand-based orbitals, belonging to the same ligand. They usually appear in the absorption spectrum of the ligands when they are not coordinated to the metal centre.
- Ligand-to-ligand charge transfer (**LLCT**) transitions take place between orbitals located in different ligands.

Due to the presence of all these possible states, the UV-Vis spectra of transition metal complexes display higher complexity than those of organic molecules. Among transition metal complexes, the most explored and promising are Ru(II), Ir(III), Os(II) and Pt(II) complexes.

Octahedral complexes of Ru(II), Os(II) and Ir(III), whose metal centres are $4d^6$, $5d^6$ and $5d^6$, respectively, display very similar features.

Their properties can be explained taking into account the degeneracy of their d orbitals, destabilized and split in an octahedral ligand field by an amount Δ . Since Δ is influenced by the different quantum number and the field strength of the ligands, such factors can affect the photophysical properties, too (**Figure 1.9**). In all compounds, absorption spectra originate from electronic transitions from the ground state to mostly singlet levels of different nature and electronic localization, as mentioned above. The emission instead arises always from transitions of triplet $^3\text{MLCT}$ or ^3LC character, with some contribution from singlet, as consequence of the high spin-orbit coupling constants of the metal unit ($\zeta = 1042, 3381, 3909 \text{ cm}^{-1}$, for Ru, Os, and Ir, respectively)³⁵.

For a metal like Fe(II), with an external electronic configuration of $3d^6$, in polyimine octahedral complexes, the amount of splitting between t_{2g} and e_g levels is small enough that the main character of the lowest-lying excited state is MC, thus not emissive. For

Os(II) and Ir(III) instead, Δ is very large and the MC levels are pushed so high in energy that usually they do not affect the emission properties.

Os(II)-polypyridin complexes display as distinguishable features the long wavelength emission and the low values of photoluminescence quantum yields, always lower than 0.1. This behaviour can be ascribed to the low-lying MLCT levels (1.6 eV) and to the occurring of radiationless deactivation pathways, as effect of the energy-gap law, differently from most of Ir(III)-polypyridin complexes, whose emission energy is higher (in the range 2.1 to 3 eV).

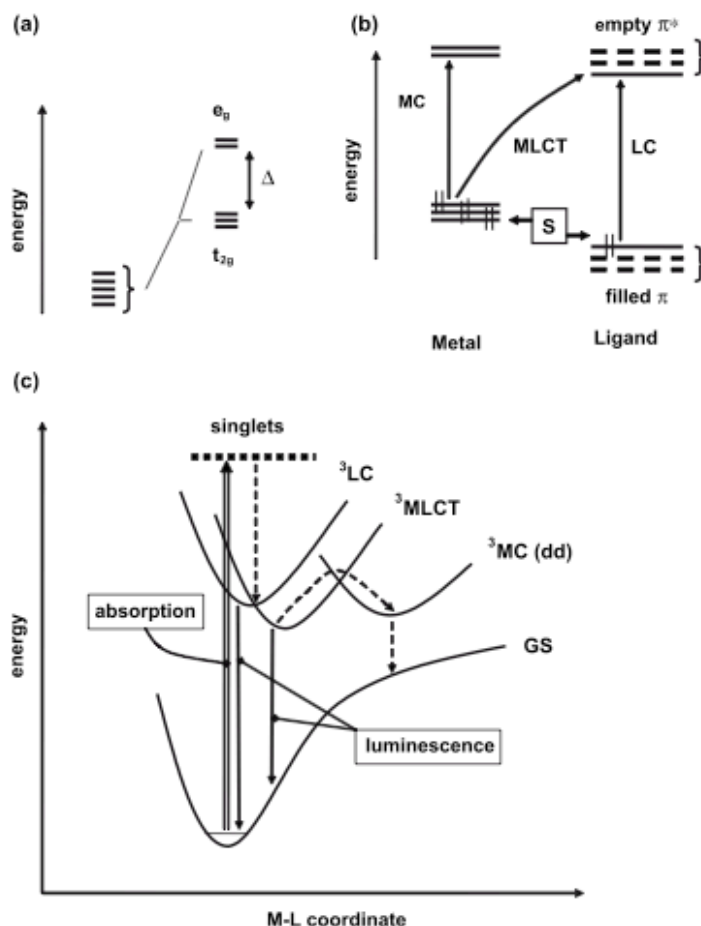


Figure 1.9. (a) d orbitals in octahedral field; (b) orbital description of MC, MLCT, and LC transitions; S is a substituent group capable of exerting electron withdrawing or releasing effects (resulting in stabilization or destabilization, respectively, of the energy level of the filled d and π orbitals); (c) electronic transitions involving MC, MLCT, and LC excited states; the MC levels are not emissive. (L. Flamigni; A. Barbieri; C. Sabatini; B. Ventura; F. Barigelletti, *Top. Curr. Chem.* 2007, **281**, 143-203)

Ru(II)-polypyridin systems display intermediate properties between Fe(II) and Ir(III)/Os(II) complexes. Its emission originates from MLCT transition, with an energy content of ~ 2.1 eV, and the non-emitting MC levels result thermally accessible.

Pt(II) d^8 complexes are very different from these d^6 , first of all for their preferential square planar geometry, that allows interactions with identical molecules, such as

intermolecular stacking, dimerization in the ground state or excimer formation in the excited state, or with other compounds, forming exciplexes.

In many Pt(II) complexes, either the MLCT or the LC states, usually are located at lower energies than the d-d states, and have intrinsically faster k_r values than the d-d (Figure 1.10), but MC excited state, very often affect dramatically luminescence properties, particularly at room temperature, since it may be thermally accessible from the lowest-energy excited state.

The photophysical properties are influenced also by the interactions with other molecules, as mentioned above, that enhance the energy of the highest occupied metal-based molecular orbital with respect to the isolated molecules and shift the lowest-energy optical transitions towards lower energies, modifying the nature of the lowest-energy excited state.

In all the cases, the pattern of coordination on the metal centre is fundamental and allows for a very fine tuning of absorption and luminescence properties of the corresponding complexes, rendering them still promising for many fields of application.

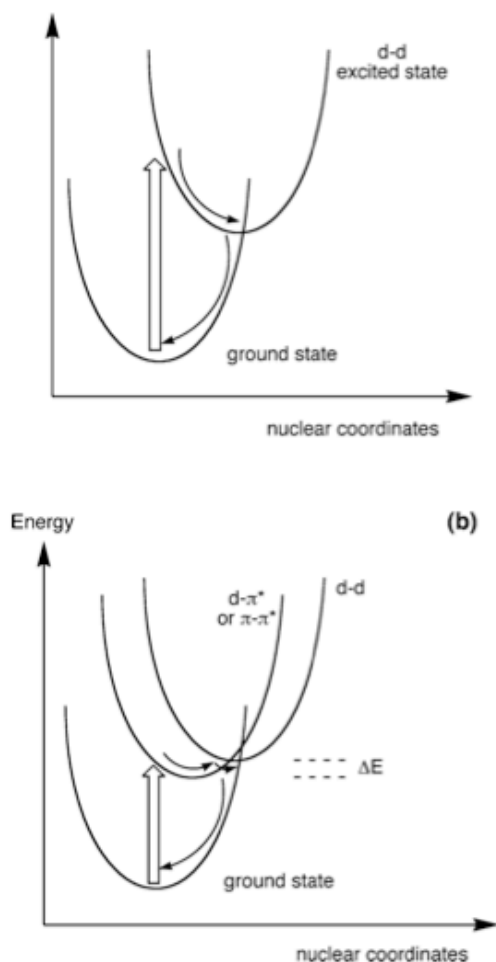


Figure 1.10. (a) Illustrating the displacement of the potential energy surface for the d-d excited state in a square planar d^8 complex, formed by population of the $d_{x^2-y^2}$ orbital, compared to the ground state. (b) Even though other excited states (e.g., d- π^* or π - π^*) may lie at lower energies, the d-d excited state can provide a thermally activated non-radiative decay pathway. Thick arrows represent absorption of light; thin ones indicate vibrational relaxation and non-radiative decay (J. A. Gareth Williams, *Top. Curr. Chem.* 2007, **281**, 205-268)

1.6. References

- ¹ P. Yang and J. P. Tarascon, *Nat. Mater.* 2012, **11**, 560-563.
- ² ^(a) P. Jordan; P. Fromme; H. T. Witt; O. Klukas; W. Saenger and N. Kraus, *Nature* 2001, **411**, 909-917; ^(b) A. Ben-Shem; F. Frolow and N. Nelson, *Nature* 2003, **426**, 630-635; ^(c) A. Amunts; O. Drory and N. Nelson, *Nature* 2007, **447**, 58-63; ^(d) J. Kargul and J. Barber, in *Molecular Solar Fuels*, ed. T.J. Wydrzynski and W. Hillier, RSC Publishing, Cambridge, 1st edn., 2012, **5**, 107-136.
- ³ M. R. Wasielewski, *Chem.Rev.* 1992, **92**, 435-461.
- ⁴ T. Förster, *Ann.Phys.* 1948, **2**, 55-75.
- ⁵ D. L. Dexter, *J. Chem. Phys.* 1953, **21**, 836-850.
- ⁶ ^(a) R. Amadelli; R. Argazzi; C. A. Bignozzi and F. Scandola, *J. Am. Chem. Soc.* 1990, **112**, 7099-7103; ^(b) A. Bignozzi; R. Argazzi; C. Chiorboli; F. Scandola; R. B. Dyer; J. R. Schoonover and T. J. Meyer, *Inorg. Chem.* 1994, **33**, 1652-1659; ^(c) A. Bignozzi; R. Argazzi; J. R. Schoonover; K. C. Gordon; R. B. Dyer and F. Scandola, *Inorg. Chem.* 1992, **31**, 5260-5267; ^(d) F. Willig; R. Kietzman and F. Schwarzburg, *Proc. Int. Symposium on Optical Materials Technology for Energy Efficiency and Solar energy*, Toulouse, 1992.
- ⁷ J. Davila; A. Harriman; L. R. Milgrom, *Chem. Phys. Lett.* 1987, **136**, 427-430.
- ⁸ Y. Terazono; G. Kodis; P. A. Liddell; V. Garg; T. A. Moore; A. L. Moore; D. Gust, *J. Phys. Chem. B* 2009, **113**, 7147-7155.
- ⁹ ^(a) T. A. Moore; D. Gust; P. Mathis; J. C. Mialocq; C. Chachaty; R. V. Bensasson; E. J. Land; D. Doizi; P. A. Liddell; W. R. Lehman; G. A. Nemeth; A. L. Moore, *Nature* 1984, **307**, 630-632; ^(b) D. Gust; T. A. Moore; A. L. Moore; A. A. Krasnovsky; P. A. Liddell; D. Nicodem; J. M. DeGraziano; P. K. Kerrigan; L. R. Makings; P. J. Pessiki, *J. Am. Chem. Soc.* 1993, **115**, 5684-5691; ^(c) S. D. Straight; G. Kodis; Y. Terazono; M. Hamburger; T. A. Moore; A. L. Moore; D. Gust, *Nat. Nanotechnol.* 2008, **3**, 280-283.
- ¹⁰ O. Gonen and H. Levanon, *J. Chem. Phys.* 1986, **84**, 4132-4136.
- ¹¹ ^(a) K. Sugiura, *Top Curr. Chem.* 2003, **228**, 65-85; ^(b) A. K. Burrell; D. L. Officer; P. G. Pleiger and D. C. W. Reid, *Chem. Rev.* 2001, **101**, 2751-2796; ^(c) J. K. M. Sanders, in *Porphyrin Handbook*, ed. K. M. Kadish, K. M. Smith and R. Guilard, Academic Press, New York 2000, **3**, 347; ^(d) T. Imamura and K. Fukushima, *Coord. Chem. Rev.* 2000, **198**, 133-156; ^(e) J. Wojaczynski and L. Latos-Grazynski, *Coord. Chem. Rev.* 2000, **204**, 113-171; ^(f) E. Iengo; E. Zangrando and E. Alessio, *Eur. J. Inorg. Chem.* 2003, 2371-2384; ^(g) F. Wurthner; C. C. You and C. R. Saha-Moller, *Chem. Soc. Rev.* 2004, **33**, 133-146; ^(h) A. Satake and Y. Kobuke, *Tetrahedron* 2005, **61**, 13-41.
- ¹² M. S. Choi; T. Yamazaki; I. Yamazaki and T. Aida, *Chem. Eur. J.* 1998 (**12**), 2668-267; (b) R. A. Haycock; A. Yartsev; U. Michelsen; V. Sundtrom and C. A. Hunter, *Angew. Chem. Int. Ed.* 2000, **39** (20), 3616-3619; (c) D. Holten; D. F. Bocian and J. S. Lindsey, *Acc. Chem. Res.* 2002, **35**, 57-69.
- ¹³ ^(a) G. McDermott; S. M. Prince; A. A. Freer; A. M. Hawthornthwaite-Lowless; M. Z. Papiz; R. J. Cogdell and N. W. Isaacs, *Nature* 1995, **374**, 517-521; ^(b) J. Koepke; X. Hu; C. Muenke; K. Schulten and H. Michel, *Structure*, 1996, **4**, 581-597; ^(c) A. W. Roszak; T. D. Howard; J. Southall; A. T. Gardiner; C. J. Law; N. W. Isaacs and R. J. Cogdell *Science*, 2003, **302**, 1969-1972.

- ¹⁴ (a) D. Kim and A. Osuka, *J. Phys. Chem. A* 2003, **107**, 8791-8816; (b) Y. Nakamura; N. Aratani and A. Osuka, *Chem. Soc. Rev.* 2007, **36**, 831-845.
- ¹⁵ Y. Nakamura; I. W. Hwang; N. Aratani; T. K. Ahn; D. M. Ko; A. Takagi; T. Kawai; T. Matsumoto; D. Kim; A. Osuka, *J. Am. Chem. Soc.* 2005, **127**, 236-246.
- ¹⁶ I. W. Hwang; T. Kamada; T. K. Ahn; D. M. Ko; T. Nakamura; A. Tsuda; A. Osuka; D. Kim, *J. Am. Chem. Soc.* 2004, **126**, 16187-16198.
- ¹⁷ N. Gfeller; S. Megelski and G. Calzaferri, *J. Phys. Chem. B* 1998, **102**, 2433-2436; (b) G. Calzaferri and K. Lutkouskaya, *Photochem. Photobiol. Sci.* 2008, **7**, 879-910.
- ¹⁸ Y. Terazono; G. Kodis; P. A. Liddell; V. Garg; T. A. Moore; A. L. Moore; D. Gust, *J. Phys. Chem. B* 2009, **113**, 7147-7155.
- ¹⁹ (a) G. R. Newkome; C. N. Moorefield; F. Vogtle; *Dendritic Molecules: Concepts, syntheses, Perspective*, VCH, Weinheim, 1996; (b) V. Balzani; S. Campagna; G. Denti; A. Juris; S. Serroni and M. Venturi, *Acc. Chem. Res.* 1998, **31**, 26-34.
- ²⁰(a) K. Kalyanasundaram, *Photochemistry of Polypyridine and Porphyrin Complexes*, Academic Press, London, 1991; (b) A. Juris; V. Balzani; F. Barigelletti; S. Campagna; P. Belser; A. von Zelewsky, *Coord. Chem. Rev.* 1988, **84**, 85-277.
- ²¹ M. H. V. Huynh; D. M. Dattelbaum and T. J. Meyer, *Coord. Chem. Rev.* 2005, **249**, 457-483.
- ²² (a) V. Balzani; G. Bergamini; F. Marchioni and P. Ceroni, *Coord. Chem. Rev.* 2006, **250**, 1254-1266; (b) M. R. Wasielewski, *Chem. Rev.* 1992, **92**, 435-461.
- ²³ (a) K. Kalyanasundaram, *Photochemistry of Polypyridine and Porphyrin Complexes*, Academic, New York, 1992; (b) V. Balzani; F. Scandola, *Supramolecular Photochemistry*, Horwood, Chichester, 1991.
- ²⁴ (a) G. Denti; S. Campagna; L. Sabatino; S. Serroni; M. Ciano and V. Balzani, *Inorg. Chem.* 1990, **29**, 4750-4758; (b) G. Denti; S. Serroni; S. Campagna; V. Ricevuto and V. Balzani, *Inorg. Chim. Acta* 1991, **182**, 127-129.
- ²⁵ G. Denti; S. Campagna; S. Serroni; M. Ciano and V. Balzani, *J. Am. Chem. Soc.* 1992, **114**, 2944-2950.
- ²⁶ (a) B. Ventura; A. Barbieri; F. Barigelletti; S. Diring and R. Ziessel, *Inorg. Chem.* 2010, **49**, 8333-8346; (b) S. Diring; R. Ziessel; F. Barigelletti; A. Barbieri and B. Ventura, *Chem. Eur. J.* 2010, **16**, 9226-9236.
- ²⁷ R. M. Clegg, *Fluorescence resonance energy transfer*. In *Fluorescence imaging spectroscopy and microscopy* 1996, 179-252. Ed XF Wang, B Herman. John Wiley & Sons, New York.
- ²⁸ (a) F. Barigelletti; L. Flamigni, *Chem. Soc. Rev.* 2000, **29**, 1-12; (b) G. D. Scholes, *Annu. Rev. Phys. Chem.* 2003, **54**, 57-87.
- ²⁹ T. Pullerits; V. Sundström, *Acc. Chem. Res.* 1996, **29**, 381-389.
- ³⁰ F. Scandola; B. Balzani, *J. Chem. Ed.* 1983, **60**, 814-823.
- ³¹ (a) A. Krieger-Liszka; C. Fufezan; A. Trebst, *Photosynth. Res.* 2008, **98**, 551-564; (b) J. Barber; B. Andersson Trends, *Biochem. Sci.* 1992, **17**, 61-66; (c) N. E. Holt; G. R. Fleming; K. K. Niyogi, *Biochemistry* 2004, **43**, 8281-8289; (d) A. Dreuw; G. R. Fleming; M. Head-Gordon, *Biochem. Soc. Trans.* 2005, **33**, 858-862.
- ³² (a) M. Grätzel, *Nature* 2001, **414**, 338-344; (b) M. Grätzel, *Inorg. Chem.* 2005, **44**, 6841-6851.
- ³³ C. A. Bignozzi; J. R. Schoonover and F. Scandola, *Prog. Inorg. Chem.* 1997, **44**, 1-95.

³⁴ F. Gao; Y. Wang; D. Shi; J. Zhang; M. Wang; X. Jing; R. Humphry-Baker; P. Wang; S. M. Zakeeruddin and M. Grätzel, *J. Am. Chem. Soc.* 2008, **130**, 10720-10728.

³⁵ M. Montalti; A. Credi; L. Prodi and M. T. Gandolfi, *Handbook of Photochemistry*, CRC Press, Taylor & Francis, Boca Raton, 3rd edn, 2006.

Chapter 2

2. Pt(II), Ru(II), Ir(III) and Rh(III) coordination assemblies with π -bonded bidentate quinonoid and thioquinonoid organometallic ligands: examples of design of chromophores with improved photophysical properties

The study of photophysics and photochemistry of transition metal complexes has received an increasing attention since the last few decades. In fact, the acquisition of a solid knowledge about their photoreactivity and on the properties of their excited states is fundamental for the elaboration of innovative synthetic strategies for the design of new chemical architectures with more and more promising qualities. The optimization of such supramolecular assemblies is thought in terms of improvement of spectral and redox features and of spatial arrangement, as central tasks for their potential application in solar energy collection/conversion and for photo- and electro-luminescent devices.^{1,2} The great attention received by transition metal complexes, in particular, is due to their big versatility and to the possibility to carefully and efficiently tune their properties towards desired directions: acting on the coordination sphere by modulating the energy levels of the low-lying metal-to-ligand charge transfer (MLCT) and ligand-centred (π - π^*) excited states, it is possible to perform programmed and precise modifications on their photophysics.

The present chapter introduces good examples of planning and application of novel synthetic strategies for the improvement of absorption and emission properties of transition metal complexes based on the self-assembly of coordination frameworks. Herein, four series of supramolecular assemblies with organometallic units will be discussed, composed of metallated quinonoid and thioquinonoid complexes, and of transition metals of different coordination geometry. Oxygen/sulfur centres of [(catecholate/benzenedithiolate)M(Cp*/bz)] (M = Ru(II), Rh(III) and Ir(III)), as organometallic ligands, chelate traditional polypyridyl/cyclometallated Pt(II) square planar and Ir(III), Rh(III) and Ru(II) octahedral luminophore building blocks, inducing a wide range of effects on the photophysical properties.

2.1. Introduction

Dioxolenes (catecholate, semiquinone, and quinone series) have received considerable attention as prominent class of compounds thanks to their important role in chemistry and biology. It is indeed noteworthy that plenty of biologically active molecules contain a quinone functions on their structure (es. vitamin K)³. The role they have in biological systems is often related to their fast electron-transfer ability and rich electrochemistry, that candidate them as main subjects for several studies. But the reported examples of their use as π -bonded ligands for metal complexes and their coordination chemistry have just developed over the past 30 years.⁴

Specific studies on these systems revealed the strong coupling between the d-orbitals of transition metal and the low-lying π^* -orbitals of the quinone unit, both very close in energy. Such interaction produces in these frameworks essentially covalent frontier orbitals (HOMO and LUMO), in which the valence π -electrons are delocalized over both metal and ligand.⁵

The quinone ligand may adopt three electronic forms as redox isomers, different in the oxidation state: the fully reduced form [catecholate]²⁻ (cat^{2-}), the one electron oxidized species [semiquinone]⁻ (sq^-) and the unreduced quinone form (q) (see **Chart 2.1**). The different oxidation states of the ligand are characterized by differences in the orbital coupling with metal d-levels and thus in the total charge distribution of the whole assembly, providing distinct electrochemical and spectroscopic behaviours.

The diketone unit (q) is a weak donor, readily subject to displacement, thus less used as

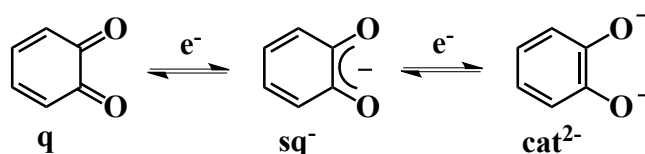


Chart 2.1. Schematic representation of the three redox isomers of dioxolene ligand: quinone (q), semiquinone (sq^-) and catecholate (cat^{2-}).

ligand, while the catecholate form is the most common coordination mode, as strong σ and π donors, nucleophilic enough to coordinate electrophilic metal ions.^{4a,6}

This different tendency implies different nature and position for the absorption bands of their assemblies, with cat^{2-} form usually acting as donor in ligand-to-ligand charge transfer states (LL'CT), and sq^- and q species, as electron acceptors in metal-to-ligand charge-transfer (MLCT) states.⁷

For instance, ruthenium complexes, when the ligand is in its semiquinone form, show an absorption in the near-IR region, due to a $\text{Ru}(d\pi) \rightarrow \text{sq}(\pi^*)$ metal-to-ligand CT (MLCT) band, instead when the ligand is in the fully oxidized redox state (q), the absorption moves in the visible region, as reported in **Figure 2.1**.⁸

This electrochromic behavior and the particular electronic structures of such systems open the way to different possible applications for the development of electrochromic material as components of modified electrodes for solar energy conversion and catalysis,^{4e,9} for modulation of optical signals¹⁰ or as anchors to semiconductor surfaces in the photovoltaic fields.¹¹

Till now, the big limit to technological applications has been the poor luminescence ability of these supramolecular assemblies,^{7,12} due to the fact that the quinone unit introduces accessible low-energy electronic states, leading to the quenching of metal centre luminescence through electron transfer mechanism.⁷

The study shown in this chapter has particular relevance from two points of view. First of all, it has widened the knowledge about dioxolene assemblies involving metals such as rhodium, iridium, ruthenium and platinum, not particularly reported in literature till now. In particular, *Thompson et al.* introduced one cyclometallated iridium complex with semiquinone ligand, revealing a proper strategy to improve emission properties of these supramolecular systems. Apart from this example, few details are offered by the literature.^{13,14}

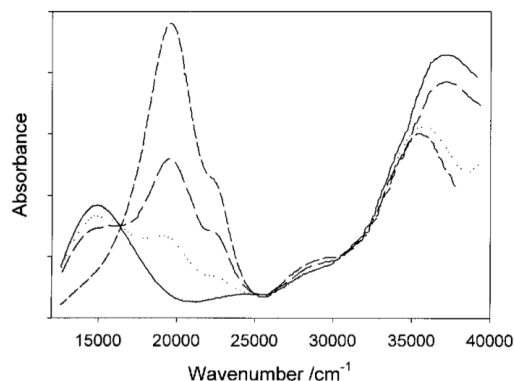


Figure 2.1. Electronic spectra recorded with an optically transparent thin layer electrode (OTTLE) cell during the oxidation of 10^{-3} M $[\text{Ru}^{\text{III}}(\text{NH}_3)_4(\text{Cat})]^+$ (as chloride, solid line) to $[\text{Ru}^{\text{II}}(\text{NH}_3)_4(\text{Q})]^{2+}$ (final --- line) in aqueous 0.2 M KCl. (From Ref. 8)

The photophysical study of the investigated systems indeed highlights the positive role of stable $\text{M}(\text{Cp}^*/\text{bz})$ (Cp^* = pentamethyl-cyclopentadienyl and bz = benzene) fragment coordination to the catecholate/thiolate ligand in turning on luminescence, both in octahedral and square planar complexes, through enhancement of the donor ability of the new “organo-metalloligand”.

2.2. Results and Discussion

2.2.1. Ir(III), Rh(III) and Ru(II) coordination assemblies with π -bonded Catecholate ligand

The first two series under analysis are composed of cyclometallated phenylpyridin Rh(III) and Ir(III), and polypyridin Ru(II) coordination assemblies, comprising an *o*-benzoquinone ruthenium complex as chelating ligand. Details about the synthesis can be found in references,¹⁵ whereas the structures are shown in **Chart 2.2** and **2.3**.

In the first series, the heterodinuclear derivatives differ for the substituent in *para* position to the nitrogen of the pyridine moiety of phenyl-pyridine cyclometallating ligand: there are indeed two ester-substituted systems (**1** and **2**, with rhodium and iridium, respectively) and four ionic derivatives, ammonium and lithium acetate-substituted (**3** and **5** with rhodium, **4** and **6**, with iridium).

In the second series instead, all the assemblies are homodinuclear, composed of two Ru(II) units, and differ for the increasing conjugation of the ancillary polypyridyl ligand on one of them. The polypyridyl moiety is bipyridine (bpy) in compound **7**, phenanthroline (phen) in compound **8** and diphenylphenanthroline (dip) in compound **9**.

The design of these compounds has been prompted by preliminary careful evaluation on the single components. It was found that organometallic moieties such as Cp^*M ($\text{M} = \text{Ru}(\text{II}), \text{Rh}(\text{III})$ and $\text{Ir}(\text{III})$) can stabilize reactive intermediates by modifying their electronic properties.¹⁶ And the combination with π -bonded quinonoid units, enhancing their donor ability (acquisition of more catecholate contribution),¹⁷ produces organometallic (OM) ligands particularly effective for the preparation of new assemblies with improved properties of luminescence.

Further developments have been obtained by changing the quinonoid OM-unit and the ancillary ligand, giving rise to compounds with panchromatic absorption with high extinction coefficients, in some cases, and unprecedented luminescent ability.¹⁷

2.2.1.1. Cyclometallated Ir(III) and Rh(III) coordination assemblies with π -bonded Catecholate ligand

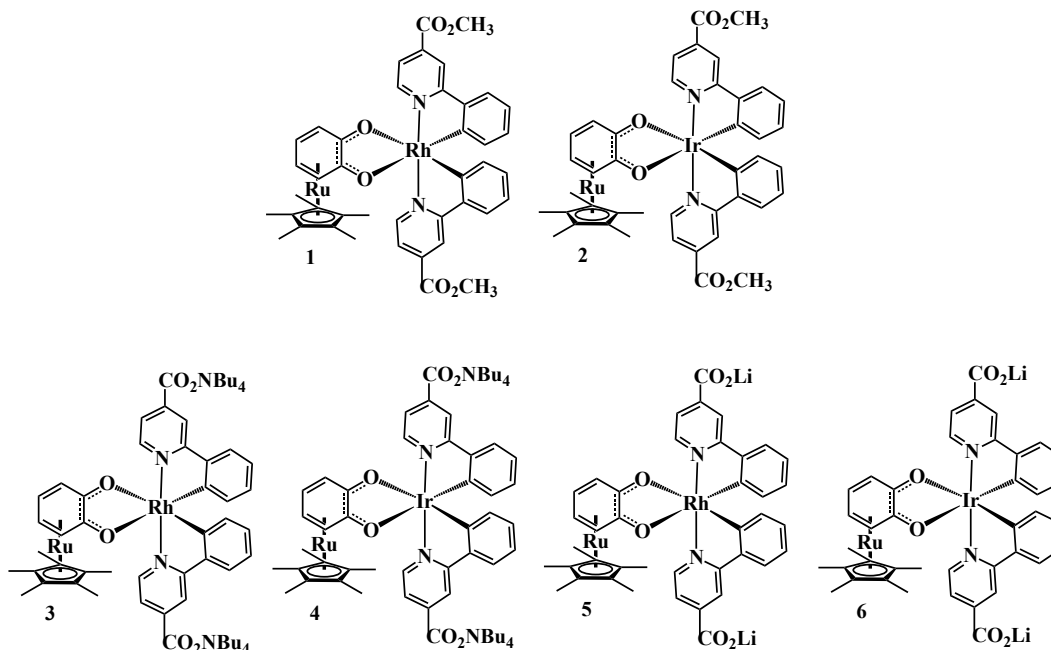


Chart 2.2. Schematic representation of the ester-substituted **1** and **2** and of the acetate-salts **3** and **5**, **4** and **6** of the cyclometallated Rh(III) and Ir(III) coordination assemblies.

Absorption. The absorption spectra of rhodium **1**, **3**, **5** and iridium complexes **2**, **4**, **6** recorded at room temperature (rt) in CH₃OH (MeOH) solutions ($c = 2 \times 10^{-5}$ M) are reported in **Fig. 2.2**, and related data are summarized in **Table 2.1**.

To a first view, for the complexes **3**, **5** and **4**, **6** the absorption profiles appear almost unaffected by the type of counterion, while the change in the metal centre introduces some modifications: on going from Rh(III) to Ir(III) absorption profiles, a red shift is clearly visible.¹⁸ The long tail towards lower energies exhibited by the Ir(III) derivatives can be explained with the stronger spin-orbit coupling of the metal (spin-orbit coupling constant values, $\zeta_{\text{Rh}} = 1259\text{cm}^{-1}$; $\zeta_{\text{Ir}} = 3909\text{cm}^{-1}$)¹⁹ that enhances the probability for singlet-to-triplet transitions to occur. This effect can be explained taking into account that in a molecule with atoms of high atomic number, spin-orbit coupling introduces a component of singlet character into the wavefunction of excited triplet state, and a component of triplet character into the wavefunction of the singlet ground state. Thus, thanks to a mixing of the states, the electric dipole transition moment for the forbidden transition acquires a reasonable magnitude and the direct absorption from singlet ground state to triplet excited state becomes partially allowed.¹⁹

The ester-substituted derivatives **1** and **2** display some sets of bands similar to that of the respective ionic congeners but significantly red-shifted as effect of the absence of the negatively charged carboxylate group on the cyclometallating ligand.

Going deeply in details, in the absorption profiles of both ester- and acetate- substituted derivatives it is possible to observe a band in the high-energy region, with λ_{max} at about

257-270 nm, originating from spin-allowed $^1\pi-\pi^*$ (^1LC) transitions centred on the phenylpyridine ligands. It approximately corresponds to that of the free protonated ligand.²⁰

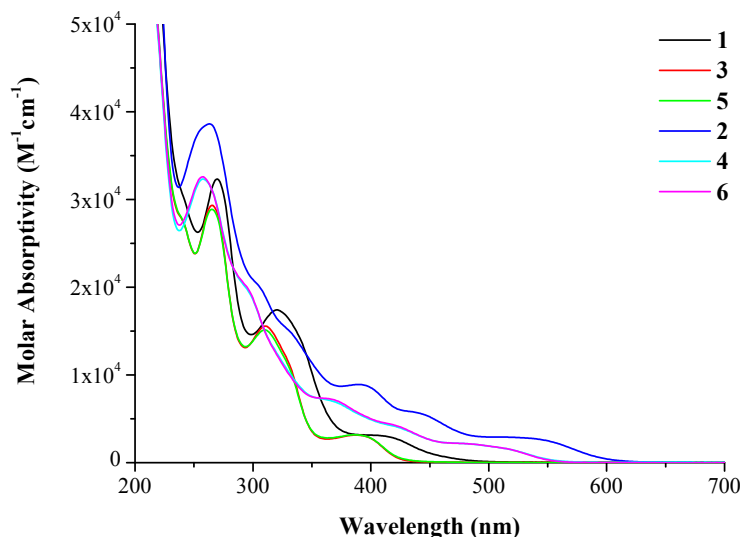


Figure 2.2. Absorption spectra of **1-6** complexes coordinated by $(\text{Cp}^*\text{Ru})(\text{cat})$ chelating ligand in CH_3OH solution at rt.

At lower energy, in the region from 350 to 500 nm for rhodium, and from 350 to 600 nm for iridium derivatives, an envelope of bands with mid values of extinction coefficient ($\epsilon < 10^4 \text{ M}^{-1} \text{ cm}^{-1}$) appears. The respective positions and absorption intensities can give some indications about their nature, anyway not of simple attribution, because of the strong mixing between metal and ligand orbitals.

The photophysical properties of transition metal complexes and of organometallic compounds were usually interpreted taking into account, as simplifying assumption, both the ground and the excited states as described by a localized molecular orbital (MOs) configuration. For this reason, the various spectroscopic transitions were basically classified as metal centred (MC), ligand centred (LC) or of charge transfer character (either metal-to-ligand, MLCT, or ligand-to-metal, LMCT). If such classification can be quite safely adopted for transition metal complexes, it is less precise for organometallic compounds, where metal-ligand bond is characterized by a large degree of covalency. Furthermore, in presence of strong electron donor ligands, the former assumption results even less valid and other types of orbitals have to be involved for a correct interpretation of the spectroscopic properties. Thus it is perfectly reasonable to assume a mixed nature for the transitions responsible for the moderately intense bands in the visible region. First of all, excited states of $^1\text{MLCT}$ nature, related to the Ir(III) and Rh(III) phenylpyridyl moieties, has to be pointed out.

Moreover, further contributions of CT character, from the occupied d metal orbitals to the π^* MOs of the metallated dioxolene moiety, have to be included together with additional components of covalent metal- C^- σ bond to ligand charge transfer ($^1\text{SBLCT}$) and mixed $^1\text{MLCT}$ /intra-valent charge-transfer ($^1\text{ILCT}$) nature.²¹ This twisted attribution can be supported by another information from the literature: in these assemblies,

particularly when the metal in the OM-linker is ruthenium, as effect of the coordination, the catecholate unit seems to give an higher contribution in the description of HOMO orbitals of the entire assemblies, while the LUMO levels are almost completely centred on the ppy ligands (see **Figure 2.3**).^{22,17c}

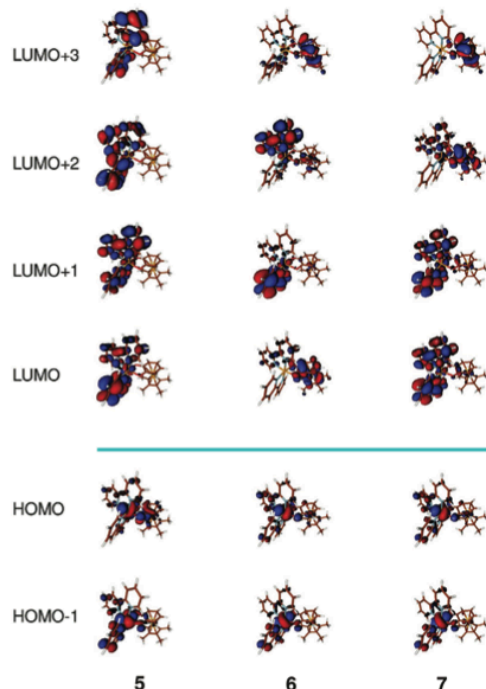


Figure 2.3. Electron density plots calculated for the bimetallic complexes 5-7 (From Ref. 22; complexes of the form $\text{Ru}(\text{bpy})_2[(\text{Cp}^*\text{M}(o\text{-C}_6\text{H}_4\text{O}_2)]$, with $\text{M} = \text{Ru}$ in 5, Rh in 6 and Ir in 7).

Emission. The photoluminescence investigation has revealed the good outcome of the adopted synthetic strategy, producing clear improvement in the emission properties with respect to the parent non-metallated *o*-quinone coordination compounds. In fact, the π -bonded dioxolene derivatives under analysis display a successful bright emission in frozen solution and moderate intensity in solution at rt.

The normalized luminescence profiles recorded at 77 K in $\text{CH}_3\text{OH}:\text{C}_2\text{H}_5\text{OH}$ (1:4) glassy solutions are shown in **Fig. 2.4**, and the relevant photophysical parameters, both at room and at low temperature, are reported in **Table 2.2**.

For rhodium derivatives **1**, **3** and **5** no emission in solution at rt has been detected, while iridium complexes **2**, **4** and **6** weakly emit with low quantum yields ($\phi = 0.5\text{--}5.2 \times 10^{-3}$) in de-aerated solution and with lifetimes in the ns range (**Table 2.2** and **Fig. 2.5**).

As expected, for all complexes **1-6**, intense luminescence at 77 K has been detected, remarkably blue-shifted for the $\text{Rh}(\text{III})$ complexes **1**, **3** and **5** with respect to the corresponding $\text{Ir}(\text{III})$ derivatives **2**, **4** and **6**, as in absorption. Further differences are revealed in the spectral profiles: complexes **1**, **2**, **4** and **6** display almost not-structured emission bands while the ionic rhodium derivatives show particularly featured structures. Again in agreement with the trend registered in absorption, the luminescence spectra of the ester-substituted systems **1** and **2** are red-shifted with respect to those of the ionic congeners, rhodium **3** and **5** for **1** and iridium **4** and **6** for **2**. Furthermore, for

the ionic assemblies, the spectral profiles of the species with the same central metal, Rh(III) or Ir(III), are almost completely superimposable (see **Fig. 2.4**), highlighting that also in emission the different cations do not induce relevant difference in the photoactive energy levels.

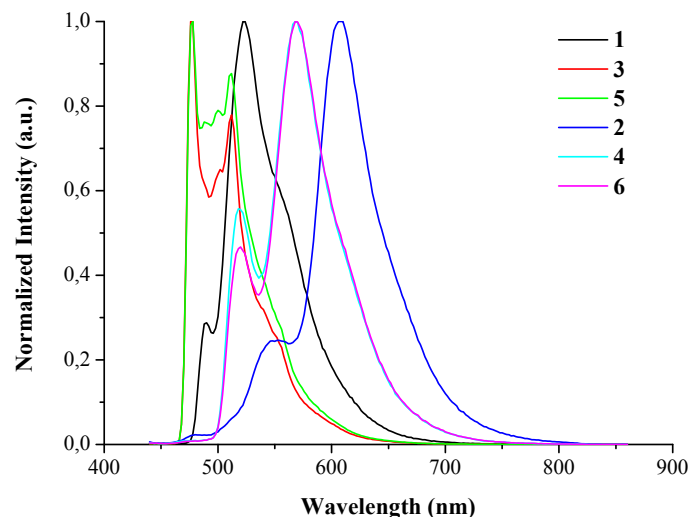


Figure 2.4. Emission spectra of **1-6** complexes coordinated by (Cp**Ru*)(cat) chelating ligand in CH₃OH: C₂H₅OH (1:4) glassy solution at 77 K.

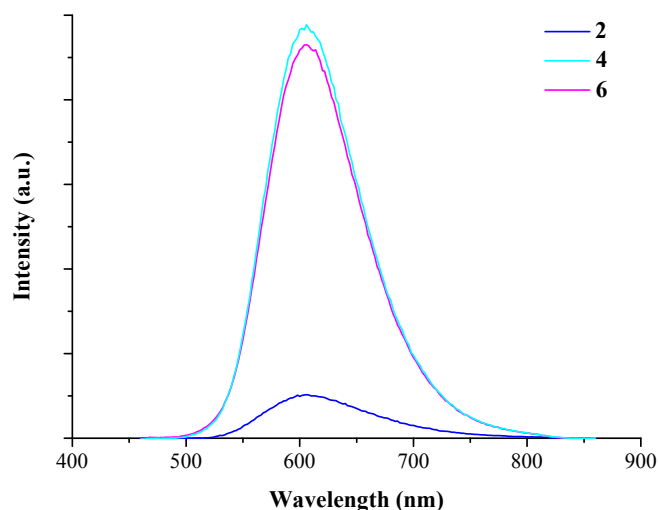


Figure 2.5. Emission spectra scaled for quantum yields of iridium derivatives **2**, **4** and **6** in de-aerated CH₃OH solution at rt.

For the iridium series, a comparison between rt and 77 K luminescence is possible: as typical feature of charge transfer (CT) excited states, on going from solution to glassy matrix, an ipsochromic shift of the emission peaks appears. This effect is called rigidochromism and depends on the reorganization of solvent molecules around the excited complex, after a charge transfer event. In solid matrix such rearrangement is prevented due to environmental restraints on molecular motion. Thus the arising excited

state stabilization that should stem from the reorganization event, cannot take place, resulting in a destabilization of the light-induced excited state.

To better understand the nature of the excited states responsible for the emission in these compounds, analysis of luminescence decays has been performed. Non-mono exponential lifetime components were required to adequately describe the recorded decays. The values of lifetimes obtained from this analysis are in the microsecond range (**Table 2.2**), consistent with emissions originating from ^3LC - $^3\text{MLCT}$ transitions, centred into the $\text{Ir}(\text{ppy})_2$ moiety.²³

Aggregation phenomena. From a deeper examination of the spectral shapes, it is possible to observe the presence of multicomponent emissions at 77 K. In particular, iridium derivatives **2**, **4** and **6** and rhodium complex **1** display a low intensity peak or a shoulder on the high-energy side of the emission curve.

These particular shapes could be ascribed to aggregation phenomena, occurring just in condensed media, and not in solution at rt, as result of the solid-state packing interactions. Such aggregation event is also in agreement with solid-state X-ray analysis. This investigation has suggested the formation of 1D supramolecular assembly, formed through π - π stacking between the phenyl ring of one cyclometallating ligand and the pyridine of another (see **Fig. 2.6**). The π - π interactions occurred in two different directions.

Additional investigations have been performed to confirm such evaluation. The main proof has been obtained through the measurement of the luminescence spectra at increasing concentrations of the complexes because under this condition the aggregate forms should increase. The experiments confirmed the hypothesis and in fact the ratio between the intensities of low and high-energy peaks rose upon increasing of the complex concentration in solution (see **Fig. 2.7**) for complex **6**. Having ascertained the origin of the multicomponent emission, a deeper investigation has been conducted to clarify the exact character of such aggregates. The observed behaviour is indeed consistent with both dimer and excimer formation, displaying broad, structureless, long-lived and large Stokes' shifted emission. These features are the main evidences achievable from emission analysis for strong π -stacking interactions between pairing molecules, and are induced by the large displacement of the excited state, occurring both in dimers and excimers. Before explaining how it was possible to establish which form of aggregation we encountered, it is necessary to clarify the difference between the two possible species.

An excimer is defined as a dimer, present in its associated form upon excitation and dissociated in the ground state. This definition is proper for systems analyzed in fluid solution, instead for rigid matrix it has to be revised due to the environmental restraints on molecular motion. In this condition an excimer has been redefined as a dimer, associated in the excited state but dissociated in the ground state, in the sense that it would dissociate in the absence of external restraints.²⁴

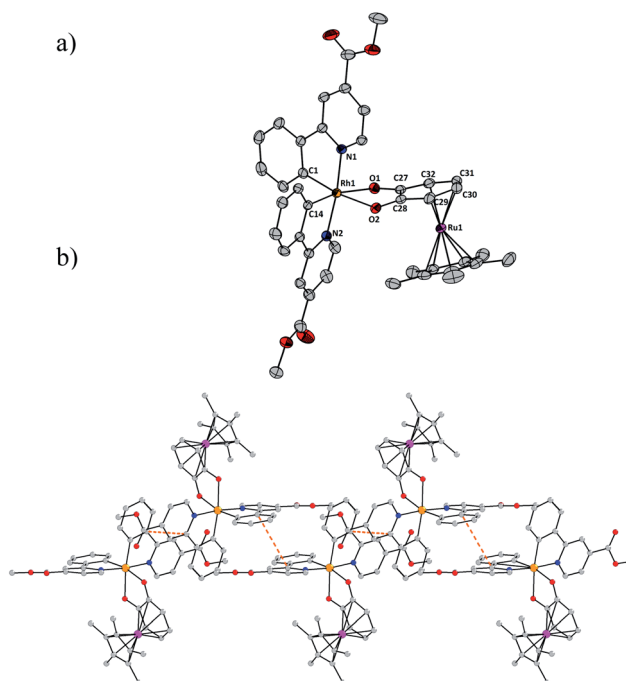


Figure 2.6. (a) Molecular structure of **1** with atom partial numbering system. (b) Solid state packing between individual units showing π - π interactions to generate 1D supramolecular chain. (From Ref. 15a)

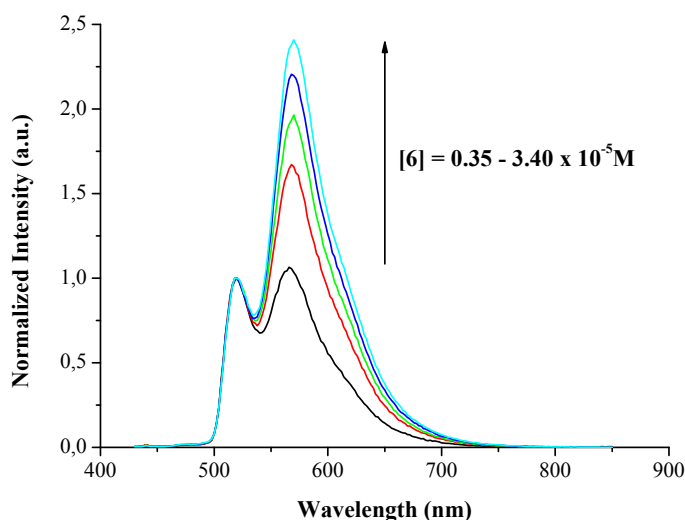


Figure 2.7. Normalized emission spectra of complex **6** in $\text{CH}_3\text{OH}:\text{C}_2\text{H}_5\text{OH}$ (1:4) glassy solution at 77 K at different concentrations ($c = 0.35\text{-}3.40 \times 10^{-5} \text{ M}$).

The way to establish the real nature of the aggregates consisted of the indirect analysis of their ground state in glassy matrix, afforded both performing emission experiments at different excitation wavelengths and recording excitation spectra at the wavelengths corresponding to the two main luminescence peaks.

The results obtained from these measurements converged perfectly: the different excitation profiles registered at the two emission peaks (**Figure 2.8**) and the dependence of the emission shape on the excitation wavelength, as can be observed from the emission map reported for compound **6** in **Figure 2.9**, let us safely infer that the aggregates are already formed in the ground state, thus they are dimers and not

excimers. And the multiple emissions are due to the excitation of both monomers and dimers present in solution (see **Figure 2.10**).

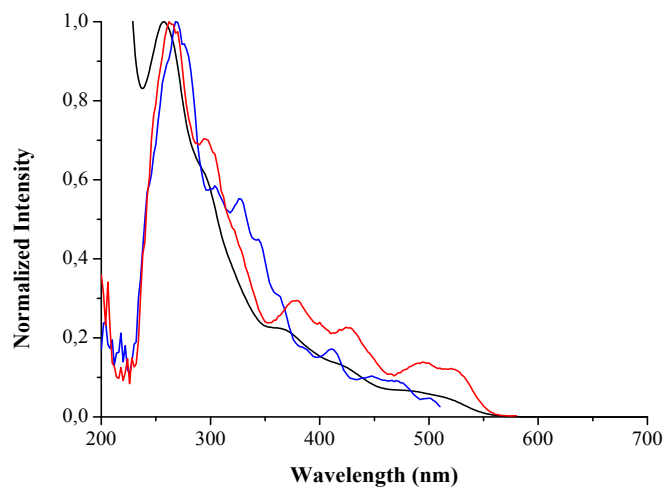


Figure 2.8. Arbitrarily scaled absorption spectrum in CH₃OH at rt (black line) and excitation spectra in CH₃OH: C₂H₅OH (1:4) at 77 K of complex **6**; $\lambda_{\text{em}} = 520$ nm (blue line) and 570 nm (red line).

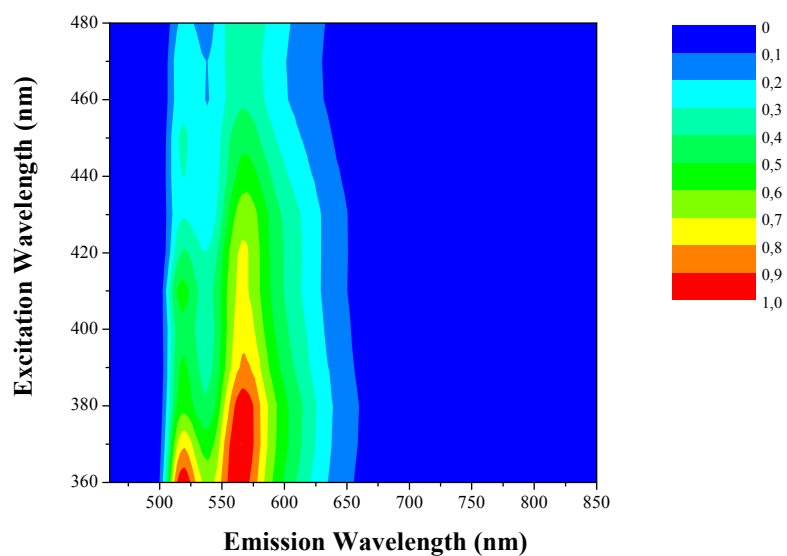
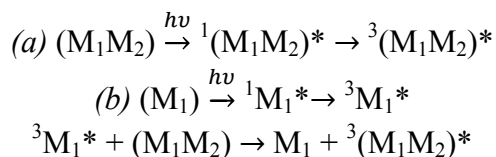


Figure 2.9. Emission map of complex **6** in CH₃OH: C₂H₅OH (1:4) at 77 K at different excitation wavelengths.

Another point to clarify is related to the mode of formation of the bimolecular excited states, achievable exciting the dimers in its ground state or (a) directly or (b) through energy transfer from the excited monomer



In the case (b), the luminescence decay of the excited dimeric species should contain a rise time component, with a lifetime corresponding to the decay time of the monomer, as a consequence of the energy transfer process. In the systems here investigated any negative lifetime component has never been observed in the kinetic analysis of the decays. Thus, it can be concluded that the dimer, already formed in the ground state, is directly excited, as also supported by XRD.²⁵

To obtain the spectral shape of the single components from the global spectra, time-resolved luminescence analysis has been performed, achieving as result the weighted mixtures of all decay components. Such experiment has been conducted by registration of the emission decay kinetic traces of the specimens in a range of wavelengths fixed between 400 and 800 nm, using one excitation wavelength. From the global analysis applied to each registered trace, the lifetimes of both monomer and dimer have been assigned and by plotting the amplitudes of the individual kinetic components as function of the wavelength, the distinct spectra of the two components have been obtained, as decay-associated spectra (DAS). These profiles should be that obtained if a selective excitation of the single components could be achieved. The detailed procedure is reported in Chapter 6.

The spectra obtained for Ir(III) complexes **2** and **6** are reported in **Fig. 2.10** (bottom) where the blue line, at higher energy, is the shape attributed to the monomer emission, well-structured and shorter-lived, while the red line, at longer wavelength and almost unstructured, accounts for the luminescence of the dimeric component, with longer lifetime. Identical experiments have also been conducted for Rh(III) derivatives **1** and **5** and the results are reported in **Fig. 2.10** (top).

It is interesting to note that the measured decay time of the monomer emission is much shorter than that of the dimer. This behaviour can be explained attributing to the dimeric phosphorescence transition a more symmetry forbidden character than that of the monomer. In this condition in fact, the non-radiative rate constant for the deactivation of the dimer is lower than for the monomer, justifying the difference in the lifetime values. However, this is not in line with the most common trend of lower lifetimes for aggregate forms. Nevertheless, *D'Andrade and Forrest* recently showed quite efficient emission from triplet excimers formed on heavy organometallic phosphor molecules.

The emission spectra displayed by the powder of such assemblies at 77 K (**Figure 2.11**) show an unstructured luminescence, red-shifted and longer-lived than in CH₃OH: C₂H₅OH (1:4) glassy matrix. These emissions can be reasonably ascribed to the excited states of oligomeric species, with higher excitonic delocalization than in monomer and dimer.

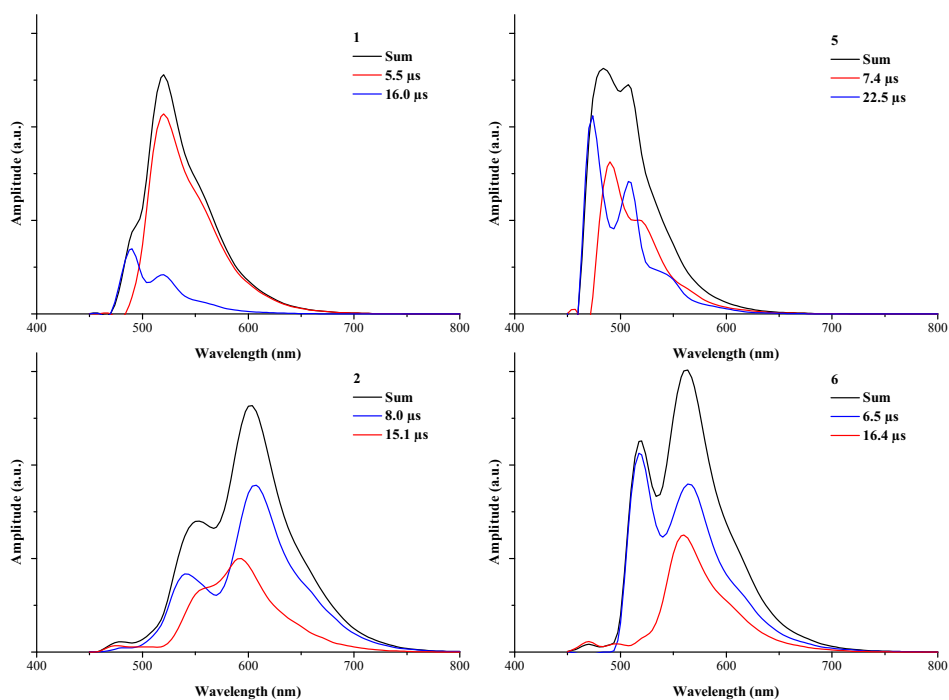


Figure 2.10. Decay Associated Spectra (DAS) of **1** and **5** (top) and **2** and **6** (bottom) in CH₃OH: C₂H₅OH (1:4) at 77 K of monomer (blue line), dimer (red line) and sum of the two components (black line).

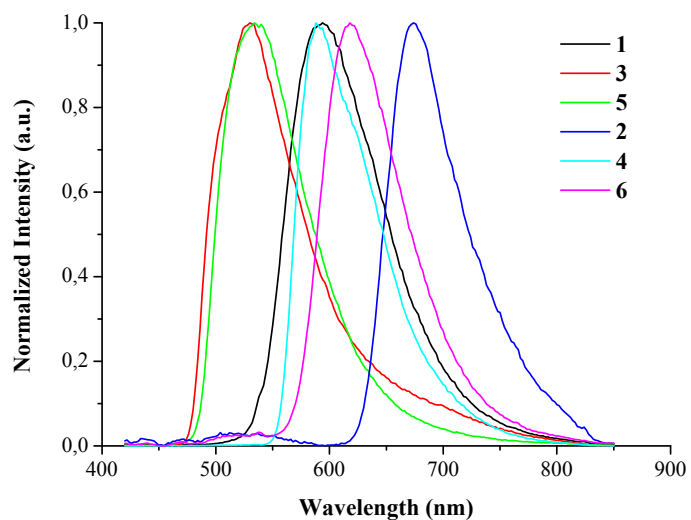


Figure 2.11. Normalized emission spectra of powder samples of **1-6** at 77 K; $\lambda_{\text{exc}} = 390$ nm.

Table 2.1. Absorption properties of the complexes **1-6**.

	λ_{\max} , nm ($\epsilon_{\max} \times 10^{-3}$, M ⁻¹ cm ⁻¹) ^[a]
1	270 (32.3), 321 (17.4), 400 (3.1)
3	265 (29.3), 311 (15.6), 388 (3.1)
5	265 (28.9), 310 (15.1), 386 (3.2)
2	263 (38.6), 302 sh (20.6), 325 sh (15.7), 390 (8.9), 431 sh (5.9), 516 (2.9)
4	257 (32.3), 290 sh (20.6), 365 (7.1), 413 sh (4.4), 476 (2.2)
6	257 (32.6), 291 sh (20.6), 360 (7.3), 414 sh (4.5), 472 (2.2)

^aIn CH₃OH solution at rt; sh is shoulder.

Table 2.2. Emission properties of the complexes **1-6**.

	rt ^[a]		77 K ^[b]	
	λ_{\max} , nm	ϕ	τ , ns	λ_{\max} , nm
1	n.d.	- (-)	- (-)	490, 524
3	n.d.	- (-)	- (-)	477, 512
5	n.d.	- (-)	- (-)	478, 512
2	606	0.6x10 ⁻³ (0.4x10 ⁻³)	37.4 (26.6)	553, 608
4	606	5.0x10 ⁻³ (3.2x10 ⁻³)	243.6 (27.3)	518, 568
6	606	5.2x10 ⁻³ (3.0x10 ⁻³)	43.6 (27.3)	520, 568

^aIn de-aerated (air-equilibrated) CH₃OH solution at rt. ^bIn CH₃OH: C₂H₅OH (1:4) mixture at 77 K. λ_{ex} = 390 nm for steady state and λ_{ex} = 370 nm for time-resolved measurements. n.d. is not detected.

2.2.1.2. Polypyridyl Ru(II) heteroleptic complexes with quinonoid organometallic linker

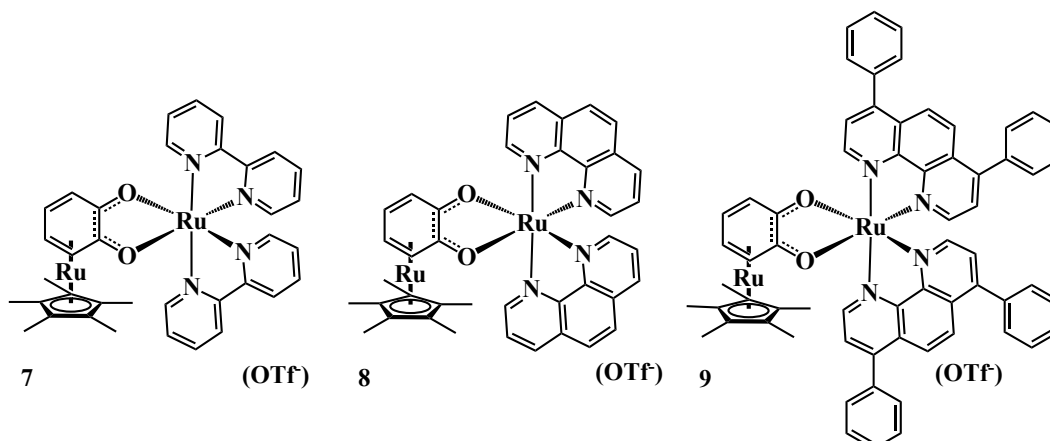


Chart 2.3. Schematic representation of the polypyridyl Ru(II) coordination assemblies **7-9** with the Ru(II)-based quinonoid organometallic linker.

Absorption. The absorption spectra of complexes **7-9**, reported in **Fig. 2.12**, have been recorded in CH₂Cl₂ (DCM) solution at room temperature and relevant photophysical data are collected in **Table 2.3**.

Going from higher to lower energy, absorption profiles of the complexes can be described taking into account the presence of three common features. At about 267-297 nm, an intense band appears as typical fingerprint of polypyridine complexes, ascribed indeed to ligand-centred (¹LC) π - π^* transitions and involving just the polypyridine moiety. At mid-energy a moderately intense band arises at about 344-363 nm, with extinction coefficient values lower than $1 \times 10^4 \text{ M}^{-1} \text{ cm}^{-1}$. Its nature is not of straightforward attribution. In the low energy side of the spectral range, a band peaking between 563 and 582 nm appears, characterized by the expected intensity for a ¹MLCT transition.²⁶

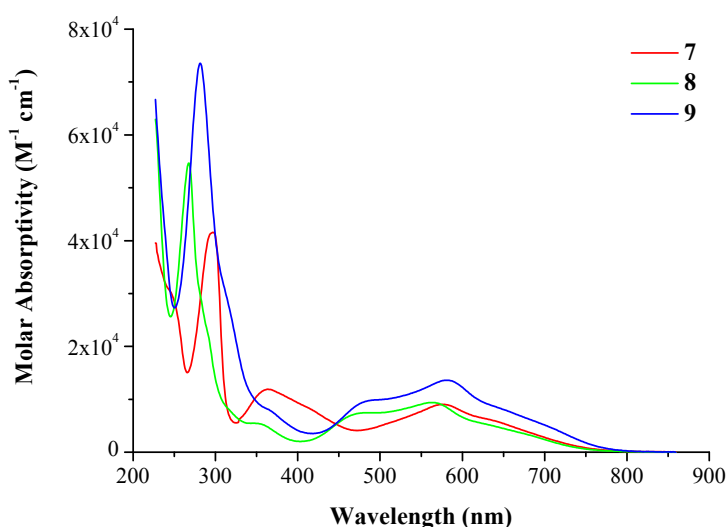


Figure 2.12. Absorption spectra of complexes **7-9** in CH₂Cl₂ solution at room temperature.

The main peculiarity of the absorption properties of complexes **7-9** is their panchromatic behavior. In fact, if compared with [Ru(bpy)₃]²⁺ as model compound,

their CT band results significantly red-shifted and more intense, tailing beyond 700 nm with not negligible extinction coefficient values, higher than $5 \times 10^3 \text{ M}^{-1} \text{ cm}^{-1}$ at about 700 nm for **9**.

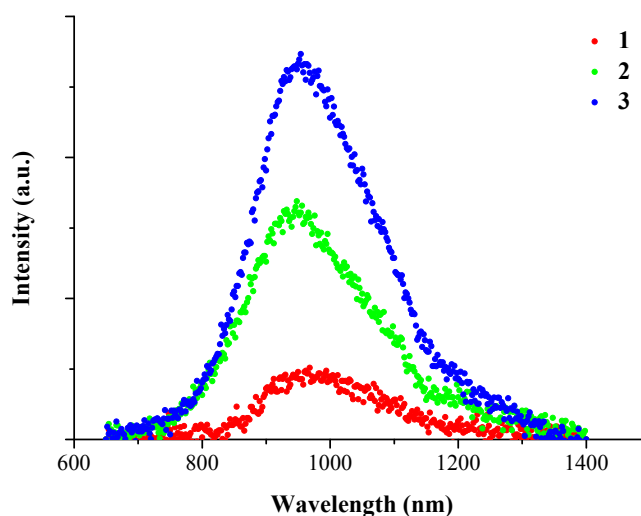


Figure 2.13. Emission spectra of complexes **7-9** in CH_2Cl_2 solution at room temperature.

Emission. The luminescence spectra of the complexes **7-9**, recorded at room temperature in CH_2Cl_2 solutions, are collected in **Fig. 2.13** and the relevant photophysical parameters in **Table 2.3**.

All investigated compounds display a clear NIR emission at room temperature in de-aerated fluid solution, in contrast to the parent non-metallated derivatives.²⁷

The strategic combination of the strong electron-donor Ru(cat) linker with the low lying-acceptor polypyridyl ligand induces a bathochromic shift of the MLCT transition, acting on the HOMO-LUMO gap.

All obtained results are consistent with a ³MLCT nature of the emitting excited state, as also confirmed by the rigidochromic effect observed in the blue shifts on passing from solution to glassy matrix.

Apart from the good result in term of extension of emission in the red region, the effectiveness in the design strategy for such class of compounds is also revealed in the trend displayed by the quantum yields, reported in **Table 2.3**, increasing as the conjugation degree in the polypyridyl ligands increases. This effect can be simply explained by means of the ligand field theory: phen and dip ligands destabilize the metal centred (MC) states, reducing the deactivation of the MLCT excited state by population of the non-emitting MC states.²⁸

In fact, the radiative constant ($k_r = \phi/\tau$) remains almost constant in **7-9** ($k_r = 1.0\text{-}1.3 \times 10^5 \text{ s}^{-1}$, **Table 2.3**) and the observed increase in both photoluminescence quantum yield and excited state lifetime has to be ascribed to a reduction of the rate of non radiative processes, k_{nr} .

The better result obtained for **9** than for **8** can be further justified taking into account that in the excited state the phenyl substituents on the dip ligand can rotate into the plane of the phen to create a more highly conjugated ligand. Such displacement favours a greater delocalization of the excited state electron.²⁹

In **Fig. 2.14** excitation spectra of investigated compounds are reported together with the corresponding absorption profiles in the region of CT bands, revealing a good superimposition that validates the attributed nature of the observed emissions.

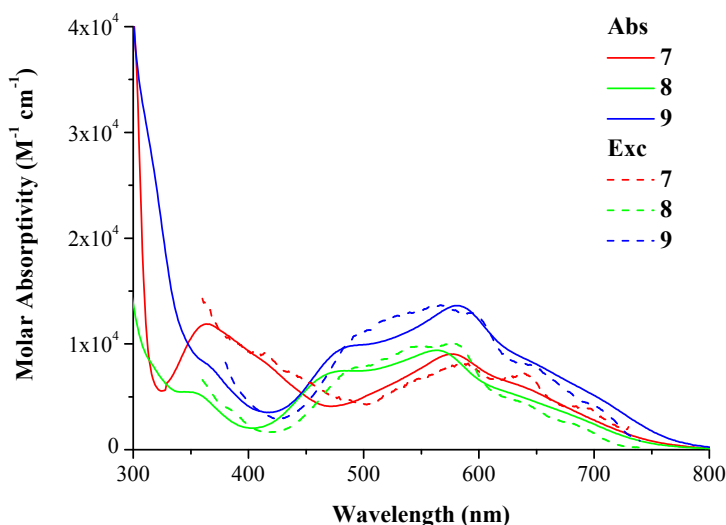


Figure 2.14. Normalized excitation spectra (dashes) compared to the relevant normalized absorption spectra in CH_2Cl_2 (lines) of complexes **7-9** at room temperature.

Table 2.3. Photophysical parameters for the complexes **7-9**.

	λ_{max} , nm (ϵ_{max} , $\text{M}^{-1} \text{cm}^{-1}$) ^[a]	rt ^[b]			77 K ^[c]	
		λ_{max} , nm	ϕ	τ , ns	λ_{max} , nm (eV)	τ , μs
7	297 (41,500), 363 (11,800), 578 (9,000)	968	3.0×10^{-4}	2.3	768 (1.61) ^[d]	1.2 ^[d]
8	267 (54,600), 344 (5,500), 483 (7,500), 563 (9,400)	948	1.0×10^{-3}	10.2	694 (1.79)	2.1
9	282 (73,500), 362 sh (8,200), 497 (9,900), 582 (13,600)	954	1.6×10^{-3}	12.3	718 (1.73)	2.9

^a In CH_2Cl_2 solution at rt. ^b In de-aerated CH_2Cl_2 solution at rt; for quantum yield $\lambda_{\text{exc}} = 460$ nm, for lifetime measurements $\lambda_{\text{exc}} = 465$ nm. ^c In $\text{CH}_3\text{OH}:\text{C}_2\text{H}_5\text{OH}$ (1:4 v/v) solution, $\lambda_{\text{exc}} = 460$ nm; for lifetime measurements $\lambda_{\text{exc}} = 465$ nm. ^d From Ref. 12b.

2.2.2. Square-planar Pt(II) chelated by novel (Catecholate/Benzenedithiolate)M complexes

Square-planar polypyridyl platinum(II) complexes have attracted much attention in recent decades because of their photochemical and photophysical properties³⁰ that make them really interesting for application in organic light-emitting devices (OLEDs),^{30,31} molecular sensors,³² photochromic materials³³ and as phosphorescent probes for bioimaging.³⁴

Moreover, these d^8 complexes, due to their free coordination sites, can undergo additional reactions of self- and cross-quenching,³⁵ exhibiting high photoreactivity³⁶ and photocatalytical properties that widen their field of applicability.

The main limit of such class of compounds is related to the presence of low-lying non-emissive metal-centred (MC) d-d excited states close in energy to the emissive MLCT states and thus thermally accessible. MC states can compete with population of the neighbors MLCTs, offering an efficient non-radiative deactivation pathway to the molecule and quenching partially or completely its luminescence in solution at room temperature.

Several strategies to overcome this limit and to fine-tune emissive behaviour have already been widely explored, comprising the increase of the MLCT states population and raise of the d-d LF excited states energy. These effects can be obtained, respectively, through introduction of strong π -acceptor ligands, that stabilize the MLCT states, and through incorporation of strong σ -donor ligand, able to push the non-emissive MC states to higher levels, as a result of the enlargement of d-d orbital splitting.

The most common approach in tuning luminescence properties consists in the coupling of linear cyanide or alkynyl groups. They, particularly with extended or conjugated π -systems and linear rigid structure with linear geometry, work as strong ligand field groups due to their strong σ -donating ability, enhancing the luminescence properties of Pt(II) complexes through the raise of the d-d state to inaccessible energies.³⁷

In this section a new approach toward the activation of Pt(II) complexes luminescence properties will be discussed, based on the strategic design of a new class of compounds obtained through chemical modification of the noninnocent 1,2-dioxolene chelating ligands and their dithiolate derivatives, at a supramolecular level, by using the “complex as ligand approach”, as reported for the series reported above.

Complexes with benzoquinone-type ligands were extensively studied because of their interesting spectro-electrochemical behavior but nevertheless, there are only relatively few catecholate complexes of Pt(II) already known,³⁸ and only recently the photophysical properties of Pt(II) heteroleptic assemblies based on mixed dioxolene and diimine ligands have been investigated.^{7,39} Here, the discussion will focus on the role of π -bonded metallated quinonoid ligands in (diimine)Pt(II) chromophores. a novel class of luminescent compounds, in which the metal in the “organometallogand” is changed from Rh(III) (**11**), to Ir(III) (**12**), to Ru(II) [**13** with Cp*Ru unit and **14** with (bz)Ru unit].

In addition, a series of cyclometallated platinum(II) complexes, thought always with the purpose to achieve improvement in luminescence properties, has been analyzed and will be reported below, with the metal centre surrounded by phenylpyridine and its two derivatives [(ppy) for **15**, 2-(2,4-difluorophenyl)pyridine (dfppy) for **16** and 7,8-benzoquinoline (bzq) for **17** complexes] and by Cp*M-dithiolate chelating ligands as OM-linkers, always in a square-planar coordination mode.

Prior to this work, only recently two simple square planar anionic cyclometallated Pt(II) complexes of the form [(C^N)Pt(benzenedithiolato)][NBu₄] have been described by *Herrero and coworkers*,⁴⁰ but they exhibited lower luminescence performances.

The synthetic procedures for the two series of Pt(II) assemblies are reported in references,⁴¹ whereas their structures are shown in **Chart 2.4** and **2.5**, respectively.

2.2.2.1. Bipyridyl Platinum(II) with π -bonded Catecholate ligand

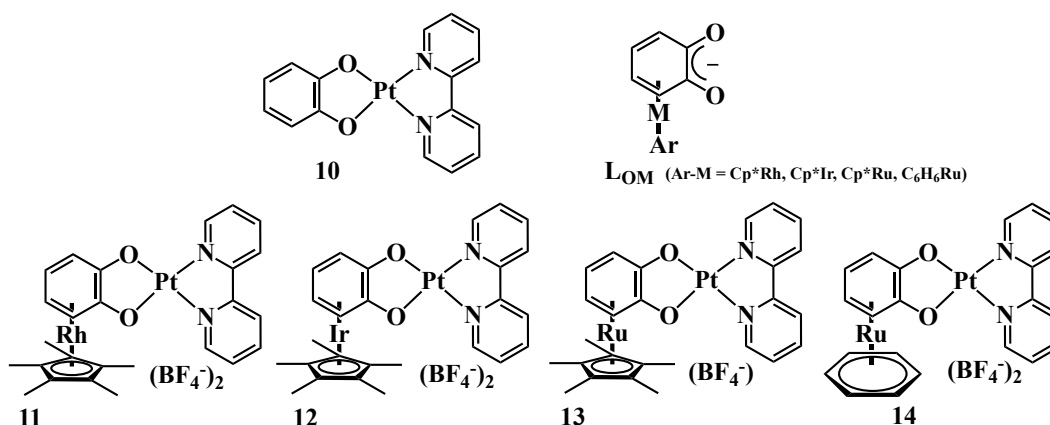


Chart 2.4. Schematic representation of the model catecholate system (bpy)Pt(II) (**10**), of the quinonoid organometallic ligand (**LOM**) and of the novel (bpy)Pt(II) coordination assemblies with Rh(III) (**11**), Ir(III) (**12**) and Ru(II) (**13** and **14**) catecholate ligand.

Absorption. The investigation on absorption properties of Pt(II) catecholate complexes **10**, **11**, **12**, **13** and **14** has been performed in dilute CH₃CN (ACN) solution ($c = 2 \times 10^{-5}$ M) at room temperature (rt) and relevant data are collected in **Table 2.4** and in **Fig. 2.15**.

The complex **10** represents the starting species for the fabrication of the series and is the non-metallated derivative, with neutral neat charge and without the Cp*M moiety attached to the quinone ligand. Its absorption profile displays peculiar transitions, extended in the visible region up to 700 nm. Starting their description from the high energy region, four bands below 360 nm (dotted line in **Fig. 2.15**) can be primarily mentioned.

The band peaking at about 290 nm has been assigned to intraligand ¹ π - π^* transitions, centred on the α -diimine fragment and is the typical identification feature of bipyridyl metal complexes.⁴² Other bands appear in the region between 290 and 360 nm, ascribable to charge-transfer transitions from the d orbital of the metal to π -antibonding orbitals of the ancillary ligand. The band responsible for the quasi-panchromatic absorption of such compound is centred at about 530 nm, with a moderately high extinction coefficient ($\epsilon_{\max} = 5200 \text{ M}^{-1} \cdot \text{cm}^{-1}$) due to the presence of the heavy atom

effect. This can be assigned to a charge-transfer transition of $L_{cat}L_{bpy}CT$ nature, involving the two chelating ligands and starting from the highest occupied molecular orbital (HOMO), mainly on dioxolene, and reaching the lowest unoccupied molecular orbital (LUMO), exclusively centred on the α -diimine. The presence of additional singlet-triplet transitions explains the wide broadening of this band.

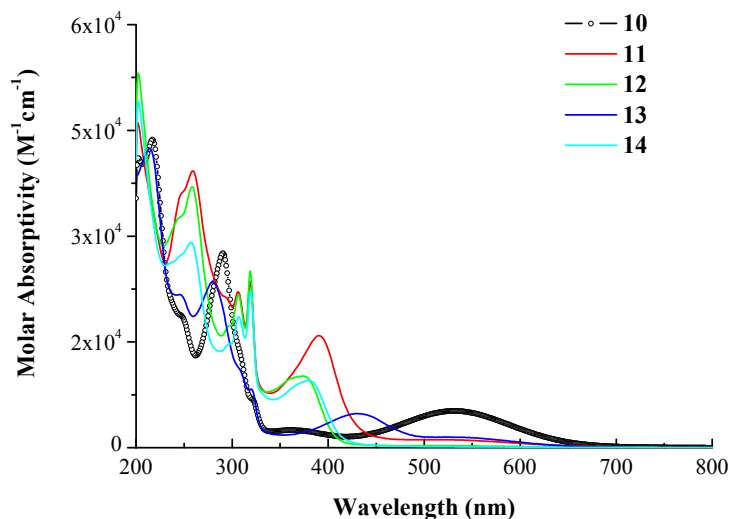


Figure 2.15. Absorption spectra of the monometallic model complex **10** and of the dimetallic assemblies **11**, **12** and **13** and **14** in CH_3CN solution at rt.

For a schematic discussion, the metallated derivatives **11**, **12**, **13** and **14** can be divided on the basis of the respective total charges that largely influence their absorption spectra. In fact, while the singly charged complex **13** exhibits good agreement with **10**, particularly below 320 nm, the doubly charged species **11**, **12** and **14** differ from the first two displaying strictly similar behaviour one to another. Anyway, if for the simplest complex **10** the assignment of the nature of observed absorption bands could be almost immediate, for the bimetallic coordination assemblies, **11**, **12**, **13** and **14**, it is not so plain and immediate.

In these complexes, the strong degree of orbital mixing between metal $d(\pi)$ and ligand $p(\pi)$ frontier orbitals, typical of organometallic compounds, characterized by large degree of covalency along the metal-ligand bond, makes difficult the conventional interpretation of the spectroscopic properties. In fact, DFT and TD-DFT calculations have been performed to achieve a correct attribution of the nature of observed bands (see **Figure 2.16**). The full dissertation about calculations is reported in the reference.^{41a} Absorption spectra of the dications **11**, **12** and **14** can be described by splitting their profiles in three main parts that differ in the intensities of the component bands but with similar shapes and positions. The first two portions are made up of two intense envelopes of bands in the high-energy region of the spectrum, respectively placed at about 260 and 300 nm. The former originates from $L_{OM}C$ and $L_{bpy}C$ transitions while the second from mixed of $L_{OM}C$ / $MLL_{OM}CT$ transitions. The marked lowering of the intensity at about 290 nm, in correspondence to the first absorption band of **10**, is probably due to the presence of triplet-triplet transitions. In the last section instead, another band arises at

about 380, blue-shifted and more intense than for **10** and **13**. Transitions of pure $L_{Ir}L_{bpy}CT$ character for **12** and of mixed $L_{Rh}L_{bpy}CT/ L_{Rh}C$ and $L_{Ru}L_{bpy}CT/ M_{Pt}L_{bpy}CT$ nature for **11** and **14**, respectively, are responsible for such band.^{41a}

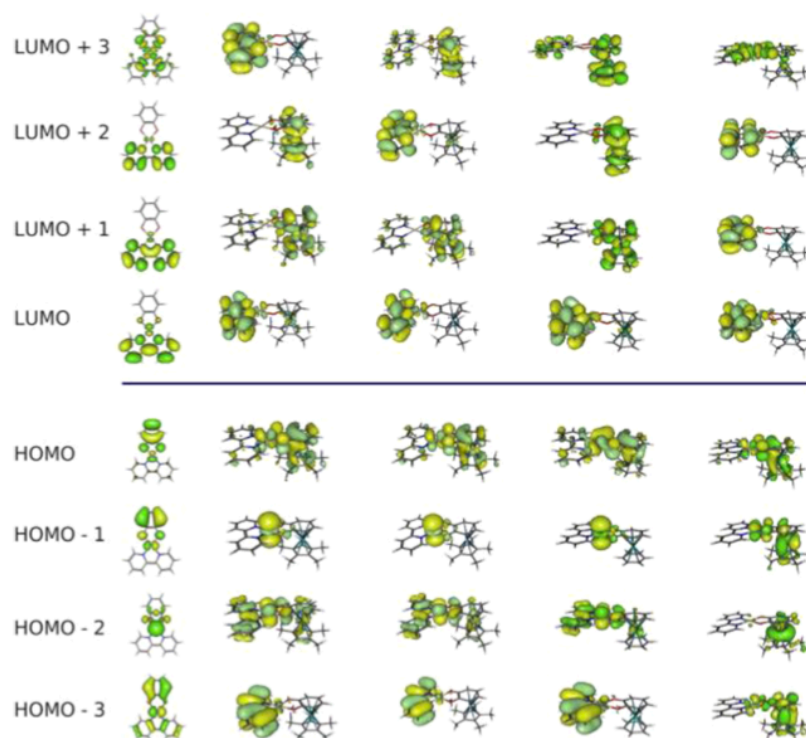


Figure 2.16. Calculated MOs of compounds **10**, **11**, **12**, **14** and **13** (from the left). (From Ref. 41a)

For the singly charged complex **13**, apart from the first band at 280 nm, associated to a $L_{bpy}C$ transition, and a little peak at about 320 nm, ascribable to $L_{Ru}L_{bpy}CT$ transitions, other two bands appear in the low energy part of the spectrum. The first band, peaking at 430 nm, is reasonably associated to charge transfer transitions, based on the observation of a solvatochromic effect. A blue shift of 16 nm is observed on going from the less polar dichloromethane to acetonitrile solution (dielectric constant values, $\epsilon = 8.93$ and 35.94 , respectively). In particular in agreement with literature data, it seems to be indeed ascribable to a mixed-metal-ligand-to-ligand charge transfer (CT) transition, from an orbital of mixed metal and catecholate composition to a lowest unoccupied orbital localized on the diimine ligand.⁴³ At 525 nm the second band arises, appearing as a shoulder of the previous one. It is very close in energy to the corresponding $L_{cat}L_{bpy}CT$ transition band in **10** but with greatly reduced intensity and can be safely attributed to transitions of similar nature.

The main differences evidenced between the complexes of the series can be explained by means of their different charge distribution within the OM-ligand, depending on the withdrawing effect of the (Arene)M moieties on the catecholate. It increases along the series of dicationic assemblies in the following order **14** > **12** > **11**. Also in the case of the monocation **13** the cat moiety acts as an electron donor toward the (Cp*)Ru unit (Pt(II) always acts as a bridge for the exchange of electrons between the bpy and OM-

ligand). Thus, in all systems, the HOMO-LUMO gap increases with the oxidation number of the metal in the (Arene)M unit. And this can explain the large blue shift observed for **11**, **12**, **13** and **14** with respect to **10**, in the absorption spectra.

Emission. The analysis of luminescence properties revealed that, apart from **13**, none of the examined complexes display emission ability in de-aerated solutions at rt, while all of them **10-14** display bright emission in glassy mixture of CH₃OH: C₂H₅OH (1:4) at 77 K. All related photophysical parameters are reported in **Table 2.4** and the associated emission profiles are collected in **Figure 2.17**.

The emission investigation highlights the double effect of the coordination of the M(Cp*/bz) unit to the cat ligand on the luminescence properties: the supramolecular assemblies **11**, **12**, **13** and **14** at low temperature exhibit both an increase of the luminescence, unlike the parent non metallated **10**, and a modulation of the emission wavelength upon substitution of the metal in the OM ligand.

The Rh(III) and Ir(III) dicationic derivatives **11** and **12** display in glassy solution at low temperature an unstructured emission band, peaking at about 590 nm with lifetimes in the μ s range and no luminescence at room temperature.

For Ru(II) derivatives **13** and **14**, mono and di-cationic respectively, the emissions at 77 K are very similar in energy ($\lambda_{\text{max}} = 515$ and 530 nm, $\tau = 30.0$ and 6.3 μ s, respectively), confirming the common nature for their emitting excited states. For **14** the emission is weaker and shorter-lived than for **13**, suggesting a lower emission quantum yield with respect to the Cp*Ru analogue.

The emission energy of the metallated assemblies can thus be tuned over a wide range, from green to orange, by simply changing the metal centre (M = Rh, Ir or Ru) in the OM linker.

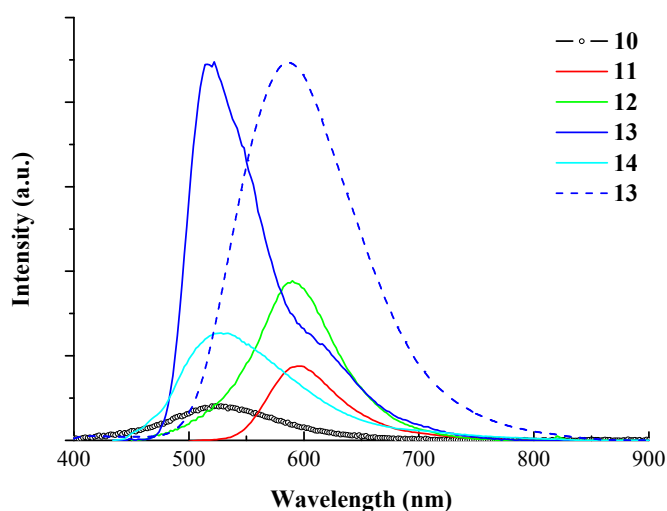


Figure 2.17. Emission spectra of the monometallic model complex **10** and of the dimetallic assemblies **11**, **12**, **13** and **14** in CH₃OH: C₂H₅OH (1:4) glassy matrix at 77 K (full lines) and of **13** in CH₂Cl₂ solution at rt (dotted line). A = 0.1 at $\lambda_{\text{exc}} = 370$ nm; the spectrum of **13** at rt has been normalized to that observed at 77 K.

Beyond the tuning effect, this organometallic ligand has also the notable effect of increasing the luminescence intensity, especially when Ru(II) is present, as already

observed in the above discussed series of octahedral heteroleptic Rh(III) and Ir(III) complexes.⁴⁴

The additional effect on luminescence properties is observed in the best performing mono-cationic assembly **13**, displaying emission at rt, too. Its orange-red luminescence, recorded in CH₂Cl₂ solution ($\lambda_{\text{max}} = 586 \text{ nm}$, $\phi = 3.4 \times 10^{-3}$, and $\tau = 56.4 \text{ ns}$) increases upon removal of oxygen ($\phi = 4.1 \times 10^{-3}$ and $\tau = 67.1 \text{ ns}$), as expected particularly when the emission is ascribed to long-lived formally forbidden triplet excited-state transitions. The value for the radiative rate constant calculated from experimental data (ϕ / τ), $k_r = 6 \times 10^4 \text{ s}^{-1}$, is comparable to that already observed for other organometallic Pt(II) square planar complexes with bpy ligands.^{30a,45} The large blue shift of the emission of *ca.* 2300 cm⁻¹ observed on going from rt to 77 K, and the broad and not-structured shape of the emission profile are all indications of a clear and reasonable attribution of CT nature to the excited state responsible for the emission.

Table 2.4. Photophysical parameters for the complexes **10-14**.

		77K ^[b]	
	λ_{max} , nm ($\epsilon_{\text{max}} \times 10^{-3}$, M ⁻¹ cm ⁻¹) ^[a]	λ_{max} , nm	τ , μs
10	245 sh (18.9), 290 (27.5), 320sh (7.0), 361 (2.5), 532 (5.2)	530	7.3
11	259 (39.3), 306 (22.1), 319 (23.6), 390 (15.9), 509 (1.1)	595 (601)	6.5
12	258 (37.0), 306 (21.7), 319 (25.1), 373 (10.1), 491 (0.3)	590 (553)	3.8
13	245 (21.7), 280 (23.6), 320 (8.3), 430 (4.8), 524 (1.5)	515 (514)	30.0
14	257 (29.1), 307 (18.5), 319 (22.2), 379 (9.5)	530 (516)	6.3

^aIn CH₃CN solution at rt; sh is shoulder ^b In CH₃OH: C₂H₅OH (1:4) at 77 K; the calculated emission energies are reported in parentheses.

2.2.2.2. Neutral Cyclometallated Platinum(II) Complexes with π -bonded Benzenedithiolate

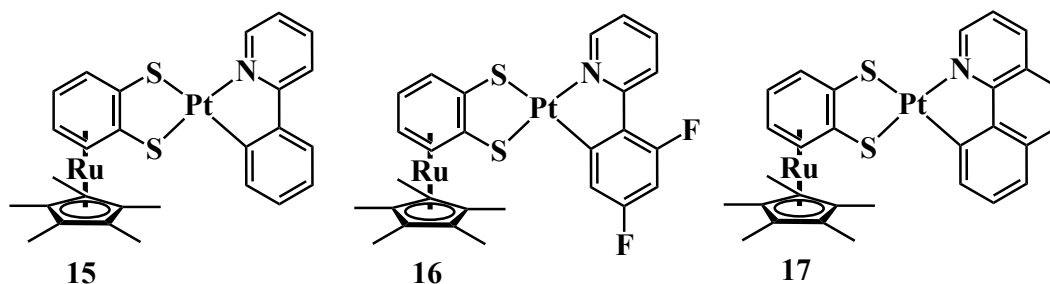


Chart 2.5. Schematic representation of the $[\text{Cp}^*\text{Ru}(\text{benzenedithiolate})]\text{Pt}(\text{II})(\text{C}^{\wedge}\text{N})$ supramolecular assemblies with different cyclometallating ligands such as phenylpyridine (ppy) (**15**), 2-(2,4-difluorophenyl)pyridine (dfppy) (**16**) and 7,8-benzoquinoline (bzq) (**17**).

Absorption. The UV-Vis absorption spectra have been measured in CH_2Cl_2 solution at room temperature for the complexes **15-17**. Their profiles are reported in **Figure 2.18** while the key parameters collected in **Table 2.5**.

For a description of absorption properties of such complexes, first of all it is important to underline the effects of $\text{Ru}(\text{Cp}^*)$ linkage to the benzenedithiolate (bdt) unit. It induces the increase of the intensity for the CT band and its blue shift ($\lambda_{\text{max}} = 426 \text{ nm}$ and $\epsilon_{\text{max}} = 9000 \text{ M}^{-1}\text{cm}^{-1}$ for **16**) with respect to that of the parent non-metallated complex $[(\text{ppy})\text{Pt}(\text{bdt})]^-$ ($\lambda_{\text{max}} = 479 \text{ nm}$ and $\epsilon_{\text{max}} = 5500 \text{ M}^{-1}\text{cm}^{-1}$).⁴⁶ This behaviour can be simply explained taking into account the stabilization of the molecular orbitals centred on the $\text{Pt}(\text{bdt})$ fragment, induced by the coordination of $\text{Ru}(\text{II})$, that does not influence the energy levels localized on the cyclometallated ligand, but anyway increases the HOMO-LUMO gap and thus the amount of energy required for the charge transfer transition towards ppy ligand.

The discussion of the main details of the absorption spectra of such complexes is conducted below moving from higher to lower energy. The assemblies **15** and **16** possess the same basic features and do not seem to be significantly affected by the different cyclometallating ligand (ppy and dfppy, respectively), nor in shape nor in intensity of absorption bands, while in the case of **17** (bzq as $\text{C}^{\wedge}\text{N}$ ligand) a new band arises at about 360 nm and some other slight differences appear.

One of the common features for the three complexes is an envelop of intense bands in the near UV region of the spectrum, between 250 and 350 nm, with value of extinction coefficient at about 260 nm in the range $20000\text{-}25000 \text{ M}^{-1}\text{cm}^{-1}$. This peak can be assigned, by comparison with literature data, to intra-ligand (IL) $\pi\text{-}\pi^*$ transitions and its energy is indeed very close to that reported for uncoordinated phenylpyridine.²⁰ An additional contribution is given by metal-perturbed ligand centred (LC) transitions on the cyclometallating ligand, appearing at about 300 nm and less pronounced in complex **17** than in **15** and **16**.⁴⁰

talk in general terms about “charge transfer to ppy” as reported in systems with similar behaviour in presence of bpy in place of ppy.⁴⁷

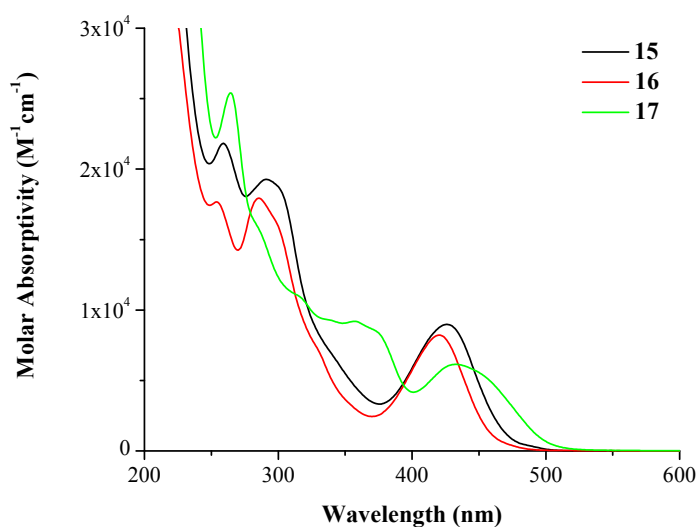


Figure 2.18. Absorption spectra of the dimetallic **15-17** complexes coordinated by (Cp**Ru*)(dithiolate) chelating ligand in CH₂Cl₂ solution at rt.

Emission. Photoluminescence has been detected for all the complexes in fluid solution and in frozen glasses of CH₂Cl₂:CH₃OH (1:1) at 77 K and the relevant data are included in **Table 2.6** and in **Figure 2.19**.

All complexes **15-17** are luminescent at low temperature and just the complex **17** has a non-negligible emission in de-aerated CH₂Cl₂ solution at room temperature thanks to its more conjugated cyclometallating ligand, as reported for similar compounds with the M(cat) chelating unit.¹⁷

The hypsochromic shift of the emission on going from rt to 77 K, higher for complex **17**, and the almost featureless broad spectrum at rt confirm the CT nature of the excited state.

The shape of emission spectra recorded at 77 K is characterized by a well-defined vibrational progression, particularly for **15** and **17**, accounting for a mixed ³LC/MLCT nature for the emissive excited states of the complexes. Such assumption is also confirmed by emission lifetime values, standing in the microsecond time range similarly to other reported cyclometallated platinum(II) complexes.¹⁸

It is important to point out that the increasing conjugation of the cyclometallating ligands along the series produces a significant red shift of the emission peaks going from **15** to **17**, tuning the luminescence color over a wide range from blue to green-orange. This result confirms that a strategic and planned modification of the C[^]N ligand can drive the emission exactly in the targeted direction.

The choice for the combination of these C[^]N ligands with the metallated quinonoid unit is motivated first of all by the positive role of the cyclometallation with respect to the chelation of the diimine corresponding ligand.⁴⁸ It is well known that the strong σ -donor ability of the cyclometallated carbon unit destabilizes the non-emitting metal-centred (d-d) states, increasing its energetic content with respect to that of the ppy ligand triplet state and thus lowering its population.⁴⁹

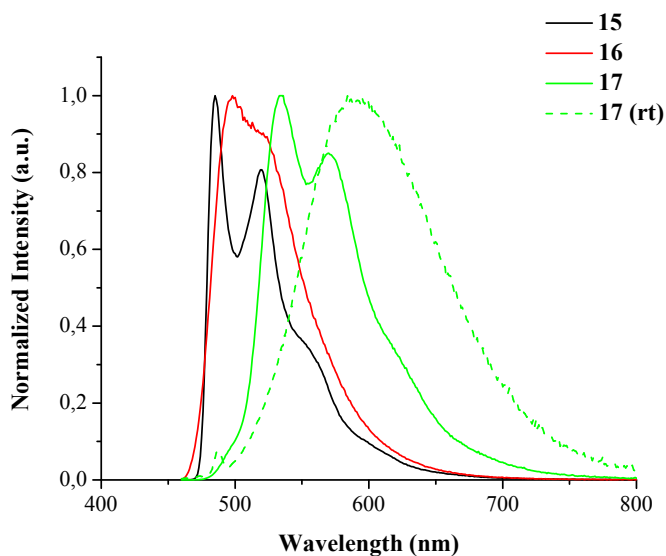


Figure 2.19. Normalized emission spectra of the dimetallic **15-17** complexes coordinated by (Cp*Ru)(dithiolate) chelating ligand CH₂Cl₂: CH₃OH (1:1) mixture at 77 K (full line) and of **17** in CH₂Cl₂ solution at rt (dotted line); $\lambda_{\text{ex}} = 425$ nm.

Table 2.5. Absorption properties of the complexes **15-17**.

	λ_{max} , nm ($\epsilon_{\text{max}} \times 10^{-3}$, M ⁻¹ cm ⁻¹) ^[a]
15	259 (21.8), 291 (19.3), 426 (9.0)
16	254 (17,700), 286 (17,900), 420 (8,200)
17	264 (25,400), 358 (9,200), 433 (6,100)

^aIn CH₂Cl₂ solution at rt.

Table 2.6. Emission properties of the complexes **15-17**.

	rt ^[a]			77K ^[b]	
	λ_{max} , nm	ϕ	τ , ns	λ_{max} , nm	τ , μ s
15	510	1.0×10^{-4}	4.7	485	6.0
16	514	0.5×10^{-4}	5.3	498	6.3
17	580	19.7×10^{-4}	157	533	59.0

^aIn de-aerated CH₂Cl₂ at rt. ^bIn CH₂Cl₂: CH₃OH 1:1 mixture at 77 K. $\lambda_{\text{ex}} = 425$ nm for steady state emission spectra and $\lambda_{\text{ex}} = 370$ nm for lifetime measurements.

2.3. Conclusions

The cyclometallated Ir(III) and Rh(III), the polypyridin Ru(II) and the bipyridyl/phenylpyridyl Pt(II) complexes containing π -bonded organometallic ligands of the form (cat/thiol)M(Cp*/bz) have been investigated focusing on their photophysical properties, both in solution at room temperature and in glassy matrix at low temperature. All of them displayed good emission properties, with bright phosphorescence in condensed media at 77 K, in contrast to that reported for similar coordination compounds with non-metallated *o*-quinone ligands. For some of them phosphorescence has been already detected in solution at rt, with moderate quantum yield, highlighting the positive role of the M(Cp*/bz) fragment coordination to the catecholate, in the enhancement of the donor ability of cat/dithiolate ligand. The effectiveness of (cat/tiolate)M(Cp*/bz) fragment as ligand appears not only in terms of improvement of luminescence properties with respect to non-metallated parent compounds, but also in the serious modification induced to the photophysical behaviour of the attached octahedral and square planar luminophore building blocks. The original use of organometallic ligands produced several effects: (1) multicomponent emission in phenylpyridine Ir(III) and Rh(III) complexes, by favouring π -stacking interactions; (2) transformation of traditional polypyridin Ru(II) complexes in good panchromatic absorbers and near-infrared emitters; (3) tuned emission of bipyridyl Pt(II) complexes over a range from green to orange, by changing the metal in the M(Cp*/bz) fragment, and (4) over a range from blue to green-orange, by changing the cyclometallating ligand on the Pt(II)(dithiolate) centre.

The first series of cyclometallated metal complexes, [(C[^]N)M(cat)Ru(Cp*)] (M = Ir(III) and Rh(III)), showed a bright emission in condensed media at 77 K, in contrast to that reported for coordination compounds with a non-metallated *o*-quinone ligand. Moreover, the strong π - π interactions, observed in the solid-state through X-ray analysis appear also in solution, materialized in the formation of dimeric species already present in the ground state. Emissions from oligomeric species arranged in 1D supramolecular chain have also been observed from the analysis of neat film at 77 K.

The second series of polypyridyl Ru(II) assemblies, [(N[^]N)Ru(cat)Ru(Cp*)] (N[^]N = bpy, phen and dip) shows unprecedented luminescent behavior, displaying panchromatic absorption and clear NIR luminescence in solution thanks to the presence of Ru(Cp*) fragment. Moreover, by simply increasing the conjugation of the polypyridyl ligands, an increase of quantum yields has been obtained.

The third series of supramolecular assemblies, [(bpy)Pt(cat)M(bz/Cp*)] (M = Ru(II), Ir(III) and Rh(III)), displayed a bright emission at low temperature, in contrast to the parent [(bpy)Pt(cat)] compound, highlighting the positive role of the coordination of the M(Cp*/bz) fragment to the cat ligand in turning on the luminescence properties. Notably, the Ru(Cp*) derivative **13** showed phosphorescence already in solution at rt with moderate quantum yield.

The fourth series demonstrated that in neutral complexes of the type [(C[^]N)Pt(S[^]S)Ru(Cp*)], the manipulation of absorption and emission properties can be easily achieved acting on the C[^]N cyclometallating ligands coordinated to the Pt(II)

centre. Noteworthy is the luminescence at rt when the Ru(Cp*) fragment is coordinated to the bidithiolate ligand, suggesting an alternative strategy for the modification of excited-state properties.

2.4. References

- ¹ (a) V. W. W. Yam and K. M. C. Wong, *Chem. Commun.* 2011, **47**, 11579-11592; (b) V. Balzani; N. Sabbatini and F. Scandola, *Chem. Rev.* 1986, **86**, 319-337; (c) T. J. Meyer and J. V. Caspar, *Chem. Rev.* 1985, **85**, 187-218; (d) G. A. Crosby, *Acc. Chem. Res.* 1975, **8**, 231-238; (e) R. J. Watts, *J. Chem. Educ.* 1983, **60**, 834-842; (f) J. F. Endicott, *Acc. Chem. Res.* 1988, **21**, 59-66; (g) F. Scandola; M. T. Indelli; C. Chiorboli and C. A. Bignozzi, *Top. Curr. Chem.* 1990, **158**, 73-149; (h) L. De Cola; P. Belser; A. von Zelewsky and F. Vogl, *Inorg. Chim. Acta* 2007, **360**, 775-784; (i) A. Juris; V. Balzani; S. Campagna; P. Belser and A. von Zelewsky, *Coord. Chem. Rev.* 1988, **84**, 85-277; (j) S. Campagna; F. Puntoriero; F. Nastasi; G. Bergamini and B. Balzani, *Top. Curr. Chem.* 2007, **280**, 117-214; (k) J. V. Caspar and T. J. Meyer, *Inorg. Chem.* 1983, **22**, 2444-2453; (l) R. T. F. Jukes; V. Adamo; F. Hartl; P. Belser and L. De Cola, *Coord. Chem. Rev.* 2005, **249**, 1327-1335; (m) S. Welter; N. Salluce; P. Belser; M. Groeneveld and L. De Cola, *Coord. Chem. Rev.* 2005, **249**, 1360-1371; (n) S. Bonnet; J. P. Collin and J. P. Sauvage, *Inorg. Chem.* 2006, **45**, 4024-4034; (o) S. Bonnet, J. P. Collin and J. P. Sauvage, *Inorg. Chem.* 2007, **46**, 10520-10533.
- ² K. Kalyanasundaram; M. Grätzel, *Coord. Chem. Rev.* 1998, **177**, 347-414.
- ³ D. W. Lamson; S. M. Plaza, *Altern. Med. Rev.* 2003, **8**, 303-318.
- ⁴ (a) D. N. Hendrickson and C. G. Pierpont, *Top. Curr. Chem.* 2004, **234**, 63-95; (b) A. B. P. Lever, *Coord. Chem. Rev.* 2010, **254**, 1397-1405; (c) M. D. Ward and J. A. McCleverty, *J. Chem. Soc., Dalton Trans.* 2002, 275-288; (d) W. Kaim and B. Sarkar, *Coord. Chem. Rev.* 2007, **251**, 584-594; (e) J. L. Boyer; J. Rochford; M. K. Tsai; J. T. Muckerman and E. Fujita, *Coord. Chem. Rev.* 2010, **254**, 309-330.
- ⁵ (a) C. G. Pierpont and R. M. Buchanan, *Coord. Chem. Rev.* 1981, **38**, 45-87; (b) C. G. Pierpont and C. W. Lange, *Prog. Inorg. Chem.* 1994, **41**, 331-442.
- ⁶ H. Masui; A. L. Freda; M. C. Zerner and A. B. P. Lever, *Inorg. Chem.* 2000, **39**, 141-152; (c) J. Moussa and H. Amouri, *Angew. Chem. Int. Ed.* 2008, **47**, 1372-1380.
- ⁷ J. Best; I. V. Sazanovich; H. Adams; R. D. Bennett; E. S. Davies; A. J. H. M. Meijer; M. I. Towrie; S. A. Tikhomirov; O. V. Bouganov; M. D. Ward and J. A. Weinstein, *Inorg. Chem.* 2010, **49**, 10041-10056.
- ⁸ R. S. da Silva; S. I. Gorelsky; E. S. Dodsworth; E. Tfouni and A. B. P. Lever, *J. Chem. Soc., Dalton Trans.*, 2000, 4078-4088.
- ⁹ (a) R. Marczak; F. Werner; J. F. Gnichwitz; A. Hirsch; D. M. Guldi; W. J. Peukert, *Phys. Chem. C* 2009, **113**, 4669-4678; (b) J. Garcia-Canadas; A. P. Meacham; L. M. Peter; M. D. Ward, *Electrochem. Commun.* 2003, **5**, 416-420.
- ¹⁰ R. J. Mortimer, *Chem. Soc. Rev.* **1997**, 39, 141-152.
- ¹¹ (a) Y. H. Wang; K. Hang; N. A. Anderson; T. Q. J. Lian, *Phys. Chem. B* 2003, **107**, 9434-9440; (b) C. R. Rice; M. D. Ward; M. K. Nazeeruddin and M. Grätzel, *New. J. Chem.* **2000**, 651-652.
- ¹² (a) A. Damas; B. Ventura; J. Moussa; A. Degli Esposti; L. M. Chamoreau; A. Barbieri and H. Amouri, *Inorg. Chem.* 2012, **51**, 1739-1750; (b) A. Damas; B. Ventura; M. R. Axet; A. Degli Esposti; L. M. Chamoreau; A. Barbieri and H. Amouri, *Inorg. Chem.* 2010, **49**, 10762-10764.

- ¹³ B. Hirani; J. Li; P. I. Djurovich; M. Yousufuddin; J. Oxgaard; P. Persson; S. R. Wilson; R. Bau; W. A. Goddard III and M. E. Thompson, *Inorg. Chem.* **2007**, *46*, 3865-3875.
- ¹⁴ (a) P. Barbaro; C. Bianchini; K. Linn; C. Mealli; A. Meli; F. Vizza, *Inorg. Chim. Acta*, **1992**, *198-200*, 31-56; (b) E. I. Szerb; A. Ionescu; N. Godbert; Y. J. Yadav; A. M. Talarico; M. Ghedini, *Inorg. Chem. Commun.* **2013**, *37*, 80-83.
- ¹⁵ (a) A. Damas; H. Sesolis; M. N. Rager; L. M. Chamoreau; M. P. Gullo; A. Barbieri and H. Amouri, *RSC Adv.* **2014**, *4*, 23740-23748; (b) A. Damas; M. P. Gullo; M. N. Rager; A. Jutand; A. Barbieri and H. Amouri, *Chem. Commun.* **2013**, *49*, 3796-3798.
- ¹⁶ (a) H. Amouri; R. Thouvenot; J. Vaissermann and M. Gruselle, *Organometallics* **2001**, *20*, 1904-1906; (b) H. Amouri; J. Vaissermann; Y. Besace; K. P. C. Vollhardt and G. E. Ball, *Organometallics* **1993**, *12*, 605-609; (c) H. Amouri; R. Thouvenot and M. Gruselle, *C. R. Chimie* **2002**, *5*, 257-262; (d) D. Vichard; M. Gruselle and H. Amouri, *J. Chem. Soc., Chem. Commun.* **1991**, 46-48; (e) D. Vichard; M. Gruselle; H. Amouri and J. Vaissermann, *Organometallics* **1992**, *11*, 976-979; (f) H. Amouri; R. Caspar; M. Gruselle; C. Guyard-Duhayon; K. Boubekur; D. A. Lev; L. S. B. Collins and D. B. Grotjahn, *Organometallics* **2004**, *23*, 4338-4341; (g) J. Le Bras, H. Amouri and J. Vaissermann, *J. Organomet. Chem.* **1998**, *553*, 483-485; (h) J. Le Bras; M. N. Rager; Y. Besace; H. Amouri and J. Vaissermann, *Organometallics* **1997**, *16*, 1765-1771; (i) J. Moussa; C. Guyard-Duhayon; P. Herson; H. Amouri; M. N. Rager and A. Jutand, *Organometallics* **2004**, *23*, 6231-6238; (l) H. Amouri, *Synlett.* **2011**, 1357-1369; (m) H. Amouri; J. Moussa; A. K. Renfrew; P. J. Dyson; M. N. Rager; L. M. Chamoreau, *Angew. Chem., Int. Ed.* **2010**, *49*, 7530-7533; (n) H. Amouri; R. Thouvenot; M. C. R. Gruselle, *Chim.* **2002**, *5*, 257-262; (o) J. Moussa; D. A. Lev; K. Boubekur; M. N. Rager; H. Amouri, *Angew. Chem., Int. Ed.* **2006**, *45*, 3854-3858; (p) J. Moussa; M. N. Rager; K. Boubekur; H. Amouri, *Eur. J. Inorg. Chem.* **2007**, 2648-2653.
- ¹⁷ (a) J. Moussa and H. Amouri, *Angew. Chem., Int. Ed.* **2008**, *47*, 1372-1380; (b) A. Damas; B. Ventura; J. Moussa; A. Degli Esposti; L. M. Chamoreau; A. Barbieri and H. Amouri, *Inorg. Chem.* **2012**, *51*, 1739-1750; (c) J. Moussa; K. M. C. Wong; L. M. Chamoreau; H. Amouri and V. W. W. Yam, *Dalton Trans.* **2007**, 3526-3530; (d) J. Moussa; M. N. Rager; L. M. Chamoreau; L. Ricard; H. Amouri, *Organometallics* **2009**, *28*, 397-404; (e) J. Moussa; K. M. C. Wong; X. F. Le Goff; M. N. Rager; C. K. M. Chan.; V. W. W. Yam; H. Amouri, *Organometallics* **2013**, *32*, 4985-4992; (f) J. Moussa; K. M. C. Wong; L. M. Chamoreau; H. Amouri; V. W. W. Yam, *Dalton Trans.* **2007**, 3526-3530.
- ¹⁸ G. Calogero; G. Giuffrida; S. Serroni; V. Ricevuto and S. Campagna, *Inorg. Chem.*, **1995**, *34*, 541-545.
- ¹⁹ M. Montalti; A. Credi; L. Prodi and M. T. Gandolfi, *Handbook of Photochemistry*, CRC Press, Taylor & Francis, Boca Raton, 3rd edn, 2006.
- ²⁰ M. G. Colombo; T. C. Brunold; T. Riedener; H. U. Gudel; M. Fortsch; H. B. Burgi, *Inorg. Chem.* **1994**, *33*, 545-550.
- ²¹ M. Polson; S. Fracasso; V. Bertolasi; M. Ravaglia and F. Scandola, *Inorg. Chem.* **2004**, *43*, 1950-1956.
- ²² A. Damas; B. Ventura; J. Moussa; A. Degli Esposti; L. M. Chamoreau; A. Barbieri and H. Amouri, *Inorg. Chem.* **2012**, *51*, 1739-1750.
- ²³ (a) L. Flamigni; A. Barbieri; C. Sabatini; B. Ventura and F. Barigelletti, *Top. Curr. Chem.* **2007**, *281*, 143-203; (b) A. Damas; B. Ventura; J. Moussa; A. Degli Esposti; L. M. Chamoreau; A. Barbieri and H. Amouri, *Inorg. Chem.* **2012**, *51*, 1739-1750.
- ²⁴ J. B. Birks, *Rep. Prog. Phys.* **1975**, *38*, 903-974.
- ²⁵ B. D'Andrade; S.R. Forrest, *Chem. Phys.* **2003**, *286*, 321-335.

- ²⁶ S. Campagna; F. Puntoriero; F. Nastasi; G. Bergamini and V. Balzani, in *Photo-chemistry and Photophysics of Coordination Compounds I*, ed. V. Balzani and S. Campagna, 2007, **280**, 117-214.
- ²⁷ (a) M. Haga; E. S. Dodsworth and A. B. P. Lever, *Inorg. Chem.* 1986, **25**, 447-453; (b) M. D. Ward and J. A. McCleverty, *J. Chem. Soc., Dalton Trans.* 2002, 275-288; (c) J. Garcia-Canadas; A. P. Meacham; L. M. Peter and M. D. Ward, *Angew. Chem., Int. Ed.* 2003, **42**, 3008-3011; (d) P. F. H. Schwab; S. Diegoli; M. Biancardo and C. A. Bignozzi, *Inorg. Chem.* 2003, **42**, 6613-6615; (e) T. Gosh; B. G. Maiya; A. Samanta; A. D. Shukla; D. A. Jose; D. K. Kumar and A. Das, *JBIC, J. Biol. Inorg. Chem.* 2005, **10**, 496-508.
- ²⁸ P. C. Alford; M. J. Cook; A. P. Lewis; G. S. G. McAuliffe; V. Skarda; A. J. Thomson; J. L. Gasper and D. J. Robbins, *J. Chem. Soc., Perkin Trans. 2*, 1985, 705-709.
- ²⁹ (a) N. H. Damrauer; T. R. Boussie; M. Devenney and J. K. McCusker, *J. Am. Chem. Soc.* 1997, **119**, 8253-8268; (b) N. H. Damrauer and J. K. McCusker, *J. Phys. Chem. A* 1999, **103**, 8440-8446; (c) T. J. Wadas; S. Chakraborty; R. J. Lachicotte; Q. M. Wang and R. Eisenberg, *Inorg. Chem.* 2005, **44**, 2628-2638.
- ³⁰ (a) J. A. G. Williams, *Top. Curr. Chem.* 2007, **281**, 205-268; (b) J. A. G. Williams; S. Develay; D. L. Rochester; L. Murphy, *Coord. Chem. Rev.* 2008, **252**, 2596-2611; (c) J. A. G. Williams, *Chem. Soc. Rev.* 2009, **38**, 1783-1801; (d) L. Murphy; J. A. G. Williams, *Top. Organomet. Chem.* 2010, **28**, 75-111; (e) K. M. C. Wong; V. W. W. Yam, *Coord. Chem. Rev.* 2007, **251**, 2477-2488; (f) K. M. C. Wong; V. W. W. Yam, *Acc. Chem. Res.* 2011, **44**, 424-434.
- ³¹ Y. Chi; P. Chou, *Chem. Soc. Rev.* 2010, **39**, 638-655.
- ³² (a) S. W. Thomas III; S. Yagi; T. M. Swager, *J. Mater. Chem.* 2005, **15**, 2829-2835; (b) S. W. Thomas III; K. Venkatesan; P. Muller; T.M. Swager, *J. Am. Chem. Soc.* 2006, **128**, 16641-16648.
- ³³ (a) J. C. Chan; W. H. Lam; H. Wong; N. Zhu; W. Wong; V. W. W. Yam, *J. Am. Chem. Soc.* 2011, **133**, 12690-12705; (b) Y. Rao; S. Wang, *Organometallics* 2011, **30**, 4453-4458.
- ³⁴ X. Mou; Y. Wu; S. Liu; M. Shi; X. Liu; C. Wang; S. Sun; Q. Zhao; X. Zhou; W. Huang, *J. Mater. Chem.*, 2011, **21**, 13951-13962.
- ³⁵ (a) W. B. Connick; D. Geiger; R. Eisenberg, *Inorg. Chem.* 1999, **38**, 3264-3265; (b) D. K. C. Tears; D. R. McMillin, *Coord. Chem. Rev.* 2001, **211**, 195-205.
- ³⁶ L. Chassot; A. Von Zelewsky; D. Sandrini; M. Maestri; V. Balzani, *J. Am. Chem. Soc.* 1986, **108**, 6084-6085.
- ³⁷ (a) V. W. W. Yam; R. P. L. Tang; K. M. C. Wong and K. K. Cheung, *Organometallics* 2001, **20**, 4476-4482; (b) K. M. C. Wong; W. S. Tang; X. X. Lu; N. Zhu and V. W. W. Yam, *Inorg. Chem.* 2005, **44**, 1492-1498; (c) W. S. Tang; X. X. Lu; K. M. C. Wong and V. W. W. Yam, *J. Mater. Chem.* 2005, **15**, 2714-2720; (d) H. S. Lo; S. K. Yip; K. M. C. Wong; N. Zhu and V. W. W. Yam, *Organometallics* 2006, **25**, 3537-3540; (e) K. M. C. Wong and V. W. W. Yam, *Coord. Chem. Rev.* 2007, **251**, 2477-2488; (f) K. H. Y. Chan; H. S. Chow; K. M. C. Wong; M. C. L. Yeung and V. W. W. Yam, *Chem. Sci.* 2010, **1**, 477-482.
- ³⁸ (a) G. A. Fox; C. G. Pierpont, *Inorg. Chem.* 1992, **31**, 3718-3723; (b) J. D. Kinder; W. J. Youngs, *Organometallics* 1996, **15**, 460-463; (c) M. J. G. Lesley; W. Clegg; T. B. Marder; N. C. Norman; A. G. Orpen; A. J. Scott; J. Starbuck, *Acta Crystallogr., Sect. C: Cryst. Struct. Commun.* 1999, **55**, 1272-1275; (d) B. Sarkar; R. Hubner; R. Pattacini; I. Hartenbach, *Dalton Trans.* 2009, 4653-4655.
- ³⁹ (a) J. A. Weinstein; M. T. Tierney; E. S. Davies; K. Base; A. A. Robeiro; M. W. Grinstaff, *Inorg. Chem.* 2006, **45**, 4544-4555; (b) J. N. M. Shavaleev; E. S. Davies; H. Adams; J. Best; J. A. Weinstein, *Inorg. Chem.* 2008, **47**, 1532-1547.
- ⁴⁰ F. Julia; P. G. Jones; P. Gonzales-Herrero, *Inorg. Chem.* 2012, **51**, 5037-5049.

-
- ⁴¹ (a) J. Moussa; L. M. Chamoreau; A. Degli Esposti; M. P. Gullo; A. Barbieri, A. and H. Amouri, *Inorg. Chem.* 2014, **53**, 6624-6633; (b) H. Sesolis; J. Moussa; G. Gontard; A. Jutand; M. P. Gullo; A. Barbieri and H. Amouri, *Chem. Commun.* 2015 (submitted).
- ⁴² S. S. Kamath; V. Uma; T. S. Srivastava, *Inorg. Chim. Acta* 1989, **166**, 91-98.
- ⁴³ (a) W. Paw; S. D. Cummings; M. A. Mansour; W. B. Connick; D. K. Geiger; R. Eisenberg, *Coord. Chem. Rev.* 1998, **171**, 125-150; (b) J. A. Zuleta; J. M. Bevilacqua; D. M. Proserpio; P. D. Harvey; R. Eisenberg, *Inorg. Chem.* 1992, **31**, 2396-2404.
- ⁴⁴ (a) A. Damas; B. Ventura; M. R. Axet; A. Degli Esposti; L. M. Chamoreau; A. Barbieri; H. Amouri, *Inorg. Chem.* 2010, **49**, 10762-10764; (b) A. Damas; B. Ventura; J. Moussa; A. Degli Esposti; L. M. Chamoreau; A. Barbieri; H. Amouri, *Inorg. Chem.* 2012, **51**, 1739-1750.
- ⁴⁵ (a) M. P. Gullo; J. B. Seneclauze; B. Ventura; A. Barbieri; R. Ziessel, *Dalton Trans.* 2013, **42**, 16818-16828; (b) B. Ventura; A. Barbieri; F. Barigelletti; J. Batcha Seneclauze; P. Retailleau; R. Ziessel, *Inorg. Chem.* 2008, **47**, 7048-7058; (c) B. Ventura; A. Barbieri; F. Barigelletti; S. Diring; R. Ziessel, *Inorg. Chem.* 2010, **49**, 8333-8346.
- ⁴⁶ F. Julia; P. G. Jones; P. Gonzales-Herrero, *Inorg. Chem.* 2012, **51**, 5037-5049.
- ⁴⁷ S. D. Cummings; R. Eisenberg, *Prog. Inorg. Chem.* 2004, **52**, 315-368.
- ⁴⁸ (a) A. Diez; J. Fournies; A. Garcia; E. Lalinde; M. T. Moreno, *Inorg. Chem.* 2005, **44**, 2443-2453; (b) S. Culham; P. H. Lanoe; V. L. Whittle; M. C. Durant; J. A. G. Williams; V. N. Kozhenikov, *Inorg. Chem.* 2013, **52**, 10992-11003; (c) V. Sicilia; J. Forniés; J. M. Casas; M. Martin; J. A. Lopez; C. Larraz; P. Borja; C. Ovejero; D. Tordera; H. Bolink, *Inorg. Chem.* 2012, **51**, 3427-3435.
- ⁴⁹ (a) L. Chassot; E. Mueller; A. von Zelewsky, *Inorg. Chem.* 1984, **23**, 4249-4253. (b) M. Maestri; D. Sandrini; V. Balzani; L. Chassot; P. Jolliet; A. von Zelewsky, *Chem. Phys. Lett.* 1985, **122**, 375-379; (c) L. Chassot; A. von Zelewsky; D. Sandrini; M. Maestri; V. Balzani, *J. Am. Chem. Soc.* 1986, **108**, 6084-6085; (d) L. Chassot; A. von Zelewsky, *Inorg. Chem.* 1987, **26**, 2814-2818; (e) J. Kalinowski; V. Fattori; M. Cocchi; J. A. G. Williams, *Coord. Chem. Rev.* 2011, **255**, 2401-2425.

Chapter 3

3. Photophysical investigation of multichromophoric arrays arranged around different types of rigid organic scaffolds

The wide and promising photophysical and electrochemical properties of polypyridyl metal complexes have prompted the investigation of these compounds during the last decades, for their potential applications in several fields. In fact, such transition metal complexes have been widely used as photosensitizers in energy conversion¹ and in chemi / electroluminescent systems², as probes³ and to build macromolecular structure⁴. The most studied family of transition metal complexes is the one of $[\text{Ru}(\text{II})\text{L}_3]^{2+}$ type, with $\text{L} = \alpha$ -diimine, thanks to the strong visible absorption, stability, efficient emission and the long-lived excited state exhibited.⁵ In addition to the most popular Ru(II) complexes, Pt(II), Os(II), and Ir(III) complexes have been also studied with increasing interest during the time.⁶

Luminescence and redox properties of such compounds are sensitive to the nature of metallic unit, coordinating ligands and local environment, all elements that are able to influence the variety of energetically accessible charge transfer, ligand field and intraligand excited states, resulting in the energetic profile of transition metal complexes.⁷

Thus, understanding the effects of all these factors on the lower lying excited states responsible for the most of photophysical and photochemical properties, it is possible to achieve the rational designing of new and more useful sensitizers and probes.

In the present chapter, Pt(II), Ru(II), Os(II), Ir(III) metal complexes have been discussed. The series under investigation have been divided in two different sections, based on distinct properties that make them interesting for distinct fields of application. In particular, the first part is devoted to the presentation of two series of multimetallic compounds, displaying good properties as antenna systems for solar energy conversion,^{8,9} while the second part is about systems exhibiting intriguing luminescence properties, useful for their possible application in practical devices, for lighting purposes.¹⁰

The works discussed below demonstrate that the smart planning of frameworks embedding metal units allows a fine control of the properties of the resulting transition metal-based architectures, enabling their application in many desired fields.

3.1. Introduction

3.1.1. Antenna systems

Polypyridine transition metal complexes have been largely employed as chromophoric units in supramolecular systems, for both fundamental studies and applicative reasons. Thanks to their rich photophysics and long-lived triplet excited states, they can be used

as electron donors/acceptors or light harvesters in properly designed artificial devices for solar energy conversion applications.

Good supramolecular architectures suitable for such purposes should contain luminophores with large cross-section, embedded into pre-organized structures, in which the control of rate and direction of the excitation energy flow among the components can be efficiently performed and controlled. The first key point in the construction of energy conveyer systems is indeed the proper energetic displacements of the excited states participating to the energy cascade. Second key point is the choice of the bridge between the different chromophores, important component not only for its structural role, resumable in the control of spatial orientation and distances of the single photoactive components, but also for the electronic communication that it has to ensure among them, not isolating completely one from the other. In arrays with photoactive units linked just by simple saturated chains, for instance, the bridge has a mere structural function and, providing only weak electronic coupling, makes energy transfer processes limited in space by the closeness of the units. Instead, when aromatic spacers are employed, a better electronic communication between the chromophores is achieved and energy-transfer can occur by super-exchange mechanism, thanks to the mediator effect of the bridge.¹¹

Moreover, using a large aromatic scaffold able itself to act as photoactive partner, it is possible to further improve the overall performances, taking advantages of a wider photon absorption ability, and to perform a better control on the energy transfer flow, conveying absorbed energy over long distances and in well defined directions, by modulating the aromatic structure.

Such strategy has been recently under exploration and has produced many reported and satisfying examples, such as star-shaped multichromophoric systems based on a truxene core with fully organic or inorganic terminal units.¹²

The current discussion, instead, is focused on the introduction of triptycene and spiro-bifluorene organic bridging scaffolds into pre-organized assemblies. Both these structures have been chosen for the good properties that they exhibit in terms of structural and photophysical suitability.

3.1.1.1. Triptycene

Triptycene belongs to the iptycene family and represents its simplest member. It is composed of three arene units, linked together by a [2.2.2] bicyclic ring system and displaced in three different planes in particular paddlewheel tridimensional structure.¹³ Such peculiar shape makes it particularly interesting for the construction of supramolecular architectures to be used in a plenty of fields. It has been employed as rotor¹⁴ or stator¹⁵ in nanodevices, for the construction of host-guest complexes,¹⁶ as molecular cage¹⁷ and chelating ligand in coordination chemistry, as a structure able to stabilize sterically bended complexes¹⁸ and highly reactive intermediates in catalytic processes,¹⁹ and in electro-phosphorescence.²⁰

Electron and energy transfer in rigid triptycene-bipyridine metal complexes²¹ and in porphyrin-based dyads and triads for charge separation²² has also been investigated.

Due to its properties already reported and to the easy functionalization of its three rings and fixed displacement in space, 2,6,14-trisubstituted triptycene has been used as

suitable building block for construction of antenna systems, linking different metallic units in a well pre-organized structure, able to promote efficient energy transfer events into the supramolecular architecture.

3.1.1.2. Spiro-bifluorene

Spiro-bifluorene is a chiral scaffold composed of two connected biphenyl units, kept in perpendicular planes by a central carbon atom of tetrahedral geometry. Due to such arrangement, the molecule displays a significant electron delocalization over the carbon atoms adjacent to the central one, giving rise to the phenomenon of the so-called “spiro-conjugation”.²³

Thanks to its structural and stereochemical properties, when the spiro-bifluorene core is functionalized in 2,2' position, it participates to the formation of particular architecture, with favourable linear and nonlinear optical properties, thanks to orthogonally arranged chromophores appended.²⁴

Furthermore, spiro-bifluorene can act itself as photoactive module, similarly to triptycene, thanks to good absorption ability and efficient emission in the blue region. Thus, it can be widely used for the construction of light-emitting devices or for optoelectronic materials.²⁵ Recently it has been applied in DSSCs, because thanks to the rigidity that it confers to spiro-based organic dyes, it is able to act against aggregation and consequent self-quenching phenomena,²⁶ besides the fact that higher rigidity for a dye has good effect on emission properties, increasing photoluminescence quantum yield (PLQY) and enlarging the range of applicability.²⁷

All these aspects make spiro-bifluorene interesting and suitable for the design of mixed-metal complexes, in which photoinduced intramolecular energy transfer events take place between the main components, in agreement to the expectations of the programmed strategy.²⁸

3.1.2. Systems for lighting

In the last century, big progress on the efficiency of lighting devices has been achieved but due to the enormously increased consumption of electricity the need for further improvements in terms of widespread availability and sustainability required the introduction of new lighting approaches. In the last two decades, a new technology has been developed, based on solid-state lighting,²⁹ able to produce visible light with reduced heat production, less waste of energy and higher resistance and durability.

The two main types of device belonging to such family are denoted as light-emitting diodes (LEDs)³⁰ and organic light-emitting diodes (OLEDs).³¹ Alternative technologies have also been proposed, such as light-emitting electrochemical cells (LECs).³² The research of phosphorescent materials to be used as dopants in such devices has attracted great attention toward transition-metal complexes as suitable emitters, prompting extensive investigation in this field since 1996.^{32b,33}

Transition-metal complexes with Ru(II), Os(II), Pt(II) or Ir(III) metal units are particularly interesting for this purpose thanks to their strong metal-ligand interaction and high luminescence efficiencies.³⁴ Such systems in combination with ancillary

(N[^]N) and/or cyclometallated (C[^]N) ligands have become good candidates not only for lighting applications but also for metal-ion sensing³⁵ and oxygen detection³⁶.

As an example, Ir(III) complexes, such as 2-phenylpyridine Iridium [Ir(ppy)₃], have found wide application in OLEDs, giving high performances and ensuring good stability.³⁷ They resulted highly suitable thanks to the several favourable properties exhibited, such as the simple tunability of emission energy and the high phosphorescent quantum efficiency at room temperature. The main limits of such systems are related to the low power efficiency and to their luminescence quenching upon increase of employed concentration.³⁸ Thus, in the attempt to further improve their overall performances, many strategies have been adopted, based on the modification of already known and employed ligands, through their proper functionalization with new electron donating or withdrawing groups or using completely original frameworks, able to enlarge the emission properties.

3.1.2.1. White emission and Julolidine

White-light-emitting materials have attracted increasing attention in recent years because the realization of highly efficient white organic light-emitting devices (OLEDs) is important to achieve energy saving of solid-state lighting, eco-friendly flat-display panels³⁹ and new designs in lighting technology.

The most simple and used approach employed till now to obtain white emission is based on the combinations of different emitters, properly chosen in order to cover the whole visible range from 400 nm to 700 nm. Unfortunately, the use of different emitting species introduces many problems because different compounds have different colour aging, thus during the time the images quality dramatically decreases, and moreover the presence of more compounds makes more difficult the device fabrication.

For such reasons, the search for single emitters able to give by themselves a panchromatic emission has been carried out and several strategies have been adopted. For instance, multichromophoric systems⁴⁰ or dyes exhibiting excited state intramolecular proton transfer (ESIPT)^{41,42} have been employed. The first approach takes advantage of arrays comprising donor and acceptor moieties in their own structure, among which only partial or frustrated energy transfer process occur, allowing the emissions from two or many units and thus at many wavelengths.⁴⁰ The second approach is based on the use of particular dyes exhibiting excited state intramolecular proton transfer (ESIPT) and thus able to give double emission from their two tautomeric forms.^{41,42}

Alternative approaches reported up to now were based on the use of panchromatic luminescent systems with mixed excited states (*e.g.* Ir(III) complex⁴³) and of species existing simultaneously in monomeric and excimeric form, with blue and red luminescence, respectively.⁴⁴ In the latter case, it is possible to achieve an efficient tuning of the colour by modifying the ratio between monomer and excimer towards the desired direction, by simply acting on the concentration.

In this chapter, a surprising series of julolidine-based white emitting compounds is reported. Organic julolidine derivatives, pre-programmed to carry out ESIPT process, and a supramolecular architecture, in which the julolidine works as bridge between two metallic chromophoric units, Ir(III) and Pt(II) based, have been investigated. The

julolidine has been selected for its ability to give N⁺O chelation on centres like boron(III) or metal, as effect of its strong electron-donating action.⁴⁵ Its basic structure has been modified through the addition to its central framework of four methyl groups that, apart from increasing its solubility, avoid the quenching caused by high concentration, in the solid state or in solutions. Julolidine based materials have already found application as red emitters in OLED technology⁴⁶ and in push-pull systems for exciplex emission at low energy,⁴⁷ while their application as white emitters, both as simple organic compounds and embedded in supramolecular architectures has not been reported till now.

3.1.2.2. Iridium(III) complexes

Cyclometallated Ir(III) complexes are considered promising candidate materials for lighting applications. They exhibited bright phosphorescence and emission lifetimes in the microsecond range, all features that make them suitable for OLED applications.

For this purpose, there have been continuous efforts to develop phenylpyridine-based cyclometallated Ir(III) complexes with finely tuned phosphorescent emissions. To better understand the studies conducted till now it is necessary to know that in general, the triplet emission of the most common phenylpyridine and derivatives Ir(III) complexes generates from metal-to-cyclometallating ligand charge-transfer (MLCT) transition state or from cyclometallating ligand-centred (LC) transition state. Moreover, for both transitions, the lowest unoccupied molecular orbital (LUMO) is usually centred on the cyclometallating ligand. For such reason, in the attempt to achieve the phosphorescence color tuning, few investigations have been conducted about ancillary ligands (LX) modification, preferring instead to act particularly on the electronic structures of the phenylpyridine-based cyclometallating ligand.

However, this strategy has been frequently limited by unfavorable side reactions and steric crowding around the Ir(III) centre, and moreover it resulted rather inefficient for the color tuning because it allows to obtain only singly emissive Ir(III) complexes.

In addition, the preparation of homoleptic tris-cyclometallated Ir(III) complexes requires hard reaction conditions and long purification procedures due to the presence of geometric facial and meridional isomers.⁴⁸ For all these reasons, new approaches have been experimented, as the use of new chromophoric ancillary ligands.⁴⁹

3.2. Results and Discussion

3.2.1. Antenna systems

3.2.1.1. Triptycene series

The family of compounds herein reported is composed of triptycene-based ligands and metal complexes and their schematic structures are illustrated in **Chart 3.1**. **1** and **2** are two types of triptycene ligands, with one and two appended bpy groups, respectively; **3**, **4** and **5** are two cyclometallated Ir(III) [C⁺N = dibenzo[*a,c*]-phenazine (dbpz) in **3** and difluoro-phenylpyridine (dfppy) in **4**] and one bipyridyl Os(II) monometallic complexes; **6**, **7** and **8** are defined dyads, because contain two photoactive subunits, that

are one metal complex [Ir(III) for **6** and **7**, Os(II) for **8**] and one triptycene ligand, linked together through acetylide bridges; **9** is a triad, with two metal complexes, Ir(III) and Os(II) based, and the ligand; and **10** is a tetrad, built with three metal complexes, two Ir(III) and one Os(II) systems, and a ligand unit. Such tetrad and triad are the supramolecular architectures of interest for the first part of this chapter, acting as good model for antenna systems. The complete understanding of their photophysical properties has been achieved by studying in details their distinct components, by means of the analysis of the other compounds properly used as models.

Model compounds have been divided in two groups to simplify the discussion below. The first group consists of **1** and **2** ligands and **3**, **4** and **5** metal complexes while the second group is composed of the three dyads, **6**, **7** and **8**.

Details about the synthesis are reported in reference.⁸

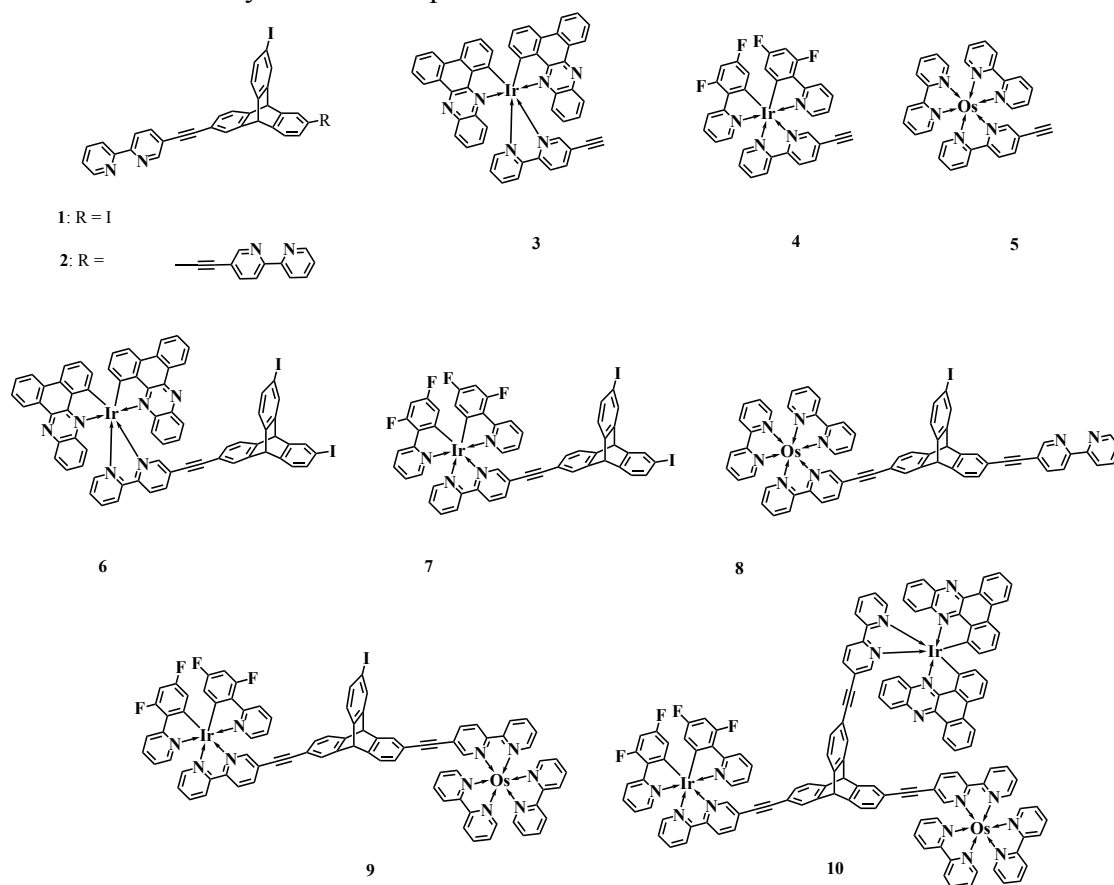


Chart 3.1. Schematic representation of the cyclometallated Ir(III) (**3** and **4**) and bipyridyl Os(II) (**5**) complexes, of the triptycene-based ligands (**1** and **2**) and of the mono- (**6**, **7**, and **8**), di- (**9**) and tri- (**10**) nuclear coordination assemblies.

Absorption. Absorption spectra of all models compounds are displayed in **Fig. 3.1** while triad and tetrad profiles are depicted in **Fig. 3.2**, recorded in any case in dilute solutions ($c = 2 \times 10^{-5}$ M) at room temperature (rt); relevant data are collected in **Table 3.1** for all systems.

Spectral profiles of the ligands, recorded in CH_2Cl_2 solutions, show a specific absorption band in near-UV region ($\lambda_{\text{max}} = 346$ nm, $\epsilon_{\text{max}} = 27400$ $\text{M}^{-1} \text{cm}^{-1}$ and 327 nm, $\epsilon_{\text{max}} = 72300$ $\text{M}^{-1} \text{cm}^{-1}$ for **1** and **2**, respectively), originating from $^1\pi\text{-}\pi^*$ triptycene core transitions, more intense in **2** than in **1** for its larger conjugated framework.

Absorption spectra of CH₃CN solutions of the two Ir(III) complexes, **3** and **4**, display largely different features (**Fig. 3.1**, **Table 3.1**). At higher energy, in the range between 240 and 300 nm, the envelop of bands displayed originates from the spin-allowed ¹π-π* py-centred transition (¹LC) and is more intense for **3** than for **4**, due to the higher degree of conjugation occurring along the 5-ring fused pyrazinic system (dbpz) than that of phenylpyridine (ppy) ($\lambda_{\text{max}} = 251$ nm and $\epsilon_{\text{max}} = 106400$ M⁻¹cm⁻¹ for **3**, $\lambda_{\text{max}} = 247$ nm, $\epsilon_{\text{max}} = 41600$ M⁻¹cm⁻¹ for **4**). In details, in this range, the shorter wavelength region is related to the absorption of the ppy ligands (ppy = 2-phenylpyridine) while the longer wavelength region, to the bpy ligand (bpy = 2,2'-bipyridine).⁵⁰

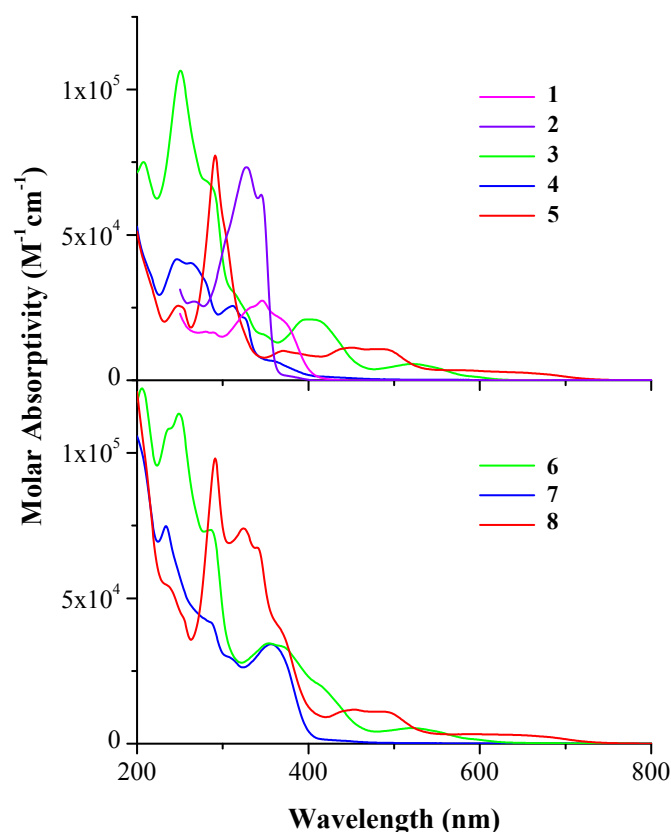


Figure 3.1. Absorption spectra of the triptycene ligands **1** and **2** in CH₂Cl₂ and of the metal complexes **3**, **4** and **5** (top), and the dyads **6**, **7** and **8** (bottom), in CH₃CN solution at rt.

In the spectral range between 350 nm and 550 nm weaker bands arise from spin-allowed transitions of mixed metal-to-ligand (¹MLCT) and ligand-to-ligand (¹LLCT) charge transfer character.⁵⁰ The low intensity tail appearing in the absorption profiles of both complexes at $\lambda > 400$ and 580 nm for **4** and **3**, respectively, can be ascribed to spin-forbidden ³MLCT transitions. The presence of the heavy atom results in a strong spin-orbit coupling ($\zeta_{\text{Ir}} = 3\,909$ cm⁻¹),⁵¹ rendering partially allowed the direct absorption from the singlet ground state to the triplet excited state.⁵²

In the absorption profile of the Os(II) complex **5**, it is possible to recognize (i) at 291 nm the typical intense ($\epsilon_{\text{max}} = 77200$ M⁻¹cm⁻¹) and narrow band of the ¹π-π* bpy-centred transition and (ii) at lower energy, the d_{Os}→π_{bpy} CT transition band, extended from 400 to 550 nm ($\epsilon_{\text{max}} \approx 11000$ M⁻¹cm⁻¹).⁵³ The weak and broad band for **5**,

appearing just like a tail in the range between 600 and 700 nm (**Figure 3.1**, top; **Table 3.1**), is associated with a formally spin-forbidden $^3\text{MLCT}$ set of transitions, also in this case, induced by the large spin-orbit coupling constant of the osmium metal ($\zeta_{\text{Os}} = 3381 \text{ cm}^{-1}$).⁵¹

The absorption spectra of the second group of models, the dyads **6**, **7**, and **8** (**Figure 3.1**, bottom; **Table 3.1**), can be interpreted on the basis of the features displayed by the units from which they originate (*i.e.*, **3**, **4**, **5**, **1**, and **2**). In fact, their profiles match reasonably well the superposition of the spectra of their single components (**Figure 3.2**).

The principle distortion with respect to the spectral sum of the components is in the region between 300 and 400 nm, where a new band ascribed to a ^1LC triptycene absorption transition appears. Such band, already reported in literature for a spiro-bifluorene-based system,⁵⁴ is attributable to the coordination by the metal centre of the ethynylene-linked bpy site, unoccupied in the free ligands **1** and **2**, arising from new bpy-metal interactions.

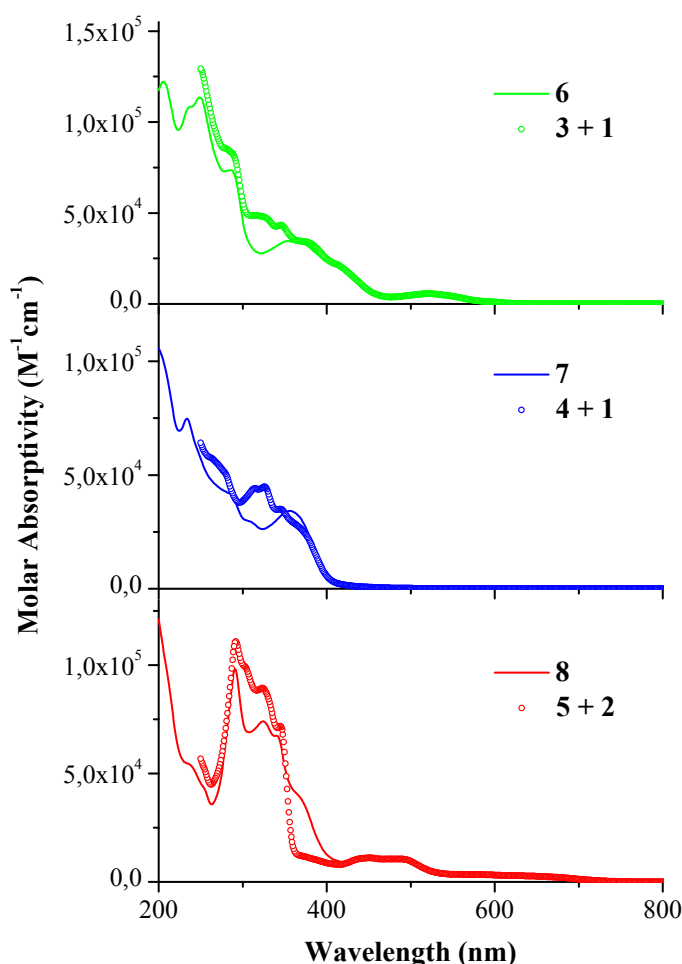


Figure 3.2. Comparison between the absorption spectra of dyads **6**, **7** and **8** (full lines) and the spectral sum of their components (dots).

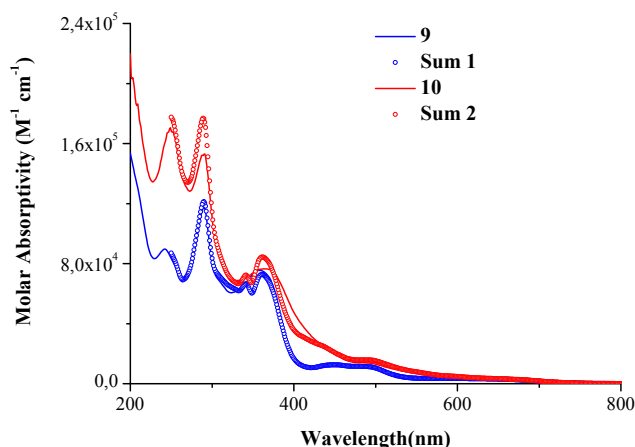


Figure 3.3. Absorption spectra of the triad **9** (blue line) and of the tetrad **10** (red line) in CH_3CN . The dots, **Sum 1** and **Sum 2**, represent the spectral addition of the model components **6**, **7** and **8** absorption corrected by the subtraction of the **1** and **2** triptycene ligands contribution, for **9** and **10**, respectively.

The absorption profiles of the multichromophoric triad and tetrad **9** and **10** show bands quite well corresponding to the absorption of the single components (see **Figure 3.3**), as revealed by the comparison with the curves obtained from the sum of models absorption profiles. In particular, to build these curves, the second group of complexes (**7**, **6**, and **8**) and the relevant bridging ligands (**1** and **2**) have been used as model compounds. In both cases, the contributions of the ligands **1** and **2** are subtracted from the sum of the dyads profiles, resulting in a good superimposition with the original spectra in both architectures, that accounts for a weak ground-state electronic interaction between the satellite metal chromophores and the triptycene scaffold.

For both systems, moving from higher to lower energy, it is possible to observe (i) the band related to the $^1\pi\text{-}\pi^*$ py-centred transition of **4** and **3** subunits ($\lambda_{\text{max}} \approx 250$ nm), (ii) the intense band typical of the $^1\pi\text{-}\pi^*$ bpy-centred transition ($\lambda_{\text{max}} \approx 300$ nm), (iii) another band originating from the ^1LC triptycene absorption transition ($\lambda_{\text{max}} \approx 360$ nm), (iv) a ^1CT transition band of lower intensity, extended from 400 to 550 nm, and (v) the tail for the $^3\text{M}_{\text{O}_2}\text{LCT}$ transition, at $\lambda > 600$ nm.

The highest energy band ($\lambda_{\text{max}} \approx 250$ nm) is more intense for trinuclear **10** than for dinuclear **9** system because of the presence of the more largely conjugated 5-fused ring moiety of the **3** subunit in the former; the same behaviour is noticed for the second peak ($\lambda_{\text{max}} \approx 300$ nm) that, obviously, appears higher in the trinuclear complex than in the dinuclear, because of the major amount of bpy groups.

Emission. Emission spectra of complexes and ligands were recorded at room temperature in air-equilibrated and de-aerated solutions (CH_2Cl_2 for ligands and CH_3CN for complexes) (see **Figure 3.4** for luminescence profiles, rescaled according to the corresponding photoluminescence quantum yields) and at low temperature in $\text{CH}_2\text{Cl}_2\text{:CH}_3\text{OH}$ (1:1) frozen mixtures (**Figure 3.5**). Relevant data are summarized in **Table 3.2**.

As it can be inferred from **Figure 3.4** and **Table 3.2**, both ligands **1** and **2** are highly fluorescent in solution in the near-UV region with short lifetimes in the nanoseconds

range ($\lambda_{\max} \approx 380$ nm and $\phi = 0.37$ and 0.56 and $\tau = 1.9$ and 0.8 ns, respectively). They display, as expected, only a slight blue shift on going from room temperature to 77 K ($\lambda_{\max} = 360$ and 380 nm, respectively). Moreover, in glassy matrixes both ligands show a well-structured and long-lived phosphorescence emission ($\tau = 145$ ms for **1** and $\tau = 166$ ms for **2**) that allows the evaluation of the energy of the lowest triplet excited state for both ligands (≈ 2.43 eV, as calculated from the highest energy phosphorescence peak).

The emission of the Ir(III) complex **4** with difluoro-ppy as cyclometallating ligand is largely blue-shifted with respect to that of the dbpz derivative **3**, both at room and low temperature, and moreover of comparable quantum yield but shorter lifetime (**Table 3.2**). **3** is particularly interesting because it displays good ability as red emitter at room temperature ($\lambda_{\max} = 660$ nm and $\phi = 0.23$, **Table 3.2**).

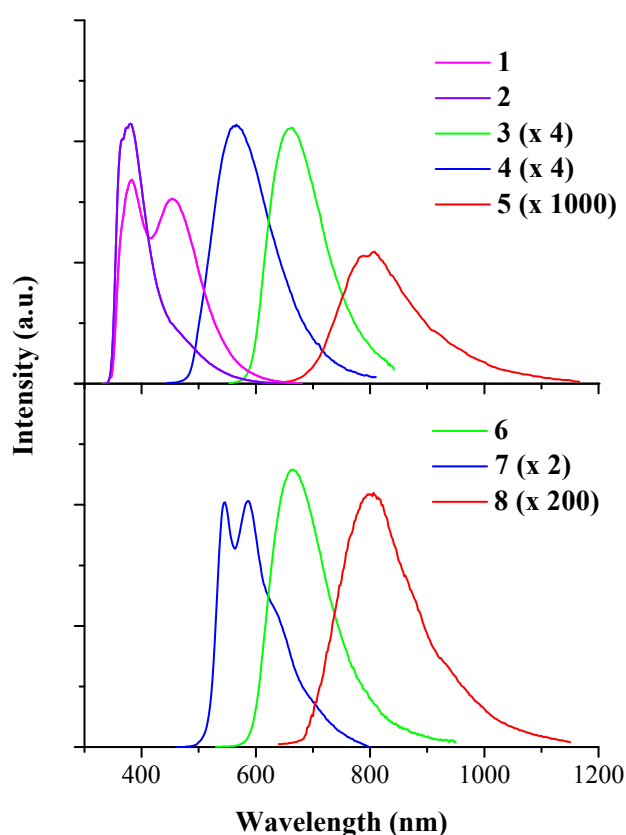


Figure 3.3. Room temperature corrected emission spectra in de-aerated CH_3CN solutions of the model metal complexes, **3**, **4** and **5** (top), and dyads **6**, **7** and **8** (bottom). Spectral areas are scaled proportional to the quantum yields.

For both **3** and **4**, the values of luminescence quantum yield in de-aerated solution are remarkably higher than those in air-equilibrated condition and the emission band moves to higher energies going from room to low temperature.

The overall photophysical behaviour is ascribable to transitions of ^3CT nature, as further confirmed by the calculated values of the radiative constants, displaying the same order of magnitude with respect to similar Ir(III) complexes, $k_r = 1.8 \times 10^5$ and $2.9 \times 10^5 \text{ s}^{-1}$ ($k_r = \phi/\tau$) for **3** and **4**, respectively.⁵⁰ In particular, for both complexes, the observed emission band can be assigned to the $d_{\text{Ir}} \rightarrow \pi_{\text{ppy}}$ transition, originating from the orbitals

mainly centred on metal and cyclometallating ligand and ending on bpy-centred orbitals ($ML_{bpy}CT$).⁵⁵

For **5**, the registered luminescence can be safely ascribed to transition of 3MLCT nature as confirmed by its blue shift moving from solution to glassy matrix (as already discussed in Chapter 2) and by the similar behaviour already reported for the parent compound $[Os(bpy)_3]^{2+}$.⁵⁶ The difference exhibited in the emission peak of **5** moved in energy of $\approx 930\text{ cm}^{-1}$ towards the red region with respect to the latter can be explained by the lower quantum yield and shorter lifetime observed for **5** ($\phi = 1 \times 10^{-3}$ and $\tau = 16.0\text{ ns}$, **Table 3.2**), possibly based on energy gap law effects.⁵⁷

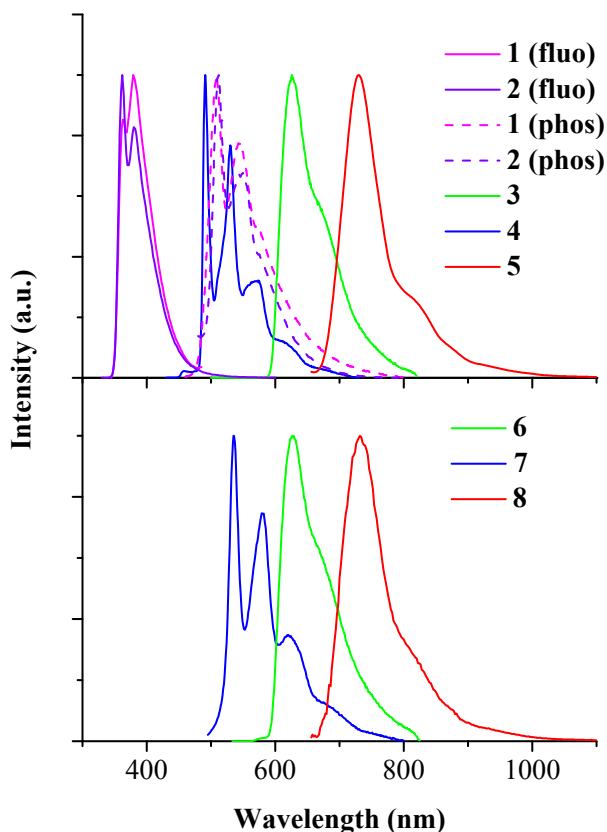


Figure 3.4. Normalized corrected emission spectra at 77 K in $CH_3OH: CH_2Cl_2$ (1:1 v/v) glassy solutions of the triptycene ligands **1** and **2** (fluorescence, full line, and phosphorescence, dotted line) and of the model complexes **3**, **4**, **5**, (top), and dyads **6**, **7**, **8** (bottom).

The introduction of the triptycene unit attached to the bpy ligand in the dyads **7**, **6**, and **8** induces some modifications on the photophysical behaviour of the complexes, with major extent for **7**. Complexes **6** and **8** maintain an emission behaviour similar to that of the parent compounds **3** and **5**. **6** displays an emission centred at 664 nm with an almost identical quantum yield and lifetime with respect to **3** (**Table 3.2**), accounting for 3CT state responsible for the emission, centred on the Ir unit. **8** shows the typical features of a 3MLCT phosphorescence with slightly higher quantum yield and longer lifetime with respect to its parent **5** (**Table 3.2**).

The case of **7** is very different and its photoluminescence quantum yield in solution is enormously decreased with respect to the parent compound **4** ($\phi = 0.073$ and 0.25 for **7** and **4**, respectively), unlike the lifetime is higher for the dyad ($\tau = 4.35$ and $0.86\ \mu s$ for **7** and **4**, respectively). Then, the emission shape appears structured at room temperature

(**Figure 3.4**, bottom) and its maximum blue-shifted by only 410 cm^{-1} on going from fluid to rigid solution. All these features account for a more pronounced ^3LC character for its emission, also confirmed by the low value of the radiative constant, $k_r = 1.7 \times 10^4\text{ s}^{-1}$.⁵⁰ The longer lifetime observed for **7** with respect to **4** can be explained taking into account the contribution to the transition of the triplet levels centred on the triptycene ligand. Such evaluation is confirmed by the comparison between the triplet energy level calculated from the emission maximum at 77 K for **7** ($E_T = 2.32\text{ eV}$) and that of the triptycene triplet, discussed above ($E_T = 2.43\text{ eV}$), both resulting at very close values of energy.

Transient Absorption. Given the differences in emission behaviour between the two Ir-containing dyads **6** and **7**, further investigation has been conducted to deeply ascertain the nature of the excited states responsible for the emission. Laser flash photolysis experiments have been performed to this aim for Ir-dyads and respective models **3**, **4**, and **1** (see **Figure 3.6**).

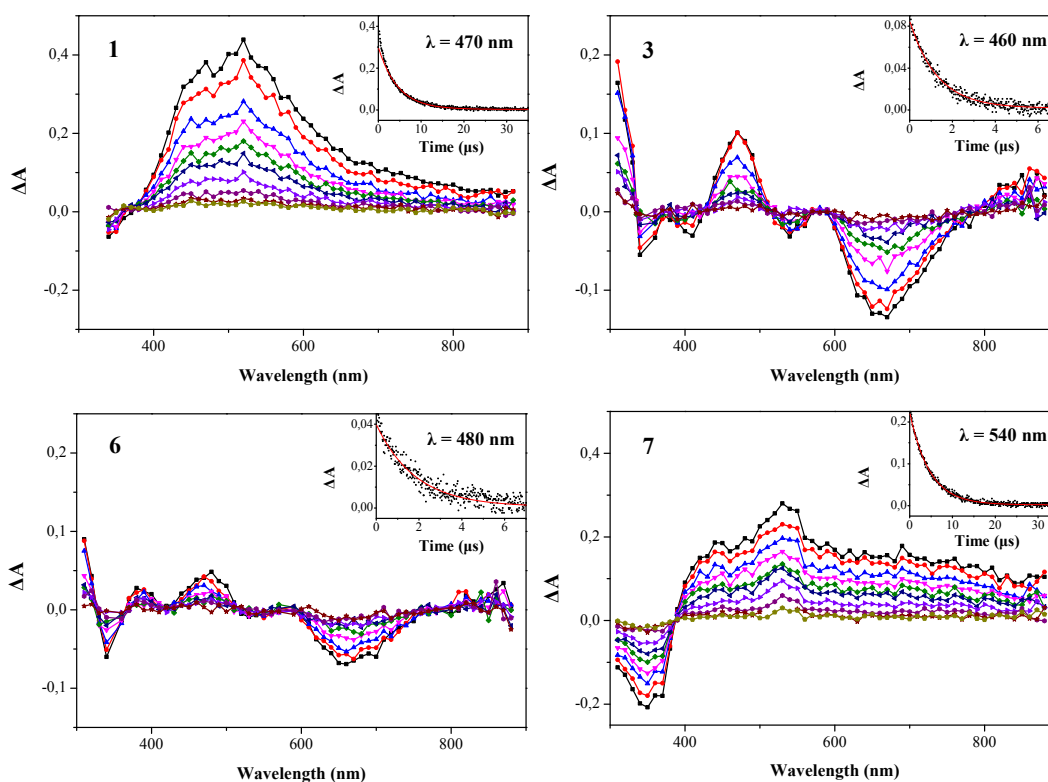


Figure 3.5. Transient absorption spectra of **1** in de-aerated CH_2Cl_2 and of **3**, **7**, and **6** in de-aerated CH_3CN solutions at incremental delay times (0-15.0 μs for **1** and **7**, 0-3.5 μs for **3** and **6**). $\lambda_{\text{exc}} = 355\text{ nm}$, $A_{355} = 0.52$, 3.1 mJ/pulse. Time evolutions at selected wavelengths and mono-exponential fitting of the decays are shown in the insets.

Ligand **2** has also been investigated for comparison purposes with respect to **1** (**Figure 3.7**). **Figure 3.6** reports transient absorption spectra of ligand **1** in de-aerated CH_2Cl_2 and complexes **3**, **7**, and **6** in de-aerated CH_3CN solutions, recorded upon excitation at 355 nm.

The different absorption spectrum for ligand **1** is composed of a broad and intense band, peaking at 470 and 520 nm (**Figure 3.6**); bleaching features due to the ground-state

absorption appear below 370 nm. Single-exponential decays are registered at any wavelength with a measured lifetime of 4.6 μs in de-aerated solvent. Ligand **2** shows very similar absorption profile and longer lifetime of 7.4 μs (**Figure 3.7**). The transitions responsible for the observed spectra involve the lowest-lying $\pi\text{-}\pi^*$ triplet state of the triptycene ligands. Transient absorption spectra of iridium complexes **3** and **6** are characterized by ground-state bleaching features in the range between 350 and 500 nm, present together with the absorption bands. In **4** spectra instead, the ground-state absorption appears just below 370 nm as for the ligands, thus it is possible to clearly distinguish the presence of an intense transient absorption band with maxima at 400 nm and a shoulder around 470 nm (**Figure 3.7**). In the region between 500 and 700 nm, absorption profiles of **3**, **4** and **6** display bleaching features ascribed to the corresponding emissions (see **Table 3.2**) while above 750 nm, a weak absorption tail emerges. For **3** and **4** the values of detected lifetimes (1.4 μs and 760 ns, respectively) show good agreement with the luminescence lifetimes (**Table 3.2**) thus observed spectra could be safely ascribed to the $^3\text{MLCT}$ excited state.⁵⁸

The spectrum of the dyad **7** is markedly different from those of its model **4** and of the other dyad **6** (**Figure 3.6**). In fact, while the latter shows the features of a $^3\text{MLCT}$ absorption, the profile recorded for **7** has features evidently comparable to the one observed for ligand **1**, with a broad absorption profile peaking at 440 and 530 nm. All these data validate the attribution of LC character made in emission analysis for the lowest-lying triplet excited state of **7**.

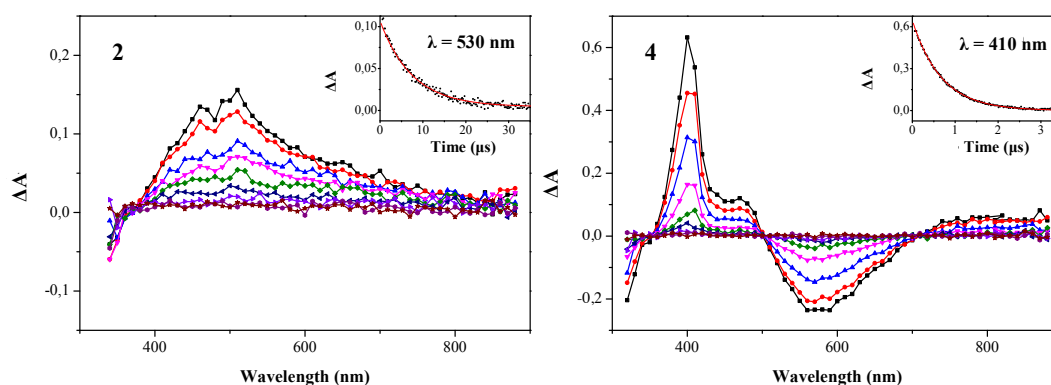
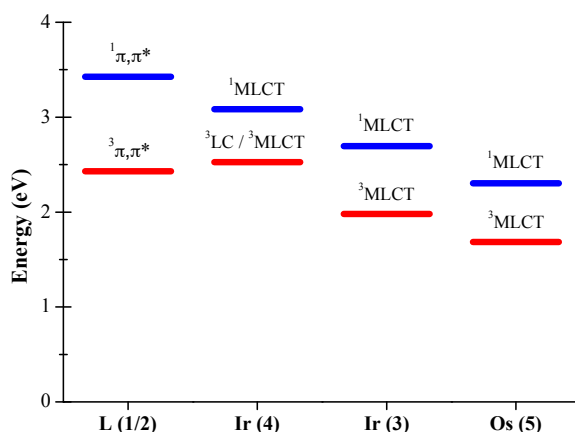


Figure 3.6. Transient absorption spectra of **2** (left) in de-aerated CH_2Cl_2 and of **4** in de-aerated CH_3CN solutions, at various delay times (0-30 μs). $\lambda_{\text{exc}} = 355$ nm, $A_{355} = 0.52$, 3.1 mJ/pulse. Time evolution for **2** at 530 nm and for **4** at 410 nm are shown in the insets.

Energy Transfer. As already discussed in the absorption section above (see **Figure 3.2**), the units that compose the arrays **9** and **10** display weak interactions in such multichromophoric systems. Indeed, the spectral sums of the components profiles and the detected spectra for the arrays are very similar, indicating no remarkable effects coming from the combination of the component units in the supramolecules.

Taking into account such consideration, it is possible to draw the diagram of energy levels for our systems by the estimation of the energies from the emission maxima observed at 77 K for the **1/2** ligands, **4**, **3**, and **5** model complexes (**Scheme 3.1**). In details, the triptycene ligand triplet level has been calculated from the maximum in the phosphorescence spectrum of **1/2**, while the metal-based singlet energy levels have been

obtained from the onset of the lowest energy $^1\text{MLCT}$ absorption band of model compounds **3**, **4**, and **5**. The obtained **Scheme 3.1** explains that, since the singlet low lying excited state for triptycene ligand is the level with the highest energy content (3.42 eV), energy transfer process starts from this state towards the metal-based singlet levels, through exoergonic processes by 0.34, 0.72, and 1.12 eV (from **1/2** to **4**, **3**, and **5**, respectively). As already discussed in emission section above, the $^3\pi\text{-}\pi^*$ and $^3\text{LC}/^3\text{MLCT}$ levels of triptycene and **4** are almost isoenergetic.



Scheme 3.1. Energy level of the excited states with respect to the ground state.

Since the absorption spectra of the single components lay in common regions one to the other, performing selective excitation of one single unit is not possible. The only exception is represented by the Os-based unit that can be selectively excited through irradiation of the $^3\text{MLCT}$ band, at $\lambda > 600$ nm, and it is indeed used as reference.

To have information about the photoinduced energy transfer events occurring in the multichromophoric arrays, multiexcitation emission maps have been registered, by exciting the systems in the region of predominant triptycene absorption, between 240 and 330 nm, and recording the emission from 340 nm to 820 nm, in order to cover the range of emission of all the involved species. The emission maps obtained in de-aerated acetonitrile solutions for the triad and the tetrad are reported in **Figure 3.8** while those of the dyads **6**, **7**, and **8** are reported in **Figure 3.9**.

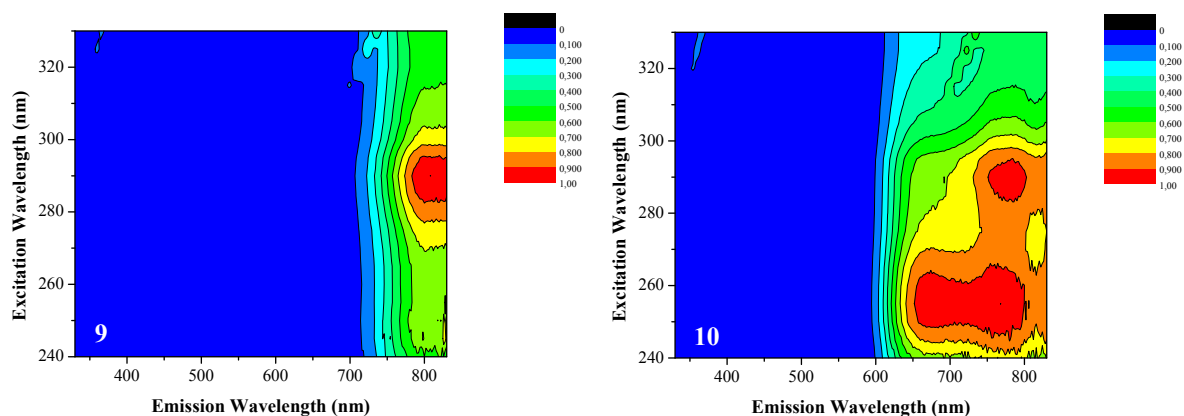


Figure 3.7. Maps of normalized **9** and **10** luminescence in CH₃CN at room temperature.

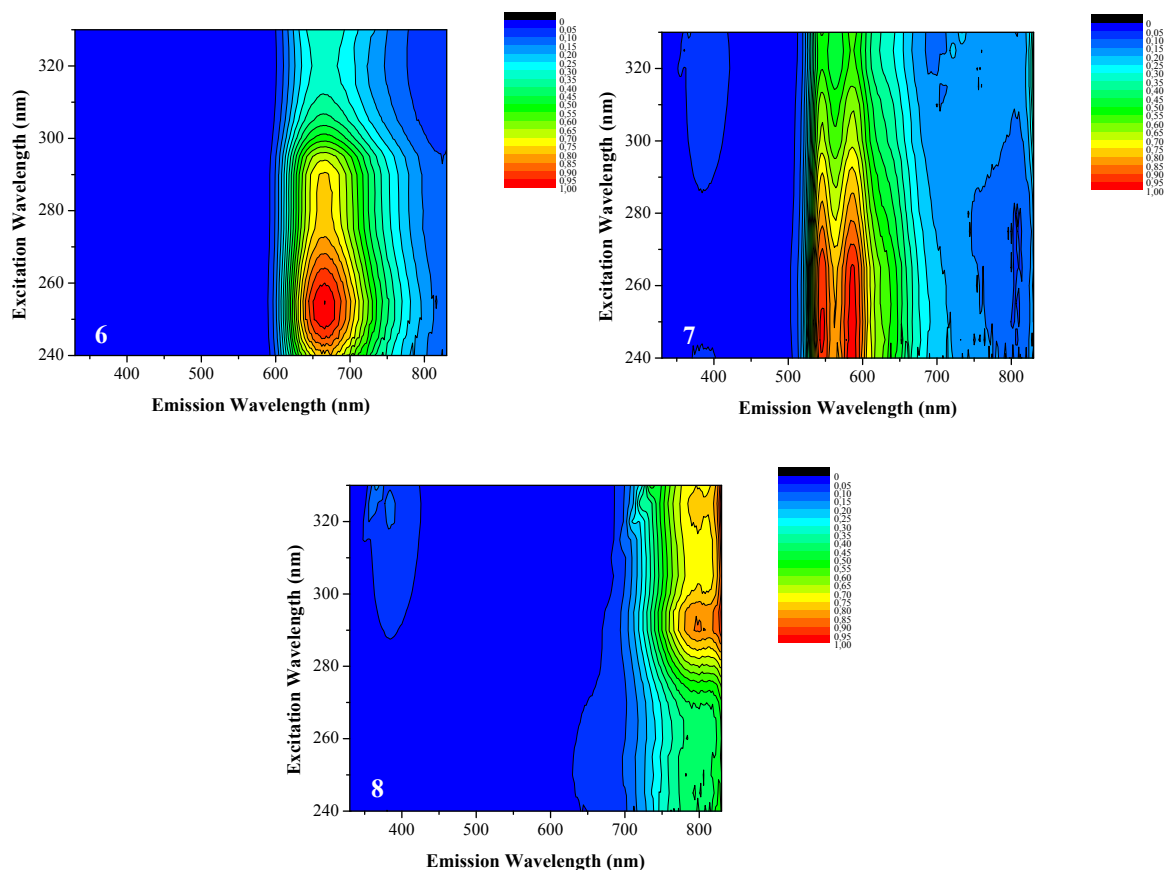


Figure 3.8. Normalized maps of **6**, **7** and **8** luminescence in CH₃CN at room temperature.

In any case no residual emission from the triptycene has been detected and also unit **4** is almost completely quenched in triad and tetrad. The emission of the tetrad, upon excitation between 240 and 270 nm, displays a clear contribution from the unit **3**, just comparable to the signal originating from Os moiety, thus strongly quenched if its high photoluminescence quantum yield in the free form (as mononuclear complex **3**) is considered (higher for **3** than for **5**). In both triad and tetrad, the emission profile is

dominated by the signal above 750 nm, attributable to the Os-based excited state, either directly excited or sensitized by energy transfer from the other units in the array.

Further and more quantitative information about the quenching processes occurring in the arrays, depending on Os unit as unique final collector, has been gained by means of time-resolved luminescence analysis, performed on **9** and **10**.

Lifetime values of 5 and 18 ns for the residual emission of the **4** and **3** units, in **9** and **10** respectively, have been measured, accounting for highly efficient energy transfer processes. The energy transfer rate constants are of $1.9 \times 10^8 \text{ s}^{-1}$ and $5.2 \times 10^7 \text{ s}^{-1}$ ($k_{\text{EnT}} = \tau_{\text{q}}^{-1} - \tau^{-1}$) with efficiencies of 0.97 and 0.93 ($\eta_{\text{EnT}} = 1 - \tau_{\text{q}}/\tau$), for the Ir(**4**)→Os(**5**) and Ir(**3**)→Os(**5**) processes, respectively (**Table 3.3**). The overlap integral J_{F} and the critical radius R_0 have been calculated by means of the available spectroscopic properties through application of the Förster's model, used for a through-space dipole-dipole interaction energy transfer mechanism. The resulting values of $J_{\text{F}} \sim 3.8 \times 10^{-14}$ and $3.2 \times 10^{-14} \text{ cm}^3 \text{ M}^{-1}$ for **9** and **10**, respectively, of $R_0 < 16 \text{ \AA}$ and the energy transfer rate constants lower by ≈ 1 order of magnitude with respect to the experimental values (**Table 3.4**) have been obtained for a separation between donor and acceptor of $d = 19 \text{ \AA}$, estimated from molecular modeling. The results obtained account for photoinduced energy transfer processes mainly based on dipole-dipole interaction mechanism. The calculation of overlap integrals have been conducted according to the bridge-mediated double-electron-exchange model, resulting in $J_{\text{D}} \sim 5 \times 10^{-5}$ and $2.5 \times 10^{-5} \text{ cm}$ for the Ir(**4**)→Os(**5**) and Ir(**3**)→Os(**5**) processes, respectively. In this case, to explain the experimental energy transfer rate constants, a small electronic-coupling term $H \sim 1.8$ and 1.3 cm^{-1} (**Table 3.5**) for **9** and **10**, respectively, is necessary, similarly to what observed in systems connected with aromatic bridges, displaying through-bond interaction.

Since the triplet emission from both iridium donors largely overlaps with the direct $^3\text{MLCT}$ absorption band of the osmium unit, the process can be considered mainly as a triplet-to-triplet energy transfer. In this case, the Dexter-type mechanism is prevailing over the dipole-dipole interaction mechanism on the basis of the selection rules, as also confirmed by the reported calculations.

Table 3.1. Absorption properties of ligands and complexes **1-10**.

	λ_{\max} , nm (ϵ_{\max} , M ⁻¹ cm ⁻¹) ^[a]
1	335 sh (25200), 346 (27400), 370 sh (20700)
2	327 (72300), 345 (63800)
3	251 (106400), 400 (20900), 519 (5600)
4	247 (41600), 312 (25600)
5 ^[b]	291 (77200), 449 (11900), 482 (11000), 580 (3900)
6	249 (113500), 286 sh (73500), 354 (34500), 520 (5400)
7	234 (74800), 287 sh (41500), 355 (34200)
8	291 (98100), 324 (74000), 455 (11700), 635 (3000)
9	242 (89600), 289 (117000), 358 (75500), 452 (12300)
10	249 (170600), 291 (153000), 363 (76500), 491sh (13800)

^a In CH₂Cl₂ for ligands and CH₃CN for complexes, at room temperature. ^b From Ref. 12d.

Table 3.2. Luminescence properties of ligands and complexes **1-10**.

	rt			77K	
	λ_{\max} , nm	ϕ ^[a]	τ , ns ^[b]	λ_{\max} , nm	τ , μ s ^[c]
1	383, 455	0.37	1.9	362, 380 509, 545 ^[d]	145×10 ³
2	380	0.56	0.8	363, 379 512, 550 ^[d]	166×10 ³
3	660	0.23 (0.032)	1300 (254)	626	20.2
4	564	0.25 (0.045)	860 (173)	491, 530, 573	5.2
5 ^[e]	798	0.001	16	736	2.3
6	664	0.177 (0.023)	2020 (258)	627	19.2
7	547	0.073 (0.007)	4350 (373)	535, 580, 620	5.8
8	804	0.001 (0.001)	39	732	0.9
9	804	0.001 (0.001)	30	736	n.d.
10	770	0.001 (0.001)	30 (30)	758	n.d.

^a In de-aerated (air-equilibrated) CH₂Cl₂ and CH₃CN solutions for ligands and complexes, respectively. λ_{exc} = 340 nm for ligands, 355 nm for **3**, **4** and **5**, 470 nm for **6**, 450 nm for **7**, 600 nm for **5** and **8**. ^b λ_{exc} = 331 nm for ligands, 373 nm for **3** and **4**, 465 nm for **6**, **7**, **5** and **8**. ^c λ_{exc} = 370 nm for **3** and **4**, 465 nm for **6** and **7**, 465 nm for **8**. ^d Phosphorescence data for ligands are obtained with pulsed lamp; λ_{exc} = 340 nm. ^e From ref. 12d. n.d. is not detected or weak signal.

Table 3.3. Experimental parameters used to evaluate the energy transfer features.

	ϕ	τ (ns)	τ_q (ns)	k_{in} (s ⁻¹)	k_{EnT} (s ⁻¹)	η_{EnT}
4 → 5	0.045	173	5	5.78×10^6	1.94×10^8	0.971
3 → 5	0.032	254	18	3.94×10^6	0.52×10^8	0.929
7 → 8	0.007	373	5	2.68×10^6	1.97×10^8	0.987
6 → 8	0.023	258	18	3.88×10^6	0.52×10^8	0.930

Table 3.4. Energy transfer rate parameters calculated according to the Förster model.

	J_F (cm ³ M ⁻¹)	R_0 (Å)	r (Å) ^[a]	d (Å) ^[b]	k_F (s ⁻¹) ^[c]	η_F
4 → 5	3.85×10^{-14}	26.0	14.5	19	3.82×10^7	0.869
3 → 5	3.20×10^{-14}	23.8	15.5	19	1.54×10^7	0.796
7 → 8	3.90×10^{-14}	19.1	9.3	19	0.28×10^7	0.510
6 → 8	3.41×10^{-14}	22.8	14.8	19	1.16×10^7	0.749

^a Inter-chromophoric distance calculated for $k_F = k_{EnT}$. ^b Mean inter-chromophoric distance calculated from molecular modelling. ^c Energy transfer rate constant calculated from the Förster model at the inter-chromophoric distance d.

Table 3.5. Energy transfer rate parameters calculated according to the Dexter model.

	J_D (cm)	H_d (cm ⁻¹) ^[a]	H (cm ⁻¹) ^[b]	λ_{cut} (nm)	k_D (s ⁻¹) ^[c]	η_F
4 → 5	5.19×10^{-5}	1.59	1.78	410	1.56×10^8	0.964
3 → 5	2.56×10^{-5}	1.09	1.30	410	0.36×10^8	0.902
7 → 8	4.50×10^{-5}	1.91	1.92	410	1.95×10^8	0.986
6 → 8	2.54×10^{-5}	1.15	1.31	410	0.40×10^8	0.912

^a Electronic interaction factor calculated at the inter-chromophoric distance d. ^b Electronic interaction factor calculated for $k_F = k_{EnT}$. ^c Energy transfer rate constant calculated at the inter-chromophoric distance d from $k_D = k_{EnT} - k_F$.

3.2.1.2. Spiro-bifluorene series

The second series of arrays under investigation is the spiro-bifluorene-based one, comprising ligand and complexes whose schematic structures are reported in **Chart 3.2**. Analyzed series comprises **11**, a spiro-bifluorene ligand, with a bpy group linked to the core through a rigid ethynylene spacer, **12**, **13** and **14**, monometallic complexes with a spiro-bifluorene unit, linked through a bpy ligand to the metal centre, Pt(II), Os(II) and Ir(III), respectively, **15**, **16** and **17**, defined tetrad, because composed of four photoactive subunits (three metal complexes and the spiro-bifluorene bridging ligand, linked through acetylide spacers). The bridging ligand, **11**, and the monometallic complexes, **12**, **14** and **13**, were used as model compounds for the study of the photophysical features, displayed by the three multichromophoric systems, **15**, **16** and **17**. The synthetic procedures for all the compounds herein presented are reported in reference.⁹

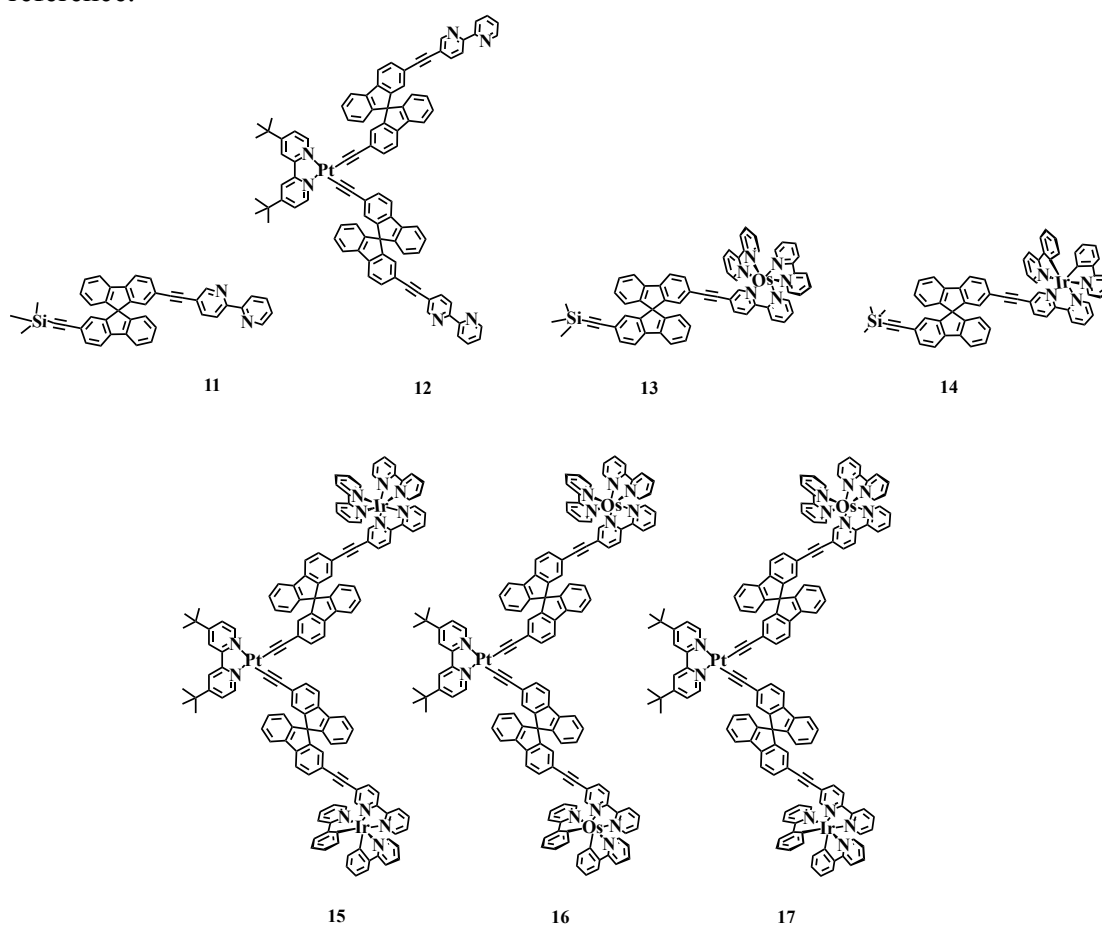


Chart 3.2. Schematic representation of Ir(III) and Os(II) chromophoric units (**12**, **13** and **14**), of the spiro-bifluorene scaffold (**11**) and of the multinuclear arrays (**15**, **16** and **17**). The charges 1+ for a single Ir and 2+ for Os have been omitted for the sake of clarity.

Absorption. Absorption details of the spiro-based ligand **11** and of the Pt(II), Ir(III) and Os(II) complexes, **12**, **14** and **13**, are reported in **Table 3.6** and related absorption spectra, recorded in dilute CH₃CN solutions ($c = 2 \times 10^{-5}$ M) at room temperature are collected in **Figure 3.10**.

Absorption profile for the ligand **11** displays an intense band in the near-UV region, peaking at 325 nm and extending up to 390 nm ($\epsilon_{\text{max}} = 109400 \text{ M}^{-1}\text{cm}^{-1}$). It originates from $^1\pi\text{-}\pi^*$ spiro-bifluorene core transition (**Table 3.6**) and, due to the higher

conjugation introduced by the ethynyl-bipyridine group, it is bathochromically shifted with respect to the one observed for the simple spiro-bifluorene (without substituents).⁵⁹ Absorption profile of Pt(II) complex **12** results very similar to that of **11** and indeed it comprises an envelop of bands, extending up to 370 nm ($\lambda_{\text{max}} = 335$ nm, $\epsilon_{\text{max}} = 99300$ M⁻¹cm⁻¹), originating from spin-allowed ¹ π - π^* transitions, centred on the ligands. The major contribution of the metallic moiety is displayed in the lowest energy band, appearing as a tail between 380 and 480 nm, attributable just to ¹MLCT transition, from the Pt(II) metal unit to the bipyridyl ligand (Pt \rightarrow dbbpy).⁵³

The spectrum of **13** is dominated by the characteristic features of the composite ligand, such as the intense and sharp band, peaking around 290 nm ($\epsilon_{\text{max}} = 104200$ M⁻¹cm⁻¹), originating from singlet spin allowed ligand centred (¹LC) transition, on the bipyridine group, and another signal around 371 nm ($\epsilon_{\text{max}} = 40500$ M⁻¹cm⁻¹), attributable to the composite ligand (¹LC spiro-bifluorene centred transition). This band appears as consequence of the coordination of metal centre by bpy group, bond responsible for the occupation of the ethynylene moiety, otherwise unoccupied in the free ligand **11**, in agreement with what reported for similar spiro-bifluorene based system.⁵⁴

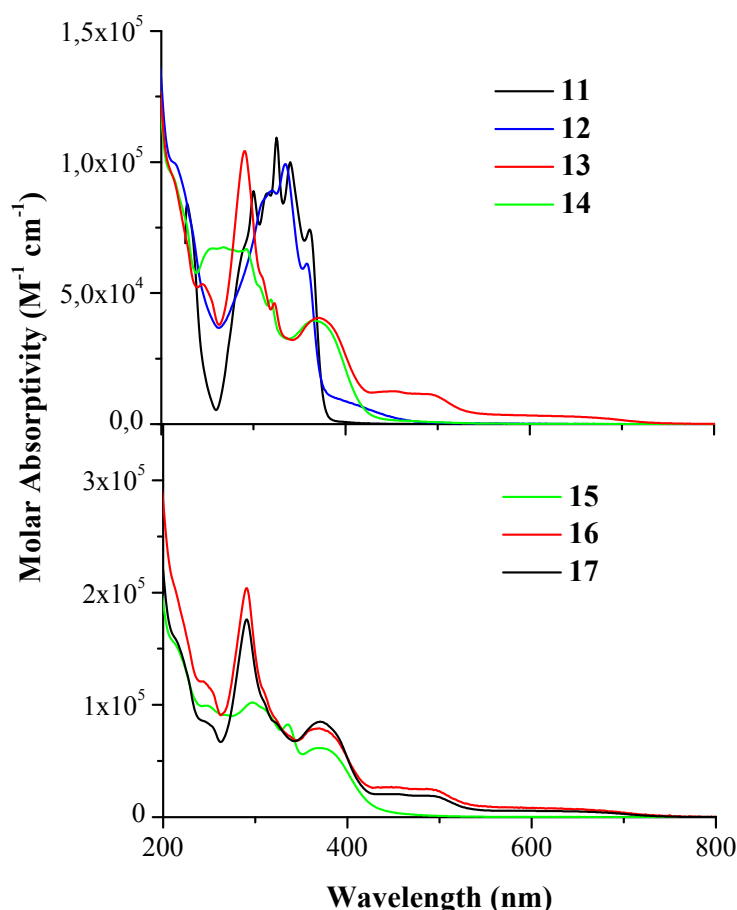


Figure 3.9. Absorption spectra at rt (top) of ligand **11** (black) in CH₂Cl₂, solution and of model complexes **12** (blue), **13** (red) and **14** (green), in CH₃CN solutions (top), of triads, **15** (green), **16** (red) and tetrad **17** (black) in CH₃CN solutions (bottom).

The metal unit gives rise to an additional band, appearing in the spectral region between 430 and 550 nm and, originating from transitions of spin-allowed mixed metal-to-ligand (¹ML_{bpy}CT) charge transfer character. The lowest energy portion of the spectral range

displays the weakest and broadest band of the absorption profile, appearing just like a tail in the region between 550 nm and 730 nm. It is associated to a formally spin-forbidden $^3\text{MLCT}$ set of transitions, enabled by the heavy atom effect. Due to the high value of spin-orbit coupling constant ($\zeta_{\text{Os}} = 3381 \text{ cm}^{-1}$),⁵¹ the direct absorption from singlet ground state to triplet excited state becomes partially allowed, through induction of states mixing.

The Ir(III) complex **14** displays an absorption profile very different with respect to the one of **13**, particularly in the UV-region between 240 and 330 nm. Here, due to the absorption of bpy and spiro-bifluorene units, a broad and not structured band, with peculiar shoulders, dominates the absorption.⁵⁰ Moving at lower energy, around 370 nm, the band originating from the coordination of the highly conjugated ligand by the metal centre appears, similarly to **13** model.

The description of absorption profiles for the trinuclear arrays, **15**, **16** and **17**, can be summarized taking into account the main features of the respective component subunits absorption (**Figure 3.10**, bottom). **15** displays absorption profile very similar to the one of the parent **14**, with the exception of the peaks intensity, as expected higher for the trinuclear than for the mononuclear system. Its absorption spectrum is quite well superimposable with the sum of the profiles of parent compounds **14** and **Pt-bpy**₂ (a model compound for the Pt unit without the spiro-bifluorene unit).⁶⁰

16 and **17** display extremely similar absorption profiles with, as main difference, the ratio between the intensities of the two peaks around 290 and 370 nm, resulting higher in **16**. Going from higher to lower energy, it is possible to observe for both the arrays, in agreement with the model **13**, the following features: (i) the intense band typical of $^1\pi\text{-}\pi^*$ bpy-centred transition ($\lambda_{\text{max}} \approx 290 \text{ nm}$), (ii) another band originating from the ^1LC spiro-bifluorene transition ($\lambda_{\text{max}} \approx 370 \text{ nm}$), (iii) a ^1CT transitions band of lower intensity, extended from 440 to 540 nm, and (iv) a tail for the $^3\text{M}_{\text{Os}}\text{LCT}$ transitions, up to 750 nm.

Emission. The luminescence features of examined complexes and ligand, as result of room (in air-equilibrated and de-aerated solutions) and low temperature investigations, are collected in **Table 3.7**. Emission profiles, recorded at room temperature in de-aerated CH_2Cl_2 for ligand **11** and CH_3CN solution for the monometallic complexes, **12**, **13** and **14**, are shown in **Figure 3.11** (top), rescaled according to the corresponding photoluminescence quantum yields. Luminescence spectra recorded at 77 K in $\text{CH}_2\text{Cl}_2:\text{CH}_3\text{OH}$ (1:1) glassy matrixes for the complexes and $\text{CH}_3\text{OH}:\text{C}_2\text{H}_5\text{OH}$ (1:4) frozen mixture for the ligand are also collected in **Figure 3.11** (bottom).

The ligand **11** shows an intense short-lived emission in solution at room temperature ($\phi = 0.75$ and $\tau = 1.16 \text{ ns}$), peaking at 404 nm, blue-shifted at low temperature, in glassy matrix ($\lambda_{\text{max}} = 371, 393 \text{ nm}$, **Table 3.7**). Moreover, at 77 K **11** also exhibits phosphorescence emission ($\lambda_{\text{max}} = 526 \text{ nm}$, $\tau = 243 \text{ ms}$), originating from the lowest-lying triplet excited state (highest energy peak at *ca.* 2.36 eV).

To better understand the real effects induced by the introduction of the spiro-bifluorene unit on the photophysical behavior of the complexes, a comparative discussion can be conducted for **12** with respect to its parent **Pt-bpy**₂ without the attached spiro-bifluorene

moiety. In particular, for **12** the photoluminescence quantum yield in de-aerated solution is decreased by more than 10 times with respect to **Pt-bpy**₂, and a strong decrease of the excited state lifetime is observed, too ($\tau = 0.49$ and $4.7 \mu\text{s}$, respectively). For these two complexes, the radiative constant ($k_r = \phi/\tau$) displays almost the same value (*ca.* $3 \times 10^4 \text{ s}^{-1}$) thus the observed decrease in the luminescence quantum yield for **12** with respect to **Pt-bpy**₂ has to be ascribed to an increase in the rate of non-radiative processes. This phenomenon is due to additional vibrational modes, introduced by the presence of the spiro-bifluorene unit and responsible for the coupling of excited state with the ground state. At 77K, **12** displays a structured emission band as effect of a well defined vibronic progression (**Figure 3.11**), not accounting for a neat ³MLCT nature of the emission, as also revealed by the millisecond range value of the registered lifetime ($\tau = 188 \text{ ms}$), but for a predominant ligand contribution.⁶¹ Such evaluation is also confirmed by the fact that the triplet level ($E_T = 2.33 \text{ eV}$, value calculated from the maximum of emission) is very close in energy to that of the spiro-bifluorene ($E_T = 2.36 \text{ eV}$), suggesting that ³ π - π^* transition centred on bpy-spiro composite ligand contributes to the description of the excited-state responsible for the emission.⁶¹ The ³LC nature of the emissive excited-state is also confirmed by the value of the radiative rate constant, calculated at rt ($k_r = 2.5 \times 10^4 \text{ s}^{-1}$), that is lower by one order of magnitude than that typical of ³M_{Pt}LCT emissions.

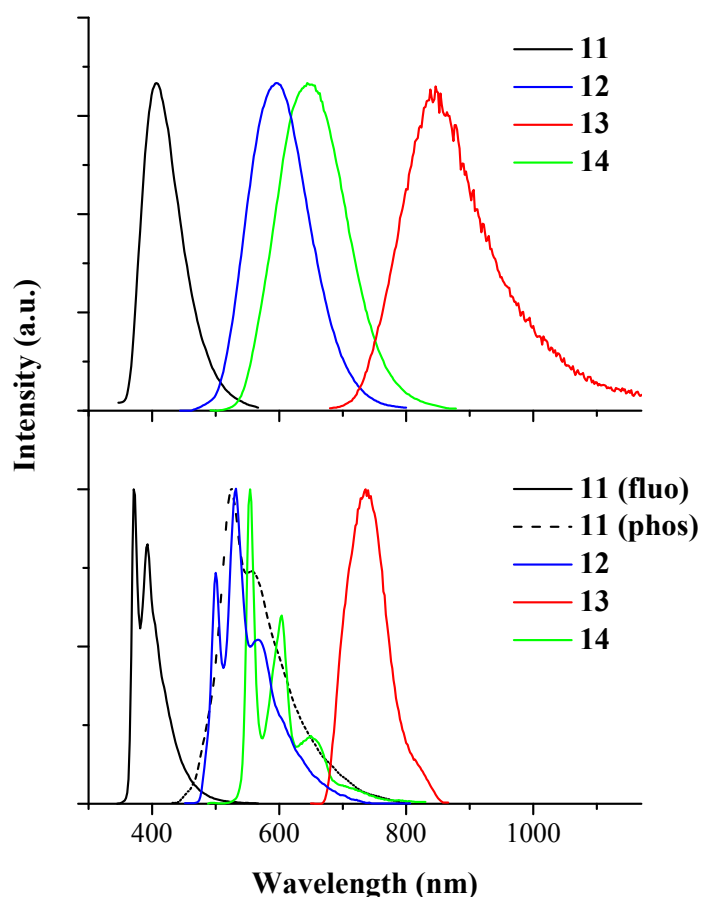


Figure 3.10. Normalized emission spectra at rt in de-aerated solution (top) and at 77 K in glassy mixtures (bottom) of ligand **11** fluorescence (black, full) and phosphorescence (black, dotted), and of model complexes, **12** (blue), **13** (red) and **14** (green).

The mononuclear complex **13** displays a broad and structureless phosphorescence band with the expected blue shift on going from solution to glassy matrix at 77 K, that might be explained by the rigidochromic effect, typically observed for luminescence of MLCT nature, as already discussed in Chapter 2.⁶² Taking into account this behavior together with literature data, the emission can be safely ascribed to ³MLCT transition.⁵⁶

For iridium complex **14**, the photophysical behaviour is also consistent with a ³CT character of the emission, as suggested by the blue-shifted maximum peak at 77 K and by the calculated value of the radiative constant ($k_r = 1.1 \times 10^5$). Further confirmation is given by the similarities observed with the parent compound $[\text{Ir}(\text{C}^{\wedge}\text{N})_2(\text{bpy})]^+$, whose emissive excited state is already reported to be of mixed ³MLCT/³LLCT character.⁶³ Albeit the large energy difference between their maxima of emission ($\lambda_{\text{max}} = 644$ and 590 nm, for **14** and $[\text{Ir}(\text{C}^{\wedge}\text{N})_2(\text{bpy})]^+$, respectively), in O₂-free environment both luminescence quantum yields and lifetimes values appear very similar ($\phi = 0.02$ and 0.018, $\tau = 179$ and 180 ns, for **14** and $[\text{Ir}(\text{C}^{\wedge}\text{N})_2(\text{bpy})]^+$, respectively).⁶³

Figure 3.12 shows room temperature luminescence profiles for air-equilibrated CH₃CN solutions of the metal complexes **12**, **14** and **13** and of the tetrads **15**, **16** and **17**, isoabsorbing at the excitation wavelength (407 nm). The compounds, in this case, have been analyzed upon excitation at the same wavelength because it is not possible to select and excite absorption bands perfectly localized at the different Pt(II), Ir(III) and Os(II) centres.

Energy transfer. The room temperature luminescence profiles of air-equilibrated CH₃CN solutions of mononuclear complexes **12**, **13** and **14** and of the trinuclear **15**, **16** and **17** are compared in **Figure 3.12**, upon excitation at 407.

In **15** and **16** the efficiencies of both Pt→Ir and Pt→Os energy transfer processes result higher than 99% with rate constants $k_{\text{EHT}} > 2 \times 10^9 \text{ s}^{-1}$, as revealed by such investigation. In fact, Pt-based emission appears completely quenched, while the Ir- and Os-based ones, for **15** and **16** respectively, are efficiently recovered, accounting for the energy transfer of overall absorbed photons into the Ir and Os subunits, respectively. It is important to notice that in both **15** and **16**, the Ir- and Os-based luminescences are longer-lived than in their corresponding models, **14** and **13**, particularly for **15**. Its value of lifetime, in de-aerated solutions, of 265 ns, against that of **14** of 179 ns, can be explained in the following way: the highest energy states ³M_{Pt}LCT and ³LC undergo fast energy transfer into ³M_{Ir}LCT and ³M_{Os}LCT excited states, that deactivate through radiative process. As it can be observed in the energy level diagram (**Scheme 3.2**), the ³LC excited state centred on the spiro-bifluorene unit has an intermediate energy with respect to the ³M_{Ir}LCT and ³M_{Pt}LCT excited states, differing from them for just *ca.* 1000 cm⁻¹ below and above, respectively (**Table 3.7**). Such energy levels distribution allows a prolongation of the lifetime observed in particular for the **15** array with respect to that of **14**, with the spiro-bifluorene centred ³LC excited state acting as energy reservoir for the two excited states close in energy and thus further repopulating the emissive Ir-centred state from the other triplet states.⁶⁴ In **16**, this trend is less evident because of the higher difference in energy between the lowest lying excited states of Pt and Os units (ΔE *ca.* 6400 cm⁻¹). In this case the reservoir effect by the ³LC state is not

effective and only the emission from the $^3\text{M}_{\text{Os}}\text{LCT}$ excited state is observed, with a comparable (within experimental uncertainties) lifetime with respect to the corresponding reference model **13** ($\tau = 31$ and 47 ns in de-aerated solution, **Table 3.7**, for **13** and **16**, respectively). At 77 K, the arrays **15** and **16** display features ascribable to emission from $^3\text{M}_{\text{Ir}}\text{LCT}$ and $^3\text{M}_{\text{Os}}\text{LCT}$ states, respectively (**Fig. 3.12**).

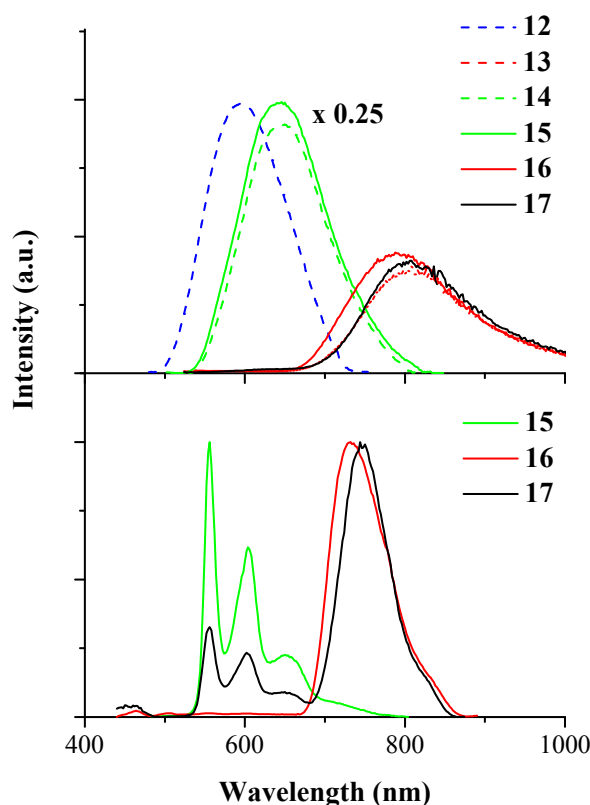
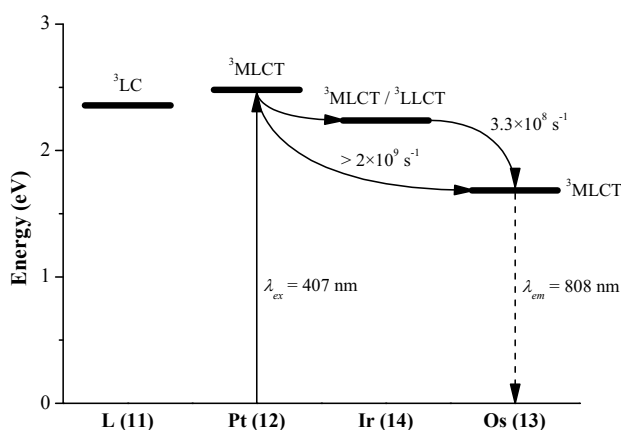


Figure 3.11. (Top) Corrected emission spectra at rt of isoabsorbing CH_3CN solution ($\lambda_{\text{exc}} = 407$ nm) of **12** (blue, dashed), **13** (red, dashed), **14** (green, dashed), **15** (green), **16** (red) and **17** (black). (Bottom) Normalized corrected emission spectra at 77 K in $\text{CH}_3\text{OH}:\text{CH}_2\text{Cl}_2$ (1:1) glassy solutions ($\lambda_{\text{exc}} = 407$ nm) of **15** (green), **16** (red), and **17** (black).



Scheme 3.2. Energy level diagram of the ligand- and metal-based triplet excited states estimated from emission maxima at 77 K and pathways for the photoinduced energy transfer processes.

From **Figure 3.12**, emission registered for **17** displays complete quenching at the region of the Pt-based emission and only less than 1% of residual emission from Ir unit appears, whereas the Os-based emission is almost completely recovered. From the quenched lifetime of the Ir-based emission (**Table 3.7**) an energy transfer rate constant $k_{\text{EnT}} = 3.3 \times 10^8 \text{ s}^{-1}$ and an efficiency $\eta = 98.9\%$ can be estimated for the Ir→Os energy transfer process. Thus, the Os moiety works as the final energy collector and the array **17** displays Os-based emission maxima and lifetimes, both at 298 and 77 K, completely corresponding to its parent compound, **13**. At 77 K, a residual Ir-based luminescence is clearly detected (**Fig. 3.12**), even if strongly quenched, as the relevant decrease in lifetime detected at 640 nm reveals, with respect to the model compound, **14** (**Table 3.7**). The energy transfer rate constant derived from these data is similar to that observed at rt, indicating a substantial independence of the process from temperature. Overall it can be deduced that in the tetrad **17** the energy absorbed by the ligand and by the Pt and Ir centres is quantitatively conveyed to the Os final collector both at rt and at 77.

Table 3.6. Absorption properties of ligand and complexes **11-17**.

	λ_{max} , nm ($\epsilon_{\text{max}} \times 10^{-3}$, $\text{M}^{-1} \cdot \text{cm}^{-1}$) ^[a]
11	300 (88.9), 315 (88.1), 325 (109.4), 340 (99.9), 361 (74.3)
12	320 (89.2), 335 (99.3), 358 (61.2), 397 (9.1)
13	245 (53.4), 290 (104.2), 323 (46.2), 371 (40.5), 453 (12.5), 600 (3.3)
14	268 (67.5), 292 (66.8), 319 (47.6), 366 (39.5)
15	246 (99.4), 297 (102.2), 335 (82.6), 372 (61.5)
16	244 (120.9), 291 (203.9), 370 (79.0), 453 (26.9), 600 (8.3)
17	244 (85.7), 291 (176.1), 371 (85.0), 451 (20.6), 600 (5.7)

^a In CH₂Cl₂ for ligand and CH₃CN for complexes.

Table 3.7 Luminescence properties of ligand and complexes **11-17**.

	rt ^[a]			77 K ^[b]	
	λ_{max} , nm	ϕ	τ , ns	λ_{max} , nm	τ , μs
11	404	0.75 (0.82)	1.16 (1.23)	371, 393	0.9×10^{-3}
phos ^[c]				526, 558sh	243×10^3
12	596	0.6×10^{-2} (1.3×10^{-2})	137 (493)	500, 532, 568sh	188×10^3
13	802	1.4×10^{-3} (1.8×10^{-3})	26 (31)	738	0.9
14	644	0.9×10^{-2} (2.0×10^{-2})	88 (179)	554, 604, 650	6.0, 13.3 ^[d]
15	646	-	108 (265)	556, 604, 650	1.8, 10.7 ^[e]
16	788	-	- (47)	732	0.8
17	640	-	- (3)	556, 602, 650	2.4×10^{-3} , 68.7×10^{-3} ^[f]
	804	-	- (28)	742	0.7

^a In air-equilibrated (de-aerated) CH₃CN solution. For quantum yield determination: λ_{exc} = 320 nm for **11**, 425 nm for **12** and **14** and 600 nm for **13**. For lifetime measurements, λ_{exc} = 331 nm for **11**, 373 nm for **12** and **14**, 465 nm for **13**, 407 nm for **15**, **16** and **17**. ^b In glassy solutions of CH₂Cl₂: CH₃OH (1:1) for the complexes **12**, **13** and **14** and of CH₃OH: C₂H₅OH (1:4) for the other complexes and for the ligand. For lifetime measurements λ_{exc} = 331 nm for **11**, 373 nm for **14**, 370 nm for **12** 465 nm for **15** and **13**, 407 nm for **16** and **17**. ^c Phosphorescence in CH₂Cl₂: CH₃OH (1:1) glassy solution, λ_{exc} = 338 nm. For lifetime measurement, λ_{exc} = 370 nm. ^d ratio 40:60. ^e ratio 30:70. ^f ratio 30:70.

3.2.2. Systems for lighting

3.2.2.1. Julolidine series

Julolidine-based ligands and complexes, whose schematic structures are reported in **Chart 3.3**, represent another topic of the current chapter. In particular, **18** and **18'** are julolidine (2,3,6,7-tetrahydro-1*H*,5*H*-benzo[*ij*]quinolizine) derivatives, with N-methylene-aniline and hydroxyl group ortho-disubstituted aromatic ring (N[^]O). **19** and **19'** are the corresponding boranil compounds, whose six-member ring is formed by the N[^]O system that chelates the boron atom of a boron difluoride group (BF₂) (they have been prepared as suitable reference dyes in which ESIPT is blocked through the

boranylation). **20** and **20'** are the monometallic phenylpyridine Ir(III) complexes with the N[∧]O chelating ligand occupying two sites of the metal coordination sphere. The difference between **18**, **19**, **20** with respect to **18'**, **19'**, **20'**, respectively, is just the presence of a triple bond instead of an iodine atom, on the N-methylene-aniline. **21** and **21'** are square planar terpyridyl (terpy) Pt(II) complexes linked through a phenyl-acetylide spacer to the julolidine subunit (in the former, it is in the open-chain form while in the latter, it is the boranil derivative). **Pt**,^{12d, 65} already reported, is used as model for the Pt(II) compounds **21** and **21'**. In the end, **22**, denoted as triad because it contains three photoactive subunits, is composed of Pt(II) and Ir(III) units, linked together by the julolidine ligand, acting as bridge. Some indications about the synthetic strategies for ligands are reported in reference.¹⁰

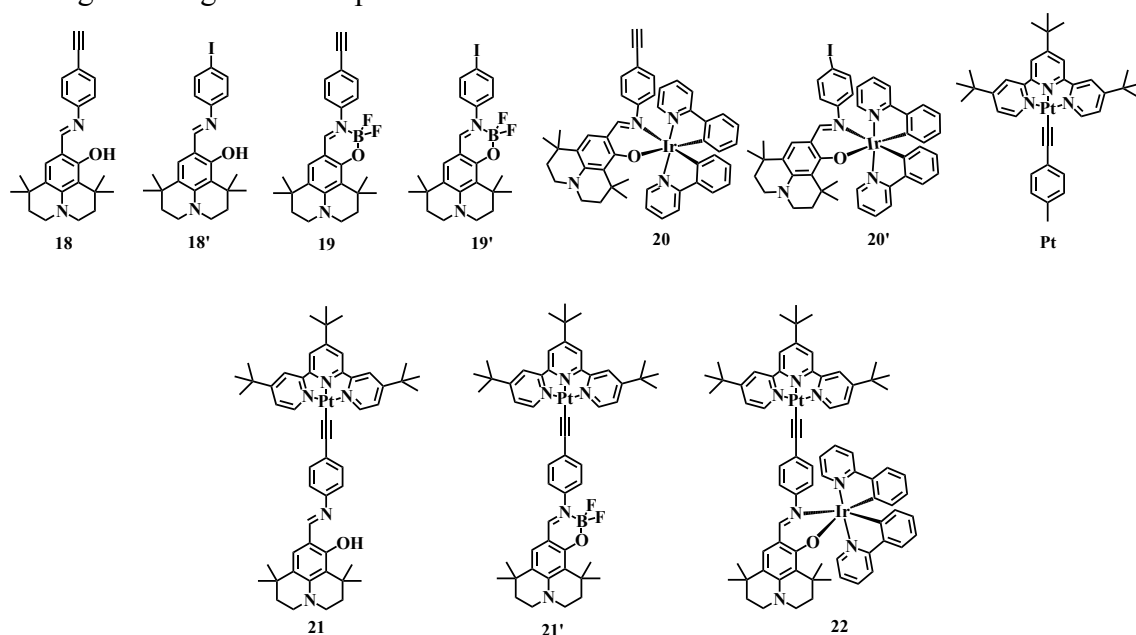


Chart 3.3. Schematic structures of julolidine-based ligands (**18**, **18'**, **19** and **19'**), Ir(III) (**20** and **21'**) and Pt(II) (**21** and **21'**) complexes and dinuclear array **22**. The charges 1+ for **21**, **21'** and **22** have been omitted for the sake of clarity.

Absorption. Absorption spectra of ligands and complexes, recorded in dilute CH₃CN solutions ($c = 10^{-5}$ M) at room temperature, are displayed in **Figure 3.13** and **3.14** and corresponding details are gathered in **Table 3.8** together with data collected in CH₃OH solutions for the ligands.

All ligands **18**, **18'**, **19** and **19'** absorb up to 450 nm with relatively high values of extinction coefficient. Their highest absorption band, peaking at about 400 nm and of broad shape, is assigned to ¹ π - π^* transitions,⁶⁶ not influenced by solvent polarity. On going from open-chain to boranil derivatives, this band is red-shifted by approximately 20 nm and increases its intensity ($\epsilon_{\max} = 40300$, 49000, 64500 and 64000 M⁻¹cm⁻¹, for **18**, **18'**, **19** and **19'**, respectively).

The spectra of **20** and **20'** display two characteristic bands, as reported for the corresponding model [Ir(ppy)₃].⁶⁷ The most intense and sharp band, peaking around 260 nm ($\epsilon_{\max} = 58800$ and 55300 M⁻¹cm⁻¹, for **20** and **20'** respectively), is assigned to singlet spin allowed ¹LC transition, centred on the phenyl-pyridine groups. Actually, its spectral position corresponds approximately to the ones of the free protonated ligand.^{67b} The second band appears at about 370 nm ($\epsilon_{\max} = 23600$ and 23500 M⁻¹cm⁻¹, for **20** and

20' respectively) and is related to ^1CT transition. The long-wavelength absorption tail is ascribed to formally forbidden $^3\text{MLCT}$ transitions, here allowed by the heavy metal effect, enlarging the spin-orbit coupling.

Absorption profiles of **21** and **21'** can be described according to the features of the model compound **Pt**⁶⁵ (see **Chart 3.3**). Going from higher to lower energy, the envelop of bands below 350 nm can be ascribed to intra-ligand (IL) $^1\pi\text{-}\pi^*$ transitions of the alkynyl bridge and of the substituted terpyridine ligand. In the visible region, the expected mixed $\text{Pt}\rightarrow\text{terpy } ^1\text{MLCT}/\pi(\text{C}\equiv\text{C})\rightarrow\pi^*(\text{terpy})\text{LLCT}$ transitions are not observed, because they are obscured by the ligand centred (LC) transitions of the julolidine moiety. The nature of this band is confirmed by the spectral position, the same of the free ligand, not affected by the presence of the metal.^{65,68}

The absorption spectra of these compounds match reasonably well the sum of the spectra of their single components (see **Fig. 3.14**). The only exception is in the presence of a shoulder in the low energy side of the lowest energy absorption band of the original spectra. This discrepancy can be explained as effect of the distortions introduced in the electronic cloud by the metal-ligand interaction. Probably both $\text{Pt}\rightarrow\text{terpy}$ and $\text{Pt}\rightarrow\text{julolidine}$ transitions are involved and the presence of $(\text{C}\equiv\text{C})\rightarrow(\text{julolidine})$ ILCT transitions cannot be excluded.

The absorption profile of the triad **22** is consistent with the sum of its components, pointing out the presence of a weak electronic coupling between them. Moving from higher to lower energy, it is possible to observe two sets of bands, as in the Ir(III) models, and to recognize the distinct contributions of all components. The specific features are listed below: (i) the most intense band, up to 350 nm, typical of $^1\pi\text{-}\pi^*$ terpy/ppy centred transitions ($\lambda_{\text{max}} \approx 258$ nm), (ii) the broad Ir(III) and Pt(II) $^1\text{MLCT}/^1\text{LLCT}$ mixed transitions band, extended from 350 to 500 nm; (iii) the $^3\text{MLCT}$ transition band, appearing as a tail with low intensity, up to 600 nm.

Emission. All ligands **18**, **18'**, **19** and **19'** and Ir(III) complexes **20** and **20'** are luminescent in liquid and frozen solutions, while the two Pt(II) compounds **21** and **21'** and the triad **22** display emission only at 77 K in glassy matrix. The luminescence features of examined ligands and complexes, obtained by analysis at room (in air-equilibrated and de-aerated CH_3CN solutions) and at low temperature (in $\text{CH}_2\text{Cl}_2:\text{CH}_3\text{OH}$ 1:1 glassy matrix), are collected in **Table 3.9** (ligands) and **3.10** (complexes) and shown in **Figure 3.15**, **3.16** (ligands at rt and 77 K, respectively) and **3.20** (complexes at rt and 77 K).

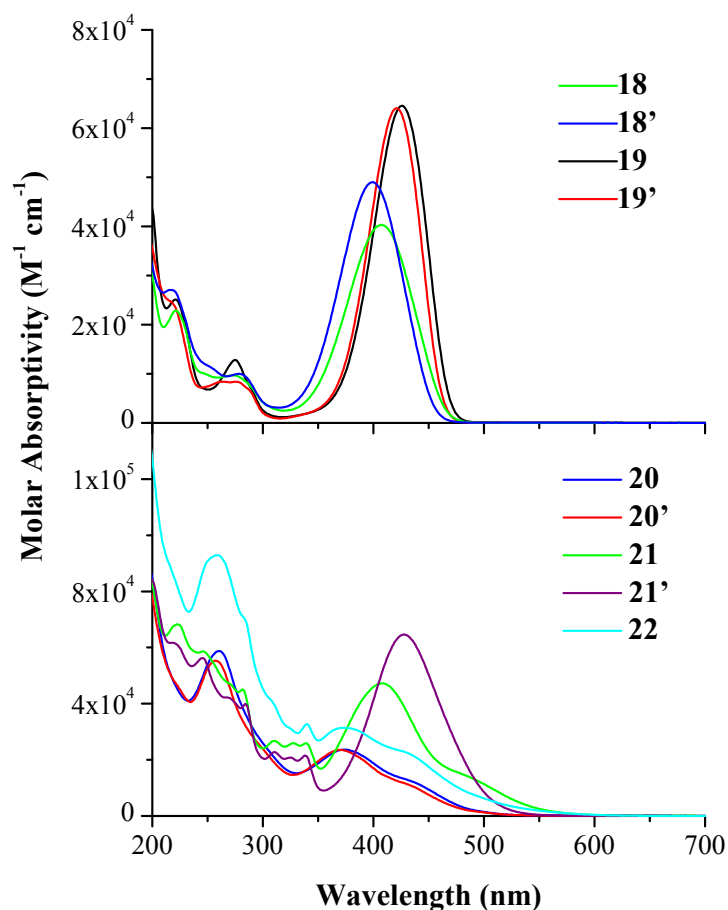


Figure 3.12. Absorption spectra of julolidine-based ligands (top) and complexes (bottom) at room temperature in CH_3CN solutions.

Ligands. The ligands under investigation display a very manifold behaviour: the open-chain systems, **18** and **18'**, have completely different luminescence with respect to the boranils, **19** and **19'**.

The highest values for photoluminescence quantum yields have been found for the close-chain **19** and **19'**, as expected for the presence of the boron chelation.^{66,69} In fact, as recently reported in literature, tetrahedral boron-complexes, incorporating $\text{N}^{\wedge}\text{N}$ or $\text{N}^{\wedge}\text{O}$ chelation, produce successful results in luminescence.⁶⁶

Their short-lived emission in solution at room temperature, peaking at about 480 nm, do not display large shift or shape modification moving from one solvent to another (**Figure 3.15**), while lifetimes and photoluminescence quantum yields are sensitive to the change of the medium (**Table 3.11**). Indeed, it has been found that increasing solvent polarity produces enhancement in the PLQYs (from 0.48 in toluene to 0.75 in acetonitrile for **19**, in air-equilibrated solution), as already reported for similar systems.^{70,71} This behaviour can be explained with an increase in k_{nr} on going from polar to nonpolar solvent, since k_{r} is usually not very affected by solvent polarity.⁷¹

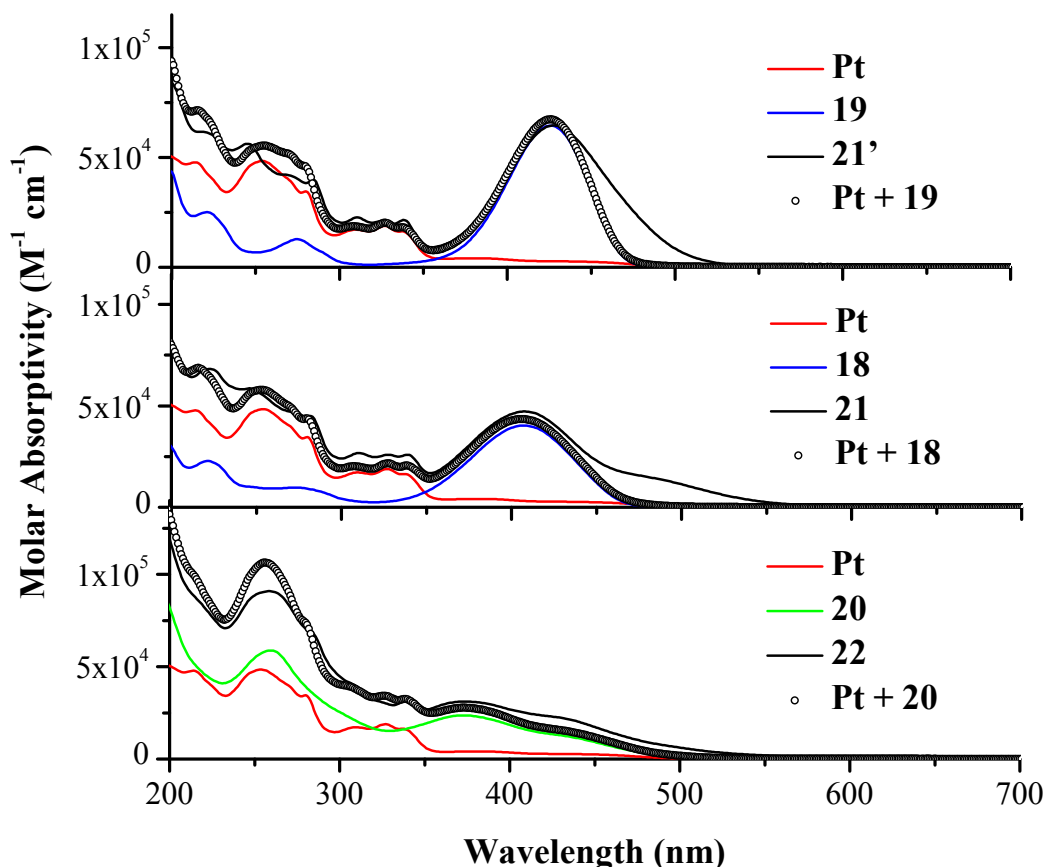


Figure 3.13. Absorption spectra of the Pt(II) complexes **21'** (top) and **21** (middle) and of the triad **22** (bottom) at rt in CH_3CN solutions. The dots represent the spectral addition of the absorption for the relative model components.

At low temperature in frozen solution, the boranil derivatives **19** and **19'** show blue-shifted fluorescence with respect to rt (picking at about 460 nm) and weak phosphorescence emissions ($\lambda_{\text{max}} = 572$ and 584 nm, $\tau = 38.1$ and 17.1 ms for **19** and **19'**, respectively), evaluable for the lowest triplet excited state and clearly detected thanks to the use of methylene iodide. Large halogens such as bromide and iodide are able to quench fluorescence and to enhance phosphorescence emissions, promoting intersystem crossing to an excited triplet state, by spin-orbit coupling of the excited (singlet) fluorophore and the halogen.⁷¹ The phosphorescence of **19'** is shorter-lived than that of **19**, due to the heavy atom effect of the iodine substituent ($\zeta_I = 5069 \text{ cm}^{-1}$),⁵¹ that promotes the $T \rightarrow S_0$ spin forbidden deactivation.

On the contrary, the open-chain julolidine derivatives **18** and **18'** show more complicated emission behaviour, both displaying a panchromatic luminescence from a variety of excited states. Such difference can be explained taking into account the ES IPT process,^{41,42} that takes place in both **18** and **18'**.

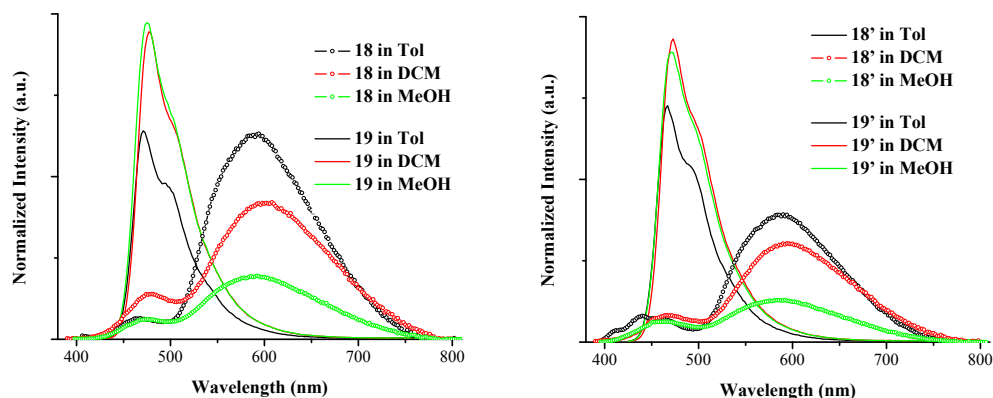
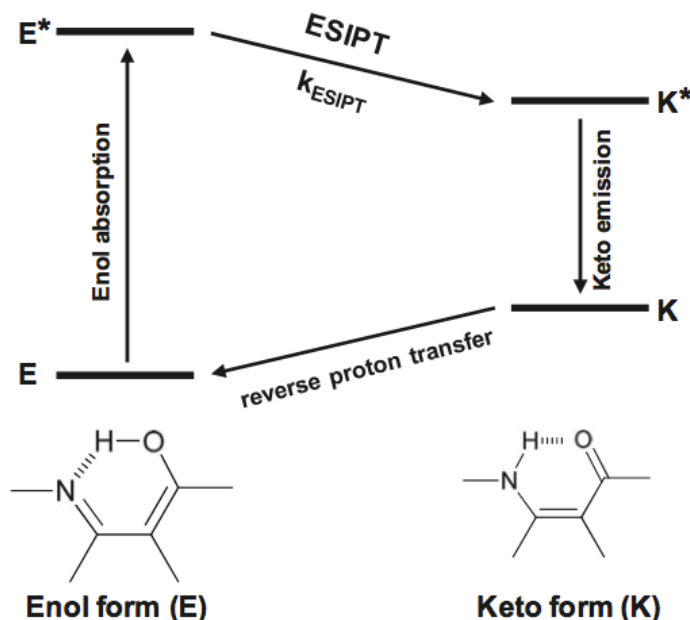


Figure 3.14. Emission spectra in different solvents at rt of **19** and **19'** (full line) and **18** and **18'** (dotted line). Spectra are scaled proportional to the quantum yields.

ESIPT. The open-chain ligands **18** and **18'** display dual and weak luminescence, due to the occurrence of the ESIPT process. In general, this phenomenon occurs upon photoexcitation in systems containing a proton donor and a proton acceptor groups in close position. The irradiation, causing the redistribution of the electronic charges, induces a fast proton transfer reaction from the proton donor to the proton acceptor group, mediated by the intramolecular H-bond. This migration is the basis of the keto-enol tautomerization, with transformation of the excited enol form (E^*) in the excited keto form (K^*). After the radiative deactivation of the second, the system comes back to the initial E form, through reverse proton transfer.⁷²



Scheme 3.3. Schematic representation of ESIPT photocycle. (From Ref. 72)

ESIPT process generally induces lowering of luminescence quantum yields with respect to non-ESIPT analogues, because it renders non-radiative deactivation pathway more competitive, favouring the internal conversion and the following vibrational

relaxation.^{72,73} The efficiency of the ESIPT process is affected by the polarity of the solvent: protic and polar solvent (as MeOH) prevents the process, hindering the proton transfer reactions, through intermolecular H-bond.⁷⁴

Figure 3.15 compares the rt luminescence spectra of ESIPT ligands with their non-ESIPT analogues in two solvents of different polarities. In emission profiles of the formers, both the tautomers can be observed but in different proportions: the residual luminescence from the E form appears at about 470 nm while the emission due to the K form is strongly red-shifted at 600 nm.

The global luminescence quantum yields for **18** and **18'** are very low: close to 10^{-3} in less polar and aprotic solvents and around 10^{-4} in methanol because of the decrease of the more emitting K form (**Table 3.11**). A consistent trend is revealed by the lifetime measurements: the K form is longer-lived in toluene (TOL) than in methanol and displays a mono-exponential decay. Its formation (rise) is not discernible because the ESIPT process takes place at an ultrafast rate. The lifetime of the E tautomer is too short and under the limits of detection of the employed apparatus (< 20 ps).

Such behaviour could be expected for systems with the active moiety inserted into a six-member ring. Actually, according to the literature, the efficiency of emission of K tautomer in non-polar solvents could be high in 5-member ring systems but not in 6-member ones for the more pronounced TICT (twisted intramolecular charge transfer) deactivation.⁷²

In condensed medium, by comparison with the emission behaviour of the boranil derivatives, the emission from singlet and triplet states of the E form can be identified with the bands peaking around 465 and 590 nm, respectively (**Figure 3.16**).^{74,75} The contribution of the intermediate band, peaking around 530 nm, can be attributed to the fluorescence of the K form. This assignment is also confirmed by the luminescence decay analysis at different emission wavelengths. At $\lambda > 600$ nm the decay is mono-exponential with lifetime in the order of ms ($\tau = 11.6$ and 54.6 ms for **18'** and **18**, respectively, **Table 3.9**), which are typical for the phosphorescence of organic compounds and comparable to those observed for the related boranil derivatives. At shorter wavelengths ($450 < \lambda < 550$ nm) double exponential decays are observed both for **18** and **18'**, with lifetimes in the ns region (**Table 3.9**). It should be noted that the presence of the iodine atom in **18'** promotes the intersystem crossing, altering the ratio between the singlet and triplet emission bands and thus the colour of the emitted light.

For this reason, the colour coordinates of such ligands in the CIE 1931 colour space have been calculated by means of the irradiance spectra obtained at 77 K and in powdered samples (**Figure 17**). The results are reported in **Figure 17** (bottom), together with the coordinates of the standard illuminants A (tungsten lamp) and D65 (noon daylight) for comparison. There is a clear difference between the yellowish-orange emission of **18'** (close to that of the standard illuminant A) and the yellowish-green emission of **18**, shifted towards the centre of the diagram. The emission output of **18** cannot be considered white but panchromatic, as all the colour components of the visible spectrum are present, but their balance is not optimized to generate white emission.

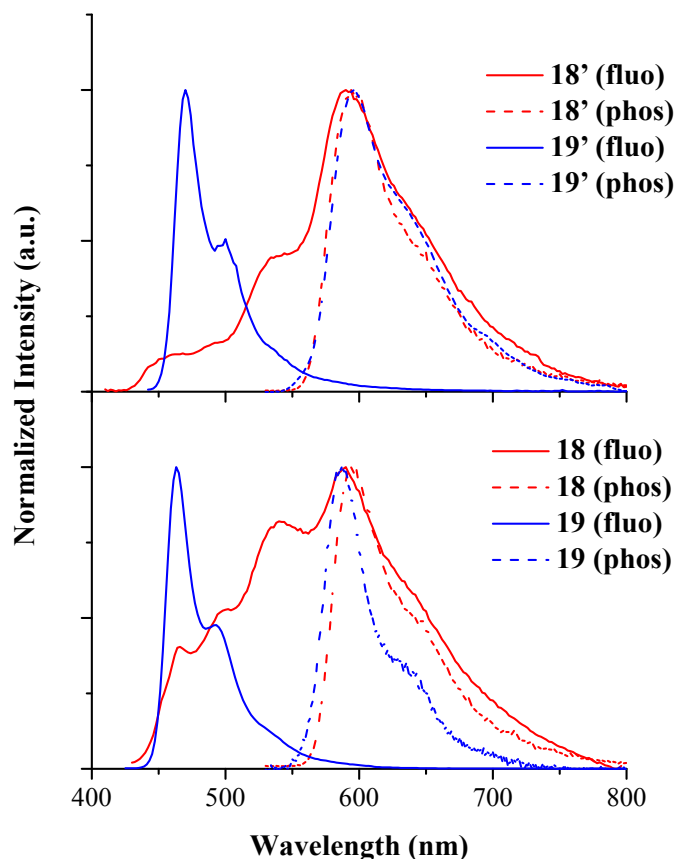


Figure 3.15. Normalized fluorescence (full line) and phosphorescence (dotted line) spectra of **18'** and **19'** (top) and **18** and **19** (bottom) derivatives in $\text{CH}_3\text{OH}:\text{CH}_2\text{Cl}_2$ (1:1) glass at 77 K.

Further investigation has been conducted on powdered samples at rt, also displaying panchromatic emission (**Figure 17**). In this case, **18** show colour coordinates similar to those already observed in glassy solution at 77 K. The situation is different for **18'**: here the emission is mainly from the singlet state, while the red phosphorescence is depressed. This leads to a more balanced white light emission having colour coordinates 0.341, 0.386 (hollow symbols in **Figure 17**, bottom). This behaviour can be explained taking into account the phosphorescence quenching by the atmospheric oxygen, to which the powder samples are exposed during the measure. Unfortunately, it was not possible to determine the absolute photoluminescence quantum yield of the powder samples because it was below the detection limit of our apparatus ($< 2\%$).

It is important to underline that the present case is different from that of *Park and coworkers*, in which ESIPT was used to prevent the energy transfer between two chromophores.⁷⁶ And moreover, the ligands here presented have the advantage to be open to simple modulation of their emission color through simple substitutions in the *para* position of the phenyl ring.

Prototropic equilibrium in acid media. The open-chain ligands **18** and **18'** have been studied in CH_3CN solution upon acidification, in order to investigate prototropic equilibrium and photophysical properties of the occurring protonated protomers. Indeed, ESIPT molecules contain both proton donor and acceptor groups and they can be protonated or deprotonated depending on the pH of the solution.

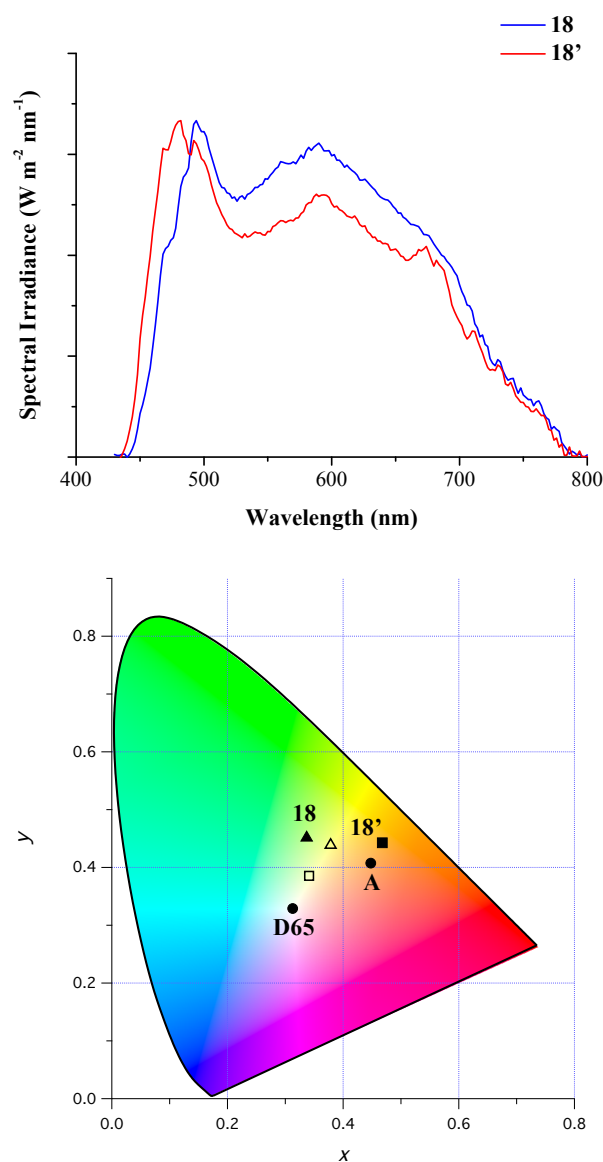


Figure 3.16. Normalized irradiance spectra of **18'** and **18** as pure powder film at rt (top). CIE 1931 spectral chromaticity coordinates of **18'** (squares) and **18** (triangles) in CH₃OH: CH₂Cl₂ (1:1) glass at 77 K (full symbols) and as powder neat film at rt (hollow symbols) and of the standard illuminants **A** (tungsten lamp) and **D65** (noon daylight) (bottom).

The current analysis has been conducted on $\sim 6 \mu\text{M}$ solutions of the ligands **18** and **18'** (also on the boranils **19** and **19'**, for comparison purpose) upon addition of increasing amount of trifluoroacetic acid (up to 1000 equivalents).

While absorption and emission profiles of **19** and **19'** are not affected by the acid addition, for **18** and **18'** absorption spectra are red-shifted compared to those registered in pure acetonitrile solution (**Figure 3.18**).

The emission reveals the clear disappearance of the keto-form and the corresponding appearance of a new species, emitting in the region between E and K forms emissions (**Figure 3.19**). This new band can be ascribed to the cationic form, given by the

protonation of imine nitrogen, and is very similar in shape and position (only slightly red-shifted) to the ones of the close-chain compounds.

Indeed, the N-protonation, in this case, interrupts the intramolecular H-bond (O-H \cdots N) producing a similar electronic distribution as in the boranils.

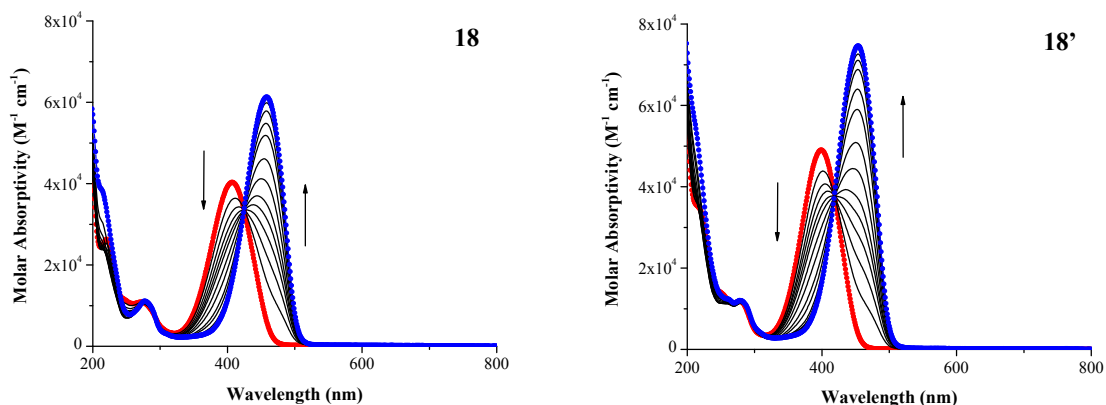


Figure 3.17. Absorption spectra of **18** (left) and **18'** (right) in CH₃CN solution ($c = 6.3 \times 10^{-6}$ M and 5.9×10^{-6} M, respectively) at rt upon addition of trifluoroacetic acid (from 0 eq, blue line, to 1000 eq, red line).

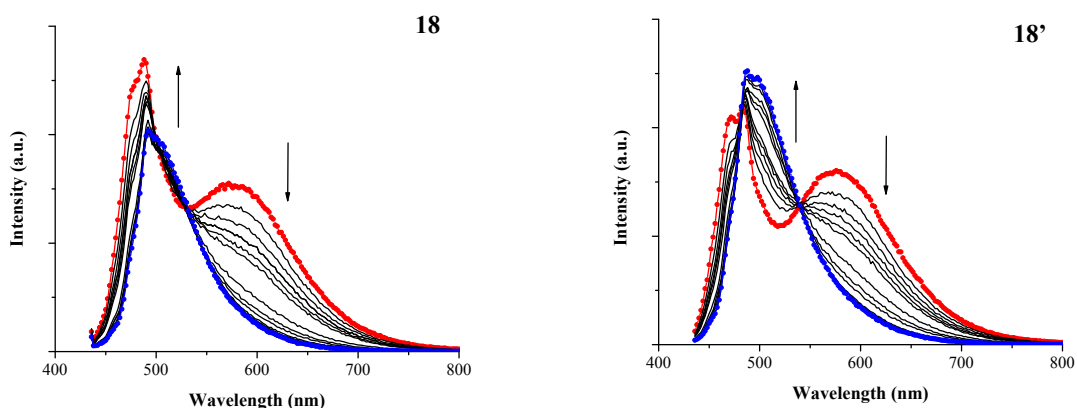


Figure 3.18. Emission spectra of **18** (left) and **18'** (right) in CH₃CN solution ($c = 6.3 \times 10^{-6}$ M and 5.9×10^{-6} M, respectively) at rt upon addition of trifluoroacetic acid (from 0 eq, blue line, to 1000 eq, red line); $\lambda_{\text{exc}} = 425$ and 420 nm, respective isosbestic points.

Complexes. The luminescence properties of Ir(III) complexes **20** and **20'** could be attributed to a ³CT nature of the emitting state, as confirmed by the blue shift of the luminescence maxima on going from solution to glassy matrix and by the broad and unstructured emission profile registered at rt (**Figure 3.20**, top). The values of radiative constants in de-aerated solution ($k_r = 2.6 \times 10^3$ and 2.5×10^3 s⁻¹, for **20** and **20'**, respectively), resulting ≈ 2 orders of magnitude lower than expected for a neat ³MLCT transition, suggests a ³LC contribution to the nature of the emitting excited state.

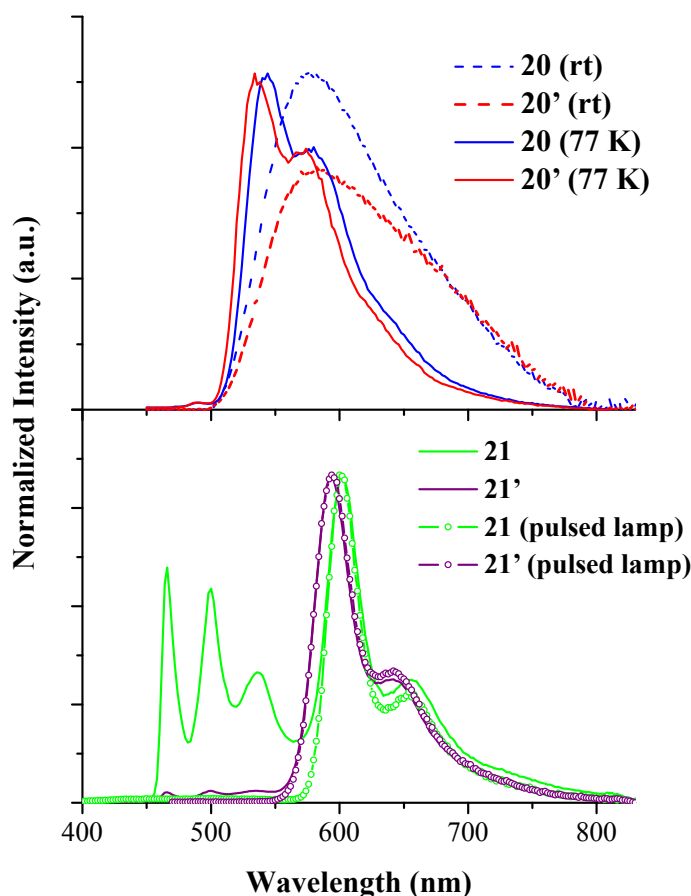


Figure 3.19. Normalized luminescence spectra of complexes **20** and **20'** at rt in CH₃CN solutions (dotted line; scaled for corresponding photoluminescence quantum yields) (top) and of **21** and **21'** at 77 K (bottom) in CH₂Cl₂: CH₃OH (1:1) glassy mixtures.

The introduction of the julolidine unit attached to the **Pt** moiety induces big modification on the photophysical behavior of the Pt(II) complexes **21** and **21'**. At odds with the intense luminescence reported for **Pt**, they do not display any emission at room temperature. At 77 K instead, luminescence spectra are very similar to the phosphorescence of the ligands, with additional bands of different nature. From the comparison of their emission profiles, recorded in gated condition after 0.5 ms delay, with those of the corresponding ligands, it is possible to assign the bands peaking around 600 nm to the phosphorescence of the julolidine portion (**Figure 3.20**, bottom). Such behavior is consistent with the energy level diagram traced for these systems, reported in **Scheme 3.3**: the triplet excited state responsible for the phosphorescence emission of the ligands lies at lower energy than that coming from ³M_{Pt}LCT one, estimated from **Pt** emission at 77K.⁶⁵ Thus it is possible to assume that a ³Pt→³L energy transfer process occurs, with population of the julolidine triplet state from the Pt→(terpy) based one. Moreover, the fact that for both complexes, phosphorescence lifetime values are much lower than in the free ligands and with double-exponential decays ($\tau = 0.6$ and 3.0 ms for **21** and 0.9 and 3.7 ms for **21'**; **Table 3.10**) accounts for a percentage of mixing of ligand-centred triplet excited-state with charge-transfer states. The additional bands, clearly visible in **21** and very weak in **21'**, originate from (i) a ¹LC excited state ($\lambda_{\text{max}} \approx 465$ nm) and (ii) the ³M_{Pt}LCT excited state ($\lambda_{\text{max}} = 500$ nm,

$\tau = 11.5$ and $11.2 \mu\text{s}$ for **21** and **21'**, respectively). The lifetimes recorded for the Pt-based emissions result slightly shorter than the one reported for the model compound **Pt**, confirming the occurring of the energy transfer process.

In the case of the triad **22**, no emission is detected at room temperature, as for **21** and **21'**. At 77 K, this compound displays a broad and multi-peak emission that covers all the visible range, with the contribution of all components. To better understand how much the single units affect the luminescence of the triad, emission maps with two different ranges of excitation wavelengths have been performed, in order to cover the entire absorption region (keeping absorbance under acceptable values for the kind of measurement). Anyway, even exciting almost selectively ligand and metal units, just slight differences in the relative intensities of the peaks were observed, without separation of the bands of the single components. Almost the same trend is observed on powdered solution. In such profile it is possible to recognize contributions of ligand (singlet and triplet states), Pt(II) and Ir(III) emissions ($\lambda_{\text{max}} = 466, 494, 564$ and 636 nm). This kind of behavior seems to highlight the nature of white emitter for the triad, as previously observed for ligands **18** and **18'** and particularly for Pt(II) complex **21**, induced by a not complete energy transfer to the ^3LC state. A precise estimation of the efficiency of such processes cannot be performed because of the low emission intensity registered for **22** at the different interesting regions.

A different behaviour is revealed for the corresponding polystyrene film, emitting clearly at 630 nm, probably from the ligand centred triplet excited (^3LC) state without any other important contribution. For comparison purpose, emissions from polystyrene films of one Ir(III) compound **20**, **Pt** and ligand **19** have been recorded, as reported in **Figure 3.21**. **20** shows a slightly red-shifted emission ($\lambda_{\text{max}} = 564$ nm) with respect to the glassy matrix, with lifetimes of the same order of magnitude, as similarly observed for **19** ($\lambda_{\text{max}} = 544, 472$ nm and $\tau = 3.46 \mu\text{s}, 2.2$ ns, for **20** and **19**, respectively; see **Table 3.12**). For **Pt**, the red-shifted peak displays a shorter lifetime values compared to glassy matrix ($\lambda_{\text{max}} = 538$ nm and $\tau = 5.2$ ns).

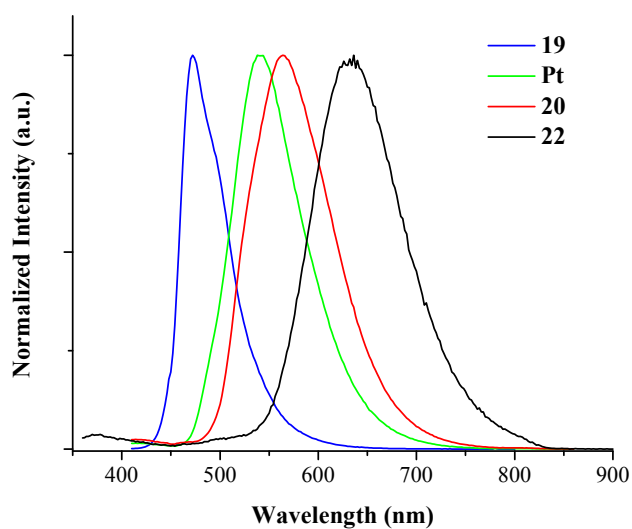


Figure 3.21. Normalized emission spectra at rt in polystyrene film of the ligand **19** and complexes **Pt**, **20** and **22**.

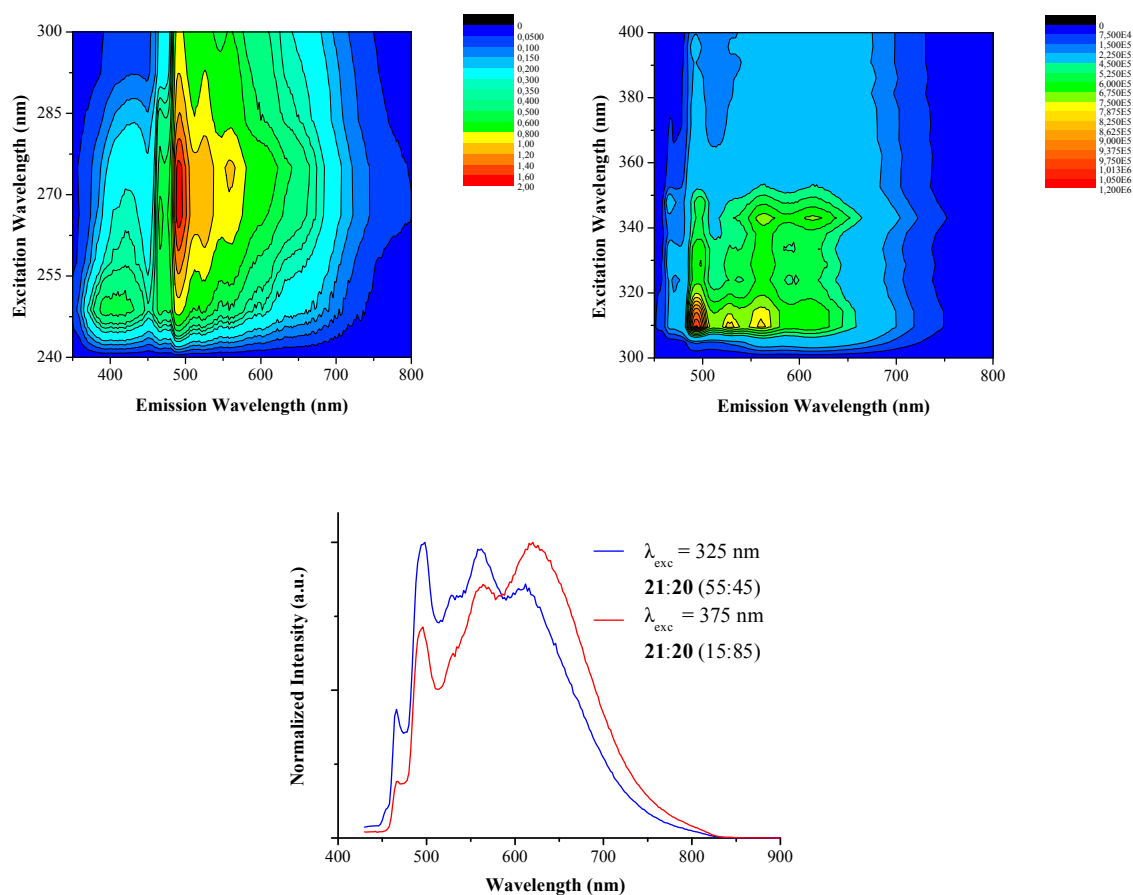


Figure 3.20. Normalized maps of **22** luminescence at 77 K in CH_2Cl_2 : CH_3OH (1:1) glassy solutions (top) at two different excitation ranges: 250 – 300 nm (left) and 300 - 400 nm (right). Normalized emission spectra at 77 K in CH_2Cl_2 : CH_3OH (1:1) glassy mixtures of **22** at different excitation wavelengths (bottom).

Table 3.8. Absorption properties of ligands and complexes **18-22**.

	λ_{\max} , nm ($\epsilon_{\max} \times 10^{-3}$, M ⁻¹ cm ⁻¹) ^[a]
18	221 (22.9), 273 (9.7), 407 (40.3) 219 (25.8), 271 (10.1), 406 (37.1) ^[b]
18'	217 (27.1), 279 (10.0), 399 (49.0) 219 (29.5), 274 (9.9), 399 (46.2) ^[b]
19	221 (25.1), 275 (12.8), 426 (64.5) 220 (30.1), 273 (13.2), 423 (62.6) ^[b]
19'	221 (23.5), 265 (8.3), 421 (64.0) 221 (25.0), 276 (8.5), 419 (62.0) ^[b]
Pt ^[c]	280 (34.6), 327 (18.9), 440 (2.6)
20	260 (58.8), 373 (23.6)
20'	257 (55.3), 370 (23.5)
21	223 (68.3), 310 (26.7), 339 (25.9), 408 (47.2)
21'	245 (56.3), 310 (22.7), 338 (21.5), 428 (64.6)
22	258(92.9), 340 (32.7), 373 (31.4)

^a In CH₃CN solutions at rt. ^b In CH₃OH solutions at rt. ^c Data from ref. 65.

Table 3.9. Luminescence properties of **18**, **18'**, **19** and **19'** at rt and at 77 K.

		rt ^[a]		77 K ^[b]	
	λ_{max} , nm	ϕ	τ , ns	λ_{max} , nm	τ , ns
18		1.1×10^{-3} (1.1×10^{-3})		464, 500, 540, 590	
E form (fluo)	480		<0.02;		1.3
E form (phos)					54.6×10^6
K form (fluo)	600		0.13		6.2
18'		0.7×10^{-3} (0.7×10^{-3})		460 sh, 540 sh, 590	
E form (fluo)	470		<0.02		1.1
E form (phos)					11.6×10^6
K form (fluo)	600		0.12		4.6
19					
fluo	479	0.75 (0.80)	1.89	463	1.84
phos			(1.97)	572	38.1×10^6
19'					
fluo	473	0.74 (0.82)	1.91	458	1.87
phos			(2.01)	584	17.1×10^6

^a In air-equilibrated (de-aerated) CH₃CN solution. For quantum yield determination: $\lambda_{\text{exc}} = 420$ nm for **19** and **19'**, 400 nm for **18** and **18'**. For lifetime measurements, $\lambda_{\text{exc}} = 373$ nm for **18**, **18'**, **19**, **19'**. ^b In CH₂Cl₂: CH₃OH (1:1) solution at 77 K, $\lambda_{\text{exc}} = 420$ nm. For fluorescence and phosphorescence lifetime measurements, $\lambda_{\text{exc}} = 373$ nm and 370 nm, respectively.

Table 3.10. Luminescence Properties of Complexes.

	rt ^[a]			77 K ^[b]	
	λ_{\max} , nm	ϕ	τ , ns	λ_{\max} , nm	τ , μ s
Pt ^[c]	605	4.7×10^{-3} (13.0×10^{-3})	313(920)	523	20.0
20	584	0.5×10^{-3} (3.4×10^{-3})	34.5(1310)	544	11.2
20'	578	0.4×10^{-3} (2.8×10^{-3})	30.8 (1140)	534	10.6
21	n.d.	n.d.	n.d.	466	-
				500	11.5
				600	0.6×10^3 , 3.0×10^3 (52:48)
21'	n.d.	n.d.	n.d.	464	-
				500	11.2
				594	0.9×10^3 , 3.7×10^3 (70:30)
22	n.d.	n.d. (3.5×10^{-5})	n.d.	466; 498; 562; 612	n.d.

^a In air-equilibrated (de-aerated) CH₃CN solution. For quantum yield determination: λ_{exc} = 330 nm for **20** and **20'** and 340 nm for **22**. For lifetime measurements: λ_{exc} = 331 nm for **20**, **20'**, **21** and **21'**. ^b In glassy solutions of CH₂Cl₂: CH₃OH (1:1). For lifetime measurements, λ_{exc} = 331 and 370 nm for **20**, **20'**, **21** and **21'**. ^c From Ref. 65. n.d. is not detected or weak signal.

Table 3.11. Luminescence properties of **18**, **18'**, **19** and **19'** in different solvents at rt

	TOL			DCM			MeOH		
	λ_{\max} , nm	ϕ	τ , ns	λ_{\max} , nm	ϕ	τ , ns	λ_{\max} , nm	ϕ	τ , ns
18		0.9×10^{-3}			0.7×10^{-3}			0.4×10^{-3}	
E form	464		< 0.02	478		< 0.02	466		< 0.02
K form	590		0.13	602		0.14	592		0.08
18'		0.7×10^{-3}			0.5×10^{-3}			0.3×10^{-3}	
E form	440		< 0.02	468		< 0.02	462		0.03
K form	588		0.12	596		0.13	586		0.07
19	471	0.48	1.04	477	0.71	1.65	475	0.72	1.76
19'	467	0.52	1.10	473	0.69	1.67	471	0.69	1.80

For quantum yield determination in air-equilibrated solutions, $\lambda_{\text{exc}} = 400$ nm. For lifetime measurements, $\lambda_{\text{exc}} = 407$ nm, for **18** and **18'**, $\lambda_{\text{exc}} = 373$ nm for **19** and **19'**.

Table 3.12. Luminescence properties at rt of the ligand **19** and complexes **20**, **Pt** and **22** in polystyrene film.

	λ_{\max} , nm	τ , ns
19	472	2.2
20	564	3.5×10^3
Pt	538	5.2×10^3
22	630	multiexp

3.2.2.2. Benzoxazolyl-phenolate Iridium(III) complexes

The fourth series discussed in this chapter is composed of six neutral Ir(III) phenylpyridine complexes with a benzoxazolyl-phenolate derivative as N[^]O chelating ancillary ligand. Schematic representations of such compounds are depicted in **Chart 3.4**. The six complexes differ for the substituent on the phenyl moiety of phenylpyridine unit (hydrogen in **23**, **24** and **25** and fluoride in the derivatives **23'**, **24'** and **25'**) and for the group attached on the ancillary ligand (-CH₃ in **23** and **23'**, -CN in **24** and **24'**, -NBu₂ in **25** and **25'**). Such series, unlike the other discussed above, does not comprise multinuclear systems but just monometallic heteroleptic complexes, anyway interesting for their remarkable lighting properties albeit the simple structures.

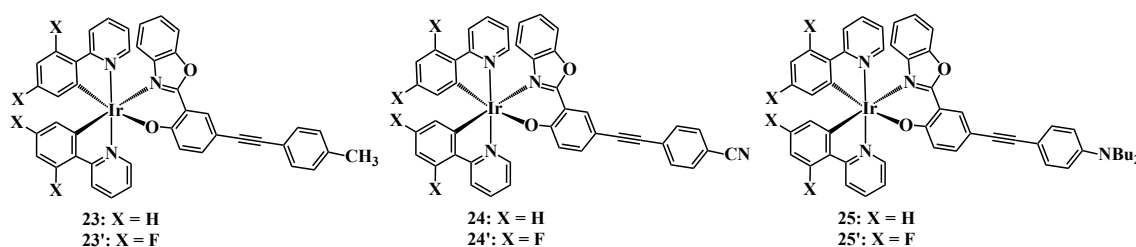


Chart 3.4. Schematic representation of the benzoxazolyl-phenolate Ir(III) complexes **23**, **24** and **25** and of their fluoride derivatives **23'**, **24'** and **25'**.

Absorption. Absorption spectra of Ir(III) heteroleptic complexes under investigation, recorded in CH₃CN solutions ($c = 1 \times 10^{-5}$ M), are collected in **Figure 3.22**, while relevant data are listed in **Table 3.13**.

The common feature for all complexes is the most intense band, already reported for the model [Ir(ppy)₃]⁶⁷ and for the Ir(III) complexes discussed above, peaking in the range between 250-260 nm ($\epsilon_{\max} \sim 5 - 6 \times 10^4 \text{ M}^{-1} \text{ cm}^{-1}$) and assigned to spin-allowed ¹LC transition, centred on the phenyl-pyridine ligands.^{67b}

In the other regions, absorption profiles of the Ir(III) compounds **23**, **24** and **25** appear very similar with respect to those of the corresponding congeners **23'**, **24'** and **25'**, respectively, revealing that no clear effect are induced by the phenyl-pyridine fluorination, while the substituent on the N[^]O ligand affects dramatically absorption features, particularly in the case of the strong electron-withdrawing -CN group, in **24** and **24'**.

The spectral region starting around 300 nm up to 360 nm is characterized by structured and intense vibronic peaks for the complexes **23**, **23'**, **25** and **25'**, attributable to singlet ligand centred (¹LC) transition involving the benzoxazolyl-phenolate unit.

For **24** and **24'**, apart from one shoulder in the low-energy side of the ppy-centred band at about 260 nm, a narrow band is clearly distinguishable at about 370 nm ($\lambda_{\max} = 371$ and 364 nm, $\epsilon_{\max} = 29900$ and 40600 $\text{M}^{-1} \text{ cm}^{-1}$, for **24** and **24'**, respectively), ascribable to ¹ π - π^* transition, localized on the N[^]O ligand with its electron-withdrawing substituent -CN, as differentiating element.

The broad and moderately intense band appearing at about 380 nm and extending up to 450-500 nm for **23**, **23'**, **25** and **25'** ($\epsilon_{\max} \sim 10^4 \text{ M}^{-1} \text{ cm}^{-1}$) originates from Ir-based spin-allowed metal-to-ligand charge transfer (¹MLCT) transitions, from Ir(III) to the cyclometalating ligand,⁷⁷ with some likely weak contribution of formally spin

forbidden triplet metal-to-ligand charge transfer ($^3\text{MLCT}$) transitions. As the presence of the heavy iridium centre results in a strong spin-orbit coupling, these singlet-to-triplet transitions become partially allowed.

Similar attribution can be done for the band that appears as a shoulder of the peak at 370 nm in **24** and **24'** absorption profiles, of comparable intensity with respect to $^1\text{MLCT}$ transitions bands observed for the other compounds.

As it can be inferred from the positions of such bands, similar for all the complexes, the changes in substitution pattern do not dramatically affect the orbitals involved in the transitions.

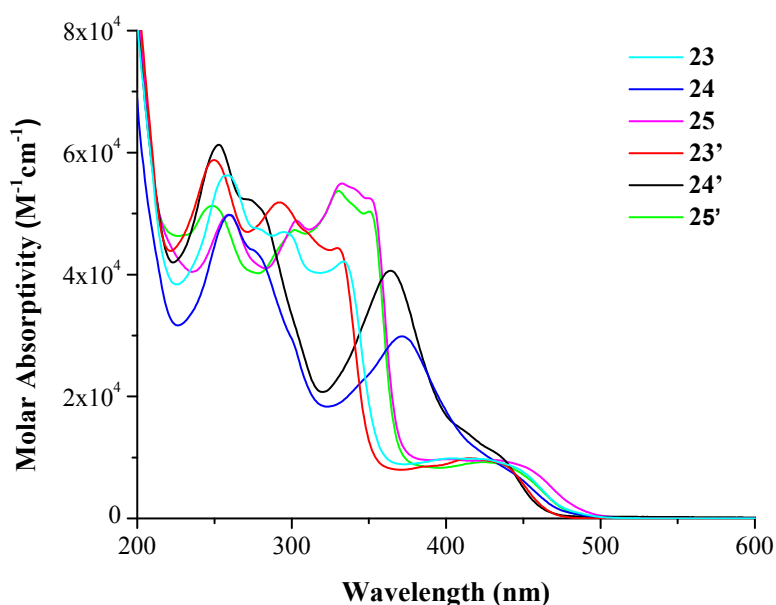


Figure 3.22. Absorption spectra at rt in CH_3CN solutions of Ir(III) complexes **23**, **23'**, **24**, **24'**, **25** and **25'**.

Emission. Emission analysis for the six compounds has been performed at room temperature in dilute CH_3CN solutions, in both air-equilibrated and air-free conditions, and at low temperature in CH_2Cl_2 : CH_3OH (1:1) glassy matrix. The recorded emission profiles are reported in **Figure 3.23** and **3.24** and the relevant data are summarized in **Table 3.14**.

From emission profiles it is possible to identify some similarities between the behaviour of the six complexes. In particular, as previously observed in absorption spectra (**Fig. 3.23**), for **25** and **25'**, complexes with the $-\text{NBu}_2$ group as substituent on the ancillary ligand, the emission profiles appear almost superimposable, with similarities in terms of both spectral shapes and wavelengths of maximum intensity of emission peaks. For the other complexes, the shapes and maxima of emission are similar inside the couples with the same cyclometallating ligand, as for **23** and **24** (in this case, the second is just slightly blue-shifted than the former of *ca.* 7 nm), and for **23'** and **24'**.

Anyway, all compounds display bright emission both at room and at low temperature. The values of PLQYs reported for the six complexes are of the same order of magnitude with respect to $[\text{Ir}(\text{ppy})_3]$ ($\phi = 0.40$)⁶⁷ (from 0.11 to 0.44 for **23**, **24**, **25**, **23'**, **24'** and **25'**, in de-aerated CH_3CN solutions).

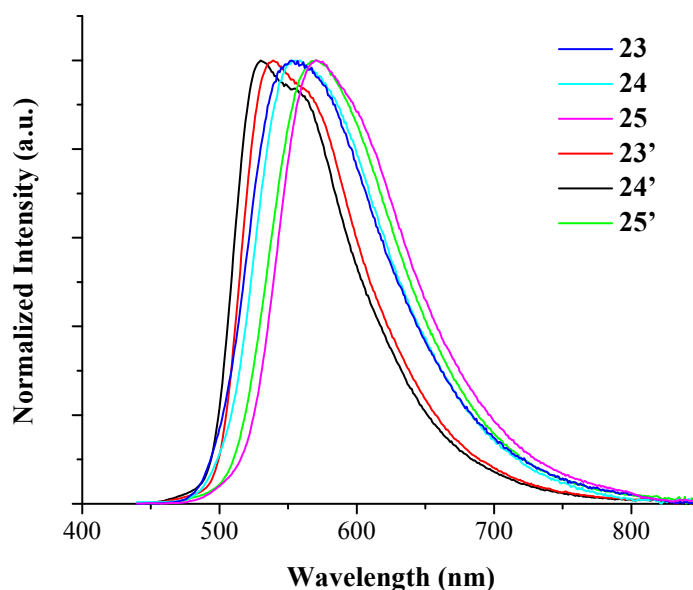


Figure 3.23. Normalized emission spectra at rt in de-aerated CH_3CN solutions of Ir(III) complexes **23**, **23'**, **24**, **24'**, **25** and **25'**.

At rt, the fluorinated derivatives **23'**, **24'** and **25'** report the highest values of lifetimes and k_r (see **Table 3.14**; $k_r = 3.5, 1.8, 1.2 \times 10^4 \text{ s}^{-1}$, respectively) and moreover, their emissions result blue-shifted with respect to those of the non-fluorinated congeners, **23**, **24** and **25**, respectively. This behavior is due to the well-known effect of HOMO level stabilization prompted by the electron-withdrawing fluoride substituent that increases the energy content of both MLCT and LC transitions.^{50,78} In glassy matrix, -NBu₂ substituted compounds **25** and **25'** display red-shifted emissions with respect to the corresponding complexes with the same cyclometallating ligand.

For all the complexes, the structured emission profiles, particularly when observed at low temperature where the fine vibronic progression is evident (see **Fig. 3.24**) (while at rt just **23'** and **24'** emission profiles appear slightly structured), account for a mixed nature of the excited state responsible for the emission, with both ligand and metal contribution (³LC/³MLCT) to the phosphorescence. Actually, the high blue shift of the profiles registered at 77 K with respect to those obtained at room temperature clearly accounts for an involvement of transitions of charge transfer character (rigidochromic effect already discussed in Chapter 2).⁶² While, as denoted by the calculated values of the radiative constants for the six compounds ($k_r = \phi/\tau$, values from 1.2 to $6.9 \times 10^4 \text{ s}^{-1}$), resulting one order of magnitude lower than those of traditional Ir(III) complexes, emitting excited state comprises an important ligand contribution. A similar mixed nature of the excited states responsible for the emission has been already reported for similar systems, further supported by TD-DFT calculation results. Such analysis has shown for the lowest triplet state, an L_AC character with a substantial amount of mixing with charge-transfer transition states of ML_CCT, L_AL_CCT, or ML_ACT nature (A= ancillary ligand; C= cyclometallating ligand).⁷⁹

To better understand the nature of excited states responsible for the emission, it is necessary to take into account, first of all, the most common orbital distribution widely reported for ppy-cyclometallated Ir(III) complexes.⁵⁰ In such systems, both the highest occupied molecular orbital (HOMO) and the lowest unoccupied molecular orbital (LUMO) are usually spread between Ir and ppy units, in particular the former over the metal unit and the anionic phenyl ring, while the latter on the neutral pyridine ring of the cyclometallating ligand.^{55,77,80,81} Furthermore, DFT calculations, performed for compounds of the form [(hydroxyphenyl-oxazole)Ir(III)(ppy)₂], similar to those under investigation, suggest the additional N[^]O chelating ligand contribution to the orbitals description. In particular, the anionic phenolate ring of the ligand seems to be involved on the HOMO description while the neutral oxazole unit contributes to the LUMO one.⁷⁹

With respect to the parent systems already reported in literature,⁷⁹ the Ir(III) compounds here discussed display bathochromic shift of their emissions as effect of the extended conjugation on the ancillary ligand. The comparison has been done with respect to the parents compounds characterized by the only oxazole unit in the N[^]O ligand ($\lambda_{\text{max}} = 500$ nm in toluene solution at rt)⁷⁹ and to those with the simple oxazole-fused phenyl unit ($\lambda_{\text{max}} = 525$ nm in toluene solution at rt)⁷⁹.

All these evaluations and comparisons with very similar systems reveal the suitability of this kind of complexes whose photophysical properties, through slight modification of the structure, can be efficiently driven in the desired direction.

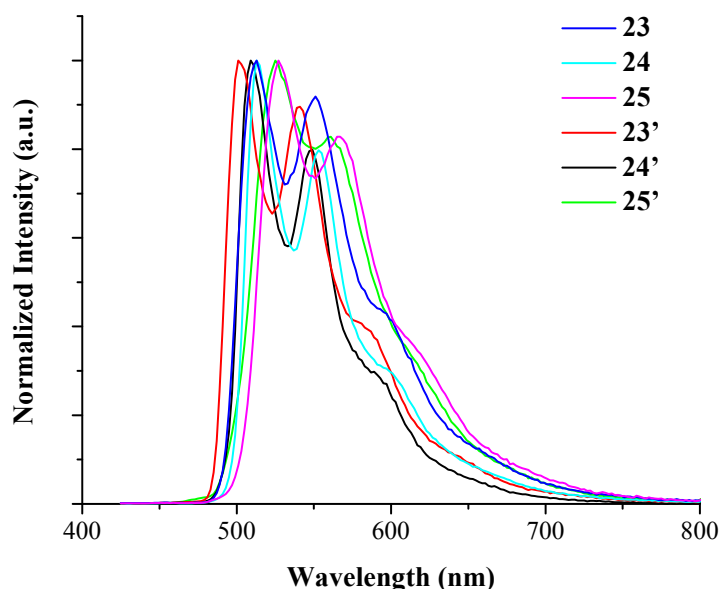


Figure 3.24. Normalized emission spectra of CH₂Cl₂: CH₃OH (1:1) glassy solutions at 77 K of Ir(III) complexes **23**, **23'**, **24**, **24'**, **25** and **25'**.

Transient absorption. Laser flash photolysis experiments have been performed to deeply investigate the nature of the excited states involved in the emission. Transient absorption spectra of the six complexes, registered in de-aerated CH₃CN solutions upon excitation at 355 nm are displayed in **Figure 3.25**.

Transient absorption spectra of the compounds with the same substituent on the ancillary ligand result composed of almost the same features, **23** and **23'**, **24** and **24'**, **25** and **25'**. The absorption profiles reported for **23** and **23'**, apart from ground-state absorption and emission bleaching, resulting in two negative peaks respectively at 310 and 540 nm, comprise two close absorption bands at 370 and 470 nm. In the low-energy side of the spectral range, another broad and intense band appears, peaking at about 780 nm and tailing in the near-infrared region. Such features result very similar to those reported for $[\text{Ir}(\text{ppy})_3]$ in CH_3CN solution,⁸² with a broad absorption band at 380 nm and another at about 900 nm, red-shifted with respect to the one reported for the discussed compounds. The differential absorption spectra registered for **25** and **25'** is composed first of all of the bleaching of the ground-state absorption, resulting as a

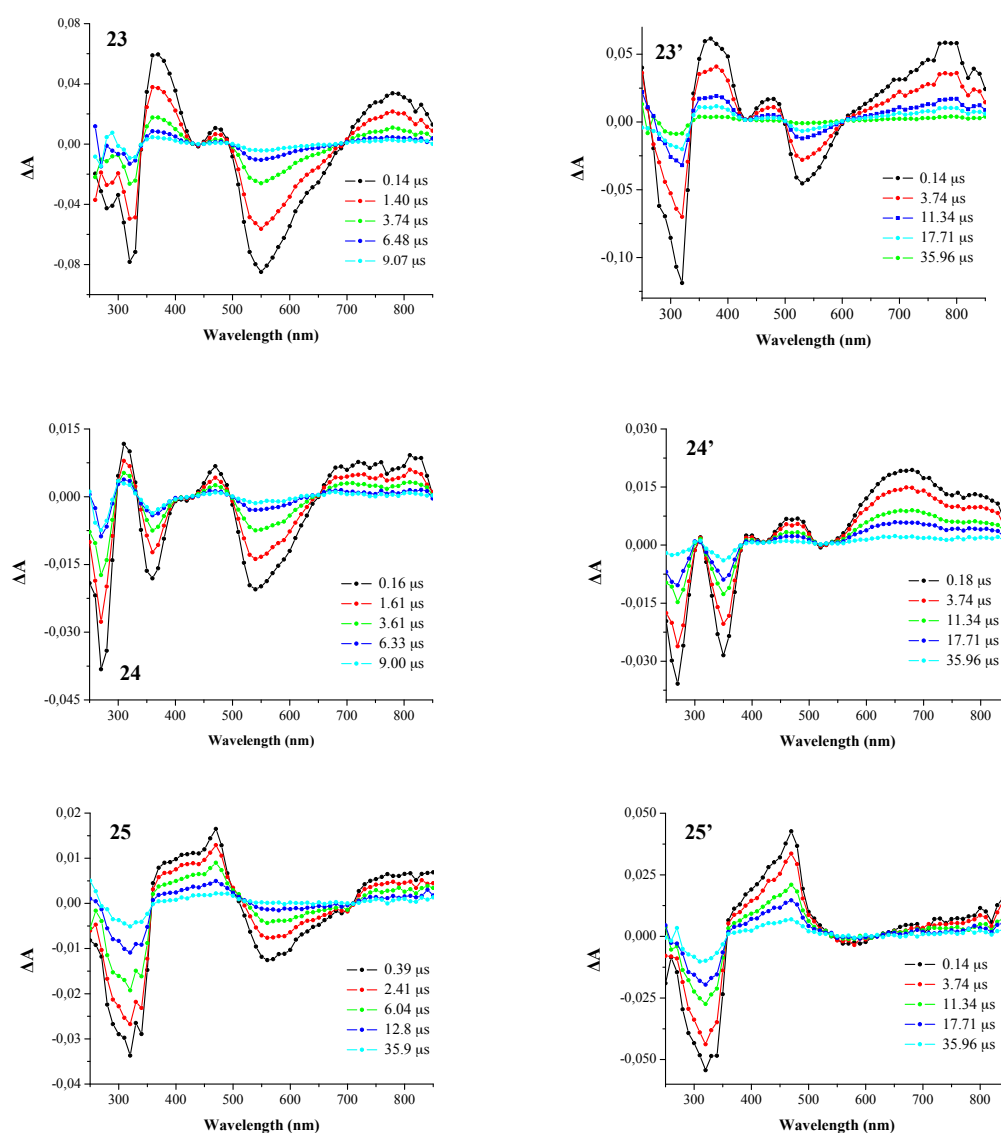


Figure 3.25. Transient absorption spectra in de-aerated CH_3CN solutions of Ir(III) complexes **23**, **23'**, **24**, **24'**, **25** and **25'**. $\lambda_{\text{exc}} = 355$ nm, $A_{355} = 0.24$, 2.1 mJ/pulse.

negative peak at 310 nm. Moving towards lower energy, a broad and intense band appears between 380 and 480 nm while around 550 nm the bleaching due to the emissions arises, with higher intensity for **25**, accordingly with its higher PLQY. For these two compounds, the particular shape of the broad highest-energy absorption bands together with the longer decay time values registered with respect to those of luminescence indicate that the absorbing excited state is not just a simple triplet state of metal-to-ligand charge transfer nature but it is the result of a wide mixing with the triplet excited state of the ligand (³LC). Probably the electron-donating ability of the substituent -NBu₂ increases the energy of MLCT state, favouring the LC state population. To confirm such evaluation, the absorption spectra of corresponding free ligands should be recorded for comparison purpose.

In **23** and **23'** excited-state absorption spectra, a pattern of three distinct absorption bands appears. They can be ascribed to the ppy radical anion, formed upon population of the MLCT state. All the bands decay with the same lifetime of 2.9 and 8.8 μs, for **23** and **23'** respectively. These values are similar to the emission excited state lifetimes (see **Table 3.14**).

The -CN substituted **24** and **24'** display similar behaviour with respect to the -Me substituted **23** and **23'**, with the only exception for the region below 400 nm. In such range **24** and **24'** do not present the absorption band around 370 nm as the congeners but a marked bleaching due to the ground-state absorption, slightly different and red-shifted with respect to that of **23** and **23'**. Thus, probably the overall transient absorption profiles would be corresponding between the two couples of complexes but the discussed band in **24** and **24'** maybe are just covered by ground-state absorption. In both cases, the profiles are consistent with ³MLCT nature transitions. The band found in all the systems around 470-480 nm, more broad and pronounced in **25** and **25'**, could be ascribed to a ³LC transition, centred in the ancillary ligand.

Table 3.13. Absorption properties of Ir(III) complexes **23-25** and **23'-25'**.

	λ_{\max} , nm (ϵ_{\max} , M ⁻¹ cm ⁻¹) ^[a]
23	259 (56300); 334 (42200); 404 (9900)
23'	250 (58800); 292 (51800); 415 (9900)
24	259 (49800); 371 (29900); 443 sh (7500)
24'	253 (61300); 364 (40600); 435 sh (10300)
25	259 (49800); 332 (54900); 429 (9600)
25'	249 (51300); 330 (53700); 425 (9200)

^a In CH₃CN solutions at rt.

Table 3.14 Luminescence properties of Ir(III) complexes **23-25** and **23'-25'**.

	rt ^[a]			77 K ^[b]	
	λ_{max} , nm	ϕ	τ , μs	λ_{max} , nm	τ , μs
23	555	0.22 (3.5×10^{-3})	3.2 (1.8×10^{-3} , 42.0×10^{-3}) ^[c]	513, 551, 600 sh	7.5
23'	537	0.44 (2.0×10^{-3})	12.7 (0.9×10^{-3} , 50.9×10^{-3}) ^[c]	502, 547, 587 sh	14.3
24	554	0.18 (2.6×10^{-3})	3.5 (1.1×10^{-3} , 40.8×10^{-3}) ^[c]	513, 553, 600 sh	0.79×10^3 , 0.19×10^3 ^[d]
24'	530	0.35 (1.0×10^{-3})	19.1 (1.7×10^{-3} , 56.5×10^{-3}) ^[c]	509, 549, 593 sh	1.32×10^3 , 0.42×10^3 ^[d]
25	568	0.19 (1.5×10^{-3})	5.8 (2.7×10^{-3} , 36.4×10^{-3}) ^[c]	527, 567 sh	13.8
25'	563	0.11 (0.8×10^{-3})	9.2 (2.0×10^{-3} , 43.5×10^{-3}) ^[c]	525, 560 sh	27.6

^a In de-aerated (air-equilibrated) CH₃CN solution. For quantum yield determination: $\lambda_{\text{exc}} = 420$ nm for all the complexes. For lifetime measurements, $\lambda_{\text{exc}} = 370$ nm for all the complexes. ^b In CH₂Cl₂: CH₃OH (1:1) glassy solution, $\lambda_{\text{exc}} = 400$ nm for all the complexes. For lifetime measurements, $\lambda_{\text{exc}} = 370$ nm for all the complexes. ^c Ratio 10:90. ^d Ratio 20:80.

3.3. Conclusions

In the present chapter, the photophysical characterization of Pt(II), Ru(II), Os(II), Ir(III) metal assemblies has been discussed. The series under investigation have been divided in two different sections, based on the distinct properties that make them interesting for distinct fields of application. In particular, the first part is centred on the presentation of two series of multimetallic compounds, displaying good properties as antenna systems for solar energy conversion, while the second part is about systems exhibiting intriguing luminescence properties, useful for their possible application in practical devices, for lighting purposes.

The first series is composed of new triptycene-based Ir-Os supramolecular assemblies **9** and **10**, with the photoactive units kept in fixed positions and in a star-shaped orientation thanks to central triptycene scaffold. They exhibit fast and efficient energy transfer processes starting from the triptycene singlet and Ir-based triplets with final population of the Os-based triplet level. Transient absorption measurements allowed us to highlight the different nature of the excited states in the Ir-containing dyads and the role of the low-lying triplet level of the triptycene scaffold.

The second series is composed of multinuclear Ir(III), Os(II) and Pt(II) arrays bearing a bridging spiro-bifluorene bis-bipyridine photoactive fragment. All individual modules

are luminescent, but in the mixed **15** and **16** complexes the phosphorescence of the Pt unit at 594 nm is quenched and exclusive emission from the Ir and the Os metal centres at 646 and 788 nm, respectively, is observed. The increase of the lifetime of the metal based emission, suggests a reservoir effect from the closely lying $^3M_{Pt}LCT$ and 3LC triplet states, resulting in a pronounced increase of the excited state lifetimes of these arrays. In the tetrad **17** the absorbed light energy is completely funnelled to the Os unit that acts as the final collector, with efficiencies higher than 99%, both at rt in the solution and at 77 K in the rigid matrix.

According to the obtained results, both the triptycene and the spiro-bifluorene frameworks can be successfully employed in the construction of efficient antenna systems, thanks to the suitable role of the organic bridge as active component in the energy cascade and as functional structural element. Moreover, the basic study performed on these architectures might be useful in the design of new light collectors in optoelectronic devices and energy conversion systems.

The third series comprises four modified julolidine ligands and the corresponding Ir(III) and Pt(II) complexes, together with a dinuclear supramolecular assemblies.

Such series results doubly interesting because both ligands **18** and **18'** and two Pt(II)-containing systems, **21** and **22**, display remarkable ability in terms of almost white-light emission. Indeed the ligands present panchromatic emission, achieved by taking direct advantage of the ESIPT effect. Similarly to them, also the julolidine-based dinuclear complex has shown white emission ability at low temperature and in powdered solution, similarly to what observed at 77 K in glassy matrix for the Pt(II) complex with the open-chain julolidine ligand. In these two cases, the white light originates from not perfectly efficient energy transfer processes to the lowest-lying (3LC) triplet excited state of the julolidine ligand. Some contribution in **21** comes from the ESIPT process occurring in its julolidine portion.

This study shows the successful combination of different strategies for emission colour modulation, achieved by simple substitution on the central frameworks in the case of the julolidine ligands, and by smart combination of active components in the metallated systems **21** and **22**. In both cases, an improvement of the obtained results can be achieved by manipulation of the frameworks through proper and simple functionalization, suggesting new approaches that can open the route to the synthesis of a new class of white light emitting systems, as promising luminescent materials in electro-optical devices for lighting (e.g. OLEDs and LECs).

The fourth series under investigation comprises six neutral Ir(III) phenylpyridine complexes with an N[^]O chelating benzoxazolyl-phenolate derivative as ancillary ligand. All complexes exhibit bright luminescence at rt, with high values of PLQYs, and at 77 K. Transient absorption measurements have been performed to clarify the different nature of the excited states and the extent of contribution of the low-lying triplet level of the benzoxazolyl-phenolate unit. This set of molecules differs from the other series reported in the present Chapter because it does not comprise rigid organic scaffold acting as bridge and no multinuclear systems appear. Anyway, the compounds are reported as good example of transition metal complexes whose photophysical properties modulation has been achieved by means of planned pattern of substitution on the main framework. In particular, such study evidenced that by substituting an hydrogen atom

with a small group (such as NBU₂, CN and Me) in the ancillary ligand, it is possible to achieve a shift of the emission from green to yellow, not affecting other properties such as the PLQY, remained around high values, and luminescence lifetimes, even higher than those of similar reported compounds.⁷⁹

The overall study explained on this chapter points out that making use of versatile ligands and proper metallic units, and starting from the knowledge and fundamental understanding of their effect on the photophysical properties, the fine-tuning of their electronic absorption, emission and excited state properties can be achieved. The innovative molecular design herein proposed, in combination with photophysical and photochemical characterization of the obtained structures, suggest that the field of transition metal complexes is not close yet and further improvement can still be achieved. Future development of luminescent transition metal complexes with better and optimized functions can enlarge their application in many different fields, such as chemo-sensing, OLEDs, OPVs and DSSCs, multi-modal imaging, diagnostics, therapy, photocatalysis, and photosensitizing for clean and renewable energy in general.

3.4. References

-
- ¹ K. Kalyanasundaram, *Coord. Chem. Rev.* 1982, **46**, 159-244.
- ² (a) K. Yamashita; S. Yamazaki-Nishida; Y. Harima; A. Segawa, *Anal. Chem.* 1991, **63**, 872-876; (b) N.E. Tokel-Takvoryan, R.E. Hemingway, A.J. Bard, *J. Am. Chem. Soc.* 1973, **95**, 6582-6589.
- ³ K. Kalyanasundaram, *Photochemistry in Microheterogeneous Systems*, Academic Press, New York, 1987.
- ⁴ (a) T. D. Tullius (Ed.), *Metal-DNA Chemistry*, ACS Symposium Series 401, American Chemical Society, Washington, DC, 1989; (b) E. Tsuchida (Ed.), *Macromolecular Complexes Dynamic Interactions and Electronic Processes*, VCH, New York, 1991.
- ⁵ (a) R. J. Watts, *J. Chem. Educ.* 1983, **60**, 834-842, and references therein; (b) J. N. Demas; B. A. DeGraff; P. B. Coleman, *Anal. Chem.* 1999, **71**, 793-800A.
- ⁶ (a) V. W. W. Yam and K. M. C. Wong, *Chem. Commun.* **2011**, 47, 11579-11592; (b) G. A. Reitz; J. N. Demas; E. Stephens; B. A. DeGraff, *J. Am. Chem. Soc.* 1988, **110**, 5051-5059; (c) E. M. Kober; J. L. Marshall; W. J. Dressick; B. P. Sullivan; J. V. Caspar; T. J. Meyer, *Inorg. Chem.* 1985, **24**, 2755-2763; (d) R. J. Watts; B. G. Griffith; J. S. Harrington, *J. Am. Chem. Soc.* 1976, **98**, 674-679.
- ⁷ (a) P. C. Ford, *Rev. Chem. Intermed.* 1979, **2**, 267-296; (b) C. Creutz; M. Chou; T. L. Netzel; M. Okimura; N. J. Sutin, *J. Am. Chem. Soc.* 1980, **102**, 1309-1319; (c) L. Sacksteder; J. N. Demas; B. A. DeGraff, *Inorg. Chem.* 1989, **28**, 1787-1792.
- ⁸ T. Bura; M. P. Gullo; B. Ventura; A. Barbieri and R. Ziessel, *Inorg. Chem.* 2013, **52**, 8653-8664.
- ⁹ M. P. Gullo; J. B. Seneclauze; B. Ventura; A. Barbieri and R. Ziessel, *Dalton Trans.* 2013, **42**, 16818-16828.
- ¹⁰ A. Nano; M. P. Gullo; B. Ventura; N. Armaroli; Andrea Barbieri, R. Ziessel, *Chem. Commun.* 2015, **51**, 3351-3354.
- ¹¹ (a) B. Albinsson; J. Martensson; *Phys. Chem. Chem. Phys.* 2010, **12**, 7338; (b) F. Barigelletti; L. Flamigni, *Chem. Soc. Rev.* 2000, **29**, 1-12.

- ¹² (a) S. Diring; F. Puntoriero; F. Nastasi; S. Campagna and R. Ziessel, *J. Am. Chem. Soc.* 2009, **131**, 6108-6110; (b) S. Diring and R. Ziessel, *Tetrahedron Lett.* 2009, **50**, 1203-1208; (c) S. Diring; R. Ziessel; F. Barigelletti; A. Barbieri and B. Ventura, *Chem. Eur. J.* 2010, **16**, 9226-9236; (d) B. Ventura; A. Barbieri; F. Barigelletti; S. Diring and R. Ziessel, *Inorg. Chem.* 2010, **49**, 8333-8346.
- ¹³ (a) J. H. Chong; M. J. MacLachlan, *Chem. Soc. Rev.* 2009, **38**, 3301-3315; (b) Y. Jiang; C. F. Chen, *Eur. J. Org. Chem.* 2011, 6377- 6403.
- ¹⁴ C. Zhang; C. F. Chen, *J. Org. Chem.* 2006, **71**, 6626-6629.
- ¹⁵ S. D. Karlen; C. E. Godinez; M. A. Garcia-Garibay, *Org. Lett.* 2006, **8**, 3417-3420.
- ¹⁶ T. Han; Q. S. Zong; C. F. Chen, *J. Org. Chem.* 2007, **72**, 3108- 3111.
- ¹⁷ C. Zhang; C. F. Chen, *J. Org. Chem.* 2007, **72**, 3880-3888.
- ¹⁸ C. Azerraf; S. Cohen; D. Gelman, *Inorg. Chem.* 2006, **45**, 7010-7017.
- ¹⁹ M. Sundermeier; A. Zapf; S. Mutyala; W. Baumann; J. Sans; S. Weiss; M. Beller, *Chem. Eur. J.* 2003, **9**, 1828-1836.
- ²⁰ H. H. Chou; H. H. Shih; C. H. Cheng, *J. Mater. Chem.* 2010, **20**, 798-805.
- ²¹ A. Beyeler; P. Belser, *Coord. Chem. Rev.* 2002, **230**, 29-39.
- ²² M. R. Wasielewski; M. P. Niemczyk; W. A. Svec; E. B. Pewitt, *J. Am. Chem. Soc.* 1985, **107**, 5562-5563.
- ²³ (a) H. E. Simmons; T. Fukunaga, *J. Am. Chem. Soc.* 1967, 5208-5215; (b) J. Sagiv; A. Yogev; J. Am. Chem. Soc. 1977, **99**, 6861-6869; (c) P. Palmieri; B. Samori, *J. Am. Chem. Soc.* 1981, **103**, 6818-6823; (d) G. Bendazzoli; A. Degli Esposti; P. Palmieri; G. Marconi; B. Samori, *J. Chem. Soc., Faraday Trans.* 1982, **78**, 1623-1631; (e) R. Gleiter; W. Schafer, *Acc. Chem. Res.* 1990, **23**, 369-375.
- ²⁴ (a) F. Rizzo; M. Cavazzini; S. Righetto; F. De Angelis; S. Fantacci; S. Quici, *Eur. J. Org. Chem.* 2010, 4004-4016; (b) X. Y. Cao; W. Zhang; H. Zi; J. Pei, *Org. Lett.* 2004, **6**, 4845-4848.
- ²⁵ (a) T. P. I. Saragi; T. Spehr; A. Siebert; T. Fuhrmann-Lieker; J. Salbeck, *Chem. Rev.* 2007, **107**, 1011-1065; (b) D. Katsis; Y. H. Geng; J. J. Ou; S. W. Culligan; A. Trajkovska; S. H. Chen; L. Rothberg, *J. Chem. Mater.* 2002, **14**, 1332-1339; (c) J. H. Park; H. C. Ko; J. H. Kim; H. Lee, *Synth. Met.* 2004, **144**, 193-199; (d) Y. H. Tseng; P. I. Shih; C. H. Chien; A. K. Dixit; C. F. Shu; Y. H. Liu; G. H. Lee, *Macromolecules* 2005, **38**, 10055-10060.
- ²⁶ D. Heredia; J. Natera; M. Gervaldo; L. Otero; F. Fungo; C. Y. Lin; K. T. Wong, *Org. Lett.* 2010, **12**, 12-15.
- ²⁷ T. Kowada; S. Yamaguchi; K. Ohe, *Org. Lett.* 2010, **12**, 296-299.
- ²⁸ B. Ventura; A. Barbieri; A. Degli Esposti; J. B. Seneclauze and R. Ziessel, *Inorg. Chem.* 2012, **51**, 2832-2840.
- ²⁹ C. J. Humphreys, *MRS Bull.* 2008, **33**, 459-470.
- ³⁰ M. H. Crawford, *IEEEJ. Sel. Top. Quantum Electron.* 2009, **15**, 1028-1040.
- ³¹ (a) C. W. Tang; S. A. Vanslyke, *Appl. Phys. Lett.* 1987, **51**, 913-915; (b) J. H. Burroughes; D. D. C. Bradley; A. R. Brown; R. N. Marks; K. Mackay; R. H. Friend; P. L. Burns; A. B. Holmes; *Nature* 1990, **347**, 539-541.
- ³² (a) T. Hu; L. He; L. Duan; Y. Qiu; *J. Mater. Chem.* 2012, **22**, 4206-4215; (b) Q. Pei; G. Yu; C. Zhang; Y. Yang; A. J. Heeger, *Science* 1995, **269**, 1086-1088; (c) K. M. Maness; R. H. Terrill; T. J. Meyer; R. W. Murray; R. M. Wightman, *J. Am. Chem. Soc.* 1996, **118**, 10609-10616.
- ³³ J. K. Lee; D. S. Yoo; E. S. Handy; M. F. Rubner, *Appl. Phys. Lett.* 1996, **69**, 1686-1688.
- ³⁴ K. M. Maness; H. Masui; R. W. Murray; R. M. Wightman, *J. Am. Chem. Soc.* 1997, **119**, 3987-3993.

- ³⁵ (a) Q. Zhao; S. Liu; F. Y. Li; T. Yi; C. H. Huang, *Dalton Trans.* 2008, 3836-3840; (b) M. Schmittl; H. W. Lin, *Inorg.Chem.* 2007, **46**, 9139-9145; (c) J. Brandel; M. Sairenji; K. Ichikawa; T. Nabeshima, *Chem. Commun.* 2010, **46**, 3958-3960.
- ³⁶ S. M. Borisov; I. Klimant, *Anal.Chem.* 2007, **79**, 7501-7509.
- ³⁷ S. Watanabe; N. Ide; J. Kido, *Jpn. J. Appl. Phys.* 2007, **46**, 1186-1188.
- ³⁸ (a) M. A. Baldo; D. F. O'Brien; M. E. Thompson; S. R. Forrest, *Phys. Rev. B.* 1999, **60**, 14422-14428; (b) M. Klessinger; J. Michl, *Excited States and Photochemistry of Organic Molecules, VCH, Weinheim*, 1995.
- ³⁹ (a) J. Kido; M. Kimura; K. Nagai, *Science* 1995, **267**, 1332-1334; (b) B. W. D'Andrade; S. R. Forrest, *Adv. Mater.* 2004, **16**, 1585-1595; (c) S. F. Service, *Science* 2006, **310**, 1762-1763; (d) F. So; J. Kido; P. Burrows, *MRS Bulletin* 2008, **33**, 663-669.
- ⁴⁰ (a) P. Coppo; M. Duati; V. N. Kozhevnikov; J. W. Hofstraat and L. De Cola, *Angew. Chem. Int. Edit.* 2005, **44**, 1806-1810; (b) A. H. Shelton; I. V. Sazanovich; J. A. Weinstein and M. D. Ward, *Chem. Commun.* 2012, **48**, 2749-2751; (c) D. Sykes; I. S. Tidmarsh; A. Barbieri; I. V. Sazanovich; J. A. Weinstein and M. D. Ward, *Inorg. Chem.* 2011, **50**, 11323-11339.
- ⁴¹ S. Park, J. E. Kwon, S. H. Kim, J. Seo, K. Chung, S. Y. Park, D. J. Jang, B. M. Medina and J. Gierschner, *J. Am. Chem. Soc.* 2009, **131**, 14043-14049.
- ⁴² J. E. Kwon and S. Y. Park, *Adv. Mater.* 2011, **23**, 3615-3642.
- ⁴³ H. J. Bolink; F. De Angelis; E. Baranoff; C. Klein; S. Fantacci; E. Coronado; M. Sessolo; K. Kalyanasundaram; M. Gratzel and M. K. Nazeeruddin, *Chem. Commun.* 2009, 4672-4674.
- ⁴⁴ (a) J. Kalinowski; M. Cocchi; D. Virgili; V. Fattori and J. A. G. Williams, *Adv. Mater.* 2007, **19**, 4000-4005; (b) E. L. Williams; K. Haavisto; J. Li and G. E. Jabbour, *Adv. Mater.* 2007, **19**, 197-202; (c) W. Mroz; C. Botta; U. Giovanella; E. Rossi; A. Colombo; C. Dragonetti; D. Roberto; R. Ugo; A. Valore and J. A. G. Williams, *J. Mater. Chem.* 2011, **21**, 8653-8661.
- ⁴⁵ (a) A. C. Benniston; S. Clift and A. Harriman, *J. Mol. Struct.* 2011, **985**, 346-354; (b) A. Nano; R. Ziessel; P. Stachelek and A. Harriman, *Chem. Eur. J.* 2013, **19**, 13528-13537.
- ⁴⁶ K. H. Lee; Y. K. Kim and S. S. Yoon, *Bull. Korean Chem. Soc.* 2012, **33**, 3433-3436.
- ⁴⁷ A. Nano; R. Ziessel; P. Stachelek; M. A. H. Alamiry and A. Harriman, *ChemPhysChem* 2014, **15**, 177-186.
- ⁴⁸ A. B. Tamayo; B. D. Alleyne; P. I. Djurovich; S. Lamansky; I. Tsyba; N. N. Ho; R. Bau; M. E. Thompson, *J. Am. Chem. Soc.* 2003, **125**, 7377-7387.
- ⁴⁹ (a) T.H. Kwon; H. S. Cho; J. W. Kim; J. J. Kim; H. H. Lee; S. J. Park; I. S. Shin; H. Kim; D. M. Shin; Y. K. Chung; J. I. Hong, *Organometallics* 2005, **24**, 1578-1585; (b) S. Kappaun; S. Sax; S. Eder; K. C. Möller; K. Waich; F. Niedermaier; R. Saf; K. Mereiter; J. Jacob; K. Müllen; E. J. W. List; C. Slugovc, *Chem. Mater.* 2007, **19**, 1209-1211; (c) Y. You; S. Y. Park, *J. Am. Chem. Soc.* 2005, **127**, 12438-12439; (d) Y. You; K. S. Kim; T. K. Ahn; D. Kim; S. Y. Park, *J. Phys. Chem. C* 2007, **111**, 4052-4060.
- ⁵⁰ L. Flamigni; A. Barbieri; C. Sabatini; B. Ventura; F. Barigelletti, *Top. Curr. Chem.* 2007, **281**, 143-203.
- ⁵¹ M. Montalti; A. Credi; L. Prodi; M. T. Gandolfi, *Handbook of Photochemistry*, 3rd ed.; CRC Press, Taylor & Francis: Boca Raton, 2006.
- ⁵² R. D. Costa; F. Monti; G. Accorsi; A. Barbieri; H. J. Bolink; E. Orti; N. Armaroli, *Inorg. Chem.* 2011, **50**, 7229-7238.
- ⁵³ B. Ventura; A. Barbieri; F. Barigelletti; J. B. Seneclauze; P. Retailleau; R. Ziessel, *Inorg. Chem.* 2008, **47**, 7048-7058.
- ⁵⁴ B. Ventura; A. Barbieri; A. Degli Esposti; J. B. Seneclauze; R. Ziessel, *Inorg. Chem.* 2012, **51**, 2832-2840.

- ⁵⁵ R. D. Costa; E. Orti; H. J. Bolink; F. Monti; G. Accorsi; N. Armaroli, *Angew. Chem., Int. Ed.* 2012, **51**, 8178-8211.
- ⁵⁶ D. Kumaresan; K. Shankar; S. Vaidya; R. H. Schmehl, *Top. Curr. Chem.* 2007, **281**, 101-142.
- ⁵⁷ E. M. Kober; J. V. Caspar; R. S. Lumpkin; T. J. Meyer, *J. Phys. Chem.* 1986, **90**, 3722-3734.
- ⁵⁸ X. Y. Wang; R. N. Prabhu; R. H. Schmehl; M. Weck, *Macromolecules* 2006, **39**, 3140-3146.
- ⁵⁹ Y. Jahng and A. Rahman, *Bull. Chem. Soc. Jpn.* 2010, **83**, 672-677.
- ⁶⁰ R. Ziessel; J. B. Seneclauze; B. Ventura; A. Barbieri and F. Barigelletti, *Dalton Trans.* 2008, 1686-1688.
- ⁶¹ J. A. G. Williams, *Top. Curr. Chem.* 2007, **281**, 205-268.
- ⁶² A. Damas; B. Ventura; J. Moussa; A. Degli Esposti; L. M. Chamoreau; A. Barbieri and H. Amouri, *Inorg. Chem.* 2012, **51**, 1739-1750.
- ⁶³ K. D. Glusac; S. J. Jiang and K. S. Schanze, *Chem. Commun.* 2002, 2504-2505.
- ⁶⁴ N. D. McClenaghan; Y. Leydet; B. Maubert; M. T. Indelli and S. Campagna, *Coord. Chem. Rev.* 2005, **249**, 1336-1350.
- ⁶⁵ (a) B. Ventura; A. Barbieri, A.; Zanelli, A.; Barigelletti, F.; Seneclauze, J. B.; Diring, S.; Ziessel, R. *Inorg. Chem.* 2009, **48**, 6409-6416.
- ⁶⁶ K. Benelhadj; J. Massue; P. Retailleau; G. Ulrich; R. Ziessel, *Org. Lett.* 2013, **15**, 2918-2921.
- ⁶⁷ (a) K. A. King; P. J. Spellane; R. J. Watts, *J. Am. Chem. Soc.* 1985, **107**, 1431-1432; (b) M. G. Colombo; T. C. Brunold; T. Riedener; H. U. Gudel; M. Fortsch; H. B. Burgi, *Inorg. Chem.* 1994, **33**, 545-550; (c) S. Sprouse; K. A. King; P. J. Spellane; R. J. Watts, *J. Am. Chem. Soc.* 1984, **106**, 6647-6653.
- ⁶⁸ (a) Vivian Wing-Wah Yam, Keith Man-Chung Wong, and Nianyong Zhu, *Angew. Chem. Int. Ed.* 2003, **42**, 1400-1403; (b) Ventura, B.; Barbieri, A.; Barigelletti, F.; Seneclauze, J. B.; Retailleau, P.; Ziessel, R. *Inorg. Chem.* 2008, **47**, 7048-7058.
- ⁶⁹ J. Massue; D. Frath; G. Ulrich; P. Retailleau and R. Ziessel, *Org. Lett.* 2012, **14**, 230-233.
- ⁷⁰ R. Ziessel; A. Nano; E. Heyer; T. Bura; P. Retailleau, *Chem. Eur. J.* 2013, **19**, 2582-2588.
- ⁷¹ J. R. Lakowicz, *Principles of Fluorescence Spectroscopy*, 3rd ed., *Springer*, New York, USA, 2006.
- ⁷² J. E. Kwon and S. Y. Park, *Adv. Mater.* 2011, **23**, 3615-3642.
- ⁷³ K. Skonieczny; A. I. Ciuciu; E. M. Nichols; V. Hugues; M. Blanchard-Desce; L. Flamigni; D. T. Gryko, *J. Mater. Chem.* 2012, **22**, 20649-20664.
- ⁷⁴ A. I. Ciuciu; L. Flamigni; K. Skonieczny; D. T. Gryko, *Phys. Chem. Chem. Phys.* 2013, **15**, 16907-16916;
- ⁷⁵ A. I. Ciuciu; K. Skonieczny; D. Koszelewski; D. T. Gryko and L. Flamigni, *J. Phys. Chem. C* 2013, **117**, 791-803.
- ⁷⁶ S. Park; J. E. Kwon; S. H. Kim; J. Seo; K. Chung; S. Y. Park; D. J. Jang; B. M. Medina and J. Gierschner, *J. Am. Chem. Soc.* 2009, **131**, 14043-14049.
- ⁷⁷ A. P. Wilde; K. A. King and R. J. Watts, *J. Phys. Chem.* 1991, **95**, 629-634.
- ⁷⁸ (a) A. B. Tamayo; B. D. Alleyne; P. I. Djurovich; S. Lamansky; I. Tsyba; N. N. Ho; R. Bau; M. E. Thompson, *J. Am. Chem. Soc.* 2003, **125**, 7377-7387; (b) V. V. Grushin; N. Herron; D. D. LeCloux; W. J. Marshall; V. A. Petrov; Y. Wang, *Chem. Commun.* 2001, 1494-1495; (c) R. Ragni; E. A. Plummer; K. Brunner; J. W. Hofstraat; F. Babudri; G. M. Farinola; F. Naso; L. De Cola, *J. Mater. Chem.* 2006, **16**, 1161-1170.
- ⁷⁹ Y. You; J. Seo; S. H. Kim; K. S. Kim; T. K. Ahn; D. Kim and S. Y. d, *Inorg. Chem.* 2008, **47**, 1476-1487.
- ⁸⁰ J. Li; P. I. Djurovich; B. D. Alleyne; M. Yousufuddin; N. N. Ho; J. C. Thomas; J. C. Peters; R. Bau; M. E. Thompson, *Inorg. Chem.* 2005, **44**, 1713-1727.

⁸¹ (a) M. G. Colombo; H. U. Gudel, *Inorg. Chem.* 1933, **32**, 3081-3087; (b) F. M. Hwang; H. Y. Chen; P. S. Chen; C. S. Liu; Y. Chi; C. F. Shu; F. I. Wu; P. T. Chou; S. M. Peng; G. H. Lee, *Inorg. Chem.* 2005, **44**, 1344-1353.

⁸² K. Ichimura; T. Kobayashi; K. A. King and R. J. Watts, *J. Phys. Chem.* 1987, **91**, 6104-6106.

Chapter 4

4. Self-organizing corroles as novel structural platform for the artificial photosynthesis

The class of tetrapyrrolic-based materials has attracted much attention during the time since the main chromophoric components of photosynthetic light-harvesting (LH) antennas and reaction centres (RC) in nature are just porphyrinoid systems with the main example of the photosynthetically active chlorophylls (Chls).

By the development of new synthetic strategies for manipulation of these frameworks, the easy functionalization of their aromatic platform made possible to drive their properties in the desired direction, conferring amphiphilic character by decoration with polar groups, or extending the electronic delocalization by appending non polar aromatic substituents. Thus, this class of macrocycles has become suitable as example of tunable scaffolds, finding applications in several fields, such as catalysis,¹ sensing,² as photosensitizers in photodynamic therapy³ and especially in dye-sensitized solar cells.⁴

Many semi-synthetic porphyrinoids have been employed as result of bio-inspired molecular mimicking, mostly based on the chlorine core.⁵ In particular, porphyrins have attracted significant interest due to the relatively simple preparation, possibility of structural modifications and suitable photophysical properties^{6,7} but now the class of the corresponding structural analogues corroles, represents the new frontier. The relatively few information about this class of compounds is probably due to the complicated preparation but fortunately in the past decade efficient synthetic procedures⁸ and good methods for peripheral substitution allowed exploitation of the potential applications of such tetrapyrrolic derivatives in several fields (*i.e.* catalysis, sensing or medicine).^{9,10} Actually, the rich coordination chemistry they revealed makes them formidable competitors¹¹ to the porphyrins.

4.1. Introduction

4.1.1. Corroles

The principal difference between corroles and porphyrins (see **Chart 4.1**) is the more condensed central core for the formers, with three protonated and one free nitrogen atoms in the free-base form (Fb). This structural difference is responsible for the lower symmetry and for the higher π electron-richness of the corroles, which in spite of the improvement induced to the chromophoric properties is responsible for the higher sensitivity toward degradation, as effect of the enhanced interaction with light and oxygen.¹² Moreover, similarly to porphyrins, the three *meso*-carbon atoms of the bridges between the pyrrolic units are very reactive. In fact to stabilize corroles, a strategy has been adopted, based on the functionalization of the central core with electron-withdrawing substituents¹³ and on the preparation of *meso*-substituted derivatives, much more stable and robust.

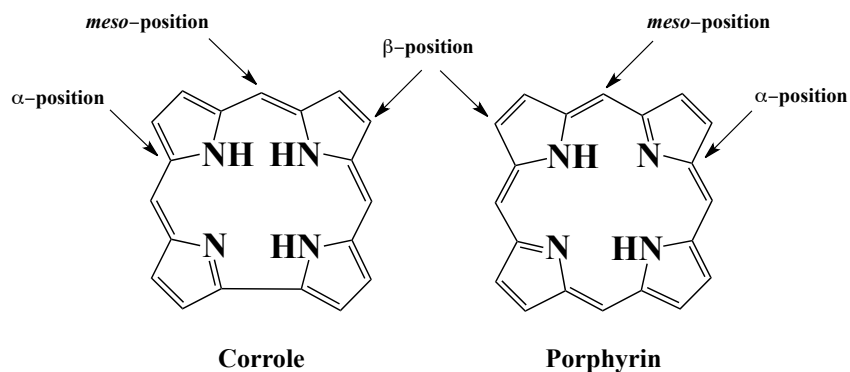


Chart 4.1. Chemical structures of unsubstituted free-base corrole (left) and porphyrin (right).

From a photophysical point of view, the main differences between corroles and porphyrins, mostly due to the structural differences discussed above, appear both in the fluorescence of the respective Fb forms, generally more intense for corroles than for porphyrins or other related macrocycles, and in the Q-bands absorption coefficients, in the visible region of the spectrum, also higher than for porphyrins.

Thus, it is important to deeply understand the structure features of such compounds, since they are the main responsible for both reactivity and photophysical properties. For instance, the high NH acidity of corroles can be explained just with structural considerations, taking into account the perpendicular position of the most acidic NH proton with respect to its own pyrrolic ring. Such proton is that of the ring linked directly to its neighbour pyrrole, rather than through the carbon bridge. Since upon release of such proton, steric relaxations stabilize the overall systems, deprotonation is highly favoured.

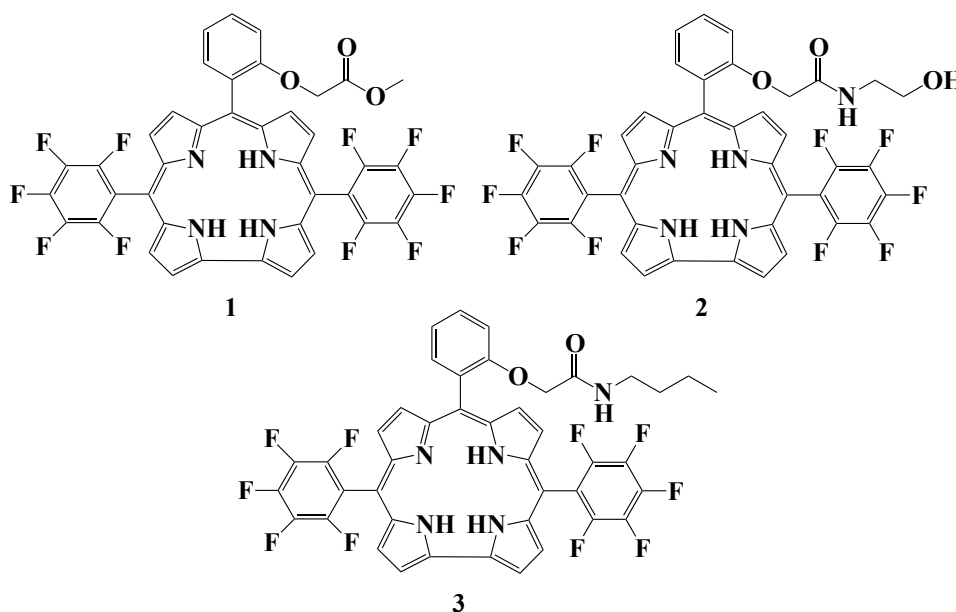


Chart 4.2. Molecular structures of free-base *trans*-A₂B-corroles **1**, **2** and **3**.

Reported X-ray analysis of corroles revealed a strong distortion from planarity for the macrocycle, displaying pyrrole rings in alternated positions, above and below the plane formed by the four nitrogen atoms; just one NH proton is coplanar.¹⁴ This kind of arrangement is imposed by steric hindrance matters between the three NH protons of the core.

Since by proper functionalization of the periphery it is possible to twist the structure, in view of potential applications, fine-tuning and optimization of certain corrole properties can be easily achieved by simple synthetic “interventions” on their framework.

In this Chapter a series of corroles is introduced (see **Chart 4.2**), whose structure decoration has produced particular modifications on photophysical behaviour.

Such investigation ascertained the effectiveness of programmed substitution pattern towards the promotion of self-organization for these molecules. The shown results propose these series of corroles as promising models of biomimetic photosensitizers in molecular devices, as valid alternative in exploiting sunlight to the most common porphyrins.

4.1.2. Self-assembly

The development of strategies to prompt the arrangement of functional heterocyclic chromophores such as corroles and porphyrins into highly ordered self-assembled arrays, is still a current research topic. It has grown in attempt to mimic natural hydrogen-bond-based self-assembly, occurring in photosynthetic organisms, due to the high efficiency that photosynthesis achieves by means of the excitonic delocalization along the large self-organized system.

Natural Chl pigments in photosynthetic systems form J-type self-aggregates and are the main responsible for ultrafast and efficient energy transfer of harvested photons towards the reaction centre. These molecules are magnesium chlorin complexes in which both central atom and peripheral substituents (hydroxyl and carbonyl groups) are involved in the self-aggregation, performed through three types of interaction: hydrogen bonding ($\text{OH}\cdots\text{O}=\text{C}$), coordination between Mg and OH ($\text{Mg}\cdots\text{OH}$) and π - π stacking among the aromatic portions.

However, since overall natural structures are complicated and of difficult reproduction through the traditional synthetic strategies (for instance, Chls are embedded in protein envelopes in many photosynthetic apparatus), simplified models and approach are required to mimic natural assemblies.

Actually self-assembly, inducing intriguing photophysical properties, can be widely adopted in the effort for fabrication of organic functional molecular nanostructures¹⁵ and stimulates a wide range of possible applications. It represents a useful method to organize large number of molecules, by using simpler approach with respect to covalent bonding. Actually, even if this last direction offers many possible strategies for the fabrication of artificial photosynthetic units, it is not always feasible in practice or could require several difficult reaction steps and sometimes, hard reaction conditions, too. Instead, self-assembly has been observed in nature as a spontaneous process, in general prompted mainly by non-covalent interactions, such as hydrogen, electrostatic and van der Waals bonding, π - π stacking, metal-ligand coordination and hydrophobic interactions, thus more easily achievable.

Porphyrins have shown to be particularly attractive building blocks in this kind of process because the favoured packing of their aromatic portions can result in enhanced

photophysical and photochemical performances, important from a technological point of view. Thus their self-organization has been widely studied in the past.

Now, in attempt to identify novel structural platform for the solar energy conversion, corroles able to perform self-organization could be good candidates. To the best of our knowledge, self-organizing corroles were not reported to date, apart from one example¹⁶ in which anyway, spectroscopic data in solution are not supported by X-ray analysis. In this Chapter a good result in such a field is discussed.

Self-aggregating corroles under analysis have been synthesized by Professor D. Gryko. He designed three *trans*-A₂B-corroles decorated with ester and amide carbonylic groups as active units toward hydrogen-bond, in order to promote self-assembly by non-covalent interactions. And similarly to porphyrins,¹⁷ also these corroles validate such approach.

Absorption, emission and aggregation properties of such compounds, whose schematic structures are depicted in **Chart 4.2**, have been investigated and presented below. They are corroles substitutes in the meso-positions with two pentafluoro-phenyl rings and one phenyl unit, linked to distinct chains for the different compounds. In particular, compound **1** is composed of an ester group in the *meso*-aryl unit, while **2** and **3** present an amide group linked to an alkyl chain, hydroxyl ending in compound **2**.

4.2. Results and Discussion

4.2.1. Absorption

UV-Vis absorption analysis has been performed at room temperature in dilute solutions of many solvents [$c = 8.5 \times 10^{-6}$ M in dichloromethane (DCM), acetonitrile (ACN), methanol (MeOH) and toluene (TOL) solutions] for the three corroles and related details are gathered in **Table 4.1**.

In general, absorption features of corroles are defined by means of Gouterman's four-orbital model,¹⁸ that describes the visible and near-UV absorption of tetrapyrrolic compounds as characterized by two sets of transitions between the two highest occupied (HOMOs) and the two lowest unoccupied (LUMOs) molecular orbitals, within the macrocyclic ring. According to such vision, two main kinds of bands compose the overall absorption spectrum of the three corroles.

The intense band appearing at high energy, at about 410 nm, is denoted as Soret-type transition, and those at lower energy, in the range between 500 and 700 nm, as Q-type transitions. This attribution is performed by analogy to porphyrins, since corroles are basically porphyrins contracted by one *meso*-carbon and have similar 18-electron π system. In fact, absorption spectra of corroles are characterized by intense spin-allowed π - π^* transitions similarly to those of porphyrins.

The molar extinction coefficient values obtained in the several solvents for both the bands are in agreement with those already reported in the literature for similar systems ($\lambda_{\max} = 406\text{-}417$ nm $\epsilon_{\max} = 1.1\text{-}1.4 \times 10^5$ M⁻¹cm⁻¹ for the B bands and $\lambda_{\max} = 559\text{-}570$ nm $\epsilon_{\max} = 1.6\text{-}2.3 \times 10^4$ M⁻¹cm⁻¹ for the first Q band).¹⁹

By comparing absorption profiles registered in different medium (see **Fig 4.1**), both extinction coefficients and wavelengths of maximum absorption appear to be not dramatically affected by changes in solvent polarity and just little differences can be observed for the two envelops of bands. First of all, it is clearly visible that in every solvent, absorption intensity of compound **3** is the lowest.

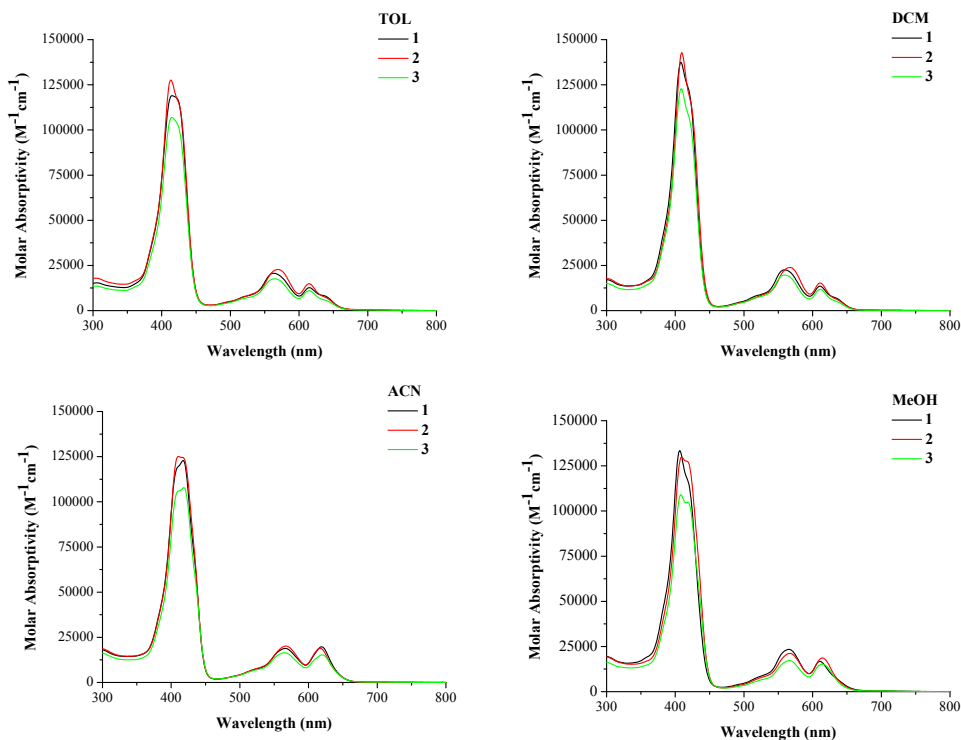


Figure 4.1. Absorption spectra of corroles **1**, **2** and **3** in toluene (top, left), CH₂Cl₂ (top, right), CH₃CN (bottom, left) and CH₃OH (bottom, right) solutions at rt

Another observation is related to the shapes of absorption bands, in particular the top of absorption peak in the high-energy region appears more flat in acetonitrile solution than in the other solvents, where instead it stretches out towards the blue region. Such non-symmetric shape can be translated as a small splitting of the Soret band, resulting in a sort of weak long wavelength shoulder on the low energy side of the main peak, as already observed in other corroles with bulky group in the *meso* positions, due to further distortion from planarity.²⁰

The two Q bands in the low energy region of the spectral range show almost equal intensity in acetonitrile unlike the other solvents, in which instead the peak at longer wavelength appears less intense than the other. In toluene and dichloromethane these two Q bands become almost three because of the appearance of a shoulder in the low energy side. Anyway all such reported differences are of very low extent if compared with the expectations produced on the basis of literature data.²¹

The shapes of both bands are usually dependent on the substitution pattern of the macrocycle that affects energy and extinction coefficient of the two related bands.²² But for the compounds under investigation, the presence of different groups in the *meso*-aryl unit does not result in different effects on the absorption profiles because such substituents probably induce similar modifications to the macrocycles symmetry. Just

for longest chain substituted corrole **3**, the B band, less intense than for **1** and **2**, seems to be more flat at the top, indicating a less pronounced domination of one tautomer to the other. NH tautomerization is widely reported for corroles, where the inner NH proton migrates around the ring (see **Chart 4.3**).²³ In absorption for corroles **1**, **2** and **3** the contributions of the two forms is not completely distinguishable because of the strong overlap of their absorption spectra, but usually the shorter-wavelength component in the Soret band is ascribed to tautomer T2 while the longer-wavelength to tautomer T1.

The same criterion can be applied for the Q bands: in the present case, the one around 611-620 nm is attributed to T2 and the shoulder tailing over 650 nm to T1. Such attribution is made according to a careful assignment already reported.²³

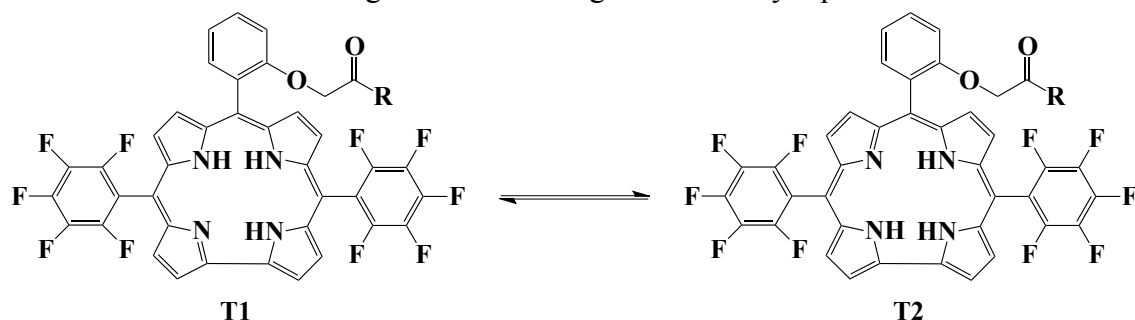


Chart 4.3. Equilibrium between two corrole NH tautomers (T1 and T2 are assigned in agreement with Ref. 23)

4.2.2. Emission at Room Temperature

Emission spectra have been recorded for air-equilibrated dichloromethane, acetonitrile, methanol and toluene solutions of corroles **1**, **2** and **3** at room temperature; de-aerated toluene solutions have been analyzed at room temperature. Resulting photophysical parameters are collected in **Table 4.2**.

Emission spectra of optically matched solutions of the three corroles are reported in **Fig. 4.2** in air-free toluene solutions at room temperature, upon excitation at 560 nm. In such condition, lifetimes and luminescence quantum yields result just slightly increased with respect to those obtained in aerated solution ($\phi \sim 0.15$ and $\tau \sim 4$ ns in air, $\phi \sim 0.16$ and τ

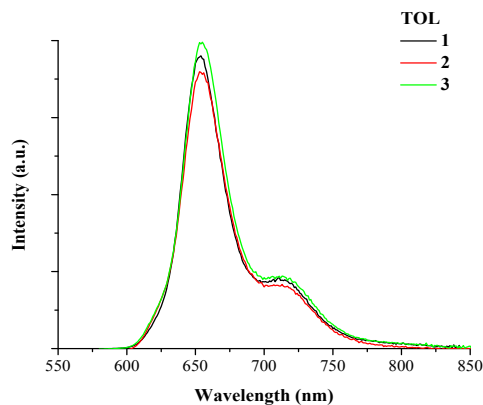


Figure 4.2. Emission spectra of corroles **1**, **2** and **3** in de-aerated toluene solutions at rt; $\lambda_{\text{exc}} = 560$ nm.

~ 5.5 ns in air-free solutions; for details see **Table 4.2**).

In the remaining solvents, the registered emission profiles result perfectly superimposable to those in toluene, indicating for all corroles a solvent independent emission behavior at room temperature. All emission curves display intense and structured profiles, composed of one peak at about 650 nm with a shoulder at longer wavelengths as result of the vibronic progression, and lifetimes between 3.7 and 4.3 ns in all the investigated solvents. Just luminescence quantum yields follow a different trend, going from a value of 0.13 in methanol to 0.15 in toluene. This effect does not seem to be directly related to solvent polarity, because the results achieved in the very polar acetonitrile solutions are similar to those in toluene. Thus, the lowest PLQY obtained in methanolic solutions might be attributed to intermolecular hydrogen bond occurring between solvent hydroxyl group and corrole core NH. This interaction increases k_{nr} through introduction of further deactivation pathways, related to the induced distortion, and thus results in a lowering of fluorescence quantum yield but without affecting the lifetime too.

As already observed in absorption spectra (**Fig. 4.1**), the different substituents in the *meso*-phenyl ring on the macrocycle core do not produce distinct effects on luminescence properties, at least at room temperature. Actually, despite substituents changing, emission profiles (**Fig. 4.2**) together with relevant photophysical parameters (**Table 4.2**) account for almost constant energy level of the emitting state and active macrocycle orbitals nearly unaffected.

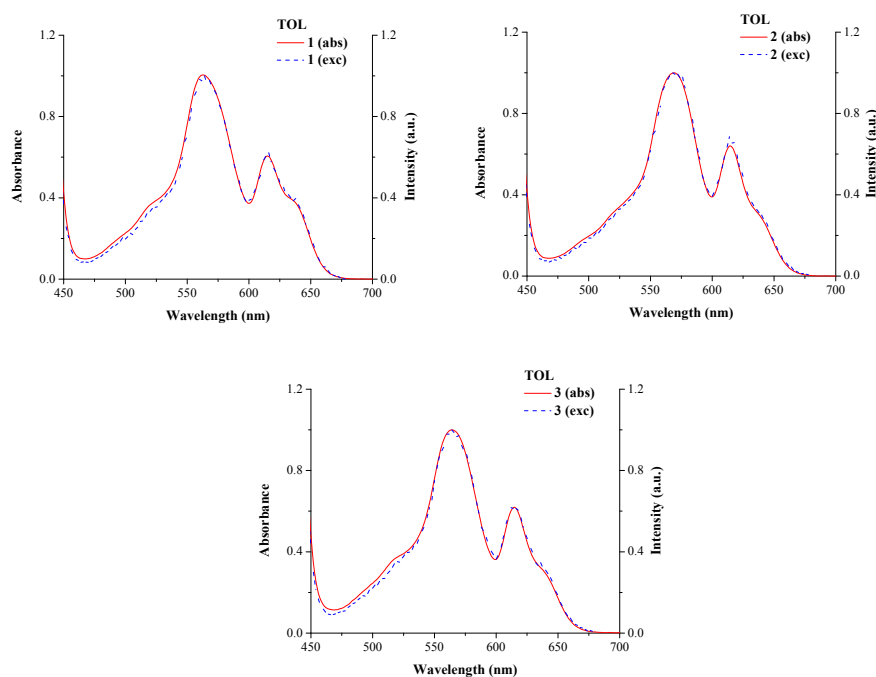


Figure 4.3. Arbitrarily scaled absorption (full line) and excitation (dotted line) spectra of corroles **1**, **2** (top) and **3** (bottom) in toluene solution at rt; $\lambda_{em} = 700$ nm.

On the basis of the above discussion, as well as by comparison with corresponding literature data, the emission can be safely ascribed to the lowest-lying singlet π - π^*

excited state centred on the corrole core, in every solvent and for all compounds, without evident contribution of charge transfer nature.

Moreover, **Fig. 4.3** reports as an example excitation and absorption spectra of compounds **1**, **2** and **3** in toluene solution, showing the perfect superimposition of the two profiles.

It confirms that emission originates just from the species detected in absorption. In particular, tautomer T1 is the main responsible for such emission thanks to an efficient thermal re-population of its emitting S_1 state (for a more detailed discussion see below).

4.2.3 Emission at low temperature and solvent effect

Emission spectra of corroles **1**, **2** and **3** have been recorded at 77 K in CH_2Cl_2 , CH_3CN , CH_3OH , toluene and mixed CH_2Cl_2 : CH_3OH (1:1) glassy solutions, upon excitation at 560 nm. The related photophysical results are summarized in **Table 4.3** while **Fig. 4.4** collects the emission profiles obtained in frozen CH_2Cl_2 : CH_3OH (1:1) solutions.

If at room temperature the behavior of the investigated compounds seems quite homogeneous, at 77 K instead it appears very tangled and of tricky interpretation, due to a clear influence of both *meso*-phenyl substituent and solvent.

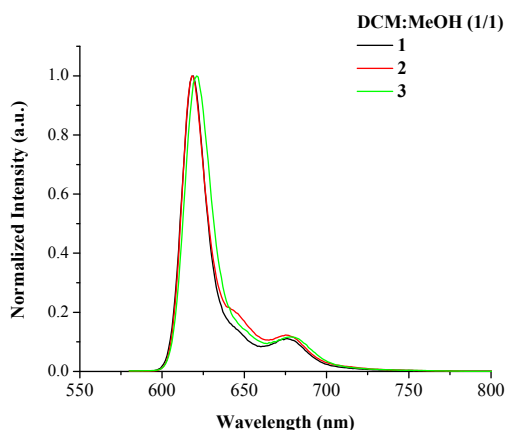


Figure 4.4. Emission spectra of corroles **1**, **2** and **3** in CH_2Cl_2 : CH_3OH (1:1) glassy solutions at 77 K; $\lambda_{\text{exc}} = 560$ nm.

A first simplifying key for explaining the nature of such spectra is given by the well-known phenomenon of NH tautomerization, already introduced in the absorption discussion above. It occurs in free-base (Fb) porphyrins and corroles but it is prominent in the latter where a lower symmetry induces structurally and electronically differences in the tautomers, making them distinguishable already at room temperature in some cases.

In the investigated compounds, at room temperature, just a very slight hump in the high-energy side of the principle emission peak can be seen as result of such phenomenon. It is not particularly evident, indicating that the fluorescence spectrum for each corrole originates only from the main emission of the tautomer T1. The preferential population of its S_1 emitting state occurs not only by its direct excitation but also as result of the efficient conversion of T2 to T1 in the excited state.²³

At 77 K, what at rt appeared just like a hump, results instead as clear peak, even more intense than the other one, in some cases. In particular, for CH₂Cl₂: CH₃OH (1:1) and pure methanol solutions, the T2 emission from S₁→S₀ transition results dominating for all corroles, with maximum of emission moved in the range 616-621 nm, as shown in **Fig. 4.4** for mixed matrixes (CH₃OH solution emissions are slightly blue-shifted). The shoulder arising at around 670-680 nm is a vibrational satellite of the former, coming from the sum of several vibrational modes.

After this discussion, it is clear that the blue shift of the emission maxima obtained at 77 K is not ascribable, as in the metallic systems previously discussed (Chapter 2 and 3), to rigidochromic effect of the solvent but rather to changes in the ratio between the two tautomeric species present in the excited state, as observed for several Fb-corroles.²⁴

For the compound **2** in both CH₂Cl₂: CH₃OH (1:1) and CH₃OH glassy solutions, an additional shoulder appears around 650 nm between the other two peaks and it becomes more pronounced by changing the excitation wavelength from 560 nm to 440 nm. In this condition, such band appears also in the emission profiles of the corroles **1** and **3**, accounting for the presence of an additional emitting species, such as T1, and probably with slightly higher absorption at 440 nm than 560 nm. The spectra obtained for **1**, **2** and **3** upon excitation at 440 nm are reported in **Fig. 4.5**. In **Fig. 4.6** excitation spectra registered in CH₂Cl₂: CH₃OH (1:1) at the preferential emission wavelength of T2 ($\lambda_{em} = 620$ nm) are shown for the range of the B bands.

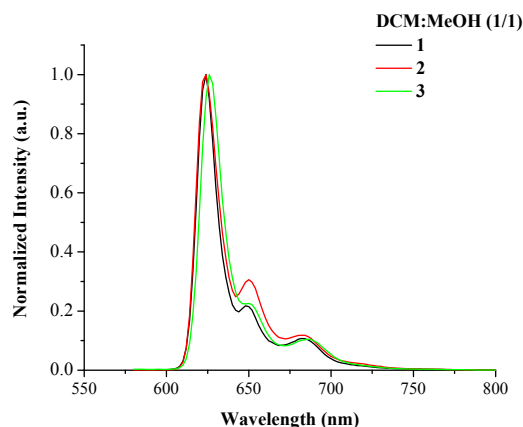


Figure 4.5. Emission spectra of corroles **1**, **2** and **3** in CH₂Cl₂: CH₃OH (1:1) glassy solutions at 77 K; $\lambda_{exc} = 440$ nm.

Here it is possible to observe that the Soret band is split in two components, ascribed to T1 and T2 respectively, with the one at lower energy less pronounced than that at higher energy. This additional experiment confirms that both species are present in the ground state also at 77 K but, moving to the excited state, due to the tautomerization equilibrium, they appear in different proportion, in agreement with the different contribution observed in emission, higher for T2, here present as principle emitter, than for T1. Moreover, the fact that T1 displays prevalent absorption in the range 425-450 nm at 77 K (see **Fig. 4.6**) validates the interpretation of the experiment reported in **Fig. 4.5** where prevalent excitation of T1 has been performed, producing an enhancement of its emission at 650 nm.

In DCM, the emission behavior is less regular than in the mixed CH_2Cl_2 : CH_3OH solvents but the trend is kept constant, displaying a slightly red-shifted T2 emission peak (around 626-632 nm) and a shoulder around 680 nm. Moreover, the band appeared for **2** in CH_3OH and CH_2Cl_2 : CH_3OH , ascribed to T1 emissions (**Fig. 4.5**), is here present in all the compounds, and particularly evidenced in **2** again (see **Fig. 4.7**, left). In toluene there is an inversion of tendency as reported in **Fig. 4.7** (right): in the emission profiles of **1** and **3**, as at room temperature, T1 is again the prominent emitting tautomer, while for **2**, emission from T2 appears slightly higher than that from T1. Corresponding behavior is observed in the vibrational shoulders at longer wavelengths, located at higher or lower energy with respect to the most intense band as function of the prominent tautomer, thus lying around 660 nm when T2 emission is the major component and around 710 nm when T1 dominates.

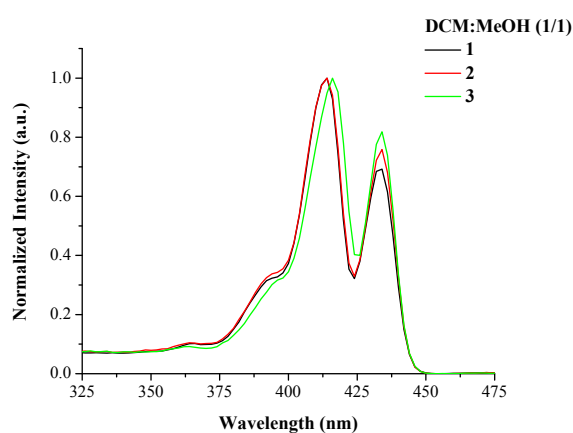


Figure 4.6. Excitation spectra of corroles **1**, **2** and **3** in CH_2Cl_2 : CH_3OH (1:1) glassy solutions at 77 K; $\lambda_{\text{em}} = 620$ nm.

The very low Stokes' shift (almost zero in toluene solutions, see **Fig. 4.8**) revealed by comparison of excitation and emission spectra recorded at low temperature is related to the minimization of relaxation processes in rigid environment and accounts for the presence of a pure Franck-Condon emitting state, with a very low degree of distortion. By comparing the excitation spectra recorded at the two distinct wavelengths of emission of the two tautomers, it is possible to confirm also the attribution of the corresponding absorption bands (clearly distinguishable in excitation spectra) to T1 at lower and to T2 at higher energy. In fact, the relative intensities of the two peaks that compose the Soret band in the excitation profiles change with the wavelength of emission: at $\lambda_{\text{em}} = 620$ nm (emission of T2), the B peak at higher energy dominates in excitation profile, accounting for a T2 nature, unlikely at $\lambda_{\text{em}} = 650$ nm (emission of T1), the lower energy peak is more intense, thus can be safely ascribed to T1.

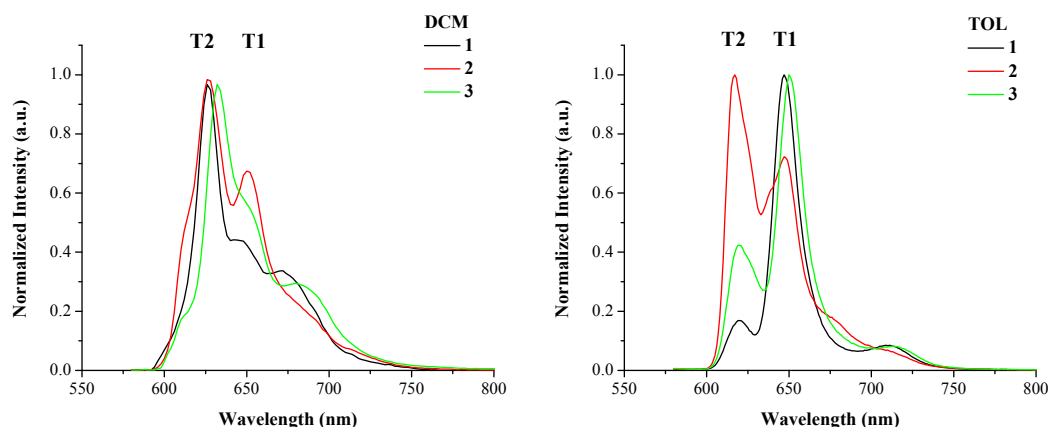


Figure 4.7. Emission spectra of corroles **1**, **2** and **3** in DCM (left) and Tol (right) glassy solutions at 77 K; $\lambda_{\text{exc}} = 560$ nm.

The peculiar influence of the temperature on emission properties represents an original feature for this class of compounds. In fact, apart from the example of pyrimidinyl-substituted systems already reported,^{24b} the emission properties in *meso*-triarylcorroles have not revealed to be temperature dependent and emission originates mainly from T1 tautomer. In the investigated compounds, the activation energies for the T1 \rightarrow T2 and T2 \rightarrow T1 tautomerizations in the excited S_1 state differ strongly, leading as usual to preferential population of the S_1 state of the T1 tautomer at room temperature. Instead, when temperature is going down, such equilibrium shifts towards the tautomer with higher energy on the ground state. It is important to stress that temperature does not change the tautomers population in the ground state but it interferes on the excited state equilibrium between them, so switching their fluorescence.

The investigated corroles, as expected, have not exhibited any phosphorescence emission in the visible and near IR range, due to the low intersystem crossing efficiency from singlet to triplet excited states, as also confirmed by the high values of fluorescence quantum yields.

4.2.3.1. Lifetime Analyses

The data obtained from lifetime analysis at 77 K are again very heterogeneous, resulting in the presence of a shorter-lived component, attributed to T2, present in toluene, acetonitrile and dichloromethane solutions and ranging from 0.4 to 1.5 ns, and a longer-lived one, ascribable to tautomer T1 (see **Table 4.4**), appearing in every solvent in the time range between 5 and 9 ns.²⁵ Such behavior is in agreement with literature data.^{19b, 21} Fluorescence decays recorded in several solvents for the emission of T1 at 77 K can be directly compared to those obtained at room temperature, since such tautomer is the only one detected at room temperature. The cooling process, instead, blocks T2 \rightarrow T1 tautomerizations allowing the emission from T2.

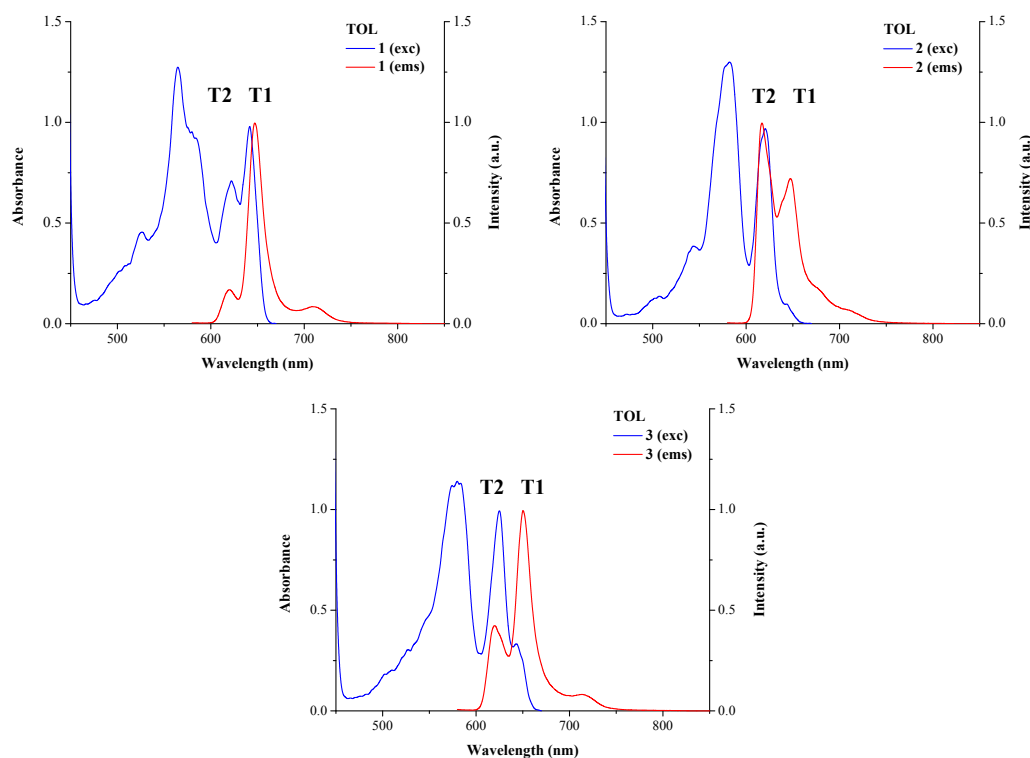


Figure 4.8. Arbitrarily scaled excitation (blue line) and emission (red line) spectra of corroles **1**, **2** (top) and **3** (bottom) in toluene solution at 77 K; $\lambda_{em} = 700$ nm; $\lambda_{xc} = 560$ nm.

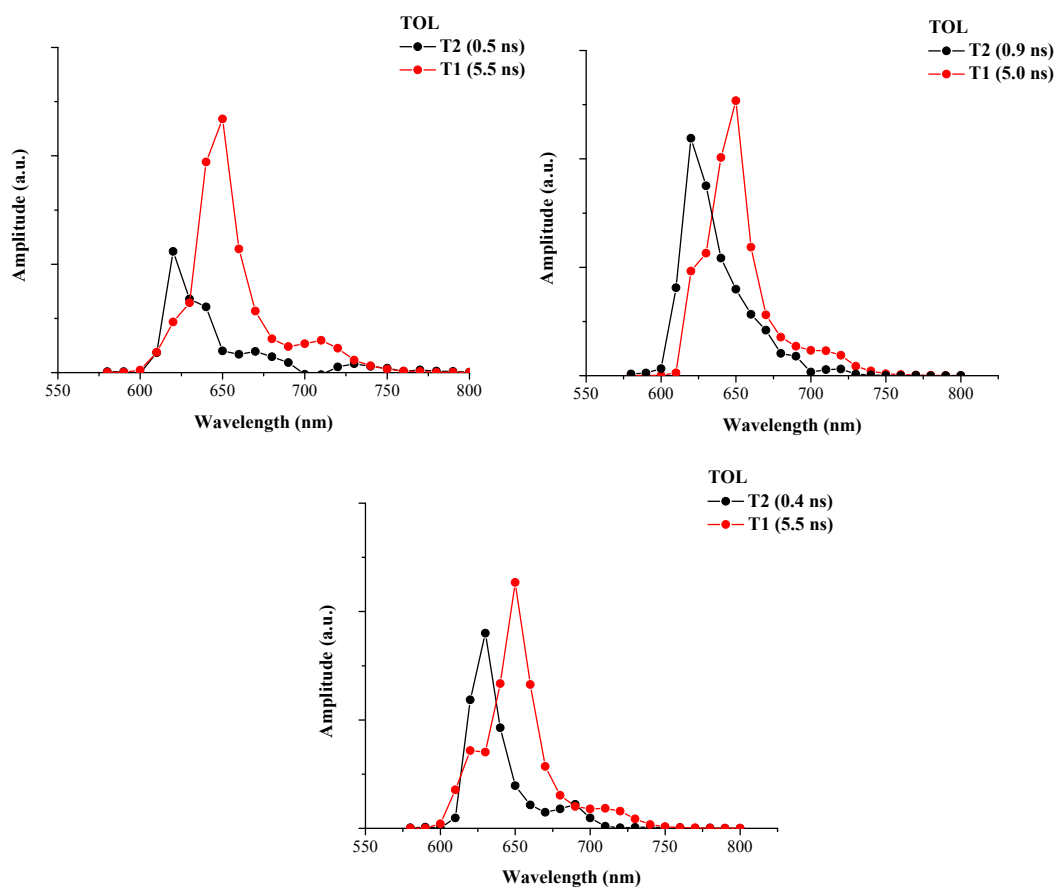


Figure 4.9. Decay Associated Spectra (DAS) for corroles **1**, **2** (top) and **3** in toluene glassy solutions at 77 K of tautomer T1 (red dotted-line) and tautomer T2 (blue dotted-line).

In order to gain the separated profiles of the two tautomers, time resolved measurements have been performed for toluene solutions of the three corroles, upon excitation at 373 nm. Two exponential lifetime components have been used to adequately describe the registered decays.

The corresponding time resolved fluorescence decay associated spectra, obtained by plotting the amplitudes of the individual kinetic components as function of the wavelength, are displayed in **Figure 4.9** for the three systems. The lifetime values obtained by the global analysis are around 5 ns for T1, with emission maximum at 650 nm and between 0.4 and 0.9 ns for T2, peaking at 620 nm.

4.3 Aggregation

In order to investigate the aggregation properties of the present corroles, UV-Vis absorption and emission spectra have been performed at room temperature on methanolic solutions, upon addition of increasing amount of water (from 0 to 80%). The selection of this couple of solvents has been done taking into account the solubility properties of the macrocycles, efficiently dissolved in methanol but not in water. Indeed, at increasing amount of the non-solubilizing solvent, the molecules should aggregate in the attempt to minimize the interaction with the unfavorable environment.

Fig. 4.10 reports absorption and emission spectra of mixed methanol/water solutions of compounds **1**, **2** and **3** at increasing content of water. Molarities of the starting solutions are chosen in order to guarantee as final corrole concentration of analyzed sample, the fixed value of 7.5×10^{-6} M, necessary to keep B bands absorption below the Lambert Beer law limits and Q bands around a value suitable for emission analysis. As shown in **Fig. 4.10**, no evidence for aggregation appears, nor in absorption nor in emission, when the amount of water is kept below 40%. Instead, at increasing water percentage, a decrease, broadening and slight blue shift (*ca.* 2 nm) of the absorption B band are registered together with a simultaneous lowering of the Q bands and a drastic emission quenching. Moreover, in absorption spectra the lowering of B and Q band intensities occurs in tandem with the appearance of an isosbestic point (at about 430 nm), as clear indication of the fact that absorption changes are not mere solvent effects but account for the growing of a new species in solution.

The so-called critical water percentage lays around 40-50% for all the corroles and represents the point of drastic change in absorbance and emission intensity.

Further information about aggregation process has been given by the parallel analyses of lifetimes for the corresponding solutions: upon increasing of the water content, registered values remained constant even for almost complete quenched samples. This behavior indicates that formed aggregates are completely non luminescent and the measured lifetime belongs just to the monomer remained in solution. Excitation spectra also confirm such evaluation, keeping the features of the monomer at every water %.

The different trend assumed by the investigated corroles in comparison with the most common J-aggregation of similar porphyrins (resulting in more prominent modifications of absorption profiles with red shift of B band), can be ascribed to the related different geometries, actually responsible for different packing modes.

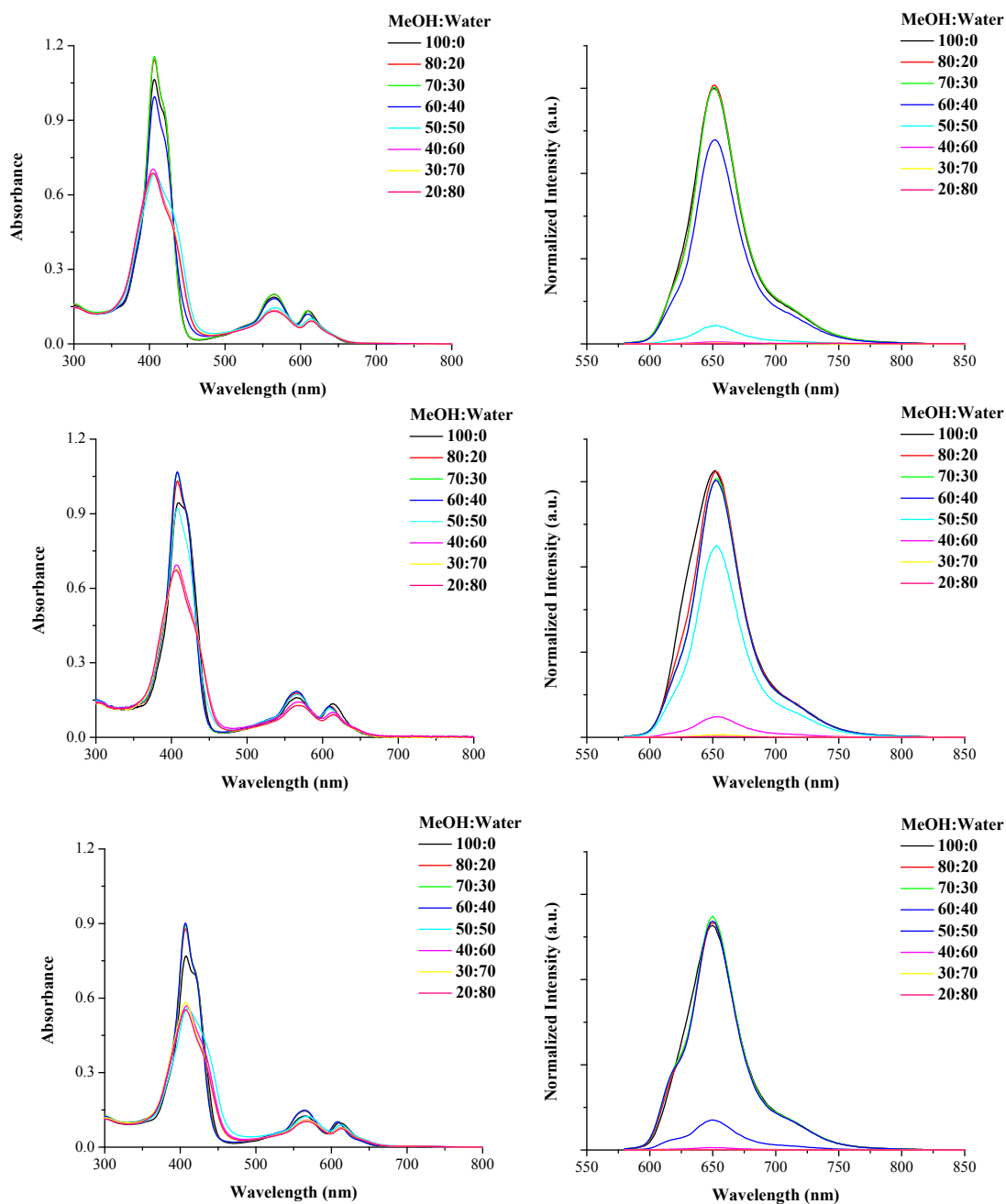


Figure 4.10. Absorption (left) and emission (right) spectra of corroles **1** (top), **2** (centre) and **3** (bottom) in CH₃OH/Water solutions (% Water from 0 to 80%) ([**1**] = 8.0×10^{-6} M; [**2**] = 7.3×10^{-6} M; [**3**] = 7.0×10^{-6} M) at rt; $\lambda_{\text{exc}} = 560$ nm.

Moreover, from the moderate observed blue shift, it is not clear if dimer formation or higher H-type aggregation take place. To obtain a certain interpretation of such phenomenon, X-ray analysis has been performed by the group of Gryko for the three compounds. Such measurement clarified that self-organization results in dimer formation, driven by intermolecular hydrogen bond, between the appended carbonylic oxygen in the *meso*-phenyl ring of one corrole and the NH of the core of the neighbor (CO \cdots HN) (see **Fig. 4.11** for corrole **3**). The resulted dimer displays its side chains

sandwiched between two tetrapyrrolic units with the phenyl moieties perpendicular to the corresponding core plane.

CD measurements have been performed on the corroles CH₃OH /Water (30:70) solutions at different proportion in order to ascertain if the aggregates display any form of chirality, but no signal has been detected.

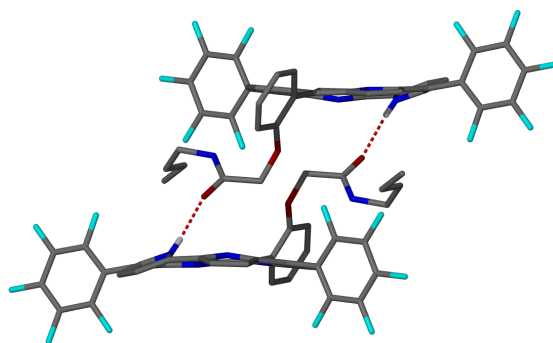


Figure 4.11. Hydrogen bonded dimer of corrole **3**.

Table 4.1 Absorption features of corroles **1**, **2** and **3** in toluene, CH₃CN, CH₂Cl₂ and CH₃OH.

	TOL	ACN	DCM	MeOH
	λ_{max} , nm (e_{max} , M ⁻¹ cm ⁻¹)	λ_{max} , nm (e_{max} , M ⁻¹ cm ⁻¹)	λ_{max} , nm (e_{max} , M ⁻¹ cm ⁻¹)	λ_{max} , nm (e_{max} , M ⁻¹ cm ⁻¹)
1	416 (119,000) 565 (20,700) 615 (12,700)	417 (123,000) 566 (18,800) 619 (19,700)	408 (137,500) 559 (22,500) 611(15,300)	406 (133,400) 565 (23,400) 611 (16,700)
2	413 (127,700) 570 (22,800) 615 (14,800)	410 (125,100) 567 (20,100) 617 (18,900)	409 (142,700) 567 (23,900) 611 (15,300)	409 (130,000) 567 (21,200) 614 (18,600)
3	415 (106,900) 567 (17,500) 615 (11,000)	419 (107,900) 565 (16,400) 620 (15,300)	409 (122,800) 559 (19,700) 611 (11,800)	408 (109,100) 566 (17,200) 614 (15,200)

Table 4.2 Luminescence properties of corroles **1**, **2** and **3** in toluene, CH₃CN, CH₂Cl₂ and CH₃OH at room temperature.

	TOL ^[a]			ACN ^[a]		
	rt λ_{\max} , nm	ϕ	$\tau, \text{ns}^{[b]}$	rt λ_{\max} , nm	ϕ	$\tau, \text{ns}^{[b]}$
1	650, 710 sh	0.155 (0.169) ^[c]	3.96 (5.3) ^[c]	648, 700sh	0.150	3.78
2	650, 710 sh	0.156 (0.160) ^[c]	3.75 (5.5) ^[c]	650, 700sh	0.154	3.81
3	650, 710 sh	0.154 (0.165) ^[c]	4.30 (5.5) ^[c]	650, 700sh	0.140	3.85

	DCM ^[a]			MeOH ^[a]		
	rt λ_{\max} , nm	ϕ	$\tau, \text{ns}^{[b]}$	rt λ_{\max} , nm	ϕ	$\tau, \text{ns}^{[b]}$
1	650, 710 sh	0.142	3.8	654, 720 sh	0.127	3.4
2	652, 710 sh	0.148	3.7	654, 720 sh	0.135	3.6
3	650, 710 sh	0.147	4.1	652, 720 sh	0.134	3.8

^a In air-equilibrated solutions. For quantum yield determination: $\lambda_{\text{exc}} = 560$ nm. ^b For lifetime measurements, $\lambda_{\text{exc}} = 373$ nm. ^c In air-free toluene solutions.

Table 4.3 Luminescence properties of corroles **1**, **2** and **3** in CH₂Cl₂: CH₃OH (1:1), CH₃CN, CH₂Cl₂ and CH₃OH at 77 K.

	DCM:MeOH (1:1)		ACN	
	77K ^[a] λ_{\max} , nm	$\tau, \text{ns}^{[b]}$	77K ^[a, c] λ_{\max} , nm	$\tau, \text{ns}^{[b]}$
1	619	6.5	632	0.7; 6.3 (30:70)
2	618	5.7	616, 656	0.8; 4.7 (50:50)
3	621	6.5	618	1.2; 5.4 (50:50)

	DCM		MeOH	
	77K ^[a] λ_{\max} , nm	$\tau, \text{ns}^{[b]}$	77K ^[a] λ_{\max} , nm	$\tau, \text{ns}^{[b]}$
1	626, 648 sh	1.3; 5.0 (50:50)	618	9.0
2	626, 650 sh	1.3; 4.2 (40:60)	618	7.8
3	632, 678 sh	1.5; 5.0(40:60)	616	8.3

^a Wavelength values from not corrected spectra. ^b For lifetime measurements, $\lambda_{\text{exc}} = 373$ nm. ^c In CH₃CN glassy solution, $\lambda_{\text{exc}} = 420$ nm.

4.4. Conclusions

Three free-base *trans*-A₂B-phenylcorrole with different substituents on the *meso*-phenyl ring has been characterized by means of absorption and emission spectroscopy. The results showed that photophysical properties of the studied compounds are governed by the lowest-lying π - π^* singlet state, responsible for high fluorescence quantum yields and lifetimes in the order of few nanoseconds.

A deep investigation has been undertaken to understand the role on absorption and emission profiles of the two NH tautomers, in different solvents and at room and low temperature. The distinct contributions of the tautomers have been assigned to the relevant peaks of emission and absorption spectra, in agreement with literature information also confirmed by experimental evaluations. It was found that the fluorescence from tautomer T1 is predominant at room temperature, unlike low temperatures, where tautomer T2 dominates in almost all the investigated solvents. Such a big temperature dependence that switches fluorescence emissions from the two tautomers is very rarely reported and opens the way to many possible applications.

Furthermore, these molecules displayed interesting properties in terms of solvent promoted self-aggregation. In very polar environment, they self-organize into dimeric species, through intermolecular hydrogen bond between the pyrrole ring of one corrole and the carbonylic oxygen of the side chain of the adjacent macrocycle. This behavior, obtained upon a precise design of the structure, candidates these compounds as novel structural platform for solar energy conversion, by mimicking natural hydrogen-bond based self-assembly.

4.5. References

-
- ¹ I. Aviy; Z. Gross, *Chem.-Eur. J.*, 2008, **14**, 3995-4005.
 - ² S. Yang; Y. Wo and M. E. Meyerhoff, *Anal. Chim. Acta*, 2014, **843**, 89-96.
 - ³ A. M. del C. Batlle, *J. Photochem. Photobiol., B*, 1993, **20**, 5-22.
 - ⁴ K. Sudhakar; V. Velkannan and L. Giribabu, *Tetrahedron Lett.*, 2012, **53**, 991–993.
 - ⁵ K. Ocakoglu; K. S. Joya; E. Harputlu; A. Tarnowska and D. T. Gryko, *Nanoscale*, 2014, **6**, 9625-9631.
 - ⁶ For selected rev. see: ^(a) S. S. Babu and D. Bonifazi, *ChemPlusChem* 2014, **79**, 895-906.; ^(b) M. K. Panda; K. Landomenou and A. G. Coutsolelos, *Coord. Chem. Rev.* 2012, **256**, 2601-2627.
 - ⁷ ^(a) C. Chappaz-Gillot; P. L. Marek; B. J. Blaive; G. Canard; J. Bürck; G. Garab; H. Hahn; T. Jávorfí; L. Kelemen; R. Krupke; D. Mössinger; P. Ormos; C. M. Reddy; C. Roussel; G. Steinbach; M. Szabó; A. S. Ulrich; N. Vanthuyne; A. Vijayaraghavan; A. Zupcanova and T. S. Balaban, *J. Am. Chem. Soc.*, 2012, **134**, 944-954. ^(b) T. S. Balaban; M. Linke-Schaetzel; A. D. Bhise; Nicolas Vanthuyne; C. Roussel; C. E. Anson; G. Buth; A. Eichhöfer; K. Foster; G. Garab; H. Gliemann; R. Goddard; T. Javorfi; A. K. Powell; H. Rösner and T. Schimmel, *Chem.-Eur. J.*, 2005, **11**, 2267-2275.
 - ⁸ ^(a) R. Paolesse; L. Jaquinod; D. J. Nurco; S. Mini; F. Sagone; T. Boschi; K. M. Smith, *Chem. Commun.* **1999**, *14*, 1307-1308; ^(b) R. Paolesse; S. Nardis; F. Sagone; R. G. Khoury, *J. Org. Chem.* **2001**, *66*, 550-556; ^(c) Z. Gross; N. Galili; L. Simkhovich; I. Saltsman; M. Botoshansky;

- D. Blaser; R. Boese; I. Goldberg, *J. Org. Chem.* **1999**, *4*, 599-602; ^(d) Z. Gross; N. Galili; I. Saltsman, *Angew. Chem., Int. Ed.* **1999**, *38*, 1427-1429; ^(e) R. P. Brinas; C. Bruckner, *Synlett* **2001**, 442-444; ^(f) D. T. Gryko; B. Koszarna, *Org. Biomol. Chem.* **2003**, *1*, 350-357. ^(g) D. T. Gryko, *Chem. Commun.* **2000**, *22*, 2243-2244; ^(h) D. T. Gryko; K. Jadach, *J. Org. Chem.* **2001**, *66*, 4267-4275; ⁽ⁱ⁾ J. P. Collman; R. A. Decreau, *Tetrahedron Lett.* **2003**, *44*, 1207-1210; ^(j) G. R. Geier; J. F. B. Chick; J. B. Callinan; C. G. Reid; W. P. Auguscinski, *J. Org. Chem.* **2004**, *69*, 4159-4169.
- ⁹ Y. Shinozaki; I. Yoshikawa; K. Araki; K. Sugawaa and J. Otsuki, *CrystEngComm* **2014**, *16*, 9155-9157.
- ¹⁰ ^(a) I. Aviv; Z. Gross, *Chem. Commun.* **2007**, 1987-1999; ^(b) L. Flamigni; D. T. Gryko, *Chem. Soc. Rev.* **2009**, *38*, 1635-1646; ^(c) I. Aviv-Harel; Z. Gross, *Chem.-Eur. J.* **2009**, *15*, 8382-8394; ^(d) I. Aviv-Harel; Z. Gross, *Coord. Chem. Rev.* **2011**, *255*, 717-736; ^(e) A. Mahammed; Z. Gross, *Chem. Commun.* **2010**, 7040-7042; ^(f) L. Kupersmidt; Z. Okun; T. Amit; S. Mandel; I. Saltsman; A. Mahammed; O. Bar-Am; Z. Gross; M. B. H. Youdim, *J. Neurochem.* **2010**, *113*, 363-373; ^(g) M. M. Abu-Omar, *Dalton Trans.* **2011**, *40*, 3435-3444; ^(h) S. Suranjana Bose; A. Pariyar; A. N. Biswas; P. Das; P. Bandyopadhyay, *Catal. Commun.* **2011**, *12*, 446-449; ⁽ⁱ⁾ D. K. Dogutan; R. McGuire; D. G. Nocera, *J. Am. Chem. Soc.* **2011**, *133*, 9178-9180; ^(k) L. Flamigni; A. I. Ciuciu; H. Langhals; B. Böck; D. T. Gryko, *Chem. Asian J.* **2012**, *7*, 582-592.
- ¹¹ For selected rev. see: I. Aviv-Harel and Z. Gross, *Coord. Chem. Rev.* **2011**, *255*, 717-736.
- ¹² Z. Gross; H. B. Gray, *Comments Inorg. Chem.* **2006**, *27*, 61-72.
- ¹³ G. R. Geier; J. F. B. Chick; J. B. Callinan; C. G. Reid; W. P. Auguscinski, *J. Org. Chem.* **2004**, *69*, 4159-4169.
- ¹⁴ Z. Gross; N. Galili; L. Simkhovich; I. Saltsman; M. Botoshnsky; D. Blaser; R. Boese; I. Goldberg, *Org. Lett.* **1999**, *1*, 599-602.
- ¹⁵ ^(a) J. M. Lehn, *Angew. Chem. Int. Ed.* **1990**, *29*, 1304-1319; ^(b) Z. G. Tao; T. G. Zhan; T. Y. Zhou; X. Zhao; Z. T. Li, *Chin. Chem. Lett.* **2013**, *24*, 453-456; ^(c) Y. J. Qin; Y. Y. Wang; M. X. Tang; Z. X. Guo, *Chin. Chem. Lett.* **2010**, *21*, 876-879.
- ¹⁶ M. Stefanelli; D. Monti; M. Venanzi and R. Paolesse, *New J. Chem.* **2007**, *31*, 1722-1725.
- ¹⁷ G. Charalambidis; E. Kasotakis; T. Lazarides; A. Mitraki and A. G. Coutsolelos, *Chem. Eur. J.* **2011**, *17*, 7213-7219.
- ¹⁸ M. Gouterman, *J. Mol. Spec.* **1961**, *6*, 138-163.
- ¹⁹ ^(a) R. Paolesse; F. Sagone; A. Macagnano; T. Boschi; L. Prodi; M. Montalti; N. Zaccheroni; F. Bolletta and K. M. Smith, *J. Porph. Phthaloc.* **1999**, *3*, 364-370; ^(b) R. Paolesse; A. Marini; S. Nardis; A. Froio; F. Mandoj; D. J. Nurco; L. Prodi; M. Montalti and K. M. Smith, *J. Porph. Phthaloc.* **2003**, *7*, 25-36; ^(c) A. Ghosh; T. Wondimagegn and A. B. J. Parusel, *J. Am. Chem. Soc.* **2000**, *122*, 5100-5104.
- ²⁰ F. Nastasi; S. Campagna; T. H. Ngo; W. Dehaen; W. Maesb and M. Kruk, *Photochem. Photobiol. Sci.* **2011**, *10*, 143-150.
- ²¹ T. Ding; E. A. Alema; D. A. Modarelli and C. J. Ziegler, *J. Phys. Chem. A* **2005**, *109*, 7411-7417.
- ²² ^(a) M. Gouterman; G. Wagniere; L. R. Snyder, *J. Mol. Struct.* **1963**, *11*, 108-127; ^(b) M. Gouterman, *The Porphyrins*, Dolphin, D., Ed.; Academic Press: New York, **1978**, *3*, 1-165.
- ²³ M. Kruk; T. H. Ngo; P. Verstappen; A. Starukhin; J. Hofkens; W. Dehaen and W. Maes *J. Phys. Chem. A* **2012**, *116*, 10695-10703.
- ²⁴ ^(a) H. T. Ngo; F. Puntoriero; F. Nastasi; K. Robeyns; L. Van Meervelt; S. Campagna; W. Dehaen and W. Maes, *Chem. Eur. J.* **2010**, *16*, 5691-5705.
- ²⁵ E. A. Ermilov; B. Büge; S. Jasinski; N. Jux and B. Röder, *J. Chem. Phys.* **2009**, *130*, 134509-134516.

Chapter 5

5. Photophysical investigation of PSI immobilized on hematite surface for solar to fuel conversion

Nowadays, the need to develop renewable energy sources stimulates the scientific research towards the design of cheap, efficient and robust devices for solar-to-fuel conversion. Direct conversion of solar into condensed and storable chemical energy can be realized within nanoscale synthetic systems, by fabrication of photo-optical cells (e.g. dye-sensitized solar cells, DSSCs), whose working principles take advantage from the knowledge of the basic concepts of natural mechanisms.

Photosynthetic process is composed of several sequential reactions, and its mechanism has not been yet perfectly clarified. Many attempts at making artificial photosynthetic systems have been made, and some of them produced successful energy conversion systems.

Since it is difficult for an artificial devices to use with good efficiency visible and near-infrared light, several research groups put effort into the synthesis of artificial reaction centre pigments able to absorb longer wavelength light, trying to mimic natural active structures. Many examples of reported assemblies are based on the use of chromophores such as porphyrins¹, covalently linked to one or more electron acceptors, like fullerenes or quinones, and secondary electron donors. Often, these frameworks are coupled with well-performing antenna systems, that efficiently absorb visible light and, incorporated to semiconductor layers, realize technological devices for fuels or photocurrent production.

In the most common devices realized for this kind of applications, nanoporous titanium dioxide² has been extensively used as semiconductor surface, deposited on a transparent electrode, as exemplified in **Figure 5.1**. Then, several light harvesters, of mixed organic and metallic nature, properly functionalized, have been anchored over such semiconductor surface to realize, through direct contact, electron injection into its conduction band. And a catalyst, like the most common platinum, promotes hydrogen evolution and closes the circuit.

Till now, systems like these have exhibited lower efficiencies than those required for practical applications, but anyway they show that solar fuel production, inspired by natural photosynthesis, is indeed achievable, prompting the investigation in this direction. In fact, further studies could offer the occasion to introduce better and better systems, by designing new ones and/or engineering those already known, to finally push their big scale applications out from laboratories.³

In this chapter, a successful example of “natur-artificial technology” is introduced.⁴ It is realized through integration of the photochemically active and stable photosystem I (PSI), coupled to its associated light-harvesting antenna (LHCI), as natural component, immobilized onto low-cost semiconductor surfaces, and offers an attractive approach to achieve hydrogen evolution with moderate efficiency.

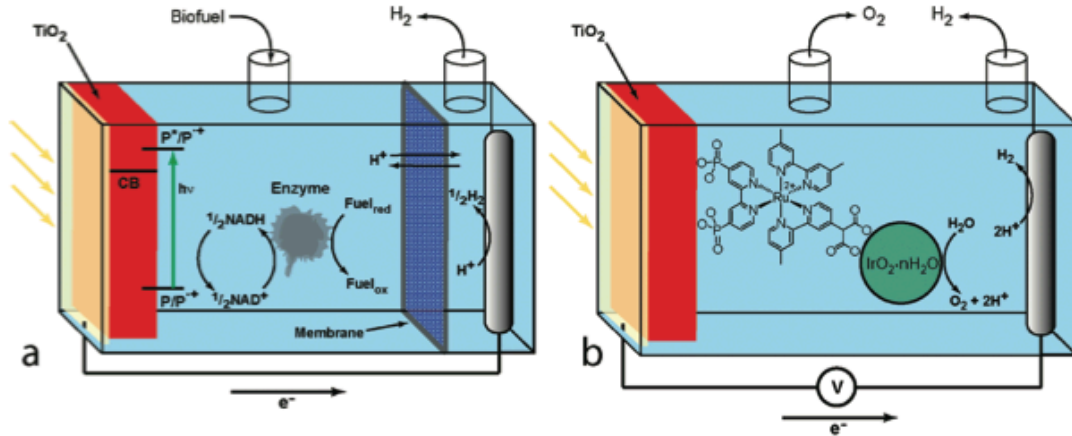


Figure 5.1. Schematic diagrams of a photoelectrochemical biofuel cell (a) and an artificial photosynthetic water splitting cell (b). Both cells use light to generate hydrogen. (From Ref. 3)

5.1. Introduction

Artificial photosynthesis is generally referred to molecular based biomimetic systems that achieve efficient harvesting of sunlight and conversion into chemical energy by reproduction of the fundamental processes occurring in nature. The natural mechanisms are conducted by two large multimeric protein-cofactor complexes, denoted as Photosystem I (PSI) and Photosystem II (PSII) and coupled to their light-harvesting complexes (LHCI and LHCII, respectively). These macromolecules have as main component the reaction centre (RC) domain, containing apart from all the electron transport cofactors, a chlorophyll (Chl_a) dimer, called P700 in PSI and P680 in PSII, as unique final energy collector of the entire absorbed light.⁵

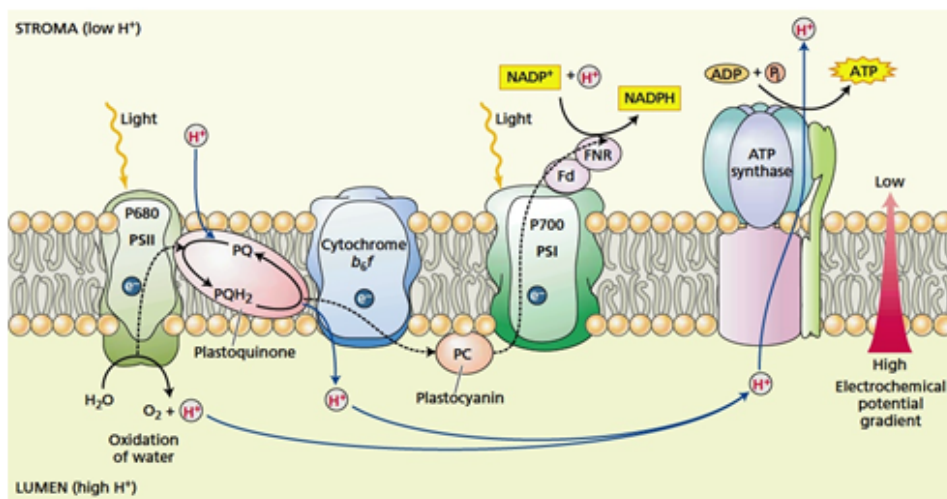


Figure 5.2. The transfer of electrons and protons in the thylakoid membrane is carried out vectorially by four protein complexes (From Ref. L. Taiz; E. Zeiger, *Plant Physiology* 2010, 5th Edition. The Benjamin Cummings Publishing Company, Redwood City – California)

These super-complexes, in living organisms like plants, algae and cyanobacteria, participate to the main photosynthetic steps. They are responsible indeed for light-

harvesting, charge separation and charge transfer processes and accomplish their function with high efficiency, despite their high structural complexity.⁶

Thus, taking into account their surprising performances and their unique light-harvesting and redox properties, together with their natural abundance, PSI and PSII can be considered as promising candidates for nanoscale design of bio-hybrid devices for solar energy conversion.

The fully integrated, stable and functional PSI-based bio-hybrid DSSC described in this chapter, displays improved solar-to-electric quantum efficiency of more than two-folds, compared to that previously reported by *Mershin et al.*⁷ He has shown a good application of stabilized cyanobacterial native or modified PSI complex as photoanodic component of a bio-hybrid TiO₂-based DSSC, with Co(II)/(III)-tris-bipyridine as the electrolyte/electron transfer mediator and a Pt cathode.⁷

Anyway, for both devices, the photocurrent production lays under the values required for a practical applicability. Thus, the real improvement that our system produces in the technological context is not in terms of application as DSSC but for photoelectrochemical H₂ production. Actually, it can sustain H₂ evolution with good performances (maximal rate of photodriven H₂ production = 744 μmoles H₂ mg Chl⁻¹h⁻¹), upon illumination with red visible light, offering a promising, stable and perfectly green bio-hybrid system for solar-to-fuel conversion.

The employed PSI-LHCI has been extracted from the extremophilic red microalga *Cyanidioschyzon merolae*, unicellular organism considered as one of the most primitive existing, even older than green algae, cyanobacteria and plants. The choice of such specific system is related, first of all, to its ability to survive to extremely hard environmental conditions, such as high acidity and temperature, suitable for its main application in solar conversion. Moreover, since it can be considered as a sort of forerunner for more advanced systems, it represents an informative model to achieve indications about the basic structure of PSI light-harvesting complexes and their evolution.⁸

This PSI-LHCI extracted from the thylakoid membranes of the *C. merolae*, upon purification and functionalization treatments, has been tested and integrated into two distinct semiconductors, α-Fe₂O₃ (hematite) and TiO₂. The description below contains some information about fabrication and electrical characterization for the PSI-based device, realized by the groups of Kargul and Ocakoglu.

The main part of the discussion will be focused on the photophysical analysis of the PSI bio-hybrid photoanodic units, performed to ascertain if the sensitizer has retained its properties also upon all purification and immobilization treatments. Such analysis has been conducted by means of steady state and time resolved fluorescence spectroscopy, with particular attention toward the photoinduced energy transfer processes, as central topic of the entire thesis.

5.2. Results and discussion

5.2.1. Nanostructuring of the PSI-LHCI-sensitized semiconductor substrates for the fabrication of a device sustaining both photocurrent production and H₂ evolution

5.2.1.1. Construction of the PSI-based photoanode

The fabrication of an efficient bio-hybrid PSI-based DSSC has been accomplished integrating redox compatible components, among which good communication occurs by means of fast and directional electron transfer events. The components arrangement follows the typical sandwich-type mode as reported for Grätzel's DSSCs (see **Fig. 5.3**): oriented PSI-LHCI multimeric assemblies are physisorbed and covalently cross-linked on nanostructured semiconducting substrate forming a multilayer structure (see **Fig. 5.4** and **5.5**); the electric circuit is closed by an electrolyte solution (3I⁻/I₃⁻ couple, obtained from an acetonitrile solution of 0.5 M lithium iodide and 0.05 M iodine) and platinumized FTO glass. In such device, the PSI plays the role of photosensitizer, extending light absorption of the photoanodic unit into the red region of the visible spectrum; moreover it has to carry out the charge separation, too.

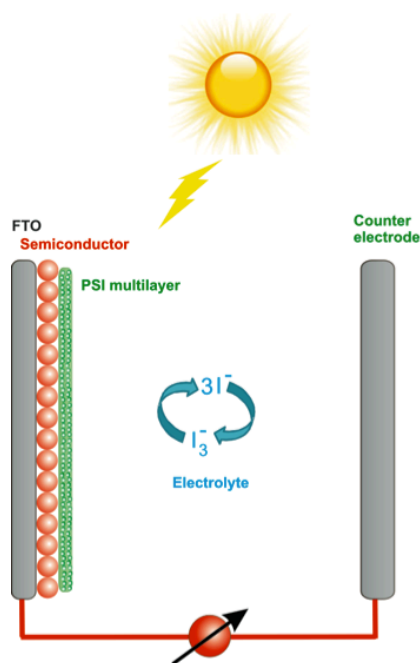


Figure 5.3. Schematic representation of fabricated solar cell with PSI-Semiconductor-FTO as photoanode.

Culturing of *C. merolae*, isolation from thylakoids and purification of crude PSI-LHCI were performed according to *Krupnik et al.* and the relevant treatments are reported in references^{9,4} and schematically depicted in **Fig. 5.5**. The obtained PSI-LHCI multilayers structure (almost 15 layers) displays the typical thickness found in the membranes of cyanobacteria (around 10.6 nm), where natural photosynthesis takes place.¹⁰ Two semiconductor substrates, TiO₂ and α -Fe₂O₃, have been employed for the

photoanode fabrication. The selection of such components is due to their well-known favourable properties of photocatalytic activity, suitable energy bands, stability, carrier transport, non-toxicity, widespread availability and low-cost.

In order to maximize the contact with the sensitizer, the semiconductive photoanodic layers have been deposited in form of mesoporous structure, thus with increased area available for PSI to adhere. By means of field-emission scanning electron microscopy (FE-SEM), a perfectly uniform film-like distribution of α - Fe_2O_3 nanocrystals has been observed, grown over the fluorine-doped tin oxide (FTO) glass plate (see **Fig. 5.4**).

Once prepared the semiconductive glass, by manipulating both its surface charge and that of PSI-LHCl, the desired controlled orientation of the complex on the surface has been achieved (see **Fig. 5.5**).

For this purpose, it was essential to be aware of the type of dependence on pH displayed by the charge distribution along the surface of the protein-complex. In fact, proper treatments with pH buffers of both PSI and semiconductor surface allowed the most convenient reciprocal arrangement, based on the specific orientation on the first layer with the side of PSI containing P700 RC unit, towards the functionalized semiconductor surface.¹¹

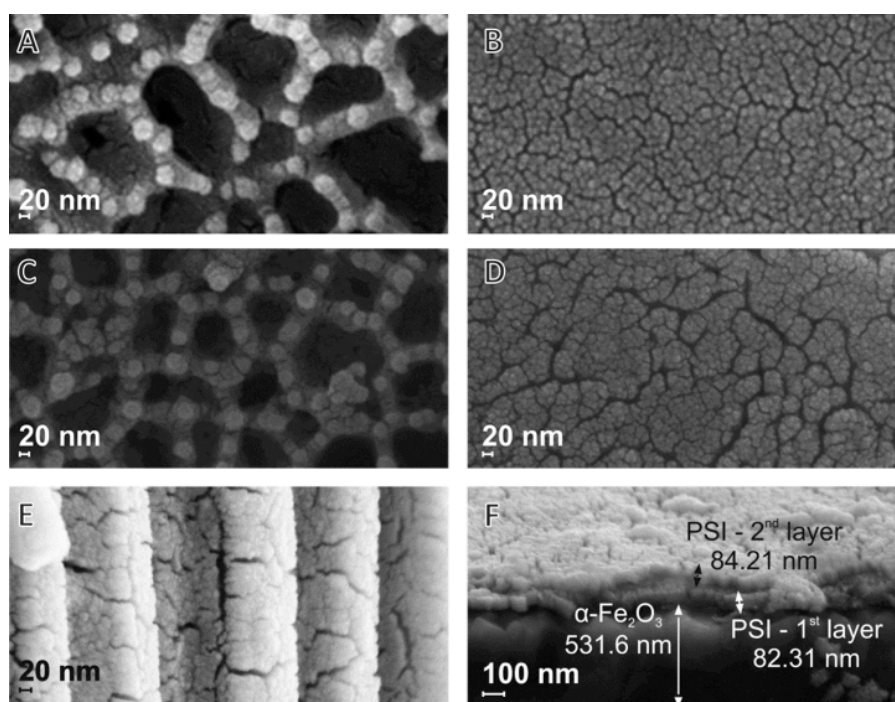


Figure 5.4. Electron microscopy imaging of PSI-based semiconductor photoanodes. Top view FE-SEM images of (A) *PSI-TiO₂-AAO* membranes, (B) *PSI-TiO₂-FTO* electrodes, (C) *PSI- α -Fe₂O₃-AAO* membranes and (D) *PSI- α -Fe₂O₃-FTO* electrodes. Cross-sectional FE-SEM images of (E) *PSI- α -Fe₂O₃-AAO* membrane and (F) *PSI- α -Fe₂O₃-FTO* electrode, from bottom to up α - Fe_2O_3 and PSI-LHCl multilayer (physisorbed first layer and chemically cross-linked second layer) (From Ref. 4)

This represents the best disposition because in PSI-LHCl, the absorbed photons promote the transition of electrons from the ground state of P700 to its highly reducing excited state P700^* , then responsible for the excited electron injection into the

conduction band of the semiconductor and from there, into the Fermi level of the FTO layer. Thus, a wrong orientation of PSI may give rise to charge recombination and short-circuiting phenomena, producing huge energy losses and decrease on the conversion efficiency of the device. That is the reason why the mutual arrangement of the main components is a central issue, so important that a deeper investigation has been necessary to establish exactly the charges localization along the complex. The calculation of surface charge maps for PSI RC domains shows significant changes in the surface charge distribution on going from pH 4 to 7, as reported in **Fig. 5.6**, revealing that both the pH values produce suitable conditions for immobilization.¹⁰

To better understand how these pH conditions can be employed, it is necessary to clarify which are the main portions of PSI to be considered from a functional point of view: the Chls dimer P700 side, with the role of final collector of absorbed photons and of injector of the excited electrons, and the [4Fe-4S] cluster F_B region, working as final acceptor unit during the step of charge separation and formation of the ionic couple P700⁺F_B⁻. Both sides are really affected by pH variations, resulting in different global polarization for the RC domain. In fact, at pH 7, the P700 side, predominantly negatively charged, and the acceptor side nearly neutral, create a lower neat charge (average charge difference around 0.58V) for the domain than that obtained at pH 4, when indeed the positively charged F_B side in combination with the less negative P700 side increase the neat charge difference in the super-complex (average charge difference around 0.67V).

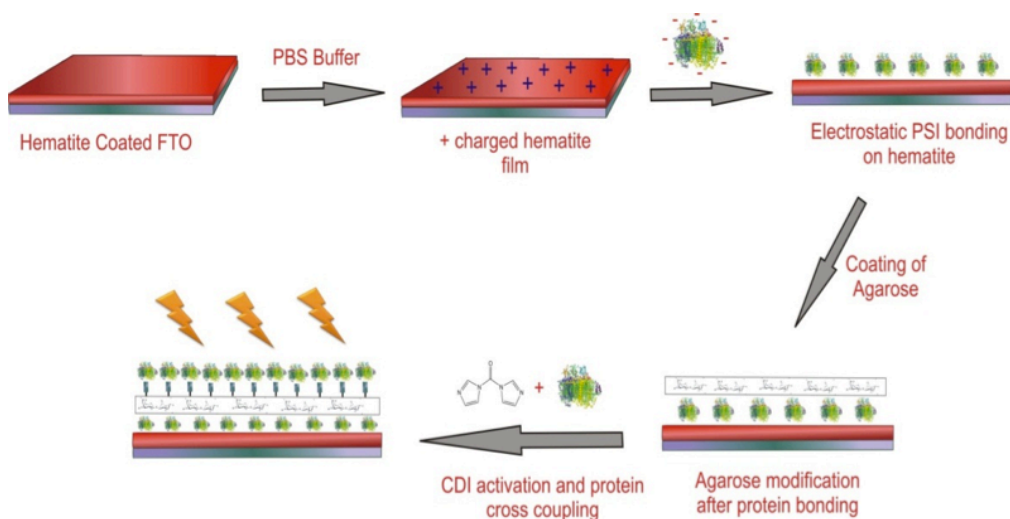


Figure 5.5. Schematic diagram for fabrication of PSI- α -Fe₂O₃-FTO electrode. (From Ref. 4)

Based on these features, PSI can be employed at both these pH conditions but constituting layers with distinct functions. In particular, PSI at pH 7.4 is used in the final photoanode to form the first layer over the semiconductor, with P700 side in direct contact with it, instead the complex at pH 4 is employed in the covalently bound layer, with the reducing side directed to the electrode surface.

In fact, even if for PSI at pH 4, the reducing side has a slightly positive charge before irradiation and as a consequence it should repulse the positive semiconductor, upon illumination of the photoanode, such arrangement realizes an optimal condition for the electron cascade to occur, favouring the flow towards the positive attractive charge of

the reducing side and thus towards the semiconductor. Indeed, the system can take advantage of the negative charge around P700 that, once excited, more spontaneously will release its photoelectrons towards the reducing side, that accepts them favoured by its positive charge.

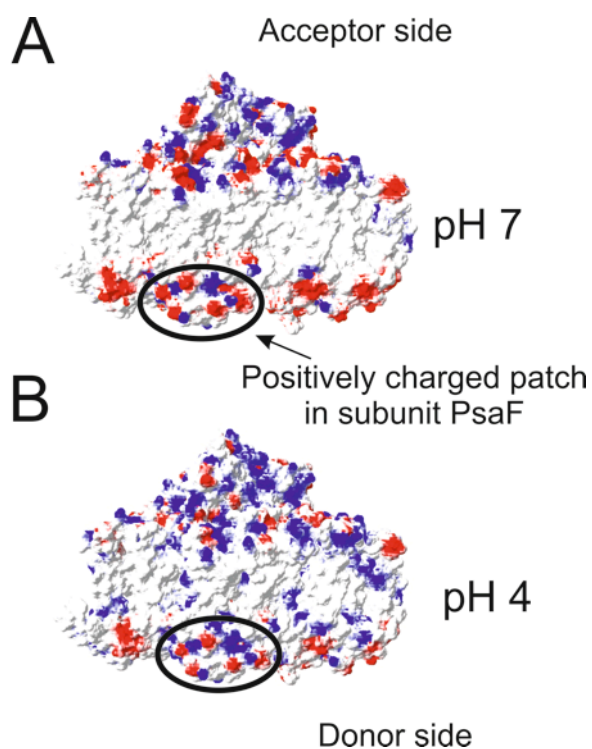


Figure 5.6. Surface charge distribution maps for *Synechococcus elongatus* PSI at (A) pH 7 and (B) pH 4. Residues rendered in blue carries positive charge whereas those depicted as red carries negative charge. Calculation were performed with the values of dielectric constant of solvent $\epsilon = 80$ and protein $\epsilon = 4$. Ionic strength was 0.1 mol/l. PsaF subunit is circled in (A), and its positively charged patch is indicated with an arrow amidst largely negatively charged surface of the donor side at pH 7. The average surface charge of the donor side was $q_{\text{pH } 7} = -0.537$ V and $q_{\text{pH } 4} = -0.145$ V, whereas for the acceptor side the average charge was estimated at $q_{\text{pH } 7} = +0.046$ V and $q_{\text{pH } 4} = +0.534$ V, respectively. (From Ref. 4)

At pH 7.4, the spontaneous arrangement of PSI is driven by the strong coulombian interaction between the more negative donor side containing the P700 unit and the positively charged electrode (see **Fig. 5.6**), resulting in an efficient physical adsorption that favours the funneling of excited electrons.

The exact procedure used for the overall immobilization process combines indeed the properties of PSI in both the pH conditions.

It starts with the treatment of hematite film over the FTO glass with phosphate buffer at pH 7.4, in order to produce a net positively charged surface. The polarized PSI with the negatively charged P700 side is prepared through dissolution of PSI in phosphate buffer at pH 7.4, too and after, deposited over the positive hematite through physical adsorption.

The following phase is centred on the covalent cross-coupling PSI-hematite. To accomplish this linkage, the hematite film was covered by an agarose solution, useful to functionalise the surface with free hydroxyl groups.¹² They are involved in the following electrode activation with the 1,1'-carbonyl-di-imidazole (CDI), through formation of the reactive imidazole carbamate intermediate,¹² species responsible, after treatment with acetate buffer, for the covalent bond of PSI (at pH 4) to the surface.

PSI immobilized according to both the procedures over the hematite surface can sustain a very long-term activity confirmed at least for 90 days.

This procedure is effective for hematite-based photoanode but not when TiO₂ is used. In fact, the step of physical adsorption on TiO₂ has been disfavoured by the negative charge induced on its surface by the pre-treatment and this is one of the reasons of the worst performances for such photoanode.

5.2.1.2. I-V characterization and investigation of photochemical activity

The solar cell built with the PSI-based photoanodic unit gave good performances if compared to similar systems like those reported by *Mershin et al.*⁷ In particular, it has displayed current densities of up to 56.9 $\mu\text{A}/\text{cm}^2$ and solar energy conversion efficiency higher than the 0.17% under standard air-mass 1.5 (AM 1.5) sunlight (see **Table 5.1**). The only parameter that has not shown improvement, nor with TiO₂ nor with hematite as semiconductor, compared to the device of *Mershin et al.* composed of ZnO/PSI anode,⁷ was the open circuit voltage, V_{oc} . The cause has to be ascribed to both electrolyte system and semiconductors, because in DSSCs the photovoltage indeed depends on the difference between the quasi Fermi level of the semiconductor and the redox potential of the electrolyte.

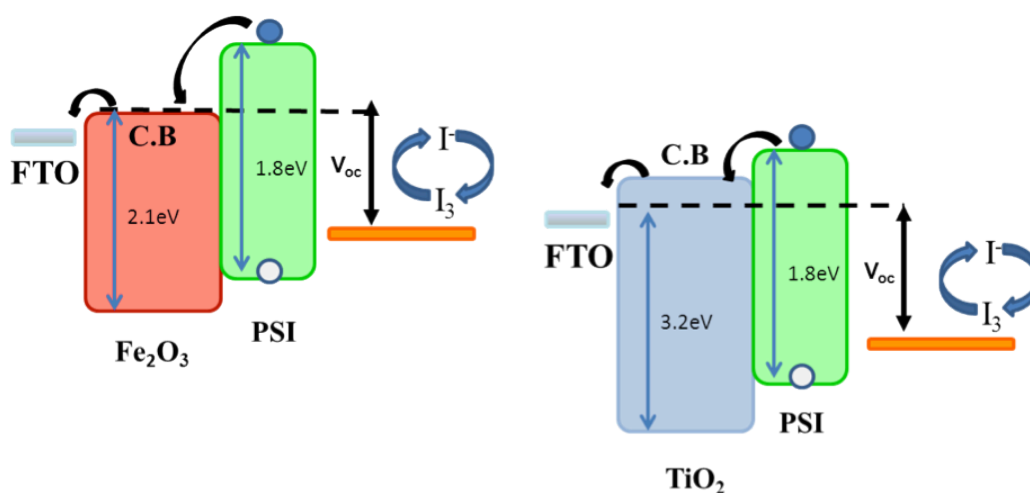


Figure 5.7. Energy band diagrams of fabricated solar cells.

If the change of the semiconductive layer has not affected the V_{oc} (kept constant, around 321 mV), the use of PSI-LHCI/ α -Fe₂O₃/FTO photoanode increased 60-fold the anodic photocurrent (I_{sc} = 56.9 μA) compared to the corresponding PSI-LHCI/TiO₂/FTO electrode (I_{sc} = 0.94 μA), thanks to the best energetic matching of the conduction band of hematite (2.1 eV) with P700* excited state (1.8 eV) (see **Fig. 5.7**).¹³

This factor makes thermodynamically favoured the electron injection from the sensitizer into the conduction band of hematite and increases therefore both photocurrent and solar energy conversion efficiency.¹⁴

Differently, despite the long story in photocatalysis and solar energy conversion of TiO₂, it displays low performances when combined with PSI because of its wide band gap (3.2 eV for the anatase form).

Apart from the *PSI- α -Fe₂O₃-FTO* and *PSI-TiO₂-FTO* photoanodes, also other electrodes with different conductive layers have been investigated, such as *PSI- α -Fe₂O₃-AAO* and *PSI-TiO₂-AAO* with anodic aluminium oxide (AAO) deposited on the glass. Also in these cases, PSI-LHCI has been immobilized by electrostatic interaction and bonds with the functionalized surface, exactly with the same procedure adopted over the FTO film. However, the cells fabricated on FTO displayed the highest conversion efficiency (over 170-fold) (**Table 5.1**). In particular, the devices *PSI- α -Fe₂O₃-AAO* and *PSI-TiO₂-AAO* suffer from 4-fold reduced open circuit voltage, due to the fast charge recombination dynamics within the AAO membrane. Furthermore, their low photovoltaic performances can also be attributed to adhesion problems of the semiconductor on the AAO/glass substrate,¹⁵ that has porous surface where α -Fe₂O₃ and TiO₂ grew as nanocrystals rather than uniform film, as over FTO, reducing the available adhesion area for PSI (see **Fig. 5.4**).

The purified PSI-LHCI complex showed photochemical activity of 940 ± 130 μ moles O₂/mg Chl/h and 710 ± 40 O₂/mg Chl/h at pH 8 and 4 respectively, as measured by the O₂ consumption assay (see **Table 5.2**) (oxygen consumption activity was calculated from the initial rates of oxygen evolution curves).

PSI-LHCI, when physisorbed or chemically cross-linked on hematite surface at pH 4, displays the same activity as in solution (see **Table 5.2**), and this is an indication of the effectiveness of PSI-LHCI and of its overall purification and immobilization treatments. Surprisingly, the photochemical performance of PSI-LHCI cross-linked to the hematite surface at pH 4 doubled, probably because of the most favourable arrangement of the super-complex, with donor-to-acceptor head-tail orientation of the consecutive PSI monolayers.

5.2.1.3. Sustained photo-electrochemical H₂ production using PSI-LHCI-functionalised hematite/FTO photoanode

The principle features candidating PSI as good system for protons to H₂ reduction are the millisecond range for the lifetime of its charge-separated state P700⁺F_B⁻ (around 60 ms), the low redox potential of its distal F_B cluster¹⁶ and the double ability to act both as electrons acceptor (P700⁺) and donor (F_B⁻). The former is important because longer lifetime for a species makes it longer available for any kind of process, allowing in the case here discussed the transfer of captured electrons to the catalyst. The second instead provides the necessary driving force for reduction of 2H⁺ to H₂ (and thus H₂ generation). All in all, the latter allows the use of PSI for generation of both anodic and cathodic photocurrents.¹⁷

The possible applicability of PSI in devices for H₂ evolution has been inferred from such properties and then confirmed by means of precise analyses.

Hydrogen evolution together with photocurrent production have been achieved through the coupling of the PSI-LHCI hematite based photoanode (working electrode) to a Pt coil (counterelectrode), both immersed in phosphate buffer at pH 7.4, and upon application of a proper bias potential¹⁸ (0.5 V vs random Ag wire as reference electrode) between them and proper irradiation. Taking into account the own photocatalytic activity of hematite, a selective excitation of PSI has been performed, applying a cut-off filter blocking the light below 590 nm, in order to excite the system at a wavelength of almost complete transparency for hematite. This condition allows the production of H₂ to be completely ascribable to PSI. To quantify the residual contribution of the semiconductor, both current and hydrogen evolution curves have been registered, besides for the electrode under analysis, for the control (α -Fe₂O₃/FTO), too. The results of these measurements are shown in **Fig. 5.8**, in combination with the corresponding analyses conducted in the dark for both control and specimen anodes. At this condition, almost no current and hydrogen are produced (full lines in **Fig. 5.8**), while upon illumination with light above 590 nm, an anodic photocurrent of $\sim 4.2 \times 10^{-6}$ A/cm² was observed for the PSI-LHCI/hematite/FTO electrode, and of 2×10^{-6} A/cm² for the control electrode, due to the residual photocatalytic activity of hematite (squared lines in **Fig. 5.8**).

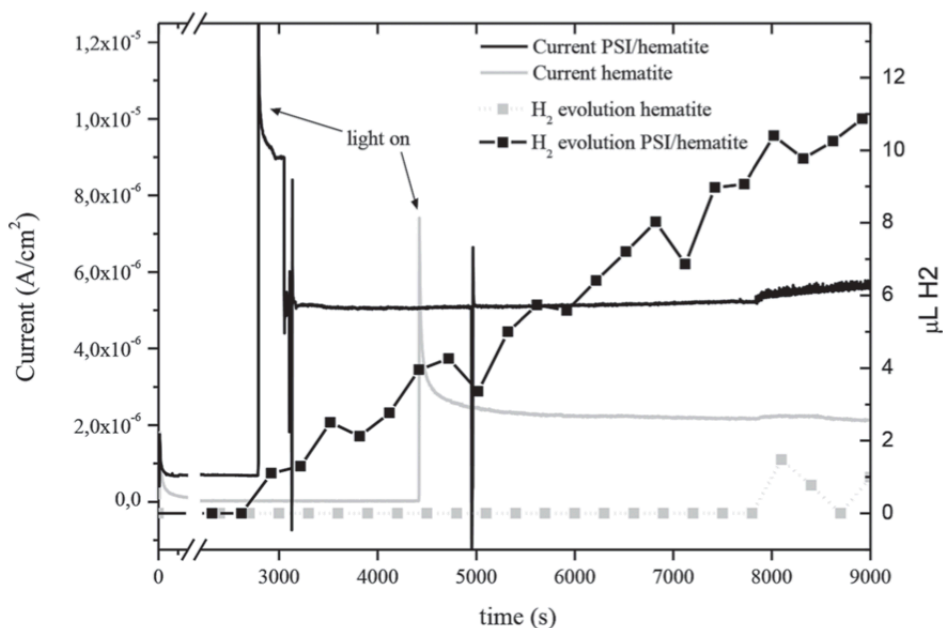


Figure 5.8. Generation of photocurrent and hydrogen evolution using PSI-LHCI-functionalised hematite photoanode. A BIAS potential of 0.5 V vs. random Ag electrode is applied. A cut-off filter of >590 nm is used. The sample is irradiated from ~ 2800 seconds onwards. Current and hydrogen evolution curves from a control (hematite/FTO) and PSI-LHCI/hematite/FTO photoanodes are shown in grey and black, respectively. (From Ref. 4)

In any cases, the anodic photocurrent generation has not shown considerable results. And the best performance has been reached in terms of photo-electrochemical H₂ production. The amount of produced H₂ was around 744 μ moles H₂/mg Chl/h, representing the highest value obtained for PSI-based solar-to-fuel nanodevices and distinctly attributable to the PSI action, since only traces of hydrogen have been detected in absence of the super-complex. To measure H₂ production, the headspace of

the vessel was continuously pumped through the GC column. Further information about the technique adopted to accomplish these results, together with the I-V measurements and photochemical activity investigation, is reported in reference.⁴

5.2.2. Photophysical investigation

The central discussion of this chapter is related to the photophysical investigation of PSI-hematite based electrodes. Such study has been performed in order to have a further proof, besides that related to the O₂ consumption reported above, about the retention of the functionalities of PSI-LHCI super-complex after all the treatments it undergoes before and during the immobilization on the semiconductor surface.

The point of view of this specific discussion is related to the twisted energy transfer events occurring in the macromolecule upon illumination.

The pigments of PSI-LHCI super-complex act cooperatively as antennas, collecting photons from the sunlight. The absorbed energy is then transferred amongst the same chromophores and finally to the P700 chlorophyll dimer in the reaction centre, working as primary photochemical trap. Here, the funnelled energy is converted into chemical oxidizing and reducing power that carries out the photosynthesis with evolution of molecular oxygen. In nature, energy transfer to the principle photoreceptor occurs with quantum efficiency that approaches unit.

Testing what happens when PSI is immobilized on the semiconductor can give information about the stability of the super-complex and about the effectiveness of the performed treatments of integration into the device. To this purpose, a deep understanding of absorption and emission properties, with particular attention on the fluorescence lifetime analysis, is essential. In fact, a better knowledge of the basic energy transfer events, as primary steps of the photosynthesis, can clarify organization and function of photosynthetic apparatus.

5.2.2.1. Absorption

PSI-LHCI super-complex contains two physically separate and distinguishable moieties in its structure: *a*) a core complex which in addition to the special reaction centre chlorophyll (Chl) pair, P700, and to the primary electron acceptors, also binds about 90 antenna Chl molecules, and *b*) the peripheral antenna complex (LHCI), binding more than 100 Chl molecules. Chlorophylls are embedded in the proteins mainly through chemical bond with their amino acid residues (for instance, coordination bonding between an imidazolyl nitrogen atom of His and a central Mg)¹⁹.

The overall pigments in the macromolecule display a strong absorption in the blue and red region of the spectrum, extended over 700 nm (see **Fig. 5.9**), and hundreds of chlorophylls and β -carotene molecules are the main absorbers. In particular, the absorption in the region between 450 and 550 nm predominantly originates from β -carotenes, while the chlorophylls cover the big portion of remaining spectral range, with absorption extended from the blue to the red region of the visible spectrum, with highest values of the molar absorptivity at $\lambda_1 = 438$ nm and $\lambda_2 = 679$ nm.

The chlorophyll molecules are the dominating species in the super-complex absorption profile. They are based on a chlorin ring, containing four pyrrole units with different substituents in the β -positions and an additional 5-membered ring. Such framework coordinates one Mg^{2+} ion through the nitrogen atoms of its core.

The keto group on the 5-membered ring is responsible for the large extinction coefficients in visible and near-infrared regions.

The UV-Vis absorption spectrum of the *C. merolae* PSI-LHCI in solution (3 μ g Chl in a buffer composed of 40 mM HEPES, pH 8, 3 mM $CaCl_2$, 25% glycerol and 0.03% DDM) is shown in **Fig. 5.9** together with that of α - Fe_2O_3 /FTO slide.

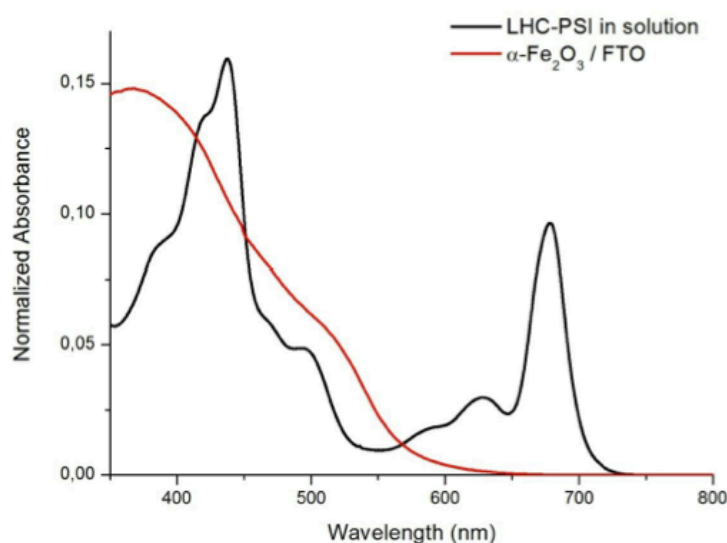


Figure 5.9. RT UV–VIS absorption spectroscopy of α - Fe_2O_3 /FTO and *C. merolae* PSI-LHCI in solution. For spectroscopy, purified *C. merolae* PSI-LHCI complex (3 μ g Chl) was resuspended in a buffer composed of 40 mM HEPES, pH 8, 3 mM $CaCl_2$, 25% glycerol and 0.03% DDM. (From Ref. 4)

The super-complex spectrum can be interpreted in agreement with the Gouterman Four-Orbital Model,²⁰ adopted for porphyrins (see Chapter 4). According to it, the absorption bands representing the fingerprint for porphyrin systems originate from two different transitions between two HOMOs and two LUMOs near degenerate frontier orbitals.²¹ The mixing of the non-degenerate corresponding two states induces a splitting in energy, giving rise to a higher energy state with greater extinction coefficient, associated to the Soret or B band, and a lower energy state with lower extinction coefficient, that originates the Q band. Both B and Q bands, arise from transitions of similar π - π^* nature²² but display different relative intensities, with the Soret more intense than the Q bands.

Possible metal centre and substituents on the ring of the chlorin frame, affect the relative energies of these transitions, altering the absorption profile. In fact, in chlorophylls, due to the symmetry lowering, the absorption spectrum appears more featured, with additional bands as result of the degeneracy removal. In particular, the effect is the doubling of Q and B transitions in the Q_x/Q_y and B_x/B_y bands, respectively. In Chls the overall Q and B bands, differently from porphyrins, display similar

extinction coefficients.^{21b} Then, the intensities of Q_x and Q_y bands are not equal and Q_x , laying at shorter wavelengths, is much weaker than Q_y . The B band does not appear in its split form because of an accidental degeneracy. The Q_y absorption band peaking at 680 nm arises from an overlap of a series of Chl spectral forms, such as those of the reaction centre, those contained in the LHCI belt, and a species of slightly different Chl contained in LHCI and characterized by few nanometres of shift for maximum absorption peaks.

Apart from the main distinguishable features, the absorption profile of multicomponent systems like PSI-LHCI, are not always of straightforward interpretation. Thus, recently further theoretical analyses have been reported to attribute carefully the exact nature of absorption bands.²³ According to the results of such calculations, the tail over 700 nm can be safely ascribed to the P700 Chl dimers.²⁴

Fig. 5.9, besides absorption shape of PSI, shows also hematite absorption spectrum (red line), with its broad and not structured profile. It can be described by the presence of three main types of transitions embedded in the broad curve: spin-forbidden d–d ligand field transitions band, centred in the metal ($t_{2g} \rightarrow e_g$), at low energy, partially allowed transition with mixed LMCT and d–d nature, at intermediate energy, and allowed ligand-to-metal charge transfer (LMCT) transitions (oxo-to-Fe charge transfer transitions) at short wavelengths.²⁵

Thus, also the semiconductive layer is able of light absorption and this has represented a problem in performing the measurements discussed above. In fact, due to its absorption ability, it can affect the amount of H_2 evolved by PSI-hematite photoanode, making difficult to quantify exactly the performances produced just by PSI units. This problem has been overcome or at least minimized, through selective excitation of the super-complex, by fixing the wavelength at 590 nm, where hematite contribution is negligible.

5.2.2.2. Emission

Steady state fluorescence spectra have been recorded at room temperature for a buffer solution (PBS at pH 7.4) of PSI-LHCI, as model, for the electrode containing only hematite on FTO glass, as mere control, and for three different PSI-containing electrodes as specimens (see **Fig. 5.10**). Two of these photoanode prototypes are composed of the complete pattern of PSI in the physisorbed and covalently cross-linked multilayer fashion on FTO and AAO surfaces respectively, while the third contains PSI just physisorbed on hematite-FTO glass.

From steady state analysis (**Fig. 5.10**), a 6-12 nm blue shift of the emission peaks has been observed on passing from the solution to the immobilized system ($\lambda_{max} = 689$ nm and 683-676 nm, respectively) (**Table 5.3**) probably as effect of the rigidity, responsible for the changes in Chl-protein interactions.

A similar phenomenon has been observed for C-phycoerythrin upon its covalent cross-linking with hematite.¹²

At room temperature, the observed fluorescence peaking at about 690 nm is ascribable to bulk chlorophyll units for all the specimens, and in particular to their low-lying excited level S_1 , efficiently populated upon rapid internal conversion from the singlet excited states at higher energies.

The shoulder at about 645 nm, particularly intense in the specimen **A**, seems to originate

from residual contamination of PSI-linked phycobilisome sub-complex, and in particular from the phycocyanin residues present in its rods, probably not completely removed during the red-alga purification.²⁶

From **Fig. 5.11** it is possible to observe that the fluorescence spectra show very small Stokes' shifts (*ca.* 10 nm) and good mirror symmetry with the lowest energy absorption Q bands.

In contrast with the high fluorescence quantum yield exhibited by pure solution of Chl

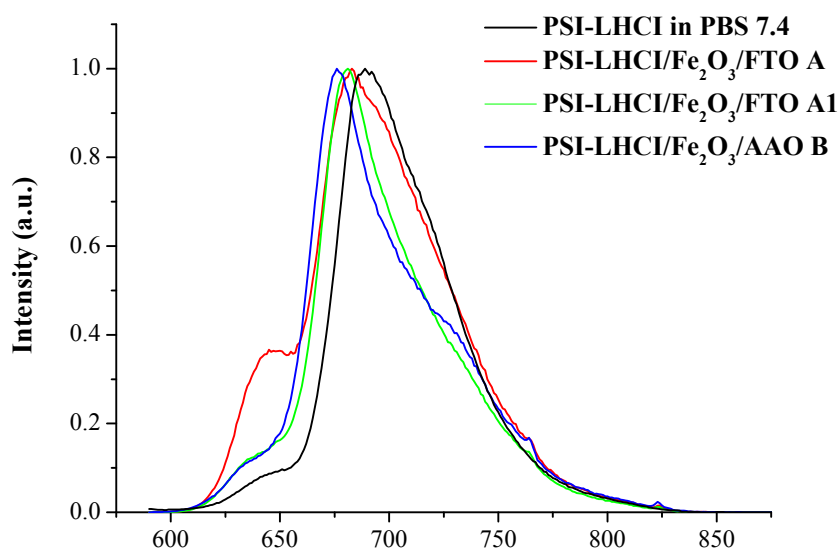


Figure 5.10. Normalized emission spectra at room temperature of PSI-LHCI in PBS 7.4 solution (black), **A** physically adsorbed on Fe₂O₃/FTO (red), **A1** covalently bound to Fe₂O₃/FTO (green), and **B** covalently bound to Fe₂O₃/AAO (blue); $\lambda_{ex} = 600$ nm.

(the value reported in literature for ether solution is around 0.3) its emission when embedded in photosynthetic apparatuses as PSI decreases dramatically. The overall mechanism responsible for such quenching has been under debate for long time and many interpretations have been produced, comprising several competition pathways.²⁷ Photochemical reactions, charge recombination phenomena, thermal deactivation and photo-induced energy transfer events to non-fluorescent pigments or to the reaction centre dimer have been supposed to participate to the global deactivation process.

In particular, here the discussion will be focused on the energy transfer pathways. In fact, for example, due to the relative stability of the oxidized state of P700, its return to the ground state by simple charge recombination seems to be disfavoured. Actually, after the initial photo-induced electron transfer responsible for the production of P700⁺ species, a series of stabilizing, rapid, secondary charge-transfer events occur preventing undesirable charge-recombination reactions by spatially separating holes and electrons. Moreover, the fact that part of absorbed energy is dissipated as heat in the P700 side increases the role of energy trap for the dimer, making the process almost completely irreversible.

As a matter of fact, the energy transfer to the P700 dimer is the main responsible for the

fluorescence quenching. Back energy transfer from reaction centres to the antennae could be possible too but, according to Butler's original model for PSI deactivation, the rate constant of energy transfer towards the RC is much higher than the one of the reverse competitive process.^{28, 27}

5.2.2.3. Energy transfer and Time resolved fluorescence analysis

The combination of absorption from the pigments of LHCI with that from the chromophores contained in the RC permits to reach optimal performances in terms of rate for the process and to capture light from a larger spectral range than that covered by the reaction centre alone.

Most antenna systems contain an intrinsic arrangement based on the displacement of lower wavelength absorbing pigments at the most distal sections, in communication with the longer wavelength absorbing chromophores, closer to reaction centre. Such organization, through energy losses as heat during the energy transfer from excited-state donor pigments to ground-state acceptor pigments, provides a degree of irreversibility to the overall process, promoting effective collection of excitation energy by the red absorber P700 dimer, as unique final collector.

The singlet-singlet energy transfer events occurring mainly between chlorophyll units can be safely described by the Förster model (see Chapter 1).

Förster theory is based on the assumption that donor and acceptor are weakly coupled and their transition dipoles interact through coulombic interaction. The mutual orientation between the pigments can affect the energy transfer process, and its rate constant is indeed proportional to the interchromophoric distance to the inverse sixth power and to the spectral overlap between absorption spectrum of the acceptor and fluorescence spectrum of the donor. Thus, a couple of pigments, to undergo highly efficient energy transfer process, has to display high values of luminescence quantum yield for the isolated donor, high values of molar absorptivity for the acceptor and good spectral overlap of donor emission and acceptor absorption.

The structural complexity of the PSI-LHCI super-complex results in an increased kinetic heterogeneity and big variability in lifetimes thus it requires time resolved investigations.

Time resolved measurements of the model PSI-LHCI super-complex in solution and immobilized on FTO or AAO surfaces have been recorded at room temperature with excitation at 637 nm. The obtained results are shown in **Figure 5.12** and **5.13** as fluorescence lifetime maps, in which the emissions registered at different wavelengths are reported as function of the time and reveal a clear elongation of emission lifetimes for the immobilized PSI with respect to that in solution.

Every kinetic trace obtained from such measurements has been adequately fitted through three or four exponential lifetime components. The resulted values of lifetime (36-38 ps, 200-240 ps, 620-640 ps and 1.47-1.63 ns) are reported in **Table 5.3** together with the corresponding global χ^2 parameters, while the decays obtained at emission wavelength $\lambda_{em} = 637$ nm are shown in **Figure 5.14** and **5.15** with the corresponding fitting. Moreover, the time resolved fluorescence decay associated spectra (FDAS) resulting from all these data, are displayed in **Figure 5.16** and **5.17**. They show similar overall behaviour with just slight differences in the shapes. In particular, for the

photoanode with PSI just physically adsorbed on the hematite surface, FDAS associated to the shorter major component displays, as for PSI in PBS solution, a more broadened band with respect to those with cross-linking, that instead are narrower over both FTO and AAO. Such difference accounts for different effects on the emitting structure induced by the different (physical and chemical) kinds of immobilization.

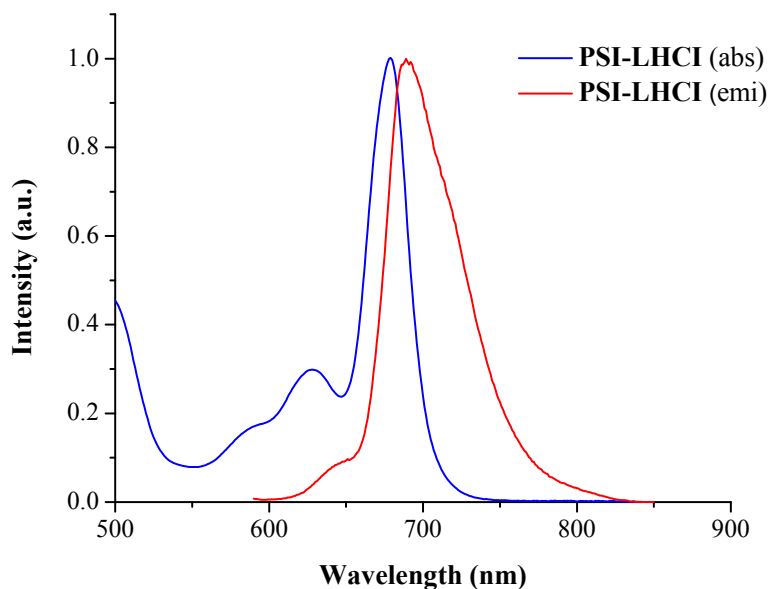


Figure 5.11. Normalised absorption (Q bands region) and emission spectra at room temperature of PSI-LHCI in PBS 7.4 solution ($\lambda_{ex} = 600$ nm).

The procedure adopted to obtain these FDAS required two main steps, such as: first of all, the convolution of the fluorescence decay with the measured instrumental response function ($fwhm \approx 230$ ps) and after, the fitting of convoluted decays to a sum of exponentials by global fitting analysis. The corresponding spectral profiles result by plotting the amplitudes of the individual kinetic components as function of the wavelength. Among the calculated lifetime values (see **Table 5.3**), the dominating shorter component is associated to photochemical trapping processes occurring in the PSI reaction centre, through energy transfer from its chromophoric units to the main quencher P700.

The fluorescence decay with lifetime around 200 ps is likely to be ascribed to the peripheral antenna systems of LHCI, quenched by the PSI core, energetically coupled to it. This phase seems to be absent in the samples prepared on the Fe_2O_3 /AAO membrane. The observed component with lifetimes around 500-600 ps indicates the presence of slowed energy transfer processes between the peripheral antennas in the LHCI and the PSI core.

This might come from a distortion of the protein structure upon immobilization on the hematite surface that can increase the distance between the pigments without affecting the overall functionality of PSI. Less than 5% of the fluorescence decay is related to processes occurring in the nanosecond time range that might be associated to uncoupled or free chlorophylls. The presence of such molecules is due to the fact that, during

device fabrication, self-assembled monolayers of photosynthetic complexes must survive both washing steps, to remove surplus of non-specifically bound materials, and drying steps, to prepare the substrate for deposition of the protective coating. Moreover, the complexity and size of PSI makes it especially sensitive to degradation and dissociation. Time resolved fluorescence analysis of the PSI-LHCI super-complex in solution and upon its immobilization on the hematite/FTO photoanode additionally confirmed intactness of PSI-LHCI, albeit the fastest ps decay component 2.5-fold slower for the immobilised PSI-LHCI super-complex, whose reason is currently unknown.

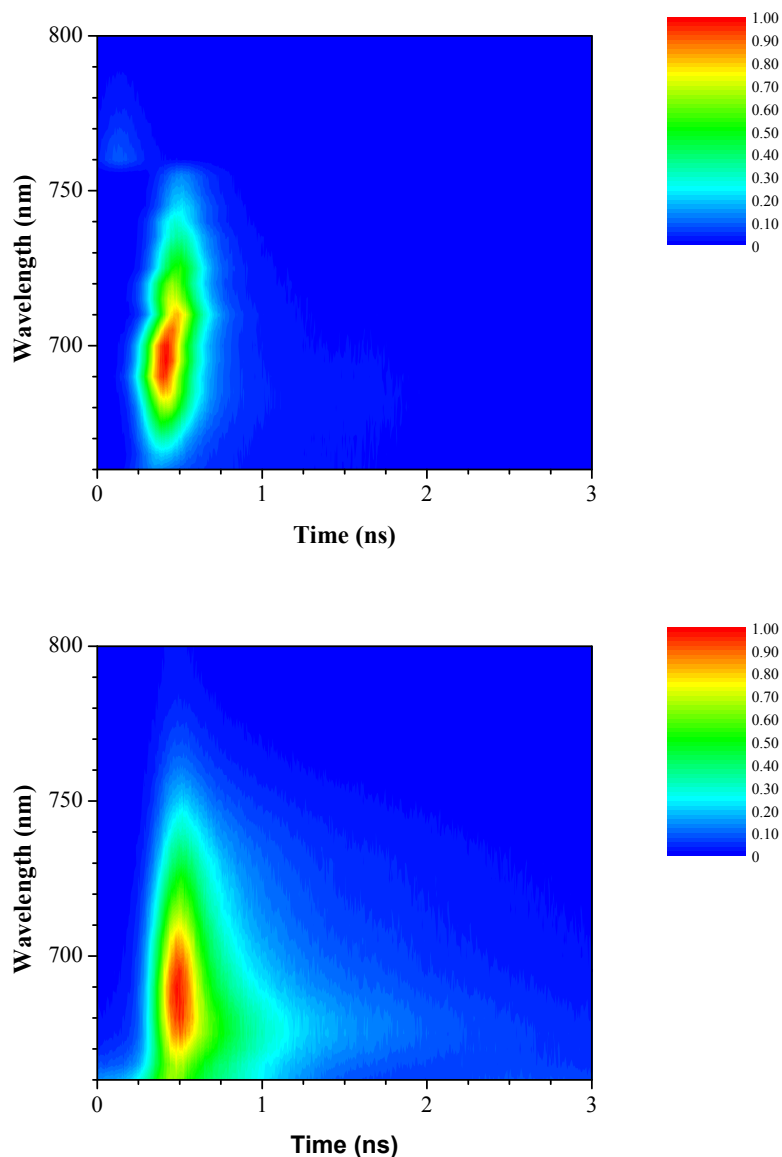


Figure 5.12. Fluorescence decay maps at room temperature of PSI-LHCI in PBS pH 7.4 solution (top) and covalently bound to Fe₂O₃/AAO (bottom); $\lambda_{ex} = 637$ nm.

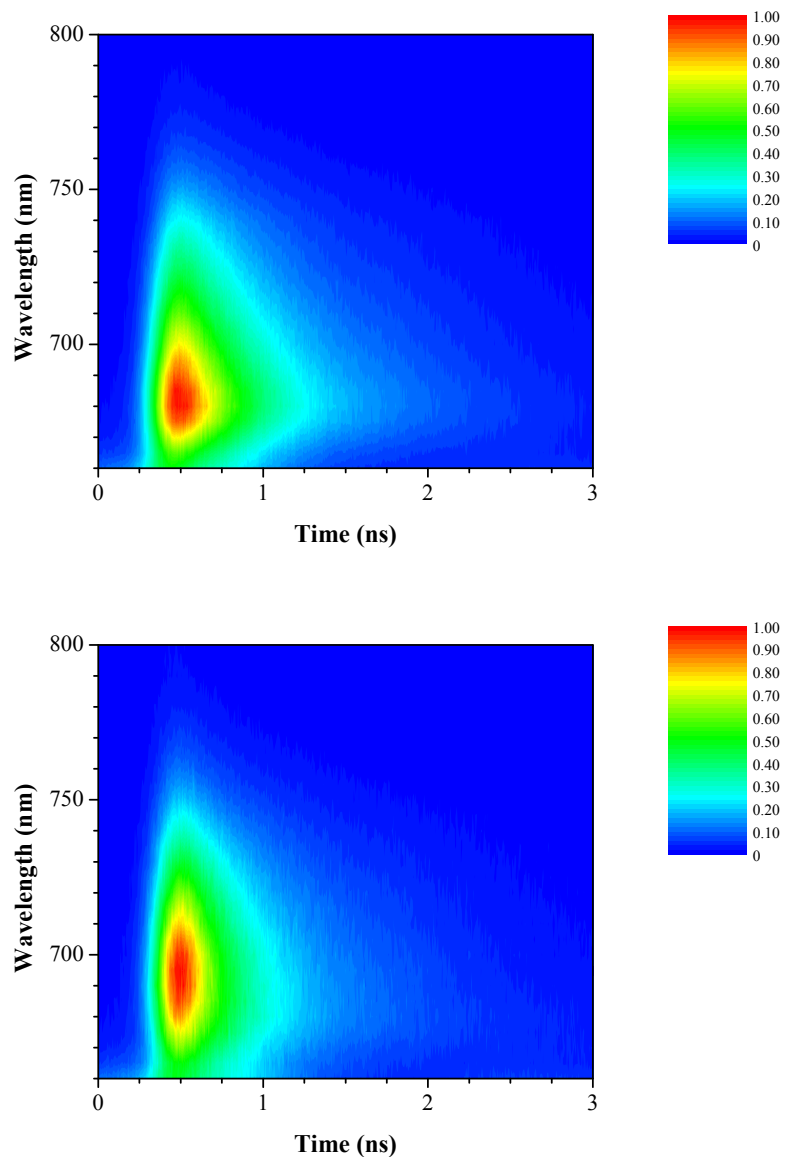


Figure 5.13. Fluorescence decay maps at room temperature of PSI-LHCI covalently bound to $\text{Fe}_2\text{O}_3/\text{FTO}$ (top) and physically adsorbed on $\text{Fe}_2\text{O}_3/\text{FTO}$ (bottom); $\lambda_{ex} = 637$ nm.

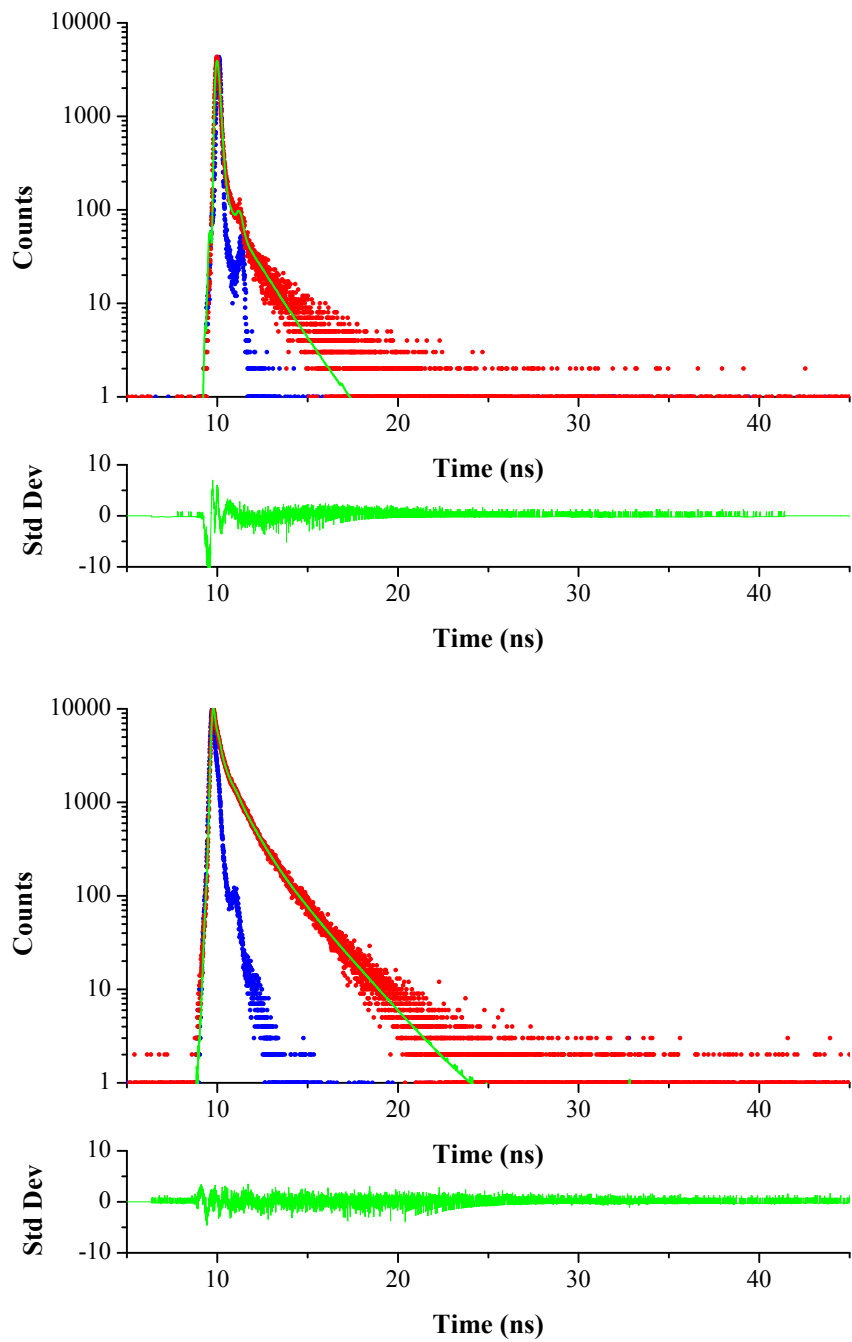


Figure 5.14. Fluorescence decays at 685 nm at room temperature of PSI-LHCI in PBS pH 7.4 solution (top) and covalently bound to Fe₂O₃/AAO (bottom); $\lambda_{\text{ex}} = 637$ nm.

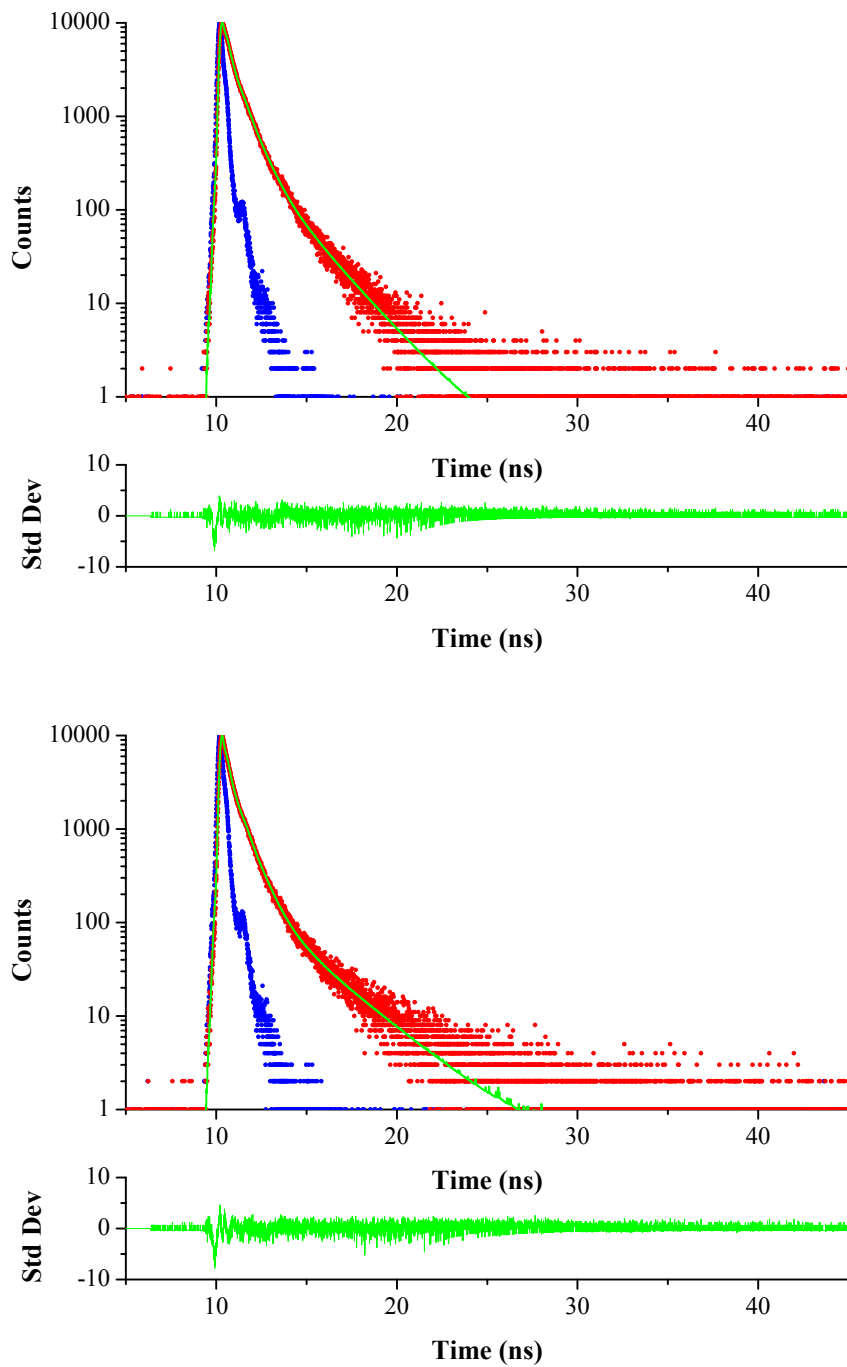


Figure 5.15. Fluorescence decays at 685 nm at room temperature of PSI-LHCI covalently bound to Fe₂O₃/FTO (top) and physically adsorbed on Fe₂O₃/FTO (bottom); $\lambda_{\text{ex}} = 637$ nm.

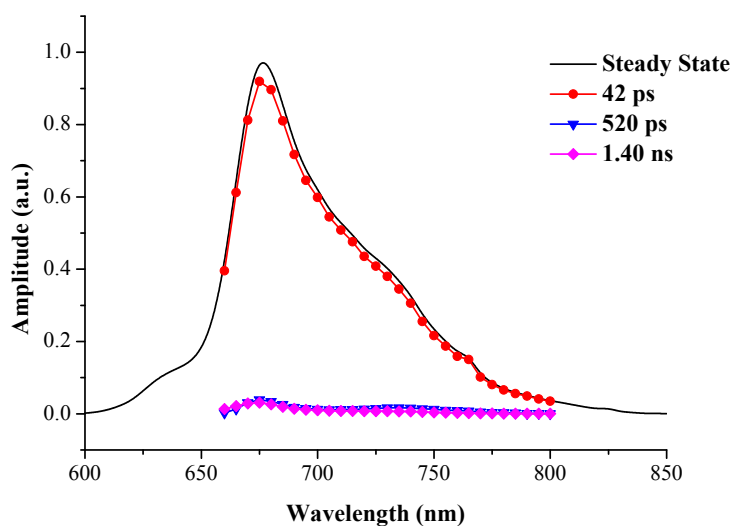
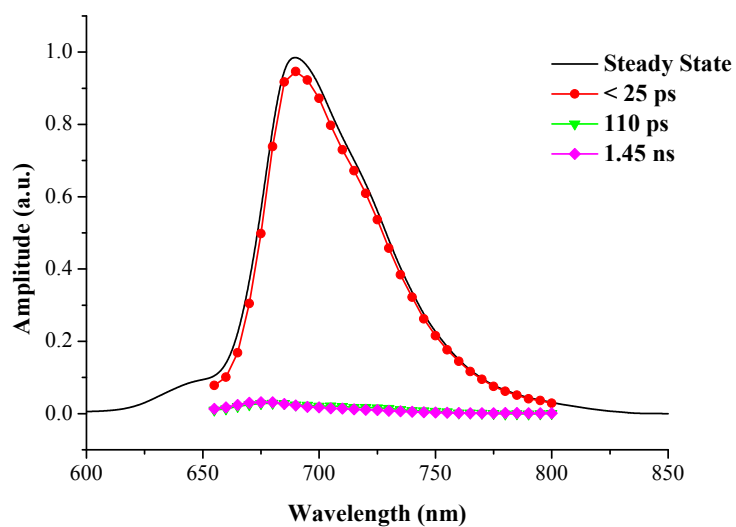


Figure 5.16. Fluorescence decay associated spectra (FDAS) at room temperature of PSI-LHCI in PBS pH 7.4 solution (top) and covalently bound to Fe₂O₃/AAO (bottom); $\lambda_{ex} = 637$ nm.

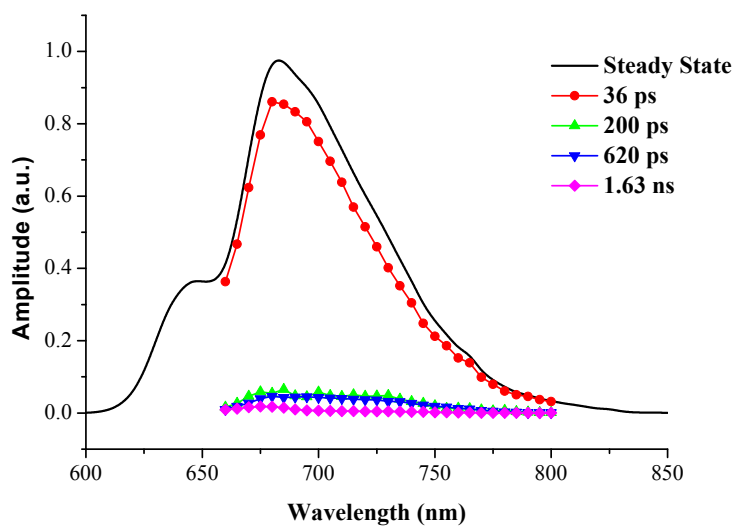
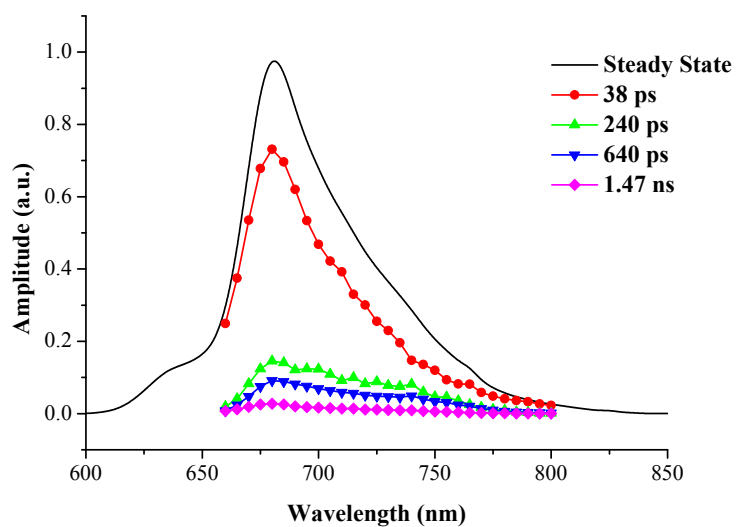


Figure 5.17. Fluorescence decay associated spectra (FDAS) at room temperature of PSI-LHCI covalently bound to Fe₂O₃/FTO (top) and physically adsorbed on Fe₂O₃/FTO (bottom); $\lambda_{ex} = 637$ nm.

Table 5.1. Photovoltaic properties of fabricated solar cells.

Solar cell	I_{sc} , μA	V_{oc} , mV	FF	η , %
PSI/TiO ₂ /FTO	0.94	260	0.60	0.026
PSI/Fe ₂ O ₃ /FTO ^[a]	56.9	321	0.56	0.170
PSI/Fe ₂ O ₃ /FTO ^[b]	18.7	295	0.38	0.021
PSI/TiO ₂ /AAO	2.50	86	0.27	0.001
PSI/Fe ₂ O ₃ /AAO	55.1	78	0.22	0.016

^a PSI immobilization at pH 4; ^b PSI immobilization at pH 7.4.

Table 5.2. Photo-electrochemical activity of *C. merolae* LHC-PSI in solid state and in vitro systems.

	Physisorbed PSI/ hematite	Cross-linked PSI/ hematite	PSI in solution pH 8	PSI in solution pH 4	PSI in solution pH 4 ^(c)
Activity, μ moles O ₂ /mg Chl/h	873.2 \pm 103	900.9 \pm 84 ^[a] 1923.6 \pm 560 ^[b]	942 \pm 127	707.8 \pm 36	630 \pm 3.6

^a PSI immobilization at pH 7.4; ^b PSI immobilization at pH 4; ^c PSI was incubated at pH 4.0 then transferred to pH 8.0 to estimate the recovery of photocatalytical activity. The activity was measured after 90 days after preparation of electrodes.

Table 5.3. Lifetime components from the global analysis of *C. merolae* PSI-LHCI fluorescence decays.

	λ_{max} , nm	τ_1 , ps	τ_2 , ps	τ_3 , ps	τ_4 , ps	Global χ^2
PSI in PBS	689	16 \pm 2	-	400 \pm 30	1470 \pm 10	0.9910
Fe ₂ O ₃ /FTO ^[a]	683	36 \pm 3	200 \pm 90	620 \pm 30	1630 \pm 50	1.0064
Fe ₂ O ₃ /FTO ^[b]	681	38 \pm 4	240 \pm 20	640 \pm 30	1470 \pm 20	1.0206
Fe ₂ O ₃ /AAO ^[b]	676	42 \pm 2	-	520 \pm 30	1400 \pm 10	1.0116

^a Physically adsorbed; ^b Covalently bound. λ_{ex} = 637 nm.

5.3. Conclusions

The photoanodes produced through physical and/or chemical immobilization over TiO₂ or Fe₂O₃ semiconductor surface of PSI-LHCI super-complex, extracted from the extremophilic red microalga *Cyanidioschyzon merolae*, have been analyzed by means of several techniques in order to establish their electrical performances and H₂ evolution ability, and by FE-SEM and X-ray analysis, to clarify their structural features.

Morphological analysis revealed that immobilized PSI-LHCI appears in a well-structured 165 nm multilayers arrangement, organized over the semiconductor as vertically oriented and highly ordered nanocrystalline nanotube arrays.

The electronic coupling between the red algal PSI-LHCI and the hematite film, has produced a bio-hybrid DSSC displaying a 2-fold improved solar-to-electric quantum efficiency compared to corresponding already reported device⁷ but currently below the practical use.

Despite the modest electric performance, a quite good result has been obtained in terms of photoelectrochemical H₂ production. Upon illumination with visible light above 590 nm and application of a BIAS potential between the PSI-LHCI/hematite photoanode and a platinum counter electrode, the highest molecular hydrogen evolution rate (744 μmoles H₂/mg Chl/h) amongst the PSI-based solar-to-fuel nanodevices is registered. Such record can be attributed to the smart engineering of the device. In fact, the large nanostructured photoactive surface area, the extended absorption of light into the red region of the visible spectrum and the stabilized charge separation within the hematite layer have been the key features of the successful results.

Another point of strength for this PSI-hematite based photoanodes has been confirmed by steady state and time resolved spectroscopy. Such techniques have demonstrated perfect retention of the photochemical properties in the macromolecule, accounting for its complete stability to the overall procedures of purification and integration into the semiconductor layer.

This positive behaviour has been observed for both physisorbed and/or covalently cross-linked PSI-LHCI on the semiconductor surface.

Time resolved experiments helped in the interpretation of steady state fluorescence emissions, revealing from fluorescence decay analysis the presence of three/four chlorophyll components, contributing to the global luminescence. Among them the lifetime values of 36-38 ps, 200-240 ps, 620-640 ps, for the shorter-lived Chls, compared to the minor component attributed to free or unbound Chls of 1.47-1.63 ns, inform that chlorophylls responsible for the emission display various degrees of quenching, maybe as function of the disposition among the layers. The shortest component indeed is ascribable to the emission of Chls of the PSI core, resulting almost completely quenched by fast energy transfer towards the P700 dimer. The lifetime around 200 ps is probably related to the peripheral chromophores of the belt LHCI, quenched through energetic coupling to the PSI core. The third relatively long-lived species, identified by a lifetime around 500-600 ps, is supposedly located in the peripheral antenna LHCI as the previous one, but its less efficiently quenched by the energy transfer towards the PSI core, due to a distortion of the protein structure upon

immobilization on the semiconductor surface, resulting in an increase of the distance between donor and acceptor. The nanosecond component reveals the presence of uncoupled or free chlorophylls but it participates just with a contribution to the global fluorescence of 5%.

Thus, taking into account the low values of lifetimes for the overall species and the resulting high efficiency of energy transfer (around 1 as in solution), it is safe to assume that the discussed immobilization processes do not affect the overall functionality of PSI-LHCI, allowing it to retain the good performances as antenna system, as shown in nature.

5.4. References

-
- ¹ (a) G. Kodis; P. A. Liddell; A. L. Moore; T. A. Moore; D. Gust, *J. Phys. Org. Chem.* 2004, **17**, 724-734; (c) P. A. Liddell; D. Kuciauskas; J. P. Sumida; B. Nash; D. Nguyen; A. L. Moore; T. A. Moore; D. Gust, *J. Am. Chem. Soc.* 1997, **119**, 1400-1405; (c) H. Imahori, *Org. Biomol. Chem.* 2004, **2**, 1425-1433.
- ² W. J. Youngblood; S. H. A. Lee; Y. Kobayashi; E. A. Hernandez-Pagan; P. G. Hoertz; T. A. Moore; A. L. Moore; D. Gust; T. E. Mallouk, *J. Am. Chem. Soc.* 2009, **131**, 926-927.
- ³ D. Gust; T. A. Moore and A. L. Moore, *Acc. Chem. Res.* 2009, **42**, 1890-1898.
- ⁴ K. Ocakoglu; T. Krupnik; B. van den Bosch; E. Harputlu; M. P. Gullo; J. D. Janna Olmos; S. Yildirimcan; R. K. Gupta; F. Yakuphanoglu; A. Barbieri; J. Reek and J. Kargul, *Adv. Funct. Mater.* 2014, **24**, 7467-7477.
- ⁵ A. Busch; J. Nield; M. Hippler, *Plant J.*, 2010, **62**, 886-897.
- ⁶ K. Brettel and W. Leibl, *BBA-Bioener.* 2001, **1507**, 100-114.
- ⁷ A. Mershin; K. Matsumoto; L. Kaiser; D. Yu; M. Vaughn; M. K. Nazeeruddin; B. D. Bruce; M. Graetzel and S. Zhang, *Sci. Rep.* 2012, **2**, 1-7
- ⁸ (a) C. Ciniglia; H. S. Yoon; A. Pollio; G. Pinto and D. Bhattacharya, *Mol. Ecol.* 2004, **13**, 1827-1838; (b) H. Nozaki; H. Takano; O. Misumi; K. Terasawa; M. Matsuzaki; S. Maruyama; K. Nishida; F. Yagisawa; Y. Yoshida; T. Fujiwara; S. Takio; K. Tamura; S. J. Chung; S. Nakamura; H. Kuroiwa; K. Tanaka; N. Sato; T. Kuroiwa, *BMC Biol.* 2007, **5**, 28; (c) H. Nozaki; M. Matsuzaki; M. Takahara; O. Misumi; H. Kuroiwa; M. Hasegawa; T. Shin-I; Y. Kohara; N. Ogasawara and T. Kuroiwa, *J. Mol. Evol.* 2003, **56**, 485-497.
- ⁹ T. Krupnik; E. Kotabová; L. S. van Bezouwen; R. Mazur; M. Garstka; P. J. Nixon; J. Barber; R. Kaňa; E. J. Boekemal and J. Kargul, *J. Biol. Chem.* 2013, **288**, 23529-23542.
- ¹⁰ P. Jordan; P. Fromme; H. T. Witt; O. Kluka; W. Saenger; N. Krauss, *Nature* 2001, **411**, 909-917.
- ¹¹ (a) R. Das; P. J. Kiley; M. Segal; J. Norville; A. Amy Yu; L. Wang; S. A. Trammell; L. E. Reddick; R. Kumar; F. Stellacci; N. Lebedev; J. Schnur; B. D. Bruce; S. Zhang and M. Baldo, *Nano Lett. Am. Chem. Soc.* 2004, **4**, 1079-1083; (b) C. J. Faulkner; S. Lees; P. N. Ciesielski; D. E. Cliffel and G. K. Jennings, *Langmuir* 2008, **24**, 8409-8412; (c) P. N. Ciesielski; C. J. Faulkner; M. T. Irwin; J. M. Gregory; N. H. Tolks; D. E. Cliffel and G. K. Jennings, *Adv. Funct. Mater.* 2010, **20**, 4048-4054; (d) P. N. Ciesielski; F. M. Hijazi; A. M. Scott; C. J. Faulkner; L. Beard; K. Emmett; S. J. Rosenthal; D. Cliffel; G. K. Jennings, *Bioresour. Technol.* 2010, **101**, 3047-3053; (e) P. N. Ciesielski; A. M. Scott; C. J. Faulkner; B. J. Berron; D. E. Cliffel and G. K. Jennings, *ACS Nano* 2008, **2**, 2465-2472; (f) N. Terasaki; N. Yamamoto; T. Hiraga; Y. Yamanoi; T. Yonezawa; H. Nishihara; T. Ohmori; M. Sakai; M. Fujii; A. Tohri; M. Iwai; Y. Inoue; S. Yoneyama; M. Minakata and I. Enami, *Angew. Chem. Int. Ed.* 2009, **48**, 1585-1587; (g) N. Terasaki; N. Yamamoto; K. Tamada; M. Hattori; T. Hiraga; A. Tohri; I. Sato; M. Iwai; M. Iwai; S. Taguchi; I. Enami; Y. Inoue; Y. Yamanoi; T. Yonezawa; K. Mizuno; M. Murata; H. Nishihara; S. Yoneyama; M. Minakata; T. Ohmori; M. Sakai; M. Fujii, *BBA-Bioener.* 2007, **1767**, 653-659; (h) O. Yehezkel; R. Tel-Vered; J. Wasserman; A. Trifonov; D. Michaeli; R. Nechushtai and I. Willner, *J. Phys. Chem. B* 2010, **114**, 14383-14388; (i) A. Badura; D. Guschin; T. Kothe; M. J. Kopczak; W. Schuhmann and M. Rögner, *Energy Environ. Sci.* 2011, **4**, 2435-2440.

¹² D. K. Bora; E. A. Rozhkova; K. Schrantz; P. P. Wyss; A. Braun; T. Graule; E. C. Constable; *Adv. Funct. Mater.* 2012, **22**, 490-502

¹³ The different solar cell characteristics such as fill factor (FF) and overall energy conversion efficiency (η) were calculated using the following equations (K. Wongcharee; V. Meeyoo; S. Chavadej, *Sol. Energy Mater. Sol. Cells* 2007, **91**, 566-571):

$$FF = \frac{(I_{\max} \times V_{\max})}{(I_{sc} \times V_{oc})}$$
$$\eta = \frac{(V_{oc} \times I_{sc} \times FF)}{P_{in}}$$

where, I_{\max} and V_{\max} are the photocurrent and photovoltage for maximum power output, and I_{sc} and V_{oc} are the short-circuit photocurrent and open-circuit photovoltage, respectively. P_{in} is the power of incident light.

¹⁴ (a) M. Cavas; R. K. Gupta; A. A. Al-Ghamdi; Z. H. Gafer; F. El-Tantawy; F. Yakuphanoglu; *Mater. Lett.* 2013, **105**, 106-109; (b) M. J. Katz; S. C. Rihaa; N. C. Jeonga; A. B. F. Martinson; O. K. Farhaa; J. T. Hupp, *Coord. Chem. Rev.* 2011, **256**, 2521-2529.

¹⁵ G. K. Mor, K. Shankar, M. Paulose, O. K. Varghese and C. A. Grimes, *Nano Lett.* 2006, **6**, 215-218.

¹⁶ (a) C. E. Lubner; R. Grimme; D. A. Bryant; J. H. Golbeck, *Biochem.* 2010, **49**, 404-414; (b) R. E. Blankenship, *Science* 2011, **332**, 805-809.

¹⁷ O. Yehezkel; R. Tel-Vered; D. Michaeli; I. Willner; R. Nechushtai, *Photosynth. Res.* 2014, **120**, 71-85.

¹⁸ The bias voltage is the amount of voltage that an electronic device needs in order to power on and promote the current flow, generating an electric field stronger than that produced by photoinduced charge separation.

¹⁹ (a) T. Oba; H. Tamiaki, *Photosynth. Res.* 2002, **74**, 1-10; (b) T. Oba; H. Tamiaki, *Bioorg. Med. Chem.* 2005, **13**, 5733-5739.

²⁰ (a) M. Gouterman, *J. Mol. Spectrosc.* **1961**, **6**, 138-163; (b) M. Gouterman; G. H. Wagnière; L. C. Snyder, *J. Mol. Spectrosc.* **1963**, **11**, 108-127.

²¹ (a) L. R. Milgrom, *The Colours of Life: An Introduction to the Chemistry of Porphyrins and Related Compounds*, OUP, Oxford, 1997; (b) M. Gouterman, *The Porphyrins*, ed. D. Dolphin, Academic Press, New York, 1978, **3**, 1.

²² D. F. Marsh and L. M. Mink, *J. Chem. Ed.* 1996, **73**, 1188-1190.

²³ (a) J. Linnanto; J. Korppi-Tommola, *Phys. Chem. Chem. Phys.* 2000, **2**, 4962-4970; (b) J. Linnanto; J. Korppi-Tommola, *J. Phys. Chem. A* 2004, **108**, 5872-5882

²⁴ E. G. Andrizhivetskaya; T. M. Schwabe; M. Germano; S. D'Haene; J. Kruij; R. van Grondelle; J. P. Dekker, *Biochim. Biophys. Acta* 2002, **1556**, 265-272

²⁵ (a) P. Liao, E.A. Carter, *J. Phys. Chem. C* 2011, **115**, 20795-20805; (b) L. A. Marusak; R. Messier and W. B. White, *J. Phys. Chem. Solids* 1980, **41**, 981-984

²⁶ (a) A. Busch; J. Nield and M. Hippler, *Plant J.* 2010, **62**, 886-897.

²⁷ G. H. Krause, *Annu. Rev. Plant Physiol. Plant Mol. Biol.* 1991, **42**, 313-349.

²⁸ (a) W. L. Butler, *Encyclopedia of Plant Physiology*, ed. A. Trebst, N. Avron, 1977, **5**, 149-167. Berlin: Springer-Verlag; (b) W. L. Butler, *Annu. Rev. Plant Physiol.* 1978, **29**, 345-378.

Chapter 6

6. Experimental Section

6.1. Absorption spectra

The experiments were carried out on solutions contained in quartz cuvettes (from 10 mm to 1 mm optical path) at room temperature. The absorption spectra were recorded with a Perkin-Elmer Lambda 950 Uv/Vis/NIR making a double baseline (100% and 0% of transmittance) or with Perkin-Elmer Lambda 650 spectrophotometer, making a single baseline (100% of transmittance). The molar absorption coefficient values were determined by applying the Lambert-Beer law; the experimental error is estimated to be $\pm 10\%$ and the precision on the wavelengths values was ± 1 nm.

6.2. Emission spectra

Steady-state photoluminescence spectra were measured in air-equilibrated and de-aerated solutions at room temperature, using an Edinburgh FLS920 fluorimeter, equipped with a Peltier-cooled R928 (200-850 nm) and supercooled R5509-72 (700-1800 nm) Hamamatsu phototubes, with different excitation wavelengths for different compounds. An Edinburgh Xe900 450W xenon arc lamp was used as excitation source. All the spectra were corrected for the photomultiplier response, unless otherwise specified, using a calibration curve supplied with the instrument. Luminescence quantum yields (ϕ) at room temperature were evaluated by comparing wavelength integrated intensities (I) of the corrected emission spectra with reference to [Ru(bpy)₃]Cl₂ ($\phi_r = 0.028$ in air-equilibrated water)¹, [Os(tpy)₂]Cl₂ ($\phi_r = 0.021$ in de-aerated butyronitrile)², quinine sulphate ($\phi_r = 0.53$ in air-equilibrated sulphuric acid 0.1 N)¹, coumarin 153 ($\phi_r = 0.544$ in air-equilibrated ethanol)³ and 5,10,15,20-Tetraphenylporphyrin ($\phi_r = 0.11$ in air-equilibrated toluene)⁴ standards, by using the following equation¹:

$$\phi = \phi_r \frac{I A_r n^2}{I_r A n_r^2}$$

where A and A_r are the absorbance values at the employed excitation wavelength, and n and n_r are the refractive indexes of the solvents, respectively for the investigated and the reference compound. The concentration was adjusted to obtain absorbance values $A \leq 0.1$ at the excitation wavelength for room temperature measurements and $0.1 \leq A \leq 0.2$ for low temperature measurements and emission maps.

Band maxima and relative luminescence intensities are obtained with uncertainties of 2 nm and 10-20 %, respectively.

The experiments at room temperature in air-equilibrated condition made use of solutions placed in quartz cuvettes (10 mm optical path), while for luminescence analyses in air-free condition, solutions were prepared by fluxing argon for *ca.* 25 minutes in homemade cuvettes (10 mm optical path) that can be sealed.

Luminescence measurements of CH₃OH:CH₂Cl₂ (1:1) or CH₃OH:C₂H₅OH (1:4) glassy solutions at 77 K were performed by employing quartz capillary tubes immersed in liquid nitrogen, and hosted within homemade quartz cold finger dewar. Phosphorescence spectra at 77 K were acquired in gated detection mode using a pulsed microsecond Xenon flash lamp µF920H with the Edinburgh FSP920 fluorimeter. Solid-state photoluminescence quantum yield values were calculated on neat films of the compounds (not controlled thickness) by corrected emission spectra recorded with the Edinburgh FSP920 fluorimeter equipped with an integrating sphere, coated with barium sulphate (diameter 10 cm) following published procedure.⁵

6.3. Luminescence lifetime measurements

Luminescence lifetimes were obtained using an IBH 5000F single-photon counting (TCSPC) apparatus equipped with a TBX Picosecond Photon Detection Module (Instrumental Response Function, IRF = 250 ps). Excitation of the samples was performed by using various light sources, such as: SpectraLED ($\lambda_{\text{exc}} = 370$ and 464 nm) and NanoLED ($\lambda_{\text{exc}} = 278, 373, 465$ nm) pulsed excitation sources, with different excitation wavelengths, and picosecond laser diode sources ($\lambda_{\text{exc}} = 407$ and 637 nm, typical pulse width < 80 ps, intensity *ca.* 4×10^7 photons/pulse) operating at a repetition rate of 1 MHz by the stabilized picosecond light pulser Hamamatsu PLP-02.

In some cases, in order to disentangle the contribution of different components to the observed global luminescence and to attribute the relevant lifetime to the single species we applied the global analysis to the individual kinetic traces recorded in time-resolved luminescence experiments (TRES). The decay-associated spectra (DAS) obtained by plotting the amplitudes of the individual kinetic components as function of the wavelength represent the true spectra of the individual decay components. These are identical to the spectra that would be obtained if the components were isolated and then measured individually.

Decay associated spectra (DAS) were obtained by global analysis of the kinetic data by using the global fitting module of the decay absorption spectra (DAS) 6.5 software (HORIBA Jobin Yvon) on the basis of a multi-exponential model:

$$F(\lambda, t) = \sum_i A_i(\lambda) \exp(t/\tau_i)$$

The goodness of the multi-component fitting was evaluated by the global χ^2 parameter and weighted residuals. The wavelength dependences of the amplitudes of the individual kinetic components were plotted as decay associated spectra (FDAS).

6.4. Transient absorption

Transient absorption investigations were conducted through nanosecond laser flash photolysis experiments, performed with a system based on a Nd:YAG laser (Continuum Surelite II, 5 ns pulse duration with an energy ranging from 1.9 to 3.1 mJ/pulse) by using its third harmonic ($\lambda = 355$ nm). Absorbance of the solutions at the exciting wavelength was $0.2 \leq A \leq 0.3$. Before the analysis the samples were bubbled with argon

for *ca.* 25 min and sealed in homemade 10 mm optical path length cells. The laser excitation beam crosses the monitoring light of a Xe arc lamp in a right-angle configuration.⁶

The light transmitted by the sample (10 mm optical path) is monochromated with 4 nm resolution and detected on a Hamamatsu R936 photomultiplier PMT or on a high-speed Silicon (DET210) or InGaAs (DET410) Thorlabs photodiodes different fotodiodes for visible and infrared regions, respectively. A digital oscilloscope in conjunction with a personal computer is used to acquire and process the signals with the Proteus and Surface Explorer softwares, respectively, by Ultrafast Systems.

6.5. Energy transfer

The rate constant for an intramolecular energy transfer process has been obtained from the equation:

$$k_{EnT} = \frac{1}{\tau} - \frac{1}{\tau_0}$$

where τ and τ_0 are the lifetimes of the emissions reported for quenched and unquenched donor, respectively. The efficiency has been evaluated from the equation:

$$\eta_{EnT} = \frac{k_{EnT}}{k_{EnT} + k_{in}}$$

where $k_{in} = 1/\tau_0$ is the intrinsic deactivation rate constant of the unquenched donor and k_{EnT} has been defined above.

For comparison purposes, the calculation of the energy transfer rates has been performed based on both the Förster and Dexter mechanisms, using corrected donor emission spectra and acceptor absorption spectra on a wavenumber scale. Computations of rate constants and the relevant spectroscopic overlap integrals were performed by using home-developed routines for MATLAB.⁷ The rate constant for energy transfer according to the Förster (k_F) and Dexter (k_D) mechanism, respectively, were evaluated by using the equations:

$$k_F = \frac{8.8 \times 10^{-25} \kappa^2 \phi}{n^4 \tau d^6} J_F$$

$$k_D = \frac{4\pi^2 H^2}{h} J_D$$

where $\kappa^2 = 2/3$ is the statistical orientation factor, ϕ is the photoluminescence quantum yield of the donor, n the refractive index of the solvent, τ the excited state lifetime of the donor in ns, d the distance between donor and acceptor in Å, as metal-metal separation (calculated from molecular modelling), H is the electronic coupling term and h is Planck's constant. The spectral overlap integrals J_F and J_D were calculated from the emission spectrum of the donor $D(\bar{\nu})$, and the acceptor absorption spectrum of the acceptor in molar absorptivity units $A(\bar{\nu})$, using the equations:

$$J_F = \frac{\int D(\bar{\nu}) A(\bar{\nu}) \bar{\nu}^{-4} d\bar{\nu}}{\int D(\bar{\nu}) d\bar{\nu}}$$

$$J_D = \frac{\int D(\bar{\nu}) A(\bar{\nu}) d\bar{\nu}}{\int D(\bar{\nu}) d\bar{\nu} \int A(\bar{\nu}) d\bar{\nu}}$$

6.6. References

-
- ¹ M. Montalti; A. Credi; L. Prodi and M. T. Gandolfi, *Handbook of Photochemistry*, CRC Press, Taylor & Francis, Boca Raton, 3rd edn, 2006.
- ² J. P. Sauvage; J. P. Collin; J. C. Chambron; S. Guillerez; C. Coudret; V. Balzani; F. Barigelletti; L. De Cola and L. Flamigni, *Chem. Rev.*, 1994, **94**, 993-1019.
- ³ K. Rurack; M. Spieles, *Anal. Chem.* 2011, **83**, 1232-1242.
- ⁴ P. G. Seybold and M. Gouterman, *J. Mol. Spectrosc.* 1969, **31**, 1-13.
- ⁵ (a) N. C. Greenham; I. D. W. Samuel; G. R. Hayes; R. T. Phillips; Y. Kessener; S. C. Moratti; A. B. Holmes and R. H. Friend, *Chem. Phys. Lett.* 1995, **241**, 89-96; (b) J. C. de Mello; H. F. Wittmann, and R. H. Friend, *Adv. Mater.* 1997, **9**, 230-232.
- ⁶ L. Flamigni; E. Baranoff; J. P. Collin; J. P. Sauvage, *Chem. Eur. J.* 2006, **12**, 6592-6606.
- ⁷ MATLAB 5.3.1, The MathWorks Inc., Natick, MA, USA (1999).

Chapter 7

7. Final Remarks

This thesis reports most of the works developed during the three years of my doctoral research activity.

It has been accomplished in the framework of the ESF-EUROCORES “SolarFuelTandem” project, whose main goal was the development of a bio-inspired nanostructured organic-inorganic heterojunction tandem cell for solar to fuel conversion.

In this project the, individual objectives of my PhD research can be summarized in three main tasks: (1) the study of the energy transfer processes occurring in supramolecular antenna systems, for collection of solar light; (2) the characterization of catalysts for the water oxidation process, focusing on the redox states of the intermediates; (3) the analysis of an integrated system for solar energy conversion.

The points (1) and (3) have been discussed in the current work of thesis, that has been centred on the study of several types of systems able to perform light-harvesting and in some cases to promote the funneling of the excitation energy in a unique desired direction, mimicking natural processes and thus representing good models for the construction of antenna systems. Instead, the point (2), related to the characterization of single-site Ru(II) catalysts for the water oxidation process, has not been treated, reason why I want at least to mention it in the end.

Actually, for the construction of light-driven artificial photosynthetic devices, apart from the challenge of achieving suitable antenna systems, also the problem to optimise the catalytic water oxidation process is of fundamental importance. To this aim, it is crucial to gain accurate knowledge about the working mechanism of the catalyst. This issue has been tackled during the three years of my PhD activity, by the investigation of a new series of single site Ru(II) catalytic systems for water oxidation.

The catalysis of water oxidation process by transition-metal complexes has received considerable attention during the last years, thanks to the accessible synthesis, strong stability, robustness and efficiency of such systems. Recently, new classes of single-site water splitting catalysts able to form dioxygen in homogeneous conditions have been prepared¹ in addition to the most widely spread multi-nuclear ones. Following the same direction, the new series of mononuclear ruthenium water oxidation catalysts of the form $[\text{Ru}(\text{cy})(\text{L})(\text{H}_2\text{O})]^{2+}$ (cy = *p*-cymene, L = 2,2'-bipyridine or similar derivatives) has been analysed, with the main goal of characterizing the transient intermediate species generated during the catalytic cycle.² In these single ruthenium complexes, the metal centre is coordinated to a bipyridyl ligand (L) and stabilized by a cyclic conjugated hydrocarbon (cy = *p*-cymene). Such systems can be considered as suitable models for the design of more efficient water-oxidation catalysts and, for this purpose, it is important to understand the pathways that lead to O₂ evolution from water and the nature of the involved intermediate species.

A detailed characterization of the one- and two-electron oxidized intermediates of the catalysts has been carried out using different techniques: for the long lived species, UV-

Vis spectroscopy supported by stopped flow apparatus, and for the transients with short lifetimes, pulse radiolysis. In the first case, $[\text{Ce}(\text{NH}_4)_2(\text{NO}_3)_6]$ has been used as sacrificial oxidant, activating the metal complex towards oxidation process. Upon addition of 10 eq. of Ce(IV) to $[(\text{cy})\text{Ru}^{\text{II}}\text{L}-\text{H}_2\text{O}]^{2+}$ in acidic solution, gradual formation of a new species is achieved, whose absorption features are ascribable to the Ru(IV) species involved in the cycle.³ In the second case, sulphate radical anion $\text{SO}_4^{\cdot-}$ has been chosen as sacrificial one-electron oxidant. The reaction between $\text{SO}_4^{\cdot-}$ and the complex at pH 1.4 in HClO_4 diluted solution yielded the one-electron-oxidized species, revealed by two distinct peaks in the absorption spectrum, that could agree with the spectrum of the elusive Ru(III) species.

The comparison between the experimental optical properties and the absorption spectra computed with time-dependent DFT based modelling, in collaboration with the group of Prof. Huub de Groot at the University of Leiden, provides a convincing validation of the proposed catalytic cycle, involving four proton-coupled electron transfer (PCET) steps, and a clear characterization of the intermediate complexes observed optically.

The good agreement between the optical data with DFT predictions establishes the general applicability of this methodology as a powerful tool in the characterisation of other water oxidation catalysts and for the interpretation of experimental observables.

The results of the study have been the subject of a publication, which is now under evaluation at the PhysChemChemPhys journal.

6.1. References

-
- ¹ (a) R. Zong; R. P. Thummel, *J. Am. Chem. Soc.* 2005, **127**, 12802-12803; (b) K. S. Joya; J. L. Vallés-Pardo; Y. F. Joya; T. Eisenmayer; B. Thomas; F. Buda; H. J. M. de Groot, *ChemPlusChem* 2013, **78**, 3 5-47.
- ² J. de Ruiter; A. Monti; M. P. Gullo; K. S. Joya; M. D'Angelantonio; A. Barbieri; H. J. M. de Groot; F. Buda, *Phys. Chem. Chem. Phys* 2015 (Submitted).
- ³ D. E. Polyansky; J. T. Muckerman; J. Rochford; R. Zong; R. P. Thummel; E. Fujita, *J. Am. Chem. Soc.* 2011, **133**, 14649-14665.